Carbon Electronics

Nano-carbons for the development of radiation sensors, image intensifiers and medical sensors

Suguru Frederick Amakubo

Department of Electronic Engineering

University College London

Great Britain

2016

Declaration

I, Suguru Frederick Amakubo hereby confirm that the work presented in this thesis is my own and my own only. Where any information that has been derived from other sources have been rightfully credited.

Suguru Frederick Amakubo

Acknowledgement

Life has never been easy for me. I was born into a difficult environment under difficult circumstances and lady Fortune didn't seem to show any clemency. However, I was not alone. At every turn of my life, there were those whom have put forth a helping hand for me. Some of those who have taught me everything I know. Some of those who I grew up with. Some of those who have cared for me and some of those who have believed in me. Sadly, not all of them are with us today. I, however do like to think that they continue to live within the lives of those they have touched. Which I am forever grateful for, includes me. It was difficult at times and sometimes it felt like a lonesome road but I like to think through their hard work they have changed my life for the better, forever. I am a product of those who have helped me and in the truest of all sense, I believe I stand on the shoulders of giants. Often the good in people is overlooked in the world we live in but please remember that I have seen the good in each and every one of you who were kind enough to help me. I will promise to pass on your acts of kindness when the time comes as it is the only way I could ever repay you all. There are too many to thank and too little words to thank you with. So, for now, thank you to each and every one of you. Until the day I do enough good for someone for them to think the same of me. Thank you.

Abstract

Carbon nano-materials, both in sp^2 (graphene like) and sp^3 (diamond) configurations are renowned for their unmatched novel properties. In particular, its extremely high electrical conductivity, radiation hardness and electron amplification are widely coveted. This investigation aims to capitalise on the above by developing blood pressure sensors, radiation detectors and signal amplifiers from the said carbon nano-materials. Namely, carbon nanotubes (sp^2 carbon) were integrated into a polymer host to form a composite. Where it has been found that by altering the surface functionalisations of carbon nanotubes (non-functionalised, -OH and -COOH) the electrical resistance of the composite could vary drastically as much as $10^{12}\Omega$ to $10^{7}\Omega$. This brings potential benefits in reduced production costs, reduced environmental damage and wider technological adoption of carbon composite based devices. Carbon nanotubes were then encased in a soft and biocompatible host, polydimethylsiloxane (PDMS), in order to fabricate an *in vivo* blood pressure sensor, exploiting its piezo-resistivity. Results have shown a successful and adequate degree of piezo-resistivity ($10^{9}\Omega$ to $10^{6}\Omega$ for 2D and 4kΩ to 750kΩ for 3D compression) at the desired size-scale of 200μm and 4mm respectively. This is a size equivalent to that of the diameter of blood vessels in question. However, further investigation into re-miniaturisation is recommended for future works. Diamond (sp^3 carbon), on the other hand, was used as a long-lasting solution to neutron detection for a Trident nuclear submarine, HMS Artful. The investigation entailed a three-phase process of: α-particle detection, LiF conversion layer addition and neutron detection. Results has shown clear signs of α-particle and neutron detection with a device efficiency of 32.3% and 48.3% respectively, as well as γ-ray transparency and sufficient Q-factor between the signal peak and detection peak. Diamond was also used as a signal amplifier that has application as an image intensifier for night-vision goggles where it was found that

by altering the surface functionalisation of nano-diamonds (H, O and LiO) one could enhance or suppress the secondary electron emission effect. Additionally, it was found that the electrical gain from the said secondary electron emission has a strong dependence on the crystal structure of the diamond layer and in turn its growth conditions. Most notably, LiO functional group was found to be more resilient towards higher temperatures (800°C) and electron bombardments but fell short in the amount of electrical gain it generated in comparison to conventional functionalisations such as H. However, the X-ray photoelectron spectroscopy (XPS) results suggest that this may be due to the lack of LiO coverage and upon further investigation, LiO may potentially bode better if not surpass the gain performance of H.

Research Presentations

1. **XXII International Material Research Congress, Cancun, 2013** Nanocarbon polymer device fabrication for medical applications (Ver.1)

2. **XXIII International Material Research Congress, Cancun, 2014** Nanocarbon polymer device fabrication for medical applications (Ver.2, revised with updated results and development, 2014)

3. **ETC (Brunel University) Open Day, 2014 [Invited speaker]** Nanocarbon polymer device fabrication for medical applications (Ver.2, revised with updated results and development, 2014)

4. **XIX Hasselt Diamond Workshop, 2014** Nanocarbon polymer device fabrication for medical applications (Ver.2, revised with updated results and development, 2014)

5. **UCL EEE Mildner Memorial Lecture and Research Open Day, 2012** Electrical conductivity in carbon-nanotube-polymer (Ver.1)

6. **UCL EEE Mildner Memorial Lecture and Research Open Day, 2013** Electrical conductivity in carbon-nanotube-polymer (Ver.2, revised with updated results and development, 2013)

7. **UCL EEE Mildner Memorial Lecture and Research Open Day, 2014** Electrical conductivity in carbon-nanotube-polymer (Ver.3, revised with updated results and development, 2014)

Contents

Chapter 1

Introduction

Carbon perhaps is one of the most versatile materials in existance. In its purest form it could both be a coveted gemstone, diamond and a worthless waste, soot. If bonded to other elements it can even form a diverse family of chemical chains known as polymers and the foundation of all life forms, amino acids. Carbon in fact is the only element on the periodic table that has a dedicated school of chemistry to itself known as organic chemistry. Of these various forms of carbon this thesis has been dedicated to two pure forms of carbon: sp^2 carbons such as carbon nanotube (hereafter CNT) and sp^3 carbons such as diamond. Although the detailed description of each carbon will be reserved to their respective chapters it is worth noting that neither sp^2 nor sp^3 carbons were explored for their impressive physical and electrical properties until recent years. Diamond for example was only known as a gemstone for the vast fraction of human history until the recent discovery of its novel semi-conductor properties. A truly fascinating fact is that during the cold war due to the lack of communication across the eastern and western hemisphere two very different forms of diamond fabrication have been invented during this time. In the east, Soviet Russia has focused on the three crucial components of diamond fabrication: carbon, heat and pressure. Their solution to the problem was to create a colossal blast chamber the size of an athletic track where they could detonate large amounts of explosives in order to instantaneously form diamonds using its pressure waves. Diamonds created in this

manner for this reason are now known as detonation nano-diamonds (DNDs)[1]. In the west on the other hand an entirely different approach was taken where diamonds were 'grown' atomic layer by layer by passing a carbon based gas over a substrate and activated either thermally or by an electrical discharge, in a process that is now known as chemical vapour deposition (CVD)[2]. Carbon nanotubes on the other hand are often seen as a more modern material due to its more rescent discovery by S. Iijima in 1991[3]. However a lesser-known fact is that CNTs were unknowingly used by Syrians as far back as 900AD[4] infused into sword steel as reinforcement agents with some reports even suggesting its use to go as far back as 2500BC. In recent years CNTs are mostly used as reinforcement agents for host materials such as in cement[5] and as semiconductor gates for field effect transistors[6] exploiting its unusually high electrical conductivity[7] and tensile strength[8]. Although the said novel properties of CNTs were well known from the early stages of its discovery, CNTs have particularly enjoyed two events that catalysed the media and academic attention that ultimately lead to the explosive increase in the number of scientific publications. One of these is the awarding of the 2010 Nobel Prize in Physics for the discovery of CNT's sister material, graphene[9] and the other the discovery of catalytic decomposition, a manufacturing method of CNTs that allowed the daily yield of CNTs to increase by 1000 folds[10] that has allowed the economy of scale to bring the price of CNTs down substantially thus allowing greater access to scientists eventually leading to the increase in the number of publications.

Chapter 2 will address the intrinsic natures of carbon most notably its electronic configuration that brings rise to the formation of multiple allotropes such as CNT, diamond, graphene and carbon onion. Each of the mentioned allotropes will be further explained with descriptions of their physical structures, functionalisations, notable defect types, doping, production methods, and electronic properties.

Chapter 3 outlines the fundamental nature of three devices that will be made during this investigation: Diamond neutron detectors, polymer composites and

heart failures monitors.

Chapter 4 reviews the experimental methods used during the investigations where the theory and objective of each method will be explained.

Chapter 5 is the first of the five experimental chapters. In this chapter the electrical properties of CNT-epoxy composites were investigated by measuring their impedance. This chapter aims to identify the influence of: functionalisation (-COOH and -OH), CNT concentration, lengths and width of the CNTs to the conductive nature of the CNT-epoxy composite. The results have shown some interesting phenomena whereby altering the surface functionalisation of the CNTs the resistance of the composite could be altered drastically by several orders of magnitude from $10^7\Omega$ to $10^{12}\Omega$ due to its influence in the degree of CNT agglomeration.

Chapter 6 aims to fabricate an *in vivo* blood pressure sensor making use of the piezo-resistive nature of CNT-polymer composites. In a similar manner to chapter 5 this investigation infuses CNTs into a polymer host. However for the purpose of bio-compatibility polydimexylesiloxane (PDMS) has been chosen as its host polymer. Impedance of the composite was measured while the composite was under pressure and the results have shown signs of pressure sensitivity. Ultimately, post miniaturisation the pressure sensitive composite is designed to be injected into a pulmonary vein in order to passively and wirelessly monitor a patient's blood pressure, thus being able to detect and alert medical personnel in the event of a heart failure.

Chapter 7 presents the investigation that was carried out by the request of BAE systems where they required a durable, radiation hard and gamma ray blind neutron radiation sensor to be used on board the latest generation Trident nuclear submarine, HMS Artful. The radiation sensor was made using a very thin film of diamond that showed evidence of successful gamma ray discrimination and neutron capturing. The diamond detector was tested in two stages: firstly the detector was tested for its alpha radiation detection capabilities followed by its neutron detection test. The alpha test was a necessary step for neutron testing as

neutrons are notoriously difficult to detect and are best made detectable by first converting them into alpha particles that diamonds are known to detect readily. Most importantly the diamond detector fabricated during this investigation is required to survive through the expected 25 years lifetime of the submarine. Thus diamond, a radiation hard material was used over conventional semi-conductors such as silicon.

Chapter 8 attempts to achieve a high secondary electron emission yield generated from the surface of a LiO functionalised diamond surface. The objective of the investigation is to achieve signal amplification by multiplying the number of electrons utilising diamond's ability of secondary electron emission, an effect where diamond ejects more than one secondary electrons per primary electrons through negative electron affinity. The measurements were taken by bombarding the surface of a diamond film on conductive silicon with electron beams and measuring the ratio between the injected electrons and the electrons ejected. The diamond amplifier fabricated in this investigation is expected to be particularly useful as signal amplifiers in night vision devices.

Chapter 9 summarises the thesis.

Chapter 10 evaluates areas of improvements that could be made for future investigations.

Chapter 2

Introduction to Carbon

2.1 Introduction

Carbon is one of the most versatile elements known to man. At the heart of this versatility lies carbon's ability to bond with foreign elements. Carbon not only has the capability to bond amongst each other in three different manners (sp, sp^2 and sp^3[11]) but it also forms a stable bond with other elements such as nitrogen, oxygen and many more[11]. This chapter aims to outline the fundamental nature of carbon as an element as well as its different allotropic forms in order to supplement the scientific understanding of this investigation.

2.2 Elemental Nature of Carbon

Carbon is the 6th material on the periodic table with chemical symbol C and an atomic mass of 12. There are 3 common isotopes of carbon: ^{12}C, ^{13}C and ^{14}C where ^{14}C is known to be radioactive with a half life of 5730$\pm$40 years[12]. Carbon naturally comes in three forms of electron hybridisation: sp, sp^2 and sp^3[11], all of which exhibit very different electrical, mechanical and topological characteristics to each other. Most notably sp^2 hybridisation has a unique trait that it could take many allotropic forms (Fig.2.1) utilising the same type of bond configuration.

Despite its elemental abundance much of carbon in its purest form such as

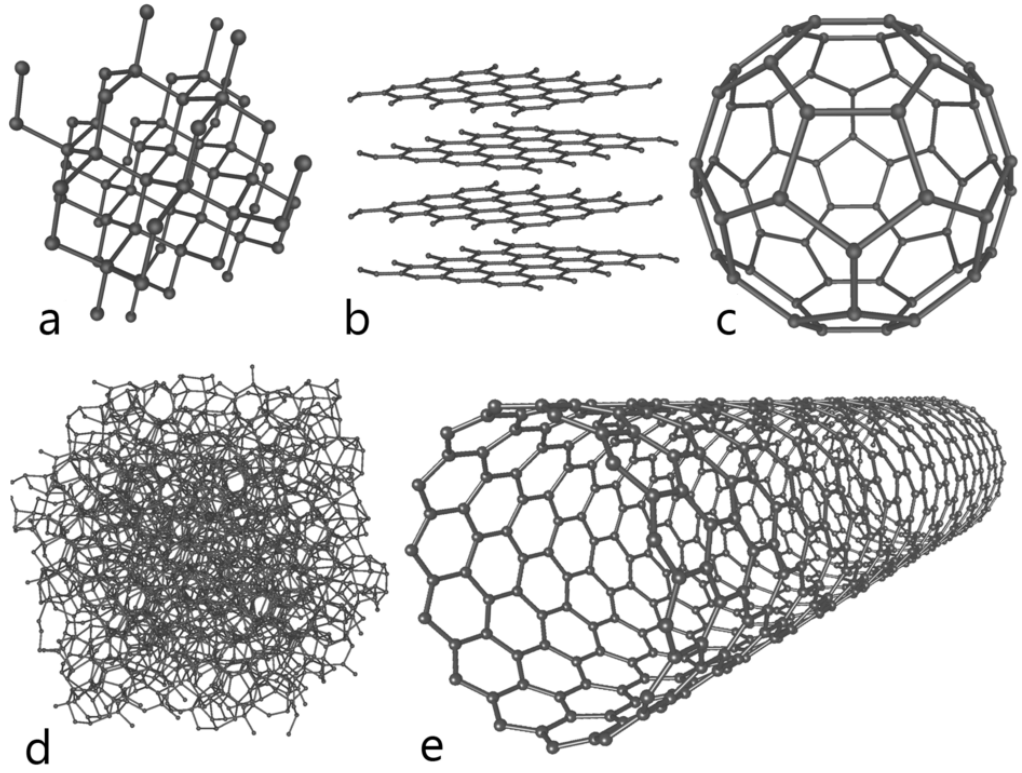

Figure 2.1: Allotropes of carbon: a) Diamond (sp^3), b) Graphite (multi layer graphene, sp^2), c) Buckminister Fullerene (sp^2), d) Amorphous Carbon (sp^2 and sp^3), e) Carbon Nanotube (sp^2)[13].

diamond and carbon sp^2 allotropes has only been explored for its novel characteristics in recent years. The increase in its scientific interest is often credited to the improvement both in measurement and manipulation of nano-scale materials. In particular the aforementioned sp^2 hybridised carbon such as carbon onions, carbon nanotubes (CNT) and graphene are all rich areas of research at the time of writing (2016) and it is still very much in its preliminary stage of development.

2.3 Hybridisation of Carbon

2.3.1 Principals of Hybridisation

As mentioned earlier carbon could be hybridised in three different forms: sp, sp^2 and sp^3[11]. The section below will describe the bond nature of the sp^2 and sp^3 hybridisation followed by its respective explanation as to how they manifest itself

in nature. sp hybridisation will be omitted for its limited importance to this research.

Hybridisation in carbon occurs as a result of the availability of four outer shell electrons and their ability to occupy different subshells of the same energy[14]. The first shell, $1s^2$ (the inner core shell) is occupied by two electron of opposite spins where due to the stability of the energy levels are inert to almost all reactions involving carbon in nature[14]. The second shell however due to Pauli's exclusion principle, which forbids fermions such as electrons to possess the same quantum number, enables electrons to potentially occupy up to 4 individual sub shells (2s, $2p_x$, $2p_y$, $2p_z$)[14]. If one of the electrons in the 2s shell were to be excited, the electron would redistribute itself into a more energetically stable state[14]. This process is known as hybridization and it will alter the shape of the bond[14]. For example if each of these subshells are occupied by one electron per subshell, it could individually form a covalent bond through sigma bonds (σ-bonds). As a result of four sigma bonds being available this will bring rise to the well-known bond geometry of diamond, tetrahedral[14]. However, of the four bonds available if the carbon exhibits three sigma bonds and one pi bond (π-bond) only three of the bonds are able to form a covalent bond creating a trigonal planar structure typically seen in graphite[14]. Although it will be further explored in the later section of this chapter it is worth noting that both of the aforementioned sigma bond and pi bond are capable of bonding to non-carbon elements that allows both sp^2 and sp^3 carbon to be functionalised[15].

2.3.2 Orbital Hybridisation of sp^2

One of the most notable features of this hybridisation is the availability of three σ-bonds and one π-bond[14]. Each of the σ-bonds typically connects one carbon atom to another, creating a hexagonal two dimensional (2D) network of carbon molecules[13]. Alternatively it could form bonds with other elements and functional groups at its terminal nodes[15]. This orbital configuration typically is highly conductive due to the availability of free flowing electrons from the π-

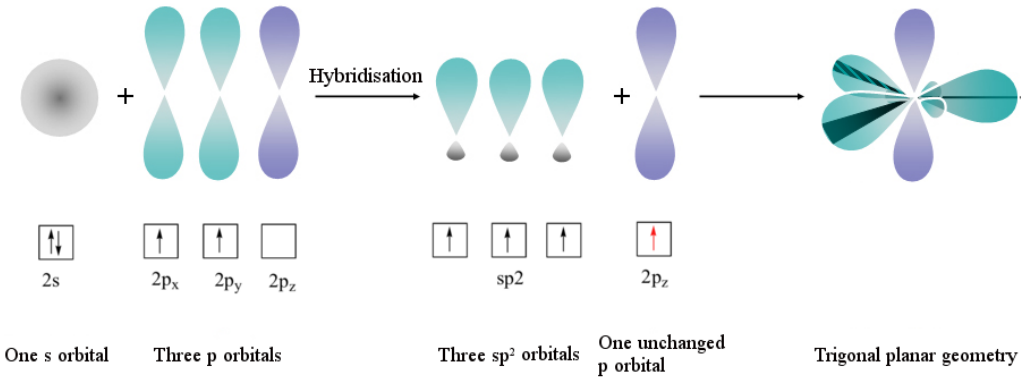

Figure 2.2: sp^2 hybridisation of carbon bonds forming a trigonal planar[16][17].

bonds[18]. Examples of sp^2 hybridised carbons include: graphene, carbon nanotube (CNT) and buckminister fullerene/carbon onion (Fig.2.1).

2.4 sp^2 Allotropes

In the process of addressing sp^2 carbon it is almost impossible to negate the importance of understanding the characteristic of each allotropes. This is principally due to the fact that many of the characteristics that are exhibited by one type of sp^2 carbon could often be explained by a typical characteristic of another. Although this will be further explained in the section below typically all forms of sp^2 carbon has a tendency to 'inherit' the character of graphene the simplest form of sp^2 carbon and the degree to which the character adheres to this tendency is dependent on how 'graphene-like' the sample is. Therefore although this investigation employs carbon nanotubes as its sole source of sp^2 carbon it will also address other forms of sp^2 carbons such as graphene and carbon onion in order to further understand the nature of carbon nanotubes.

Graphene Graphene is the simplest allotrope among sp^2 carbons. It is a single sheet of carbon arranged in a hexagonal web held together by three sigma bonds in a trigonal structure (Fig.2.2). Despite its recent academic attention the material itself has been known to man for many years as graphite, a multi layer variant of graphene (Fig.2.1b). It has however in recent years received a vast amount

of media coverage due to the awarding of the Nobel prize in 2010 to researchers Geim and Novoselov in Manchester University[9]. Recent findings has suggested that graphene in its isolated state is predicted to have an electron mobility as high as 200,000$cm^{-1}V^{-2}$ when suspended in vacuum (5×10^{-5}mTorr)[19] far superior to that of its industry standard counterpart, silicon which has a mobility of $1200\pm100cm^{-1}V^{-2}$[20]. The electron mobility of graphene however is currently facing a number of technical challenges. One example of this is the need to find graphene a suitable substrate. Graphene, despite being known for its extremely high intrinsic strength[21], suffers from the fact that it is a single layer of carbon making it a very fragile material to work with. Despite media hearsay of it being able to withstand the weight of an elephant standing on a pencil it is simply no match for a thicker bulk material. Therefore in reality graphene is extremely delicate and requires a suitable substrate to reinforce it. However the electron mobility of graphene was unfortunately found to decrease substantially once it comes into contact with another material[19]. Therefore while currently at the time of writing graphene is seen as a material that holds great potential it struggles to withstand the test of practice. Its true value lies in the fact that by understanding the base characteristic of graphene one could use it as a reference to benchmark against when investigating other derivative materials such as carbon nanotubes (CNTs) and carbon onions/buckyballs (Fig.2.3). As many of these other sp^2 allotropes has the tendency to inherit some of the characteristics from graphene and the more 'graphene-like' they are the greater the tendency for them to show similar characteristics to graphene.

One example of this is the diameter of the CNTs. Graphene as mentioned earlier is known for its high electric conductivity[19]. In light of this, if one were to look at a CNT with a large diameter where the surface curvature of the CNT would be relatively small. The surface of the CNT locally will appear flatter, somewhat resembling the surface of graphene. Thus the greater the diameter of CNT is the more graphene like it is and thus the greater the electric conductivity will be [22].

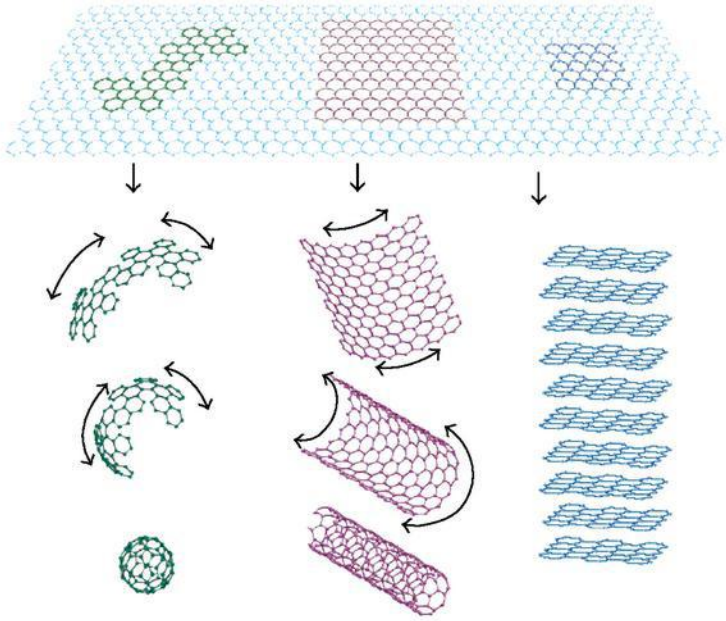

Figure 2.3: Formation of different sp^2 allotropes from graphene. From the left to right: bucky ball/carbon onion, carbon nanotube and graphite[23].

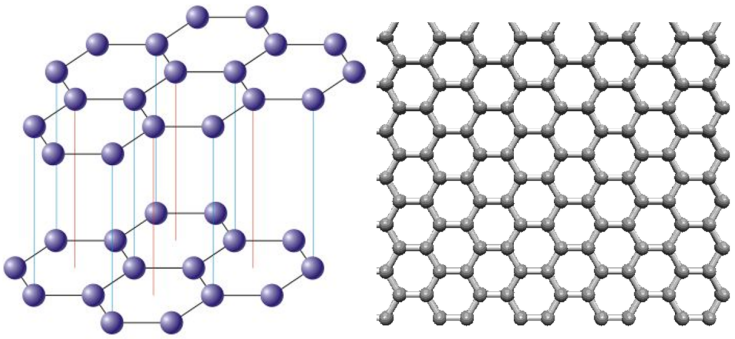

Figure 2.4: Side view of double layer graphene and birds eye view of graphene (left to right)[24][25].

Carbon Onion/Fullerene Buckminsterfullerene was first discovered in 1985 by Kroto *et al.* from Rice University[15]. In their findings they have discovered Buckminster fullerene, or C_{60} a ball of sp^2 carbon that resembles a football (Fig.2.1c) consisting of 12 pentagons and 20 hexagons[26]. This ball of carbon is in fact one form of carbon nano-onion (CNO), a sphere of carbon that consists of concentric carbon shells (Fig.2.5).

However carbon onion as seen from Fig.2.3 could also be made entirely out of

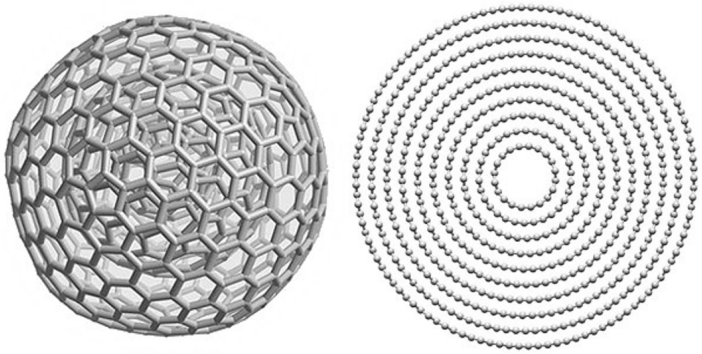

Figure 2.5: Side view of CNO and cross section of CNO (from left to right)[27][28].

hexagonally arranged carbons. CNO is seen to have multiple application due to its high surface area and the presence of both π (pi) and σ (sigma) bonds that allows functional groups to be added to the surface[10]. The addition of functional group is further supplemented by the fact that sp^2 carbons could be perforated[29] by a process called 'activation' typically using KOH to allow further access to the π and σ-bonds on the inner layers (Fig.2.6).

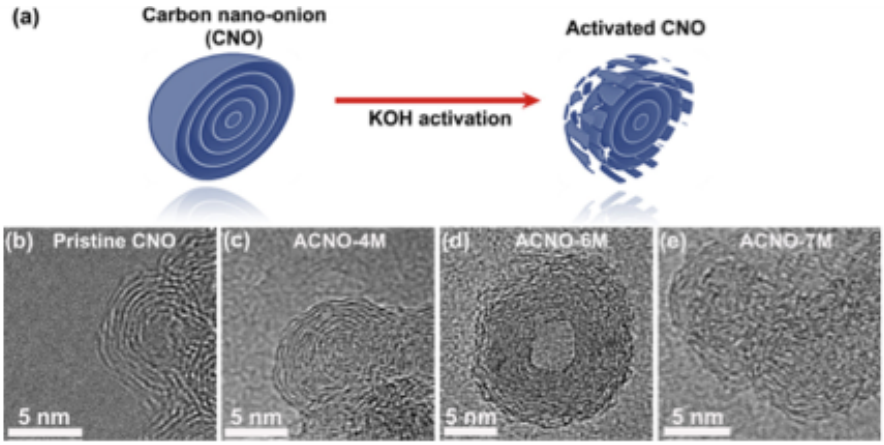

Figure 2.6: (a) Chemical activation of CNOs in KOH. (b) TEM image of non-activated CNO, (c) Activated CNO using 4 mole of KOH, (d) Activated CNO using 6 mole of KOH, (e) Activated CNO using 7 mole of KOH[29].

Activation is a process not only reserved for CNOs but its effect is universal across the whole of the sp^2 carbon allotropes. However due to CNO's high curvature geometry CNOs tend to be much more reactive than CNTs and graphene. Although typically activation of sp^2 carbons are carried out by a reducing agent

such as KOH[29] it could just as effectively be carried out by an oxidizing agent such as nitric acid or sulphuric acid[30].

Moreover CNOs are known to be able to have multiple derivatives (Fig.2.7) such that they are able to be tailored to its various application. The use of CNOs ranges widely from super conductors[31], liquid crystals[32] to H_2 fuel storage[33] but above other uses CNOs probably have undergone the most development as electron acceptors in solar panels[34]. In fact many available solar panels at the time of writing are being made using fullerenes[26] and no other compound class is known to surpass fullerenes as an electron acceptor[34].

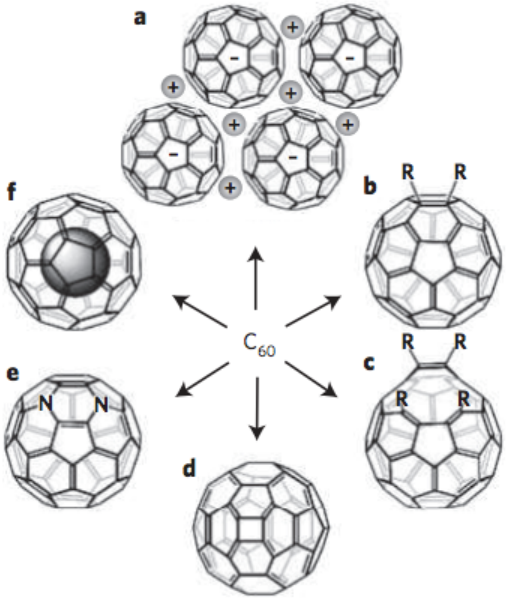

Figure 2.7: Derivatives of CNO/fullerene: (a) fullerene salt, (b) exohedral adduct, (c) open-cage fullerene, (d) quasi-fullerene, (e) hetro-fullerene, (f) endohedral fullerene[26].

Carbon Nanotube The last allotrope of sp^2 carbon, carbon nanotube (CNT) was first discovered in 1991 by Iijima *et al.* at NEC[3]. Structurally, CNT is a rolled up layer of graphene often capped at both ends with fullerene like lid to form a tube. They come in both single wall and multiple wall variants and they are known to be extremely rigid[8]. However, the most important feature of all is its electrical characteristic where they are able to be both metallic and

semi-conducting depending on its chirality[35] (Fig.2.8).

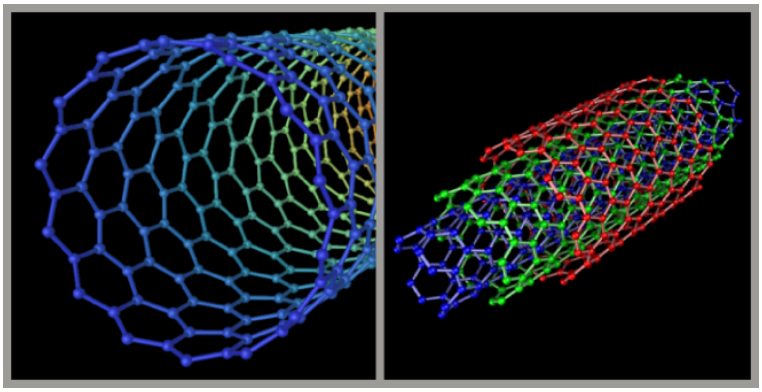

Figure 2.8: The cross sectional view of single and multiple walled carbon nanotube (left to right respectively)[36].

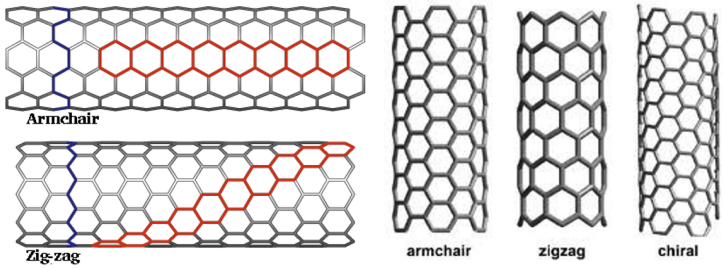

Figure 2.9: Side view of various chiral structures that carbon nanotube could take[37][38].

The electrical nature of each chirality are:

- Armchair = Metallic[35]
- Zig-Zag = Semiconducting[35]
- Chiral = Metallic or Semiconducting[35]

In particular the metallic nature of CNTs are most widely utilized in the field of polymer composites.

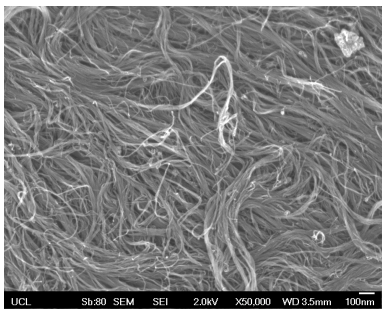

Figure 2.10: Scanning electron microscope (SEM) images of CNTs.

2.4.1 Fabrication of CNTs

Bulk Production of CNTs Despite the promising characteristics of CNTs much of it is yet to diffuse into mainstream applications. One of the reasons for the latency in widespread application is due to its carcinogenicity originating from its structural resemblance to asbestos[39]. However much of the blame is to lie with the cost of CNT production. Traditionally CNT production in a typical factory was limited to 50-120g per day[10] using methods such as electric arc discharge and laser ablation[10]. However recent development into CNT production from chemical vapour deposition (CVD)/thermal decomposition has enabled the bulk production of CNTs to the extent that the economy of scale was able to bring the price down to as low as £159.60 per 10g (Sigma Aldrich, multi-walled CNT, diameter×length 110-170nm×5-9μm, No.659258-10G, price at 2014)[40]. It is reported that a typical factory by using CVD could yield amounts as large as 50kg per day[41]. Therefore much of modern commercial CNTs are produced using CVD, where hydrocarbon gases (such as methane) are catalised by metal nano-particle (Co and/or Fe) in a pressurised furnace at 1000-1100^{o}C with precursors for the CNTs to grow from (e.g. $Fe(CO)_5$ for linear growth[41] or Al_2O_3 for orthogonal growth[42]). However despite CVD's best efforts to make CNTs a viable candidate for many specialised applications it still suffers from the issue of purity. The CNTs produced in this manner is usually contaminated by some nominal amount of amorphous carbon, fullerenes and metal catalysts (e.g. Co, Ni, Fe etc...)[10], where catalyst allows the formation of CNTs by dissolving

the carbon creating an environment where new bonds could freely form. In an effort to improve its quality the CNTs produced in industry are usually washed and purified to >95% before being sold. Fig.2.11 represents the flow chart of the purification process.

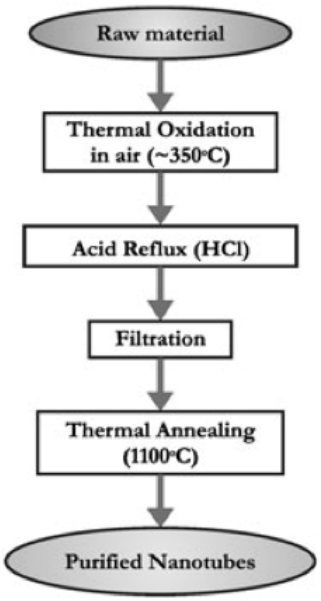

Figure 2.11: The purification process of industrially produced CNTs[10]:

1. Amorphous carbon is removed by oxidation upon heating to 350°C. CNTs would survive this process due to its stable sp^2 bond structure. This process also releases some of the metal catalyst trapped within the carbon confinement.

2. Metal catalyst is washed away using heated HCl (reflux).

3. The washed solution is then filtered to extract the CNTs.

4. The CNTs are then finally annealed at 1100°C in order to remove surface defects.

One should note at this point that inevitably due to the nature of the process the sp^2 carbon cage surrounding the metal precursors are broken in order to

release them. The CNTs produced in this manner has a tendency to be somewhat damaged. The chemical process used is identical to that of the one used in the activation method for carbon onions and this process is also known to add carboxylic and hydroxyl groups to the exposed sigma bonds[10].

Individual Production of CNTs Many in the academic circle may opt to have individual CNTs to experiment on. Under those circumstances it is wise to produce CNT anchored onto a substrate. Typically a catalyst is deposited on a substrate and heated to 600-1000°C in the presence of a carbon source gas such as methane[43] or alcohol vapour[44] (Fig.2.12).

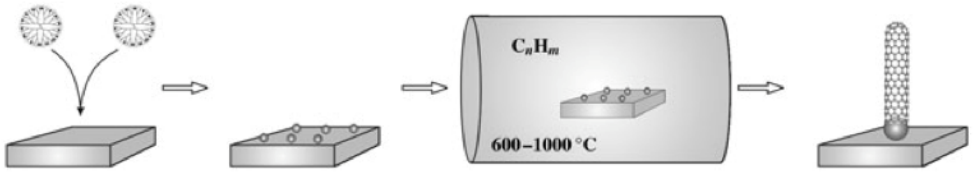

Figure 2.12: The production of individual CNTs. From left to right: deposition of catalyst particles, catalysts on substrate, annealing of substrate and catalyst, growth of CNTs on catalytic precursors [10].

Aside from the advantage of having control over the access to individual CNTs. CNTs grown in this manner could be varied in diameter by controlling the size of the catalyst precursor that it is grown from[45].

2.4.2 Reactive Sites of CNTs

Being a product of sp^2 carbon, CNTs are generally known to exhibit excellent chemical stability. For this reason inducing a chemical reaction to add functional groups to CNTs have traditionally proven difficult. However CNTs inherently has a few chemically vulnerable reaction sites that could be exploited for functionalisation:

1. The tip of the CNT. CNTs can come in two tip configurations: capped and uncapped. If the tip was to be uncapped the reactants has a direct access to the σ-bonds allowing the reaction to occur relatively easily[46]. On the other

hand if the CNTs are to be capped it has a fullerene like dome on the top where the pinnacle is likely to consist of a 5 carbon member ring (pentagon). This particular location is known to be more reactive than its 6 member[47] variant due to the strain that is forced upon each individual bonds, where the 5 member rings geometrically are bonded to each other with a greater strain in comparison to bonds in a 6 member ring. It is generally accepted that such strain allows the bonds to require less energy to break creating a vacant σ-bond reaction site for functional groups to bond to.

2. Curvature of CNTs. If the CNTs were to have a large diameter the curvature of the surface will be low. Looking at this from a topological perspective it allows us to say that the CNT shell is more 'graphene like'. Therefore the greater the diameter the lower the curvature and the closer the reactivity it will be to graphene[10], which as stated earlier is known to be extremely low. For this reason CNTs of smaller diameter is known to be more reactive than their wider variants.

   Another point to note that is often overlooked is the reactivity of CNTs from within the CNT itself. It is know that the reactivity of addition reaction on a concaved surface is extremely low[30]. This may seem rather deceiving at first as the reaction is occurring on the very same surface as it does from the outside. However, exploiting this property there has been investigations into the use of fullerenes, a fully concaved carbon surface to encapsulate reactive materials such as hydrogen to be used as car fuel storage[33].

3. Defect sites. All sp^2 carbons allotropes are known to be prone to a certain type of bonding inconsistency called the Stone-Wales defect. This is a structural inconsistancy that consists of two 7 carbon member rings and two 5 carbon member rings instead of its usual 6 (Fig.2.13). Typically 1-3% of the carbons in a CNT is known to be a part of the said defect[48].

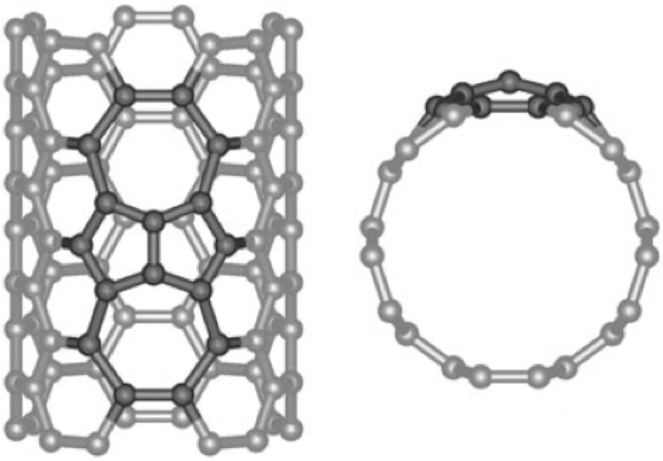

Figure 2.13: Stone-Wales defect. The carbons are connected through 7 member and 5 member rings that has a notable arching on the surface (image right)[10].

This defect holds significant importance to functionalisation as addition reactions are known to be favoured at these sites[49]. This stems from the fact that Stone-Wales defect forces the sp^2 plane to create an arch which in effect creates a locally curved reaction location that for the reason stated above are known to be more reactive.

2.4.3 Functionalisation of CNTs

Analogously to that of graphene and CNOs, CNTs could also be functionalised either by an addition reaction to the π-bonds or by adding a functional group to the σ-bonds by breaking the hexagonal structure open (Fig.2.14). However in general it is know that the addition reaction prefers σ-bonds formation to that of π-bonds[10].

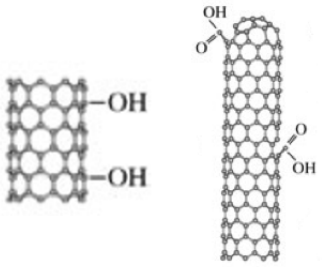

Figure 2.14: Addition reaction to the π-bonds (-OH) and to the σ-bonds (-COOH)(left to right)[10].

Two of the most important functionalisation methods are:

- Oxidation and carboxyl-based coupling[10]. The initial addition of –COOH through acid oxidation allows for other additional functional groups to react. This type of functionalisation will rely on the formation of σ-bonds by breaking open the hexagonal structure[10].
- Addition reaction to side wall[10]. Various functional groups are able to be added to the surface of the CNT (or any sp^2 carbon structure) utilising the π-bonds on the surface without the need to break open the hexagonal structure.

Oxidation of CNT and Carboxyl-Based Coupling This process was a major step towards the modern day sp^2 functionalisation due to the fact that it was able to break open the chemically stable hexagonal structure providing a location for the chemical species to be attached to. The process occurs in two stages, firstly a sacrificial functional group (-COOH) is added to the newly vacant σ-bonds. This is then followed by the secondary reaction that replaces the sacrificial functional group, with a plethora of available functional groups (Fig.2.15). The process first breaks open the sp^2 structure by ultra-sonicating the CNTs in a solution of sulphuric and nitric acid[50]. The chemically vulnerable sites such as that of the 5 member ring CNT cap and the Stone-Wales defects are broken open to form perforations along the side walls[10] followed by an oxidative

etch by the acid. The act of doing so will add the sacrificial -COOH group that could then undergo secondary reactions such as amination. Unfortunately the process of etching is also known to cause CNT fragmentation, where the CNTs are typically shortened to the length of 100-300nm[10]. However some research have claimed to have retained the CNTs' electronic and mechanical properties by using less vigorous methods such as reflux in nitric acid[51].

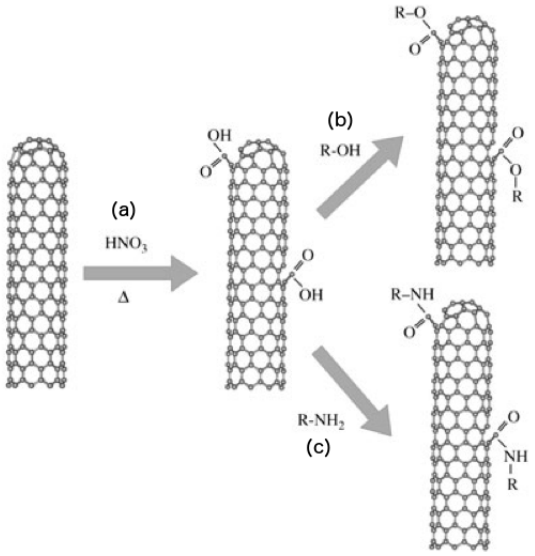

Figure 2.15: (a) Oxidation of CNTs to break the σ-bonds and addition of carboxylic groups, (b) Esterification of –COOH functionalised CNTs, (c) Aminisation of –COOH functionalised CNTs[10].

The process of esterification in Fig.2.15b will be of particular importance in the later section of chapter 5 when identifying the potential cause of the decrease in resistance observed from a –COOH functionalised CNT-polymer composite.

One additional point to note is the ability of the carboxylic group (-COOH) on CNTs to reduce the van der Waal's force amongst each other[10]. In another words -COOH functionalised CNTs are likely to avoid the formation of clusters that CNTs are known to do so inherently due to improved energetic stability.

In addition to the above effect –COOH functionalization is known to change the zeta potential, a property that indicates the solubility of a material. Research has shown that the –COOH functional groups will enhance the solubility of CNTs

into hydrophilic materials including hydrophilic polymers such as polyethylene glycol (PEG)[52].

Addition Reaction to CNT Side-Walls This particular type of functionalisation does not require σ-bonds to be broken open due to the fact that all of the required bondings comes from the coupling of the π-bonds present on the surface of the CNTs and the functional groups. This process usually requires a simple thermal activation of functional groups which is known to prefer CNTs of smaller diameter due to its enhanced reactivity[53]. Fig.2.16 represents many of the common addition reactions that are available to CNTs.

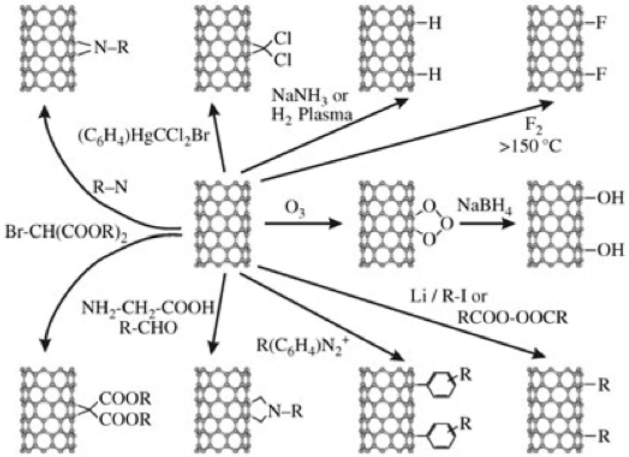

Figure 2.16: Examples of possible addition reactions[54].

Initial experiments has shown that only about 1 to 3 out of 100 carbon atoms of the total surface of the CNTs were functionalised through addition[55]. However more recent findings has found that this figure could be increased to >10%[10]. The overall coverage of functional groups however could be increased to up to 15% by employing the process of fluorination[56]. During this approach one would cover the CNTs with fluorine groups followed by a nucleophilic replacement reaction to add a different functional group onto its surface. The replacement reaction is known to be energetically much more preferable than that of the direct addition of functional groups and are known to achieve better coverage of functional

groups[54] (Fig.2.17).

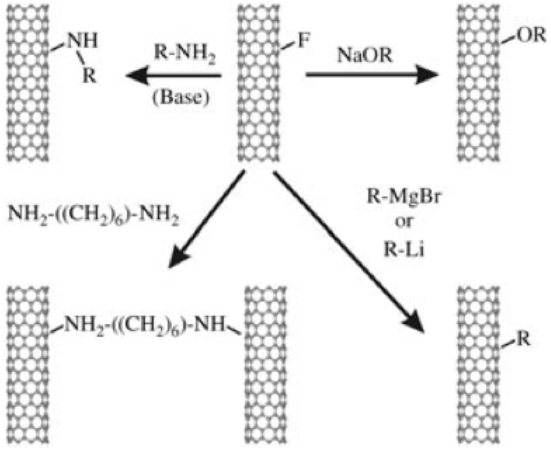

Figure 2.17: Possible nucleophilic substitutions of fluorine[10].

Whether the functionalisation was carried out by oxidation or addition it is worth noting that this approach is how –OH functional groups are added to CNTs. This holds particular importance in chapter 5 when understanding the nature of the hydrogen bonding between the CNT and the polymer chains in a composite.

2.4.4 Bandgap of CNTs

CNTs produced in the manner as described in the section 2.4.1 is not necessarily designed to bias the chirality of CNTs. The CNTs produced in this manner has the tendency to be $\frac{1}{3}$ metallic and $\frac{2}{3}$ semi-conducting [57]. The band gap is considered to be open for semi-conducting and closed for metallic. Another factor that affects the band gap is CNT diameter. Semi-conducting CNTs' band gaps are known to be inversely related to the diameter of the CNT[10]. As mentioned earlier in the section 2.4.2 one way of looking at this effect is to use graphene as a reference. The greater the diameter of the CNT is the smaller the curvature will be. Therefore looking the surface locally it is more 'graphene like' where graphene is known to have no bandgap thus closed and conducting. One common method of discriminating between the metallic and semi-conducting CNTs is the application of electric fields. This method exploits the fact that the electrical conductivity of

semi-conducting CNTs could be modulated by applying a field to it[58]. Freshly produced semi-conducting CNTs usually exhibit a p-type characteristic where the holes are the majority carriers[59] thus upon exposure to electric field the semi-conducting CNTs undergo field effect carrier migration. In contrast metallic CNTs are known to be oblivious to the presence of electric fields[59]. Therefore by applying the field on and off one could identify the type of CNTs that one has (Fig.2.18).

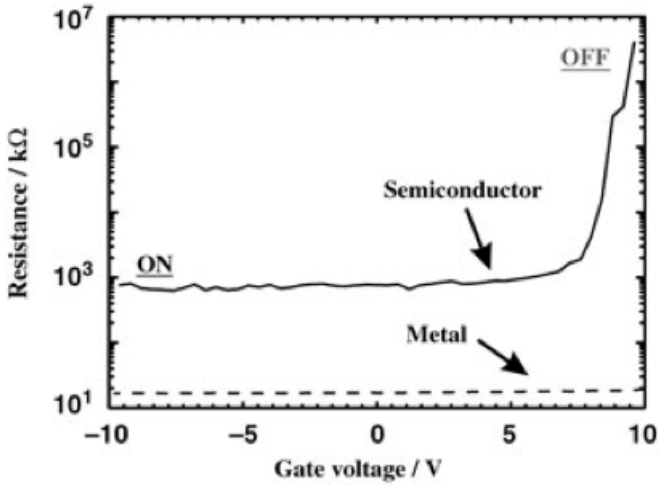

Figure 2.18: Dependence of room-temp resistance of metallic and semi-conducting CNTs on an external gate voltage[10].

2.5 sp^3 Allotropes

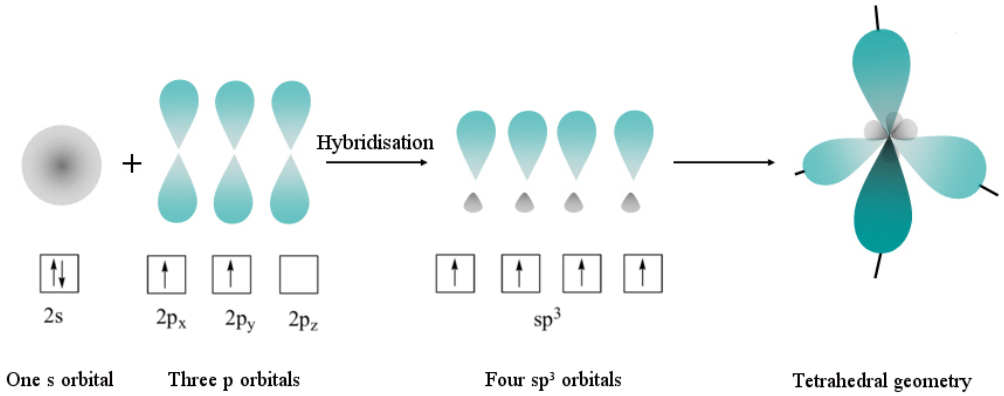

Figure 2.19: sp^3 hybridisation of carbon bonds forming a tetrahedral[16][17].

Diamond sp^3 is perhaps the purest of the three carbon hybridisations in the sense that it only forms one type of allotrope, diamond. Hybridisations of this class is known to be formed entirely out of four σ-bonds[16][17] and it therefore lacks the freestanding electron provided by the π-bond that is required for conduction to occur. Intrinsically therefore this form of carbon is typically a semiconductor with a wide band gap of 5.48eV[60] (Table.2.1). Moreover due to the presence of the rigid and defined 3D structure, diamond unlike the sp^2 allotropes can only take one form of crystal structure, tetrahedral[16][17].

Surprisingly, despite its novel characteristics[60] (Table.2.1)(Table.2.2) diamond has a rather common crystal structure. Diamond is a face centre cubic with a unit length (a_0) of 0.3567nm at room temperature[61] where each unit cube contains 8 atoms. Following the calculations below one could deduce that the C-C bond length and the density of diamond as:

$$C - C\,bond\,lengths(d) = \frac{1}{4}\ of\ cubic\,body\,diagonal \tag{2.1}$$

$$Therefore : d = \frac{(\sqrt{3})a^0}{4}\ \approx 0.154\text{nm} \tag{2.2}$$

Since there are 8 carbon atoms present in a unit cell the density of diamond is:

$$Diamonddensity = \frac{num.\ of\ atoms}{volume}\ = \frac{8}{a^0}\ = \frac{8}{3.567 \times 10^{-10}}\ = 1.76{\times}10^{29}\text{m}^{-3} \tag{2.3}$$

[62]

This value exceeds the density of every material currently known which in turn explains how diamond is the hardest (hardness of 10 on the Mohs scale[60] (Table.2.1), the most thermally conductive[60] (Table.2.1, stiffest and the least compressible[60] (Table.2.1) material known to man. However it is important to remember that the density of diamond varies according to the number of atoms in a miller plane. Diamond being a face centre cubic crystal has three distinct

planes: 100, 110 and 111[62] where each of the planes contain a different number of carbon atoms[62]. The significance of the planar atomic density is often overlooked but the difference in density happens to have a direct influence on growth and etch rates[63]. This is due to the fact that planes with greater number of carbon atoms require an equally greater number of bonds. Therefore if a certain plane were to have more atoms than another, both the process of etching (bond breaking) and growth (bond forming) will require greater energy and time per plane. Therefore 111 plane which holds the greatest number of carbon atoms in a diamond lattice[62] (Fig.2.20) is in fact the hardest plane of the aforementioned three and the process of polishing and etching on the 111 plane often takes much longer than the other two planes[63]. If one was to use a single crystalline diamond this does not bear much importance since the etch rates over the entire surface would be uniform. However if one was to use polycrystalline diamonds the etch rate would vary according to the orientation of each individual grain thus one must take precaution when exposing polycrystalline diamonds to etchants.

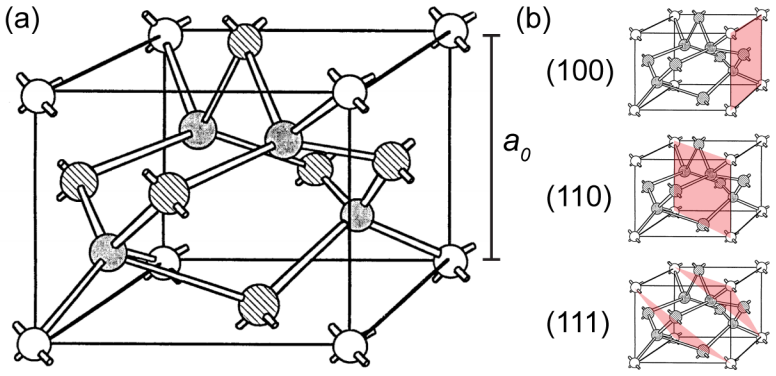

Figure 2.20: (a): Crystal structure of diamond, a face centre cubic crystal with a unit length of a_0. (b): the Miller planes of diamond lattice containing different number of carbon atoms[60].

Property	Value
Relative hardness	10 Mohs
Knoop hardness	8000
Abrasive hardness	140,000
Modulus of elasticity	700-1200GPa
Young's modulus	1000GPa
Poisson's ratio	0.1-0.29
Volume compressibility	$18\times10^{-10}m^2N^{-1}$
Density(300K)	$3515.25kgm^{-3}$
Atomic concentration(300K)	$1.763\times10^{23}cm^{-3}$
Bulk modulus	442.3GPa
Thermal expansion	$1.05\times10^{-6}K^{-1}$
Sound propagation velocity	18.2 km s^{-1}
Thermal conductivity(300K)	2000 $Wm^{-1}K^{-1}$

Table 2.1: Mechanical properties of diamond[60].

Property	Value
Dielectric constant(300K)	5.5-5.7
Dielectric strengths	1000kVmm^{-1}
Bandgap type	Indirect
Bandgap	5.48eV
Electron mobility	1800cm^{2}V^{-1}s^{-1}
Hole mobility	1200cm^{2}V^{-1}s^{-1}
Relative permittivity	5.57
Intrinsic resistivity	$10^{16}\Omega$cm
Saturation electron velocity	2.7×10^7cms^{-1}

Table 2.2: Electric properties of diamond[60].

2.5.1 Diamond Fabrication

Fundamentally three components are required for the fabrication of diamond: heat, pressure and carbon. As seen from the phase diagram below[64] (Fig.2.21), diamond has a tendency to form under extremely high pressure and heat. This unfortunately does mean that under most naturally occurring circumstances diamond has difficulty forming. However nature does make an exception in volcanic activity where both heat and pressure are abundantly available. If one was to have carbon in this thermodynamic system, diamond is expected to form. The formation of diamond does however face further complications due to energetic preference between sp^2 and sp^3 bonds. Despite the fact that sp^3 carbon σ-bonds being one of the strongest and the most stable bond in existence (711 kJ/mol[65][66]), sp^2 carbon σ-bonds (524 kJ/mol[65]) energetically sits at a lower more stable state of 2.87 kJ/mol[65] causing diamond to be the metastable state of carbon[64]. In

essence carbon under heat and pressure prefers to be in a graphitic structure than diamond. Therefore in order to fabricate diamond one must overcome this energetic preference in one way or another.

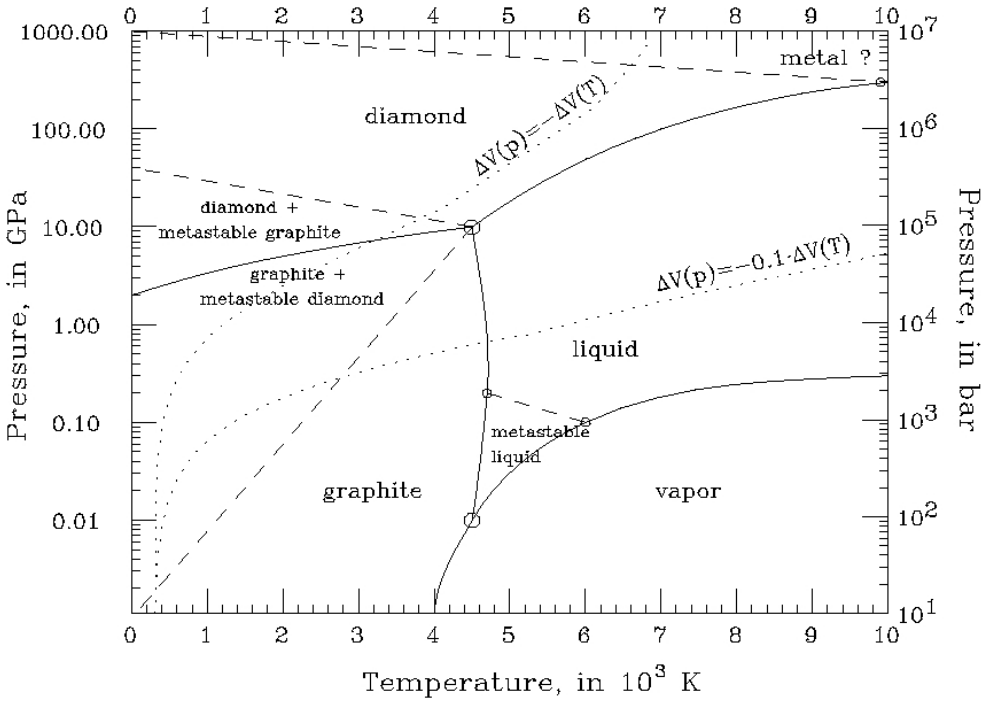

Figure 2.21: Phase diagram of carbon representing the relationship between temperature and pressure[64].

Although there are multiple different methods available to create diamond, there are three main school of diamond fabrication: High Pressure High Temperature (HPHT), Chemical Vapour Deposition (CVD) and Detonation Nano-Diamond (DND) method.

HPHT High Pressure High Temperature method (HPHT) is an attempt to recreate the formation of diamond in nature by mimicking the conditions deep under the Earth by applying high temperature and high pressure to graphite[65]. It was first devised in 1955 by General Electric (US), AESA (Sweden) and Institute of High-Pressure Physics (USSR)[67]. They found that although the process of converting graphite to diamond is technically possible at moderate pressures and temperatures[64] (Fig.2.21). Due to the high kinetic barrier (Fig.2.22), it

was found that the rate of transformation decreases with increasing pressure, resulting with an impractical conversion rate. Empirically however it was found that with a much higher temperature and pressure (approx. 3300K, >130kBar respectively[67]) there is a resurgence of conversion rate, enough for one to observe an acceptable degree of graphite to diamond transformation. Attempts to reduce the kinetic barrier have been carried out in the past with one of the more successful attempts being the use of catalysts, where the principle function of the catalyst is to dissolve the carbon that allows the formation of 4 sp^3 bonds without the need to break 3 sp^2 bonds reducing the energy requirement.

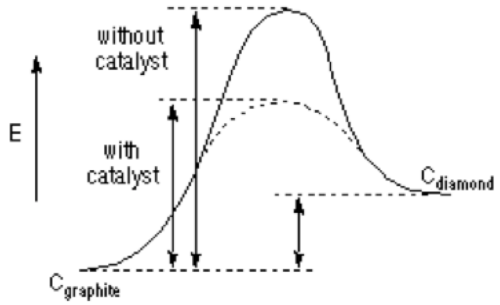

Figure 2.22: Energy diagram of the conversion between graphite and diamond with and without catalyst[68].

Conveniently the metal catalyst required for the lowering of the energy barrier was found to be an excellent solvent for graphite allowing the removal of the undesired sp^2 carbon contaminants. The process is now known as solvent-catalyst process and it was first developed by General Electric and AESA. A molten transition metal such as iron, nickel, cobalt, chrome, platinum and palladium[69] was found to dissolve carbon readily. The reduction in the energy barrier was found to be extensive and the newly required pressure and temperature was 55kBar and 1600K respectively[69] a substantial improvement over its previous values. The process itself is rather simple, the molten solvent-catalyst mix is passed over a growth substrate, typically over a highly epitaxial diamond layer that the carbon being deposited on could conform to its crystalline structure promoting growth of a crystalline diamond layer.

The following two methods have a very interesting history. It is almost unheard of in the modern era for two completely different approaches to be developed in parallel without having any influence on each other. Quite simply because if one method shows potential one will try to understand why it showed its benefits and apply it to another. This tendency holds particularly true in the modern era aided by the improvement of global communication where scientific publications became widely available regardless of one's geographic location. This however was not quite the case so between 1947-1991. The rise of the Cold War has caused the Iron Curtain to come down, effectively isolating the eastern and western political hemisphere. The halt in the communication has bought about the development of Chemical Vapour Deposition (CVD) in the west and detonation in the east. Both methods are widely used in the diamond community to this day attributed to the various benefits one has over the other.

Chemical Vapour Deposition (CVD) Chemical Vapour Deposition is a method of diamond fabrication that uses a substrate akin to the HPHT method outlined in the previous section. The difference however lies in the fact that CVD requires neither high temperature nor high pressure. In fact advancements in modern CVD technology has allowed diamond growth at sub atmospheric pressure[70] (20-30Torr) and at a relatively modest temperature[71] of approx. 700°C, contributing significantly to the safety and the purity of the diamond fabricated (due to the lack of need for catalysts). Although this will be elaborated later in this section it is perhaps best to discuss the origin of the method first. The idea of the method itself was surprisingly incepted before the invention of HPHT in 1954 by Eversole *et al.*[2] whilst working at the Union Carbide Corporation. However CVD did not bloom until 1956 when two USSR scientists Spitsyn and Beryagin purposed the deposition of carbon using CI_4 and CBr_4[72] as carbon sources at temperatures of 800°C-1000°C[72] and at a pressure of 4×10^{-4}Pa[72]. Its potential as a method of fabricating diamond however was rather limited at its time due to its limitation in purity where the fabricated diamond was found to be plagued

with the formation of sp^2 carbon co-deposits that contaminated the end product. Although there have been some valiant attempts to remove the sp^2 carbon such as those by Angus and Deryagin who have discovered that sp^2 carbon contaminants could be removed by atomic hydrogen etch[71], it was unfortunately widely considered by many that the growth rate was simply too slow for any commercial viability[71]. However, in the 1980s there was a watershed moment due to the discovery of the effectiveness of using both hydrogen and methane radicals simultaneously during growth. Researchers at the National Institute for research in Inorganic Materials (NIRIM), Japan has discovered that by using a blend of both methane and hydrogen radicals one could both deposit carbon on the surface as well as remove the unwanted sp^2 carbon[73]. Not only has this allowed the growth of high purity diamond more importantly this method has commercially significant growth rates[73]. Furthermore the growth was possible at the aforementioned modest pressure and temperatures of 20-30Torr[70] and approx. 700°C[71] respectively negating the need for an expensive high pressure chamber as well as improving its safety by only having the need to work with easily manageable temperatures and pressures.

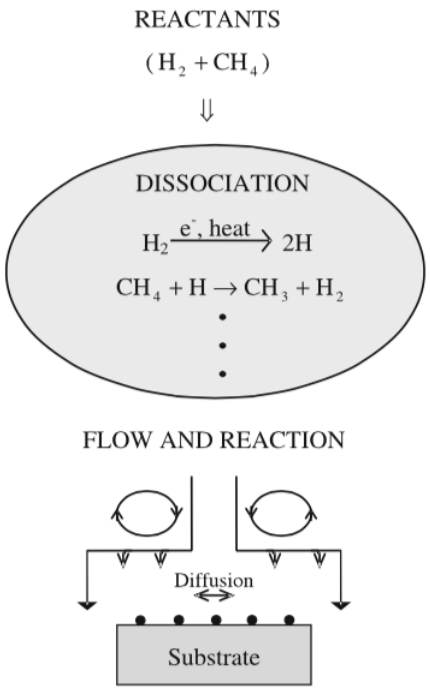

Figure 2.23: CVD growth process of diamond using methane and hydrogen radicals[72].

Initially NIRIM used tungsten hot filaments to create radicals above the diamond template to grow diamond[73]. However the use of tungsten filament faced some contamination issue of its own due to its inherent need to have a non-carbon filament present in the growth chamber. Therefore immediately after the success of the tungsten method, NIRIM devised another process using microwaves to indirectly generate hydrogen and methane plasma. The process is now known as microwave plasma enhanced CVD (MWPECVD)[74]. It is worth noting at this point that the process mentioned above is not exclusively reserved for diamond substrates. In fact if one was to 'seed' a surface of any generic substrate such as silicon (Si) and gallium arsenide (GaAs) with nano-scopic grains of diamond, nano-diamonds (NDs), upon extensive growth it will grow a sizeable diamond film on its surface.

Detonation Nano-Diamonds (DNDs) The last method of fabricating diamond, detonation is rather explosive in nature. As previously mentioned in order

for diamond to form one would need three components: carbon, heat and pressure. Detonation as the name suggests attempts to achieve this through explosion. This method was particularly favoured by the Soviets and was heavily developed during the Cold War[75]. However as stated before due to the presence of the Iron Curtain it was not until much later that its development was shared with the western world[75]. The idea itself surprisingly was not invented by USSR but by an American company called Du Pont de Nemours in the 1960s[76] for this very reason this process is sometimes refered to as the Du Pont method. This method forms diamond by exploding carbon precursors such as graphite, coal and carbon black mixed with metal catalysts (Cu, Al, Ni) and graphite (6-10%) to prevent re-graphitisation[76]. Upon ignition, the explosion propagates a pressure wave that compresses the carbon precursors with a pressure of approx. 140GPa converting the carbon into diamond[76]. The yield was rather poor however that a mere 5% of the carbon mass introduced were able to transverse into the diamond phase[76]. Interestingly however, upon inspection of the produced diamond there seemed to have been a bimodal size distribution. In another words there were nano-diamonds of two very different sizes that formed in a single explosion. The smaller type of the two was a modest 1 to 4nm in size while its larger sibling was 10 to 150nm in size[76]. Another notable point is that this particular method allows the formation of lonsdaleite, a diamondoid that on some Miller planes are known to have a hardness that surpasses the hardness of pure diamond[77].

The Du Pont method as mentioned earlier was further developed by USSR where its revised approach was invented. The revised method employs carbon-based explosives to generate the shock waves and heat required for the diamond formation. The advantage of using carbon-based explosive lies with the fact that it eliminates the need for a separate carbon source since the explosive itself is supplying the carbon. The most common explosive of choice for this method is a blend of 2-methyl-1,3,5-tetranitrobenzene (TNT) and hexogen (carbon, nitrogen, oxygen and hydrogen with a negative oxygen balance. i.e. the oxygen content is lower than its stoichiometric value) in a 60/40 ratio respectively[78].

To suppress graphitisation this process is usually carried out in either a wet or dry coolant (ice and inert gas respectively) that stabilises the carbon in the diamond phase[78]. The diamond formation occurs in a two-step process. Initially, a detonator residing at the core of the TNT and hexogen mantle will explode, compressing the mantle which in turn generates a tremendous amount of heat that results in its chemical decomposition[60] (Fig.2.24). The process will then release a vast amount of energy in a matter of a fraction of a millisecond[60] generating temperature between 3000-4000K[60] and pressures between 20 to 30 GPa[60]. This forces the free standing carbons to coagulate into a carbon cluster[79] that is represented by the Chapman-Jouguet point on the phase diagram[80] (Fig.2.25) converting itself into nano-diamonds of approx. 5nm in size per primary particle unit[76]. Upon inspection of the detonation soot it was found that 40-80% of the soot was in fact diamond making this a commercially sound method of nano-diamond production[60].

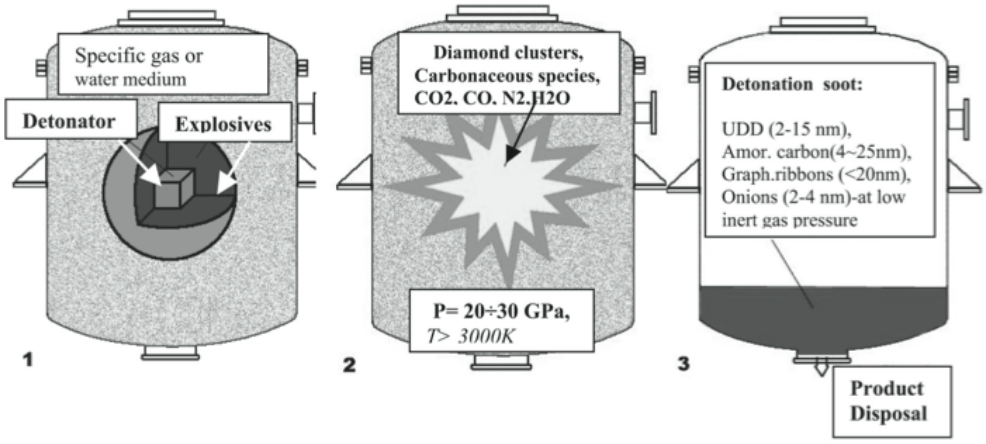

Figure 2.24: Flow diagram of a typical detonation method: 1) Explosive charge in a blast chamber composed of a detonator core and an explosives mantle in a coolant. 2) Detonation, initiating a decomposition of explosives. 3) Resulting soot consisting of various forms of carbon (NDs, carbon onion, graphite ribbons and amorphous carbon)[60].

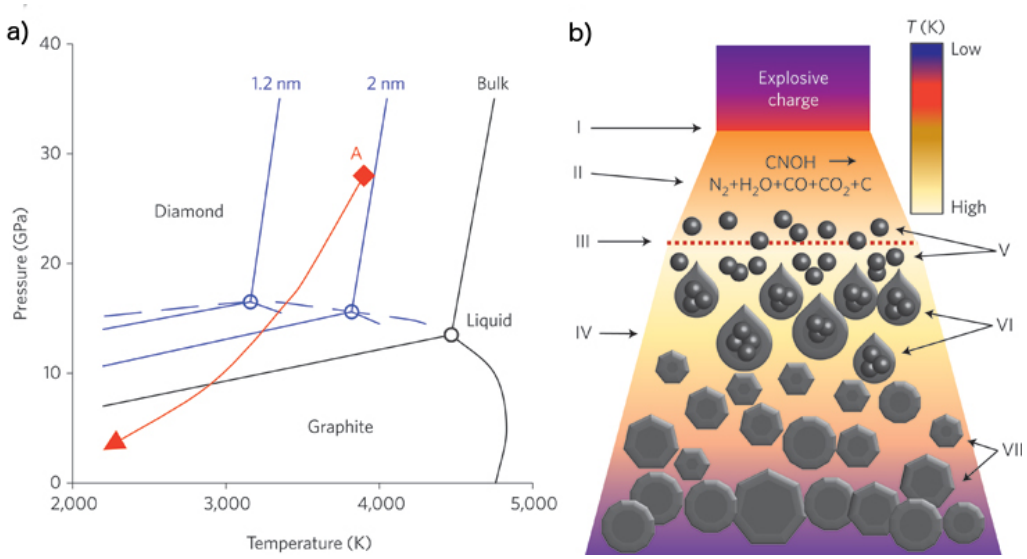

Figure 2.25: a) Phase diagram of diamond with its respective sizes of the clusters at different pressure and temperature. 'A' denotes the Chapman-Jouguet point, which represents the pressure and temperature of the detonation projectile (in this case carbon) immediately after detonation. Upon detonation the carbon primary particles are typically 2nm in size. As the temperature and pressure subsides the surrounding carbon condenses onto the cluster causing it to growing in size (approx. 5nm[76]), followed by the coagulation of primary particles. As the pressure and temperature decreases the conditions for diamond-graphite phase threshold approaches. The diamond cluster will then stop growing in size and starts to form graphitic shells around its diamond core. b) Change in temperature and the state of carbon before, during and after detonation. I: Detonation wave front, II: Decomposition of explosives, III: Chapman-Jouguet plane, point 'A' in diagram a), IV: Expanding detonation products, V: Formation of carbon nano-clusters, VI: Coagulation into nano-droplets, VII: Crystallisation and growth of diamond core and graphitic shell development[80].

Purification Within its very core of the detonation clusters formed in the above manner is diamond. However as described in Fig.2.25 they are encased in concentric shells of sp^2 graphitic layers[81] (Fig.2.26). In order for one to exploit the benefits of the nano-scale sp^3 structure, one must first remove the said graphitic shells. Interestingly by adopting the principles addressed in the earlier section of carbon onions one could use similar techniques to remove the sp^2 layers. For example, nano-diamond clusters in its raw state is in effect carbon onion with a sp^3 core. Therefore if one was to eradicate the sp^2 shells one could adopt the activation method used to perforate the carbon onion shells, namely the use of

aqueous KOH, aqueous H_2SO_4 and pure nitric acid is most commonly used to remove the graphitic layers[10][81] (Fig.2.26). It is worth noting at this point that both KOH and H_2SO_4 require the presence of water to be effective. This is due to the fact that the actual active ingredient of the oxidation process that breaks down the σ-bonds of the graphitic layers is in fact the hydronium ion (H_3O^+) that forms as a result of the redox reaction between water and a strong acid or a strong base[10]. In light of this it may be useful to reflect on the influence of surface curvature to reactivity that was previously discussed in relation to carbon onions. If a sp^2 structure has a curvature, the σ-bonds will be under mechanical strain. Energetically speaking they require less energy for the bonds to break thus are more vulnerable to reactions in comparison to the very same structure without curvature causing its reactivity to increase. This elevation in reactivity aids the removal of the sp^2 layers. One of the additional benefits of using the aforementioned acids are their ability to dissolve any inorganic impurities that has been used in the detonation process[10]. As outlined in the Du Pont method the production of nano-diamonds could involve metal particles such as copper, aluminium and nickel[76]. Therefore if one were to aim to increase the purity of the nano-diamonds, one would have to remove the said metal impurities in one way or another. Therefore the reagents used to remove the graphitic shell being an excellent solvent to extract the metal nanoparticles is an elegant solution that kills two birds in one stone.

Upon the successful removal of sp^2 graphitic layers one must then separate the fused primary nano-diamond particles[80][81] (Fig.2.25, Fig.2.26) from its parent cluster. Extensive study carried out by Eiji Osawa has shown that sonication could successful separate large clusters of nano-diamonds that are bonded together by van der Waal's force[81] (Fig.2.27). Typically a 30-50μm cluster could be de-agglomerated into 2-3μm clusters, which upon further intense sonication could be further broken down into 100-200nm clusters[81]. However at this stage the bonds that are connecting the primary nano-diamonds are C-C σ-bonds[81]. If one was to attempt to further breakdown the clusters into primary particles one will need

to physically pulverise the clusters using bead milling[81]. The process of doing so will result in the production of 4-5nm nano diamond primary particles[81]. A noteworthy point about the said primary particle is its surface conditions. The surface is known to be polar due to the presence of oxygen based functional groups such as hydroxyl groups (-OH), C-H groups and sp^2 patches that has formed as a result of the diamond to graphite conversion that occurred due to the shear impact during bead milling[81]. This directly results in both the black appearance of nano-diamonds and the high solubility of nano-diamonds in water and other polar solvents[81].

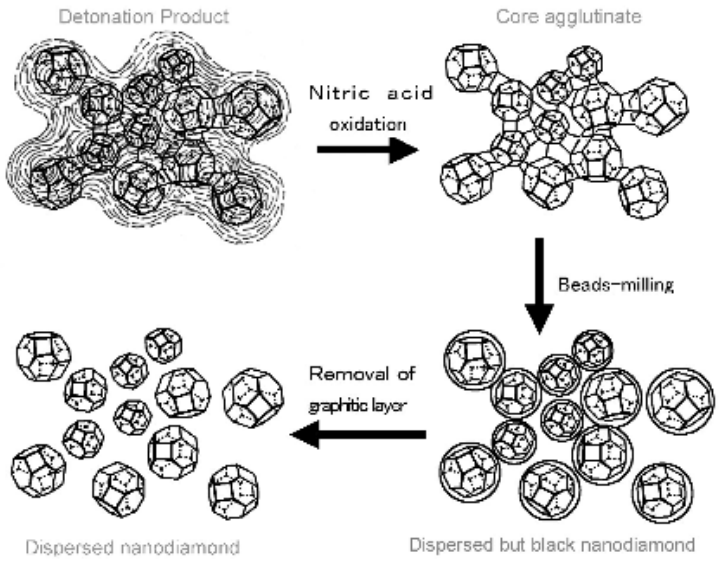

Figure 2.26: Purification process of detonation nano-diamonds post detonation. Detonation products are exposed to oxidizing agents to remove the graphitic outer layers. Upon exposure of the agglomerated sp^3 core, the agglomerate is broken down into its primary particles. Followed by the further removal of its newly formed sp^2 layer from the bead milling collision[81].

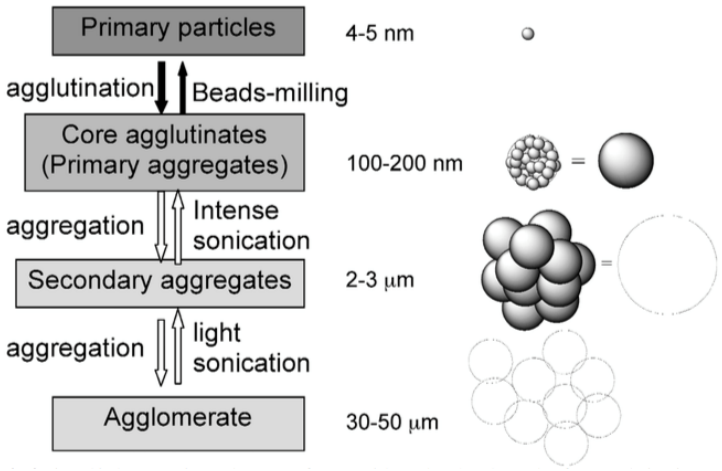

Figure 2.27: The dispersion system to break down the agglomerated nano-diamond clusters post detonation into smaller aggregates[81].

2.5.2 Crystallinity

One of the most important benefits brought about by the recent development of diamond fabrication is the ability to vary its crystal structure. Diamond as mentioned earlier is a face centre cubic crystal[62] (Fig.2.22). Therefore if one were to clone this unit repeatedly one would achieve a perfect diamond lattice, the single crystalline diamond (SCD). However, in reality diamonds as with the likes of most other crystal structures in existence are more often than not peppered with defects. If for instance a piece of diamond was to constitute of multiple crystalline facets[82] (Fig.2.28) the diamond of this type will be known as a poly-crystalline diamond (PCD). This could then be further subcategorised into micro-crystalline diamond (MCD) and nano-crystalline diamond (NCD) depending on the average grain size of the individual facets.

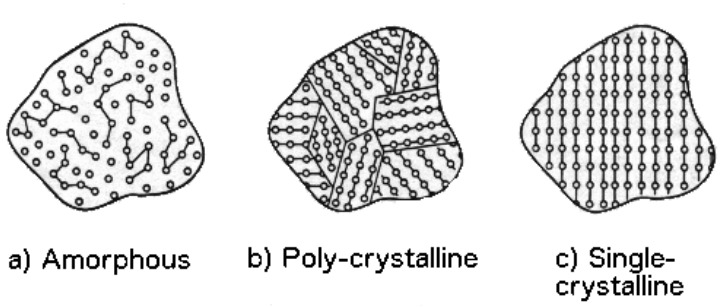

Figure 2.28: Different crystallinity of diamond: a) Amorphous, no stable order of σ-bonds; b) Poly-crystalline, clear σ-bonds order but with multiple facets; c) Single-crystalline, σ-bonds ordered in a single facet[82].

Electrically speaking, single crystalline diamonds are known to have superior carrier mobility due to the lack of grain boundaries that inhibits the flow of holes and electrons[83]. Nebel for example has found that on average PCDs have a hole mobility 10-40 times smaller than that of SCDs where PCD and SCD hole mobilies are 3-40$cm^2V^{-1}s^{-1}$ and 70-165$cm^2V^{-1}s^{-1}$ respectively[83]. Similarly PCD is known to have a shorter drift distance (mean free path) than SCD due to the lack of grain boundaries[83]. However, polycrystalline diamond does have its place in terms of commercial convenience and growth on complex surfaces. For example in Chapter 8: SEE the use of nano-diamonds and their growth will be outlined where the investigation is designed to develop the next generation night vision goggle amplifiers. This process requires nano-diamonds to be grown in a narrow channel with limited accessibility which is simply impossible to achieve without the excellent particle mobility of nano-diamonds. It is worth mentioning that of the three fabrication method described earlier HPHT and CVD is capable of growing SCDs if one was to use a SCD substrate providing a foundation for the diamond to repeat its crystal units as it grows. Detonation on the other hand is solely reserved for nano-diamonds. However, the nano-diamonds made in this manner could then be seeded onto a large substrate such as silicon and be used as a platform to grow a large surface area and cost effective PCD that pertains commercial significance.

Poly crystalline diamond as mentioned earlier is an umbrella term for any

multi faceted diamond crystals, which could then be subdivided into categories based on their grain size, such as micro-crystalline and nano-crystalline diamonds. Both of the above categories are known to have their places in various applications. For example nano-crystalline diamonds excel in low surface roughness attributed to its finely grained crystals. However they do suffer from low carrier mobility typically in the range of 10-90 $cm^2V^{-1}s^{-1}$ due to the abundance of grain boundaries[84][85]. Micro-crystalline diamonds on the other hand may be rougher but it retains a respectable carrier mobility and mean free path[83]. Despite their differences the fabrication method of NCD and MCD is near identical in that they both require CVD or HPHT as its growth method. As seen from the diagram below[86] (Fig.2.29), once the substrate has been seeded with nano-diamonds one could then grow the diamonds to form a diamond film, although this process will later be further discussed in Chapter 8: SEE. Typically for one to achieve MCD growth one will require exposure to methane and hydrogen plasma in a 1:100 ratio respectively whilst for a NCD it is typically grown in 5-20% methane[84][87]. The difference in the grown crystal is bought about by the rather aggressive nature of hydrogen plasma, more specifically by its ability to suppress renucleation of carbon provided by methane. During growth, the methane plasma could either donate its carbon atom to a pre-existing diamond surface by following its crystal lattice or alternatively it could physically 'attach' itself on the growth surface without following the direction of the facet. The latter process is known as renucleation and this could potentially build a foundation for another grain of diamond with a different facet to the grain below[86] (Fig.2.29). In a low methane environment the abundant hydrogen radical could then remove the loosely bonded renucleated carbon atom, preventing the generation of a new grain. This will in turn allow a new incoming carbon to correctly follow the crystal structure of the grain below. It is worth noting at this point that the grain below is less prone to the hydrogen etch due to the support it receives from its neighbouring carbon atoms that provides multiple σ-bond supports. In contrast, the lone unsupported carbon atoms receives little resistance for its removal. On the other hand if one was to use a

higher methane content. The rate of nucleation will overcome the hydrogen etch rate thus continuously creating new grain structures typically of less than 100nm in size[87] bringing rise to the formation of NCD.

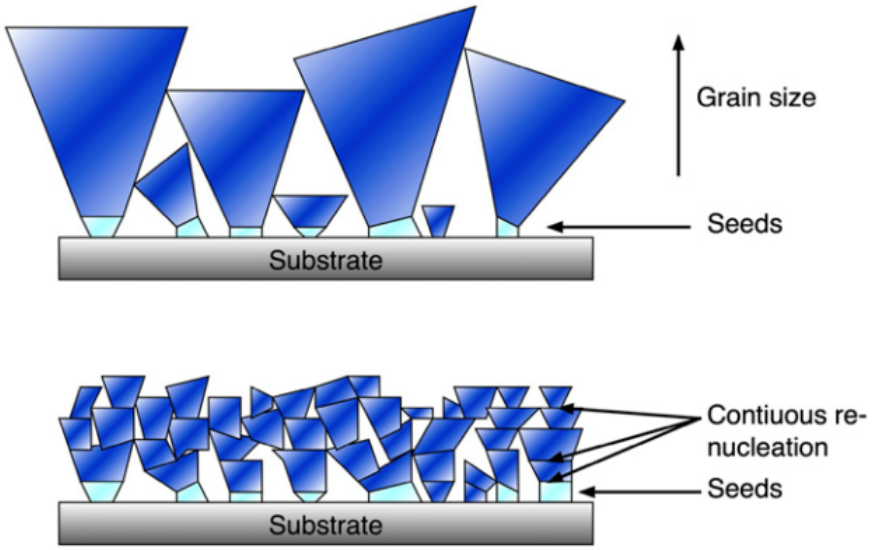

Figure 2.29: (Top): Growth of MCD with larger grains as a result of uninterrupted growth of grain following its facets, (Bottom): Growth of NCD with finer grains due to constant re-nucleation forming new facets to the grains below[86].

2.5.3 Functionalisation

Akin to the previously outlined functionalisation methods for sp^2 carbon, sp^3 carbon such as diamond could also be functionalised. Conventionally however, the term termination is preferred over functionalisation due to its very nature of attaching itself to the 'terminal' σ-bonds on the outer surface of the tetrahedral shape[88] (Fig.2.30).

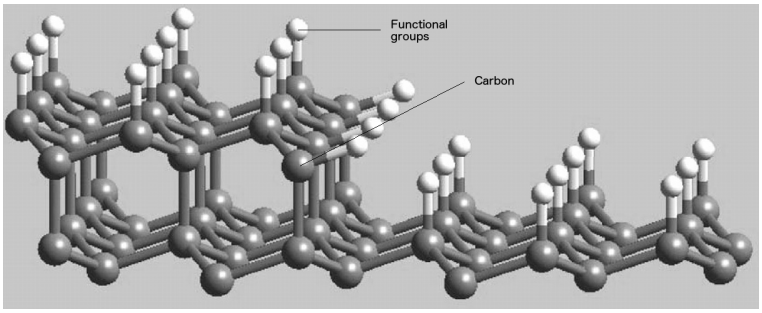

Figure 2.30: Surface of a terminated diamond with functional groups attached to the terminal σ-bonds[88].

As seen from the figure above, diamond being a tetrahedral has σ-bonds where various functional groups could occupy. Despite it being a significantly small fraction of the entire bulk, surface termination is known to bear substantial influence over the electronic nature of diamond. This effect is particularly pronounced when the surface to volume ratio is large, namely in the case of nano-diamonds. One example of this termination is hydrogen. If a piece of intrinsic (thus non-doped) diamond is hydrogen terminated it is known to support surface conductivity by creating a redox reaction with moisture[89][90] (Fig.2.31).

$$2H_3O^+ + 2e^- \Leftrightarrow H_2 + 2H_2O \tag{2.4}$$

[89]

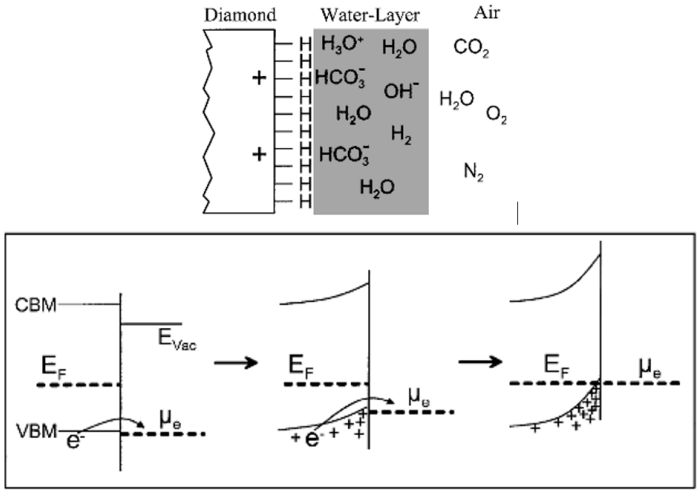

Figure 2.31: (Top), Redox reaction on the surface of a hydrogen terminated diamond in air; (Bottom), The band bending at the surface of diamond as a result of the redox reaction allowing charge carriers to flow freely thus making hydrogen terminated diamond conductive in air[90].

The most important aspect of hydrogen termination however is in the fact that it is the most common default termination after CVD growth. As discussed earlier CVD relies on methane as the carbon source and hydrogen as the etchant that moderates the nucleation and promotes crystalline growth. Therefore the abundant presence of hydrogen radicals will then cause itself to be the most common functional group to occupy diamond's terminal σ-bond. Consequently the process of hydrogen termination is commonly used as a 'cleaning' step to eradicate surface contaminants as well as providing a uniform and known surface termination that could then be used to further terminate the sample with another functional group[91] (Fig.2.32). Again, this would be further emphasised in Chapter 8: SEE where the purity of the surface termination will have significant effect on the outcome. It is also worth noting that hydrogen terminated diamonds are known to be heavily hydrophobic with a zeta potential as high as >60mV[92] while the addition of hydroxyl group (-OH) is known to cause the very same diamond to be hydrophilic[80], a feature particularly useful when suspending nano-diamonds in an aqueous solution. The use of termination is not limited to the change in solubility, some have even reported of augmenting diamonds with novel features

such as fluorescence using –NHOR termination[80]. Broadening the use of diamond with a plethora of applications making diamond one of the most versatile research materials in existence.

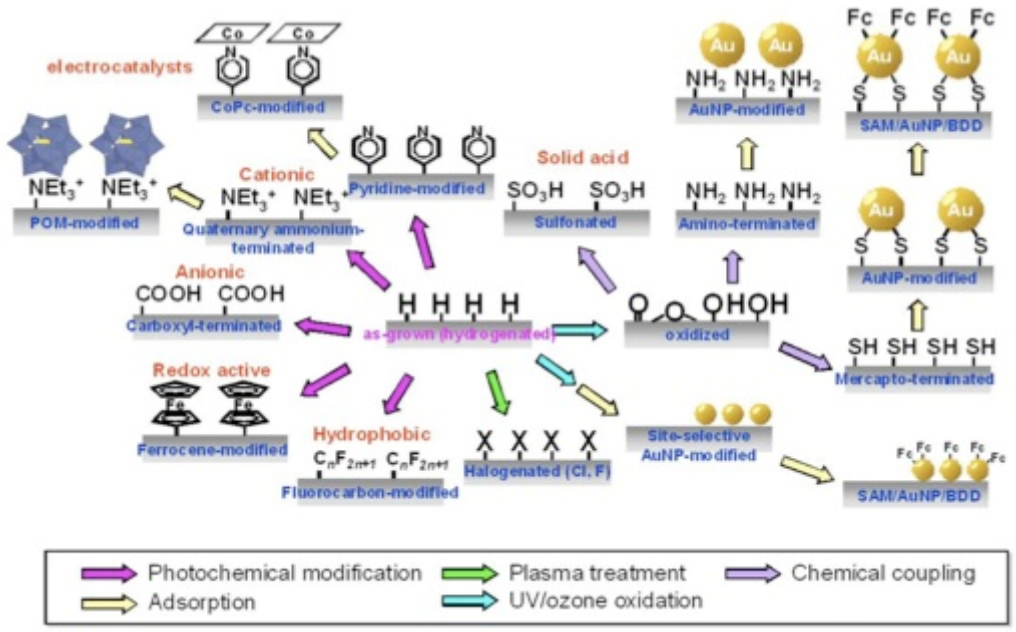

Figure 2.32: Various terminations that could be derived from having a clean and uniform hydrogen terminated surface with their respective processes[91].

Another common termination is oxygen, a termination that is often seen as an opposite counterpart to hydrogen due its electro negative nature. This will hold particular importance later in chapter 8: SEE when addressing the yield of secondary electron emission. For the time being however it is perhaps prudent to focus on its association with carboxylic (-COOH) and hydroxyl (-OH) functional groups. These terminations (-O, -OH and -COOH) are often added to the surface through a process known as acid bath where a diamond sample is exposed to a highly concentrated, saturated and heated acid. As with the likes of hydrogen termination, acid cleaning is often used as a cleaning process to eradicate any surface contaminants to give the surface a clean slate. Further processes could be used to alter its termination[80] (Fig.2.33).

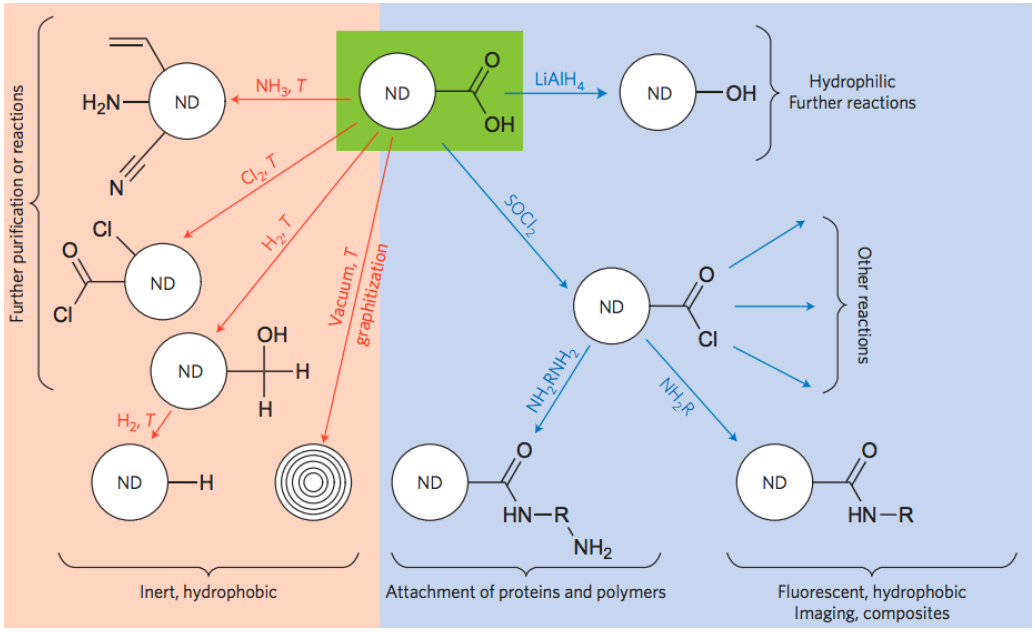

Figure 2.33: Various terminations that could be derived from having a clean and uniform acid bath treated –COOH terminated nano-diamond surface with their respective processes[80].

2.5.4 Doping

Following the previous discussion of growth and termination it is now perhaps appropriate to discuss an alternative approach to manipulate diamond's electric character, doping. As with the likes of other semi-conductors such as silicon and GaAs, diamond could also be doped with p-type and n-type dopants to augment its conductive nature. However due to diamond's extremely stable crystal structure one cannot simply anneal the diamond with dopants in order to diffuse them through the surface as you would with the likes of Si and GaAs. In order for one to infuse dopants into diamond one would have to either force dopants in with high-energy bombardments such as ion-implantation or by adding them into the crystal structure during growth[81]. The former fell out of favour in recent years due to the rather aggressive nature of the approach. Ion implantation inherently requires ions to be bombarded at the target surface in order to forcefully embed the ion into the diamond lattice. This unfortunately does mean that σ-bonds in the path of the bombarded ion can be destroyed forming defects in the diamond

lattice. Traditionally, most defects caused by ion implantation are able to be rectified by annealing the sample post exposure. However as mentioned earlier sp^3 carbon is energetically less stable than sp^2carbon[65][64][66]. Therefore the process of annealing would risk graphitising the diamond that in itself is a defect. Notably the presence of the said graphite could give rise to electrical effects that could erroneously be misidentified as the effect of doping from the implanted ions[93]. A far more benign approach to doping diamond is to infuse the dopants into the crystal lattice during growth. Effectively one is fusing the dopants into the crystal lattice as it is being formed thus avoiding the defect formation that the diamond would otherwise experience under ion implantation. Both HPHT and CVD are known to be effective using this approach. However due to the lack of contaminants CVD under most circumstances is preferred. However HPHT is credited to be the first approach to successfully dope artificial diamonds by Werntorf in 1959[94]. Werntorf has achieved this by infusing boron, a p-type acceptor into the HPHT catalyst mixture. Interestingly, despite the fact that this approach is now very much obsolete the dopant of his choice, boron, remains to be the most widely used dopant to this day. This is largely attributed to the fact that it requires the lowest activation energy amongst all p-type and n-type diamond dopants currently known of 0.37eV[95]. Currently as of the time of writing it is common to add diborane (B_2H_6)[96], tri-methyl borane[97], boron oxide[98], boric acid[99] and solid boron[95] during CVD to infuse boron into the diamond lattice. Doping in this manner brings rise to a rather impressive set of hole mobilities of: 1870$cm^2V^{-1}s^{-1}$ at 292K with a boron content of $10^{16}cm^{-3}$ [100], 1620$cm^2V^{-1}s^{-1}$ at 290K with a boron content of $4\times10^{14}cm^{-3}$[101], 2000$cm^2V^{-1}s^{-1}$ at 290K with a boron content of $5\times10^{13}cm^{-3}$[102] and 1840$cm^2V^{-1}s^{-1}$ at 290K with a boron content of $2.3\times10^{14}cm^{-3}$[97]. If one was to simply look at the number of boron atoms added to the diamond lattice however it may seems rather excessive. This is due to the fact that at room temperature only a mere 1% of the boron dopant is activated[103]. The number of activated borons could however be increased by increasing the dopant concentration[95][104] (Fig.2.34) exploiting

the reduction in activation energy bought about by the increase in the number of boron. The increase in dopant concentration does however bring about two unfavourable impacts. Firstly, boron being a charged impurity it will contribute to carrier scattering, impeding the hole's flow. Secondly, if the dopants were to be densely populated it will form a metallic impurity band where conduction could occur by quantum tunneling[105]. This process is known colloquially as 'hopping conduction' and at boron concentrations of 3×10^{20}cm^{-3} the boron activation energy is very near to 0eV but the carrier's mobility is suppressed to a miniscule <3cm^{2}V^{-1}s^{-1}[105]. For this reason a moderate and measured amount of boron doping is advised.

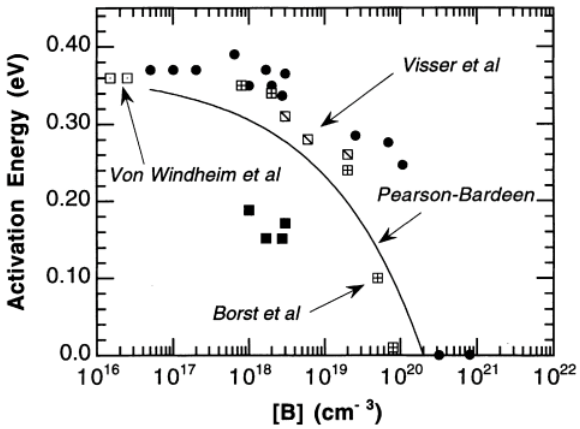

Figure 2.34: Relationship between boron activation energy and boron concentration. As one could see the greater the number of boron the lower the activation energy is. Notably at boron concentration $>2\times10^{20}$cm^{-3} the activation drops to 0eV[104].

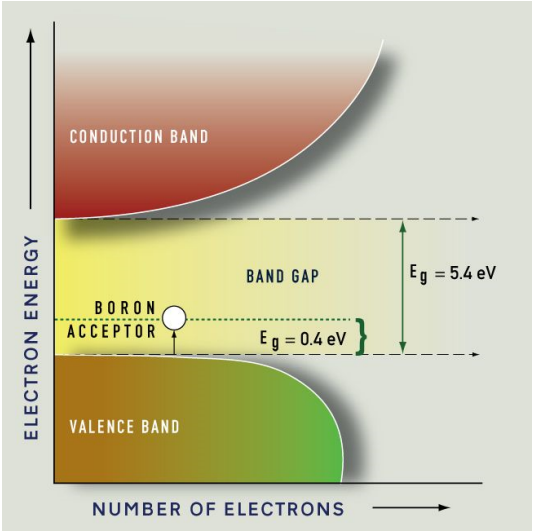

Figure 2.35: Band diagram of a boron doped diamond with its band gap energy and its acceptor energy band gap. Lowering the amount of energy required enabling conduction to occur at room temperature[106].

As with the likes of p-type dopants, n-type dopants have also been investigated by many. However, n-type dopants have not received as much attention as opposed to its p-type counterpart. Much of this is due to the fact that the diamond community already has a well established dopant, boron that works very well at room temperature. In addition to this the two main candidate for n-type doping: nitrogen and phosphorus has shown very little potential. Nitrogen, for example despite it being considered the more suitable choice of the two due to its similarity in atomic size to carbon was reported to have an activation energy as high as 1.7eV[107] which prohibits the activation of carriers at room temperature. Phosphorus on the other hand has shown more promise where some has even reported a carrier mobility of $420 cm^2V^{-1}s^{-1}$ at room temperature from a dopant concentration of $2.8\times10^{16}cm^{-3}$[108] and activation energy of 0.46eV[109]. Some have even gone as far as predicting activation energies as low as 0.2eV[110][111] and 0.4eV[112]. However due to the size difference of phosphorus and carbon the incorporation of phosphorus into the diamond crystal has proved rather difficult[113]. The combination of the above factors has resulted in the heavy reliance on boron as the dopant of choice culminating to its use taking the lion's share of all doped

diamond related research.

2.5.5 Secondary Electron Emission (SEE)

Secondary electron emission is a phenomenon where one or more electrons generated as a result of an incoming electron or photon interacting with matter is released from a system[114] (Fig.2.36). Although the effect was first discovered on silicon[115] and gallium arsenide[116] SEE was also later observed on diamond in 1992 by Merini *et al.* who have observed up to 45 secondary electrons generated by a single primary electron on diamond[117].

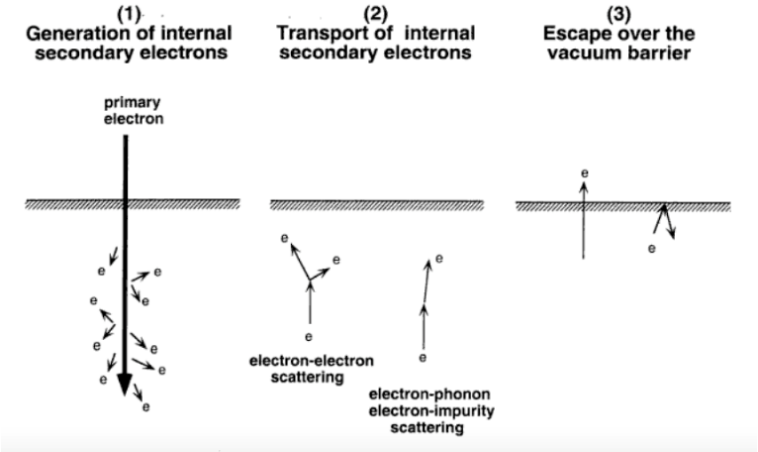

Figure 2.36: Three stages of SEE[114].

Mathematically speaking the most common method of quantifying the amount of electrons 'gained' by each electron is by representing it as a ratio of secondary electron to primary electron (gain, δ)(Eq.2.5)[114].

$$gain(\delta) = \frac{Secondary\ electrons}{Primary\ electrons} \tag{2.5}$$

The gain will later be used as an important yardstick in Chapter 8: SEE where one aims to achieve secondary electron emission from various different diamond terminations. Before explaining the role of terminations on SEE however one must understand the logic behind the specific conditions where diamonds are able to exhibit SEE. It may seem rather odd initially to think that a phenomena that

originates from the bulk region of the diamond to be affected by surface chemistry. However the role of termination is in fact not in the generation of the secondary electrons but in its ejection mechanism. It is widely known that termination has a profound effect on the band structure of semi-conductors[118] much in the same way as a dopant would. Therefore depending on the overall charge of the terminal group the bands could bend up if the termination is negative or down if it's positive. The concept is perhaps best described diagrammatically, from Fig.2.37[118] below:

- Positive electron affinity (PEA) = As one could see from diagram (a) if the electron affinity of the system is positive thus requires additional energy for electrons to be freed from the system it is considered to be of positive electron affinity (PEA)[118], a band structure typically seen from a positive termination free diamond surface[114].

- Effective negative electron affinity (Effective NEA) = If on the other hand some parts of the conduction band minima is to reside above the vacuum energy level through band bending[118] such in the case of diagram (b), thus allowing some electrons to be liberated from the surface. It is considered to be of effective negative electron affinity (effective NEA)[118]. Some examples of materials with said band structure are Si[115] and GaAs[116] that was verified to have an overall positive electron affinity with a negative tail by the likes of Yater *et al.*[119].

- True negative electron affinity (True NEA) = If one was to have a band structure where the vacuum energy is lower than the entirety of the conduction band minima as seen in diagram (c), it is considered to have true NEA. The electrons are therefore free to leave the system as they please. Most importantly this allows the entirety of the electrons in the conduction band to escape the confine of the system thus semi-conductors with true NEA has the most number of electron available to partake in SEE. An example of a material in this class is CsO terminated diamonds[114][118].

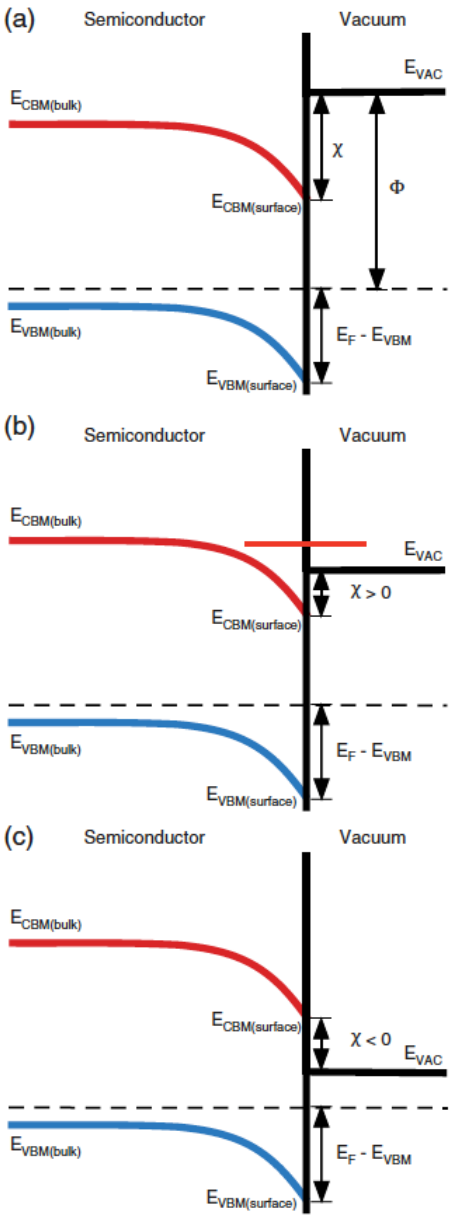

Figure 2.37: a) Positive electron affinity band diagram where the vacuum energy level is comfortably above the conduction band minima, b) Effective negative electron affinity band diagram where due to band bending some parts of the conduction band minima is above the vacuum energy level, c) True negative electron affinity band diagram where the entirety of the conduction band minima is above the vacuum energy level[118].

Another approach to understand the above concept is through electrical dipole moments. Depending on the charge of the terminal group, the surface will be subjected to dipole moments where depending on its polarity enables the elec-

trons generated by the primary electron to be catapulted out of the diamond (Fig2.38)(Fig.2.41)(Fig.2.42) or repelled back into the diamond electrostatically (Fig.2.39). If for instance the surface of a diamond was to be terminated with a positive species such as hydrogen (a terminal group known to induce NEA[120] to diamonds) the electron will be able to be escape from the diamond surface readily. Whilst on the other hand if the surface was to be terminated with oxygen, a very well established negatively charged termination, the SEE was found to be suppressed[121].

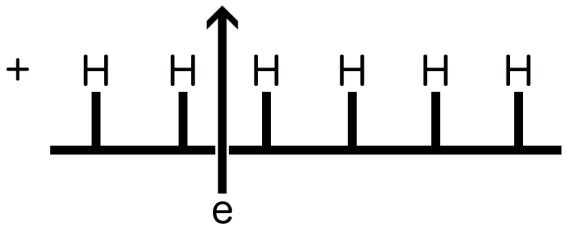

Figure 2.38: SEE from a hydrogen terminated (positive) surface where the electron is being liberated from the diamond surface through the assistance of the dipole on the surface.

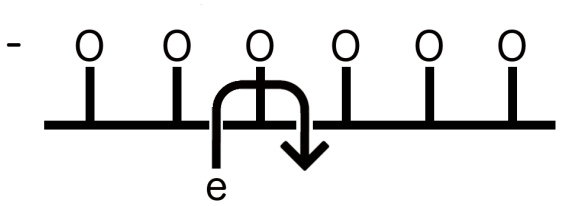

Figure 2.39: Inhibition of SEE caused by the electrostatic repulsion by the negatively charged oxygen termination.

The above premise is rather straightforward in the sense that the terminations have a very clear and defined charge polarity. The question one ought to ask to oneself is, what will happen if there is a hetro-elemental termination? The answer lies in the overall electro negativity of the termination. For example LiO whilst

having both a positive component, Li and a negative component, O it was both theorised[122] and confirmed through experimentation[118] to show SEE. It may seem paradoxical to observe electron emission from terminal groups with both a positive and negative charge present. This however could be explained by the net electro negativity of the termination being positive (Table.2.3). As seen from the diagram below (Fig.2.40)[118] the electrostatic potential at the surface of a LiO terminated diamond sample has a strong electrostatic potential peak originating from the oxygen molecule. However the strong and positive electronegativity of lithium overpowers this, exhibiting SEE.

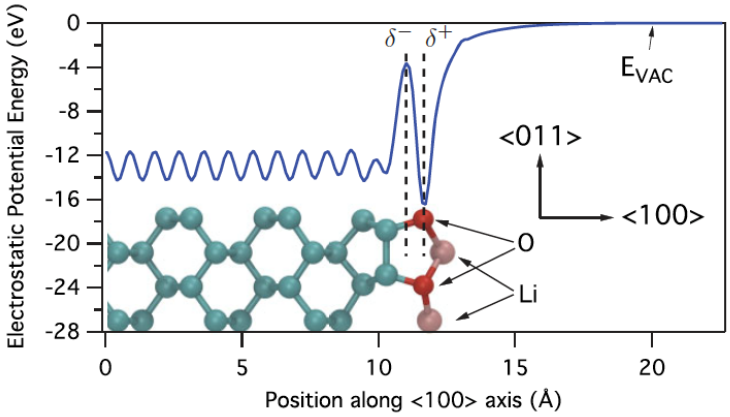

Figure 2.40: The electrostatic charge of a LiO terminated diamond sample along the 100 plane. As one could see the lithium and oxygen forms a dipole that the electrons could utilise to induce SEE. Interestingly the negative terminal of the dipole electrostatically is centred between the C-O bonds and not on the oxygen nucleus. Another notable fact that one could deduce from the diagram is the uniform and muted electrostatic potential among the bulk. This implies that if one was to take into account of the influence of the bulk diamond to the dipole one could expect near negligible influence. This assumption however is limited to intrinsic diamond thus diamond sans dopants[118].

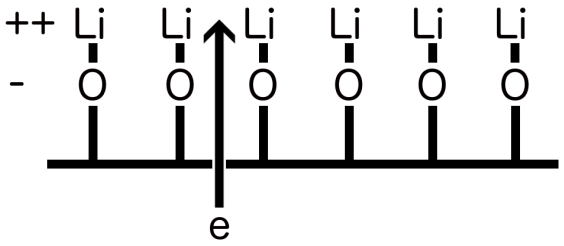

Figure 2.41: SEE from a LiO terminated diamond surface where the net positive electronegativity has allowed the liberation of an electron (Table.2.3)(Table.2.4).

Lithium oxide however is in fact not the only alkaline metal oxide to be investigated in the past. Earlier attempts has included other larger alkaline metal elements such as caesium[114][118]. This element interestingly is known to generate a significantly larger SEE gains than lithium[118]. A finding of which W. E. Pickett and others have attributed to the large atomic radius of caesium resulting in a greater dipole moment to eject the electrons out from the diamond surface[123]. This falls in agreement with the Pauling electronegativity calculations of the terminations below (Table.2.4) where caesium has shown a greater degree of electro positivity in comparison to that of lithium (Table.2.3).

Element	Pauli Electronegativity
C	2.55
H	2.20
O	3.44
Li	0.98
Cs	0.79

Table 2.3: Pauli electronegativity of various elements[124][125][126].

Terminal Bond		Total Pauling electronegativity	Terminal Polarity
C-H	2.55 - 2.20 =	+0.35	+ve
C-O	2.55 - 3.44 =	-0.89	-ve
O-Li	3.44 - 0.98 =	+2.46	+ve
O-Cs	3.44 - 0.79 =	+2.65	+ve

Table 2.4: Table of calculation of Pauling electro negativity. As seen from the above H, Li and Cs are net positive whilst O is electro negative. Cs is marginally more electropositive in comparison to Li due to a greater number of electronic shells. Carbon was omitted from the O-Li and O-Cs electronegativity calculations based on the aforementioned findings by O'Donnell *et al.* where the terminal carbon atom presents negligible influence to the electrostatic potential of the surface.

Somewhat ironically the size of caesium that has bought about the large SEE gain values, has in itself become the source of complications. Due to its large size, caesium has faced steric hindrance during the process of covering the surface of diamond over the oxygen termination, resulting in a rather sparse coverage of caesium leaving the electro negative oxygen to cover a large portion of the surface (Fig.2.42).

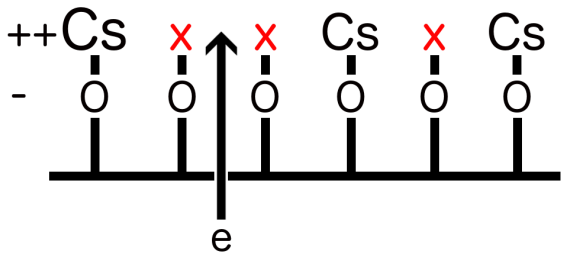

Figure 2.42: CsO terminated diamond surface where overall the electrons are able to escape due to its large dipole moment. While some areas that are unable to be covered by caesium due to its size (denoted by 'x') exposing the electronegative oxygen.

Another known issue faced by CsO terminated diamond is its sensitivity to

heat. It has been found that due to the large radius of caesium the binding energy of caesium is rather poor[118]. Studies have shown that CsO will dissociate at 500°C[127] while other terminations such as hydrogen will dissociate at 740°C[128]. Therefore it is logically sound to employ a much smaller alkaline metal that is able to both avoid steric hindrance and maintain high bond strength. Lithium, an element that is a member of the alkaline metal family that also has the same number of electronic shells as oxygen and carbon was therefore considered to be the prime candidate as a replacement for caesium. As seen from the table of bond dissociation energies (Table.2.5) one could see that the bond strength between C-H and O-Li are extremely similar, 338.4±1.2[129] and 340.5±6.3[129] respectively. The bond energy between O-Cs (293±25[129]) is considerably smaller than that of O-Li, implying a greater resistance of LiO termination to temperature in comparison to CsO with LiO's heat resistance estimated to be in the same league as the H termination.

Bond	Bond dissociation energy($kJmol^{-1}$)
C-H	338.4±1.2[129]
C-O	1076.62±0.06[130]
O-Li	340.5±6.3[129]
O-Cs	293±25[129]

Table 2.5: Table of bond dissociation energies of various terminations.

SEE and doping Upon initial inspection the relationship between doping and SEE may not be apparent. After all SEE is a near surface effect with very little need for a long carrier mean free path that is provided through doping. The key paradigm here is charging, it is an often overlooked concept that if a semiconductor system pertains a charge it indicates the presence of an excess number of charge carriers. Electrically speaking this condition is almost an exact replica-

tion of a doped semi-conductor. Therefore analogously to a doped semiconductor one would observe band bending from a charged system[131]. In another words through the injection of electrons (i.e. the primary electrons injected into the diamond surface to induce secondary electrons) the bands could bend upwards as though the system has been n-type doped at the surface. This works against the surface band bending caused by various net positive surface terminations (such as H, LiO and CsO) thus reducing the number of secondary electrons available to undergo SEE. One method of circumventing the issue is by providing the diamond sample with a conductive channel that could be utilised to drain the excess charge. Most commonly this is carried out by using a conductive boron doped diamond sample where many have successfully obtained high gain values[114]. The build-up of charge is also known to reduce the gain by reducing the primary electron momentum[114] where in extreme cases it could even go far as to cause the primary electrons to be repelled from the surface[114]. The use of boron however has to be addressed with caution. Miller *et al.* and Shih *et al.* found that not only boron doping could aid the SEE yield but it could also impede it[132][133]. Specifically, if the concentration of boron doping is too low the diamond will have too short a mean free path to drain the charge build up[114]. If the concentration of boron doping is too high on the other hand the charge carriers will suffer from scattering where the secondary electrons would find it difficult to find its way out of the diamond surface[114]. The negative effect of excessive boron doping is outlined in the graph[133] (Fig.2.43):

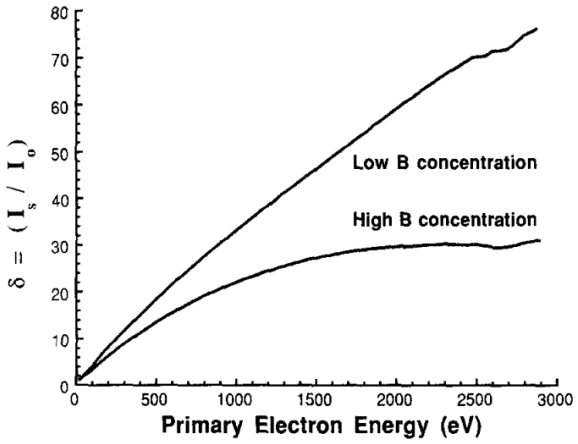

Figure 2.43: Effect of boron doping concentration on the SEE yield. As one could see the high B concentration (resistivity: 50-170Ωcm) has a significantly lower gain value over the low boron doped sample (resistivity: 50,000-170,000Ωcm)[133].

A concept that holds strong ties to doping is crystallinity. Doping being a form of impurity will inevitable interfere with the crystal structure of its host diamond. Notably it will introduce grain boundaries that as mentioned earlier in the chapter are known to scatter the charge carriers[114]. Therefore doped diamonds inevitably will not only suffer from the scattering due to the charged boron nuclei it will also be affected by its grain boundaries. This is of particular interest with regards to Chapter 8: SEE where the prospect of using a poly crystalline diamond and nano diamonds to generate SEE will be investigated.

Beam energy Another important factor to consider when measuring the SEE of a sample is the incident electron beam energy. Simply put the SEE yield from a diamond surface falls into one of three regimes. Firstly, the low electron energy regime where the electrons do not have enough energy to generate a sufficient number of secondary electrons through inelastic scattering (Fig.2.44a). As one could imagine the gain from this energy range has the tendency to be rather poor simply due to the deficiency of secondary electrons[114]. The high-energy range on the other hand has a surplus of energy to generate numerous secondary electrons and therefore has a rich supply of electrons available to undergo SEE. However due to the great penetration depth of the primary electrons of this energy range the

secondary electrons are buried deep into the bulk where the secondary electrons are forced to travel through a large distance across the diamond bulk in order for it to reach the surface[114]. If the distance between the secondary electron and the surface is great (particularly if it is greater than the mean free path) it has the tendency to be absorbed into the diamond bulk, as well as undergoing scattering both from dopant nuclei and grain boundaries. Both of these factors are known to impede the secondary electrons to escape from the surface resulting in poor gain[114] (Fig.2.44c). Interestingly this is not the only cause of reduced gain from high energy electrons. It is also due to the fact that the production rate of secondary electrons is non-linear[133]. Therefore the primary electrons will not generate as much secondary electrons along its tracks when it has the most energy but generate a substantially larger amount of secondary electrons once it has lost some of their momentum[133] (Fig.2.45) deep in the bulk away from the surface. Shih *et al.* has suggested that this may be due to the fact that slower electrons has a greater interaction time that allows the primary electrons to transfer the energy to generate secondary electrons[133]. The final energy range, the mid-energy is where the SEE could enjoy the best of both worlds where the primary electrons has enough energy to generate secondary electrons with the benefit of its penetration depth being shallow enough to induce SEE near the surface, thus are able to yield the maximum amount of secondary electrons[114] (Fig.2.44b). The maximum amount of SEE gain generated is known as the peak gain of which diamond naturally is know to have approximately 3[114]. Chapter 8: SEE aims to improve on this by varying the crystallinity and termination of the diamond samples.

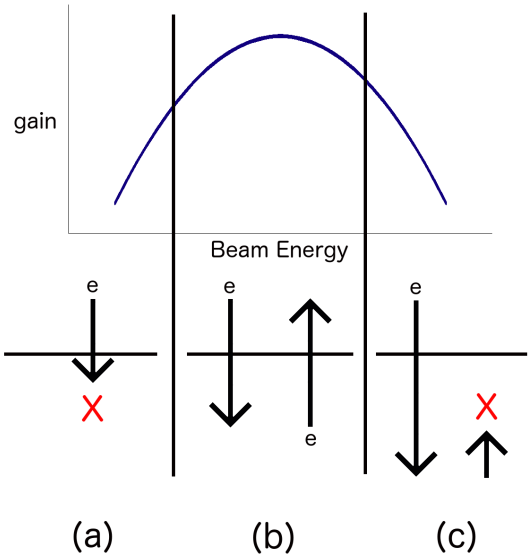

Figure 2.44: The relationship between SEE gain and the beam energy of the primary electron. As one could see from a) if the energy of the primary electron is too small it will not be able to generate secondary electrons due to the lack of energy. c) the higher end of the energy range similarly suffers from a low gain due to the fact that the primary electrons are too deeply embedded into the bulk of the diamond where the secondary electrons are unable to escape from the surface. b) on the other hand has the optimum amount of energy that allows both the generation of electrons and the emission from the surface thus has the greatest amount of gain.

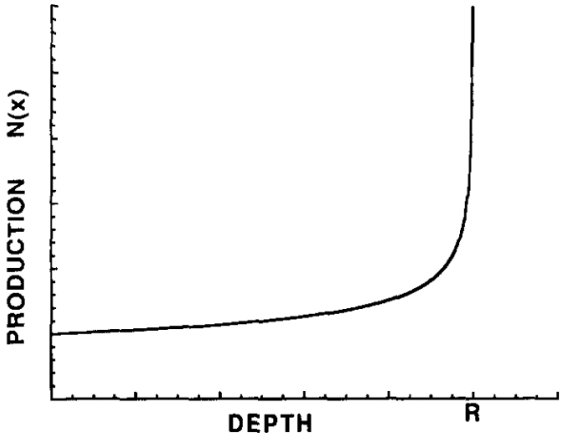

Figure 2.45: The relationship between the production rate of secondary electrons by a primary electron against its penetration depth. As one could see there is a sudden increase in production rate at R, the terminal penetration depth of the electron, where the primary electrons have enough interaction time to generate secondary electrons[133].

Throughout this investigation two forms of electron beam energy control will

be employed: the electron gun output and electrostatic repulsion. The former as the name suggest is operated by controlling the acceleration of electron within the electron gun induced by the electric field. The latter on the other hand relies on the definition of electron volts(eV). The unit of energy eV is defined as the energy gained by an electron when a electric potential at the electron is increased by one volt[134]. Therefore if an electron was to have an energy of 700eV and it was to be repelled by a potential applied to the sample surface of -400eV. The net energy that the electron has is 300eV. By controlling the electron gun output to control the energy of the electrons in large increments and by applying the fine-tuning using electrostatic repulsion the energy of an electron could be finely controlled.

Influence of surface contaminants By the very nature of surface effects, SEE is notoriously sensitive to surface contaminants. As well as the obvious physical contaminations such as dust, moisture plays a significant role in affecting the SEE yield. Maier *et al.* and Takeuchi *et al.* have suggested that due to the polar nature of water it is known to cause charge transfer at the surface causing an upward band bending that works against the NEA[90][135]. Alternatively, moisture could also play havoc with the hydrogen termination. Water is known to convert hydrogen terminations (-H) to an hydroxyl group (-OH) over time which again due to its lower electro negativity results in an upward band bending reducing the NEA favourable to SEE[118].

Alternative methods of SEE Although this investigation will solely use electron beams to initiate SEE, alternative methods do certainly exist. Studies by Yater *et al.* for example has shown that one could even generate secondary electrons by exposing the diamond sample to sub-bandgap photons from a hydrogen terminated (thus band bent) surface[136].

Application SEE is used in the field of amplification, most commonly as a photo-multiplier[114]. The very nature of SEE rapidly increasing the number of electrons from a single electron has proved to be ideal as night vision amplifiers

that requires operation under extremely small signal strengths. There are two main schools of signal amplification: reflection and transmission where reflection generates SEE from the same surface of entry of primary electrons[137] (Fig.2.46) while transmission relies on SEE from the opposite surface to the entry of primary electrons[137] (Fig.2.46).

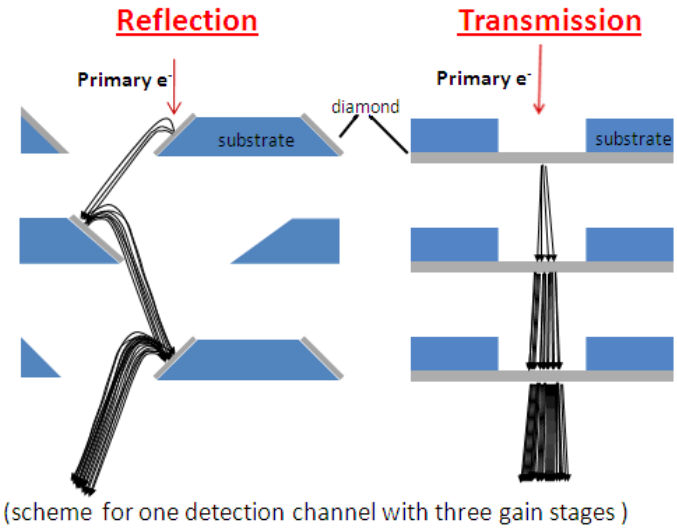

Figure 2.46: Two different types of electron multiplication using SEE[137].

This investigation will use reflection as its sole mode of electron amplification, for the reason being that it will be best suited in its application with micro channel plates (MCPs) a glass plate with an array of hollow tubes running through from the top surface to the bottom[114][138] (Fig.2.47). The significance of MCPs lies in its ability of its inner layer of the tubes to be coated with diamond that is capable of generating SEE. Therefore if one was to have a single electron entering the diamond-coated tubes within the MCP it will be able to cascade down the tube increasing its number dramatically until there is a significantly large number of electrons enough to generate a signal for the night vision device[114]. Although there are possible losses along the multiplication process, theoretically a single electron should be able to induce the number of electrons equal to the gain times the number of SEE generation events the electrons have undergone[139] (Fig.2.48). Algebraically the above could be summarised as:

$$gain = e^{\frac{GL}{d}} \tag{2.6}$$

where:

G is the gain factor, a property summarising the inherent characteristic of the inner channel wall material represented by the electric field intensity within the channel[114]. This factor will vary according to the extent of the coverage of diamond along the inner surface and its termination.

L is the length of the channel.

d is the diameter of the channel

As seen from the equation above the greater the gain factor, G the greater the gain will be. One of the cornerstone properties that influences the gain factor is the termination. Therefore Chapter 8: SEE will attempt to find the ideal termination to achieve the greatest amount of gain. Thus benefiting the signal strengths of the night vision devices.

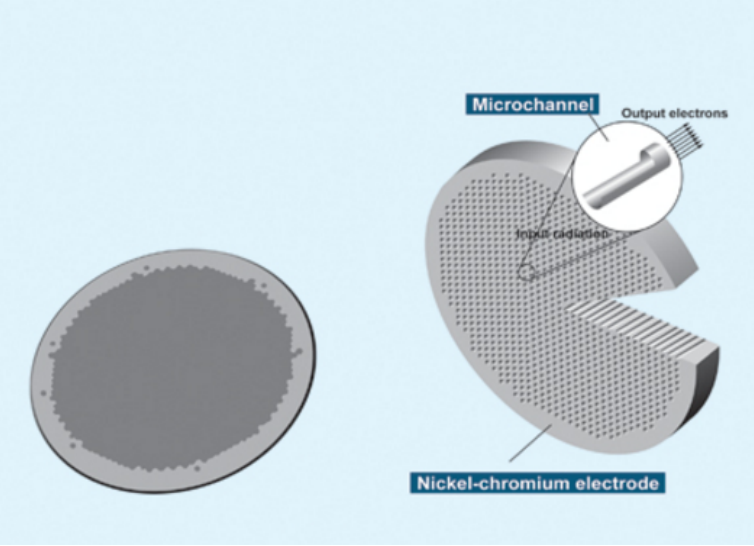

Figure 2.47: The structure of MCP. The MCP consists of narrow tubes typically of 15-50μm[114] and lengths 2mm[114].

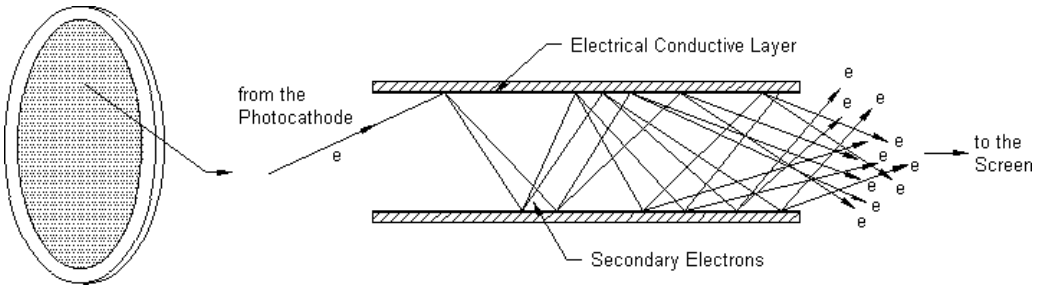

Figure 2.48: The process of signal amplification through SEE. A photon hits the scintillator screen attached to the surface of the MCP (left) converting the photon into an electron. The electron will then induce SEE once it penetrated the diamond coated inner surface of the MCP tubes followed by the generation of electrons that further induces SEE over each generation[139].

Chapter 3

Introduction to Neutron Detectors, Polymer Composites and Blood Pressure Sensors

3.1 Neutron Detectors

A neutron is a subatomic particle consisting of two down quarks and one up quark that contains no charge and is one of the essential components atomic nucleus along with protons. It was first discovered by H.C. Webster in 1932[140] and later found its use as an activation particle for a nuclear fission reaction[141] by Hahn *et al.* in 1939. The fission process as seen from the reaction equation below[142] (Fig.3.1) inherently produces a multiple number of neutrons per reaction which could then further initiate a chain reaction that releases a tremendous amount of energy in the process. Industrially, this heat generated by the reaction is often used in nuclear power plants and nuclear submarines as energy sources.

The energy released is equal to the mass lost during the reaction determined by the Mass-Energy equivalence equation (Eq.3.1)[143] that was first derived by Albert Einstein in 1905[144]. The net mass lost during the fission reaction is considered to be equal to the energy produced during an ideal reaction.

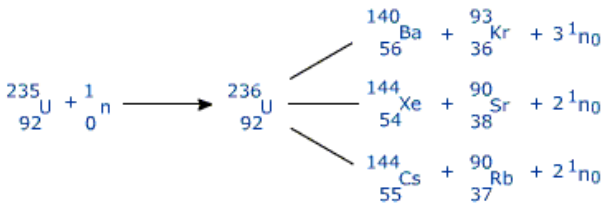

Figure 3.1: A typical nuclear fission reaction between ^{235}uranium and a neutron creating a plethora of different reaction products. Notably all of the reactions produce more than one neutron that could in turn induce a chain reaction that quickly grows the number of neutrons and the amount of energy released[142].

$$E = mc^2 \tag{3.1}$$

Typically the above fission reactions (Fig.3.1) produces neutrons with energies between 3.3eV-1.7MeV (slow/thermal neutrons)[145]. Nuclear fusion is known to produce neutrons of higher energies, typically of 14.1MeV (fast neutrons)[146]. The two energy regimes are separated by the ^{12}C,n interaction threshold (5.8MeV)[147] (Fig.3.2). Neutrons with energies greater than 5.8MeV are known to directly interact with ^{12}C, including diamond (Fig.3.3) producing an α-particle and a ^{9}Be particle. α-particles produced in this manner are immediately absorbed by the surrounding diamond bulk creating charge. By measuring the charge the number of α-particle captured could then be determined through electrical measurements. Since the number of α-particle is directly proportional to the number of incoming fast neutrons one could therefore indirectly determine the number of neutrons. However for the slower thermal neutrons due to the lack of energy to meet the ^{12}C,n interaction criteria additional measures such as the use of a conversion layer (typically ^{10}B or ^{6}Li[148]) that converts the neutrons into α-particles is required(Fig.3.3).

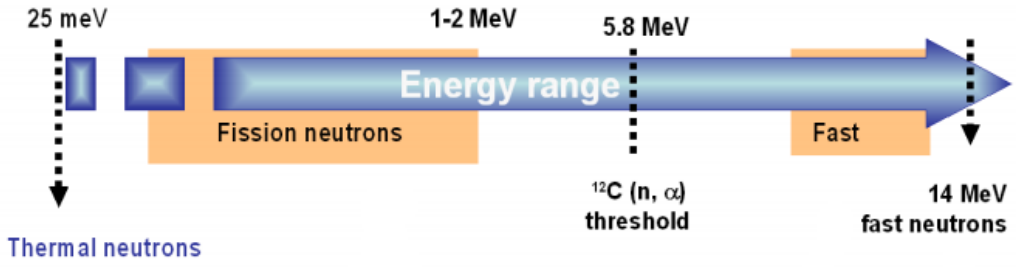

Figure 3.2: Energy spectrum of neutrons. The lower energy neutrons on the left hand side of the spectrum are thermal neutrons typically from a fission reaction while fast neutrons on the right are typically from a fusion reaction. Neutrons with energies greater than the 5.8MeV threshold are capable of directly interacting with diamond[147]

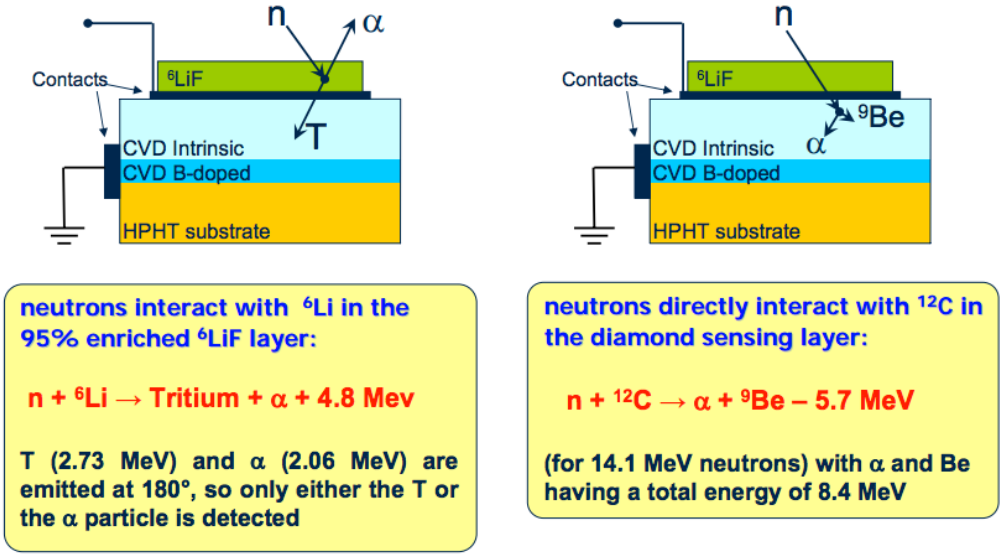

Figure 3.3: Two methods of neutron detection using diamond. The slow thermal neutrons with low energies (left) will interact with the ^{6}LiF (conversion layer) that will convert a neutron into a charge bearing tritium and an α-particle which in turn will be absorbed by the diamond and detected. Fast neutrons with energies greater than 5.8MeV on the other hand (right) will be able to interact with the ^{12}C (diamond) directly producing a ^{9}Be and an α-particle which by measuring its charge one could also determine the number of incoming fast neutrons[149].

At this point it is very important to remember that the interaction above is not a simple case of one to one exchange of charge per incoming particle. In another words a single incoming radiation particulate could create a shower of charges in its penetration track. Although the exact energy profile of the alpha particles created by the conversion layer depends on the testing conditions (such

as the thickness of the conversion layer that could absorb the α-particle and the crystallinity of the diamond layer that could scatter the charge carriers[150][83]). By using the above example (Fig.3.3) where the α-particle is said to have an energy of 2.06MeV, one could estimate the number of electron-hole pair (e/h pair) produced by one α-particle to be:

$$\text{num. of e/h pair} = \frac{\text{energy of alpha particle (2.06MeV)}}{\text{energy required to form an e/h pair (13.6eV)}} \tag{3.2}$$

13.6eV is the generally accepted energy required to produce an electron-hole pair in diamond[151].

3.1.1 Neutron Health Hazard

Ever since the discovery of radiation its detrimental effects to the human body has been heavily researched. Neutrons in particular are of high interest due to the plethora of known tissue damage they could cause. For example S.B Field in 1977 has found that exposure to neutrons causes cell necrosis in the short term directly damaging the skin, cartilage, bone, nervous systems and lungs[152]. This is followed by the long-term damage that inhibits the healing process by suppressing mitosis, the ability for a cell to self-replicate, a crucial process of healing. The process was found to be comparable to but more destructive than other known hazardous radiations such as x-rays[152]. However this very nature of cell destruction and growth suppression is now being used in cancer therapy by directing the radiation to cancer cells preventing their growth and inducing their eradication[153].

3.1.2 Developmental History of Neutron Detectors

Following the discovery of the toxicity of neutrons and its benefits, neutron detectors have been widely developed from as early as 1932 Curie-Joliot[154] and Chadwick[154] who discovered that materials such as hydrogen, carbon dioxide

and glass windows were capable of capturing neutrons. Following this discovery, many have since attempted to quantify their capturing rate as well as finding a more suitable detector medium that has a greater rate of neutron capture. Its historical development has been documented by Brooks *et al.* who categorised the development of neutron detectors into three eras: 1932-1959, 1960-1979 and 1979 to present day. Brooks *et al.* described 1932-1959 as being the period where elemental detection methods such as cloud chambers[155], recoil telescope[156][157], nuclear emulsion[157] and organic scintillators[158] have been invented. Most importantly however during this period the ^{3}He-proportional counter spectrometer[159] was invented. ^{3}He not only was one of the earliest detector materials to be discovered but it remains one of the best neutron capturing materials available to this day. This particular method relies on the charged reaction products that form as a result of the interaction between the ^{3}He and neutrons, much akin to the previously outlined ^{6}Li and ^{10}B conversion layers. The true importance of this method however lies in the fact that it has laid a foundation for the charge based neutron detection system that is still being used by current generation neutron detectors. This system acted as a precursor to the second era of 1960-1979 when the solid-state semi-conductor detectors (as opposed to the gaseous ^{3}He detectors) such as those made of silicon and diamond have been invented. Another crowning achievement of this era was the invention of the Multi Channel Analyser (MCA). The main benefit of this device is in its ability to count the number of incoming radiation events of different energies and arrange them into different channel windows (bins) that produces a count vs channel number graph. It is essentially a tool that could profile the charge generated by the neutrons (and other radiations) and build a histogram of the incoming neutrons based on the amount of charge they generate. The output from the said multi-channel analyser holds particular importance in Chapter 7 where one attempts to detect α-particles and neutrons. Since the incoming radiation is capable of creating multiple charge bearing electron-hole pairs where its number is proportional to the energy of the radiation, by measuring the charge generated one could indirectly measure its

energy. For this reason, if one knows the peak energy of a radiation source (such as 5.486MeV for α-rays emitted by americium-241[160]) one could convert the channels into energies by using the peak position from the count vs channel number graph as a calibration point (simply by dividing the known peak energy by the number of channels between 0 and the signal peak position). Now that one knows what each of the channels are worth in energy one could graph a count vs radiation energy plot. This conversion process will then allow the use of the detector as a radiation energy spectrometer by referencing the said graph. The progress seen in the final era of 1979-present is a direct descendant of the transistor revolution. The development of faster computers has promoted the invention of intricate and computation heavy devices that has allowed the measurement of neutrons to be processed with greater precision and speed. In particular the aforementioned multi channel analyser is now able to measure and sort the neutron energies using a greater number of channels bringing greater accuracy to the neutron energy profile (Fig.3.4).

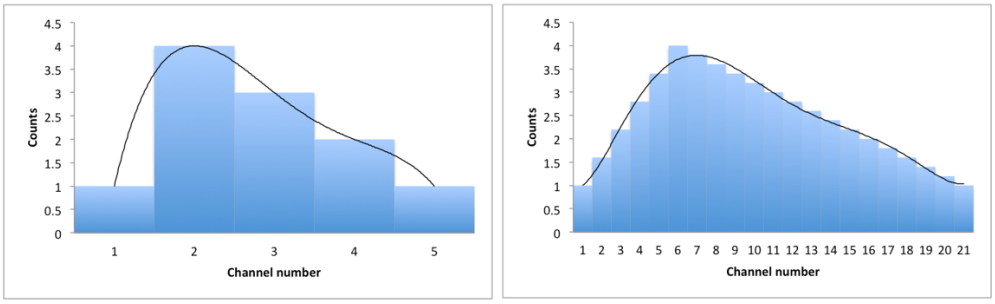

Figure 3.4: Example neutron histogram model of an identical radiation source using a larger channel width (left) and smaller channel width (Right). The energy profile with narrower channel bins provides a more accurate representation of the neutron energy distribution.

3.1.3 Efficiency Issue

The above mentioned method of solid state neutron detection (and every other device based methods) suffers from one common issue, efficiency. All devices in practice are imperfect and therefore they are inherently unable to detect all of

the charges generated by the radiation. Some of the potential reasons behind this includes the attenuation caused by the medium the radiation travelled in, such as air and conversion layer[150] as well as the scattering due to defects in the diamond layer such as traps, voids and grain boundaries[83]. Whatever the cause may be, the number of detected charges are reduced resulting in false signal peak position and neutron count. The latter is of particular importance in Chapter 7 since it aims to develop a neutron detector to be on board a Trident nuclear submarine which monitors the radiation exposure to the crew, where an accurate determination of dosage is imperative.

This very issue however could be addressed by calculating the device efficiency mathematically and compensating for it. In order to do so one will have to take two factors into account: radiative intensity loss and attenuation. Radioactive materials as the name suggests releases radiation in a radial manner thus it follows the inverse square law. This means that if there is a gap between the source and the detector there will be radiation loss in its tracks reducing the amount of radiation that reaches the detector. Attenuation on the other hand is a type of radiation loss that comes from the loss of energy to the medium that the radiation is travelling in. If the radiation were to have lost its entire energy before reaching the detector it will be unaccounted for giving a lower reading than its true count.

Radiative Intensity Loss Work by Knoll *et al.* has shown that the intrinsic efficiency, ϵ (the efficiency of the device based on the number of radiation quanta incident on the device) as[161]:

$$\epsilon = \frac{\text{num. of pulses recorded}}{\text{num. of radiation quanta incident on detector}} \tag{3.3}$$

In mathematical form the efficiency is defined as[161]:

$$\epsilon = \frac{N4\pi}{S\Omega} \tag{3.4}$$

where:

ϵ is intrinsic efficiency

N is the number of recorded event under the full energy peak (Fig.3.5)

S is the radiation quanta emitted by a source over the measurement period

Ω is the solid angle between the source and the detector (Fig.3.6)

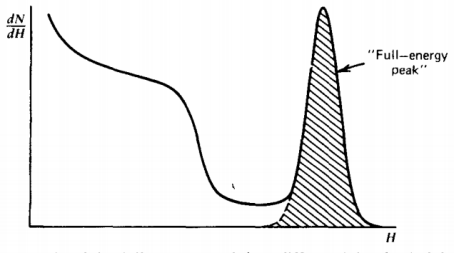

Figure 3.5: Example of the countable events under the full energy peak.[161]

If the source is sizeably smaller than the detector and the distance (d) between them is much greater than the diameter of the detector (a), thus $d \gg a$. The value of Ω reduces to[161]:

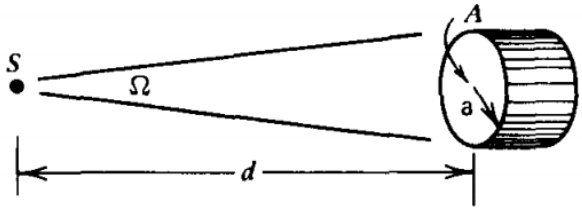

Figure 3.6: Illustration of the relationship between the solid angle, source and detector for a point source.[161]

$$\Omega \cong \frac{A}{d^2} = \frac{\pi a^2}{d^2} \tag{3.5}$$

If on the other hand the source was to be comparable to the size of the detector (Fig.3.7) the equation will be approximated to[161]:

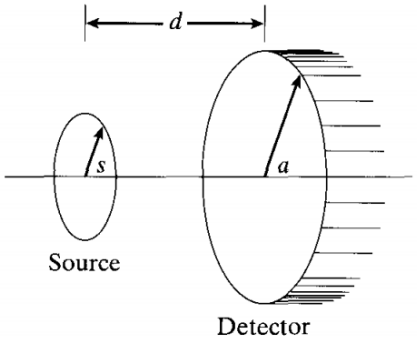

Figure 3.7: Illustration of the relationship between the source and detector for a non-point source.[161]

$$\Omega \cong 2\pi\left[1 - \frac{1}{(1+\beta)^{1/2}} - \frac{3}{8}\frac{\alpha\beta}{(1+\beta)^{5/2}} + \alpha^2\left[\frac{5}{16}\frac{\beta}{(1+\beta)^{7/2}} - \frac{35}{16}\frac{\beta^2}{(1+\beta)^{9/2}}\right] - \alpha^3\left[\frac{35}{128}\frac{\beta}{(1+\beta)^{9/2}} - \frac{315}{256}\frac{\beta^2}{(1+\beta)^{11/2}} + \frac{1155}{1024}\frac{\beta^3}{(1+\beta)^{13/2}}\right]\right] \quad (3.6)$$

where:

$$\alpha \equiv \left(\frac{a}{d}\right)^2 \quad \text{and} \quad \beta \equiv \left(\frac{s}{d}\right)^2$$

By substituting the available parameters into the above one could determine the efficiency of the detector. This however is under the assumption that the radiation suffers no loss to attenuation.

Attenuation This investigation concerns itself with two types of radiation: α and neutrons. α testing involves transmission through air and air only whilst neutrons will travel through both air and polyethylene. The α attenuation is rather straight forward, in short there will be no intensity loss as long as the detector is placed within range[161]. This stems from the fact that α-particles experiences a gradual loss of energy as they travel through the absorbing medium. Therefore as long as the medium is homogeneous and the α-particle is from a

mono-energetic source they will experience a sudden drop in intensity once it reaches the radiative limit[161]:

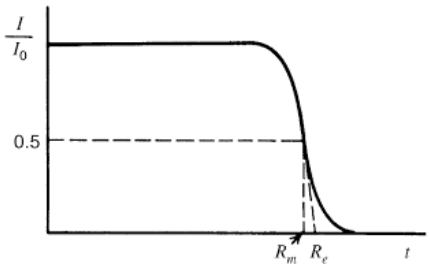

Figure 3.8: Illustration of the relationship between the intensity and range of α particles[161].

In particular, findings by Jesse *et al.* has shown that α-particles of energy 5.3MeV has a range of at least 3.84cm[162] thus indicating that as long as the α-particle has an energy of 5.3MeV or greater it will not suffer attenuation until at least 3.84cm. Therefore by placing the detector fabricated in Chapter 7 at a distance closer than 3.84cm one could effectively disregard the attenuation of α-particles.

Neutrons however unlike α-particles are known to decay exponentially[161]:

$$\frac{I}{I_0} = e^{-N\sigma t} \tag{3.7}$$

where:

I is the number of transmitted neutrons with absorber

I_0 is the number of transmitted neutrons without absorber

N is the number of nuclei per unit volume

σ is the neutron cross-section (m^2)

t is the thickness of the absorber (m)

The neutron mean free path, λ is given by[161]:

$$\lambda = \frac{1}{N\sigma} \tag{3.8}$$

The key parameter here is cross-section. Studies by Teitsma has shown the cross-sections of nitrogen (78% of air) and oxygen (22% of air) to be as little as 11.4×10^{-24}cm and 4.24×10^{-24}cm respectively, giving a combined cross-section of 9.8×10^{-24}cm[163]. By applying this and the density of air, 0.538×10^{20}atoms per cm^3[163] to the formula above, the mean free path of neutrons in air is considered to be 1897cm. This length in comparison to what is used in Chapter 7 (45.7cm) is nominal and therefore the attenuation of neutrons in air could be considered negligible.

Polyethylene, on the other hand (the other material which neutrons has to transverse through in Chapter 7) has a greater interaction rate due to its hydrogen content[161]. The purpose of passing neutrons through polyethylene is to achieve greater detection rate. In neutron detection it is common practice to use a polyethylene moderation sphere know as a Bonner sphere (named after one of the inventors: Bramblett, Ewing and Bonner[161]) to scatter neutrons as well as reduce their speeds to enable increased detection by the thermal neutron detectors:

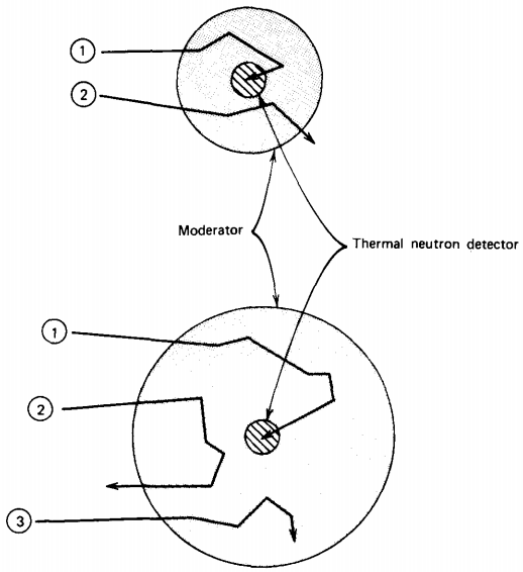

Figure 3.9: Illustration of the moderation process of neutrons by a Bonner sphere. 1) represents the neutrons that were successfully scattered into the neutron detectors for detection. 2) represents the neutrons that were scattered but was not captured by the detector. 3) represents the neutrons that were absorbed into the Bonner sphere as a result of having too thick a moderation sphere[161].

As seen from the diagram above and below (Fig.3.9 and Fig.3.10) it is important to have the correct Bonner sphere size for the energy of the neutrons one is trying to detect. If the Bonner sphere was to be too large the scattered neutrons could be lost to absorption and if it was to be too small the scattering will be insufficient for detection:

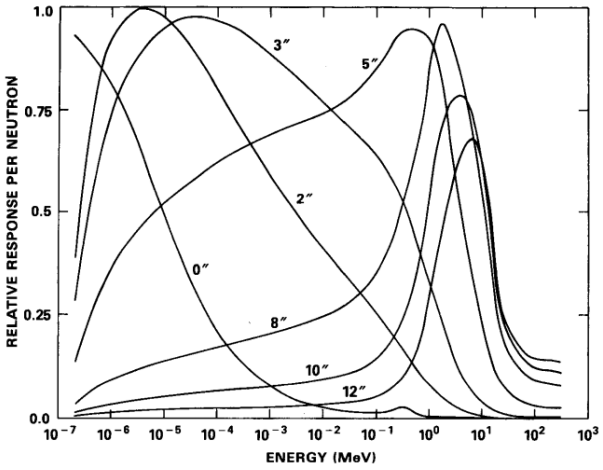

Figure 3.10: The energy dependence of the relative detection efficiencies of Bonner spheres of various diameters[161].

In the interest of this investigation the Bonner sphere to be used in Chapter 7 was chosen to be 8inches in line with the neutron source with peak energies of 3.5 and 5MeV. This will allow for 80% of the neutrons that interacts with the Bonner sphere to be detected by the detector. Therefore when calculating the solid angle during the device efficiency calculations the 8inch diameter silhouette will be used as the area of detection. The number of the calculated incident neutrons will then be reduced to 80% to account for the absorbed and stray scattered neutrons (2 and 3 from Fig.3.9). For this investigation the Bonner sphere will be modelled as a plane to fit the mathematical model of Eq.3.5, although this will result in a slight overestimation of the neutron flux due to the curvature of the sphere. Considering it is a safety measure to be used on board a nuclear submarine a slight overestimation was preferred over underestimation.

3.1.4 Basic Design of Neutron Detectors

Having discussed the recent development of neutron detectors one may question what the current state of neutron detectors may be. The basic design of the modern neutron detectors has not seen much change since the early 1960s to the late 1970s[164]. The ^{3}He detector has laid a foundation of the charge based detection mechanisms i.e. a system which counts the number of incoming neutrons by measuring the amount of charge being generated[164]. Structurally speaking, a detector typically has three components: contacts (charge collectors), interaction medium and conversion layer (Fig.3.11). ^{3}He detectors however are an exception to this structure in that the interaction medium (^{3}He) has a dual purpose of also being the conversion layer (Fig.3.11a).

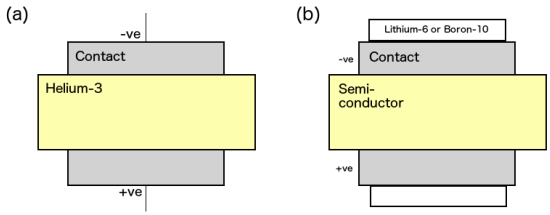

Figure 3.11: Cross-sectional view of the a) ^{3}He detector with ^{3}He interaction medium/conversion layer and contacts b) semiconductor neutron detector with a ^{6}Li or ^{10}B conversion layer and metal contacts.

If one was to expose the ^{3}He detector (Fig.3.11a) to neutrons each incoming neutron will generate a charged particle in accordance to the equation below[165] (Eq.3.9):

$$^1_0n + ^3_2He \rightarrow ^1_1 proton + ^3_1 H + 765keV \tag{3.9}$$

The charges generated in the above manner will then be pulled apart towards the contacts by the electric field generated by the applied bias across the contacts (Fig.3.12).

What is truly elegant about the above design is that the interaction medium also happens to be a neutron to charge conversion material, which is a simple

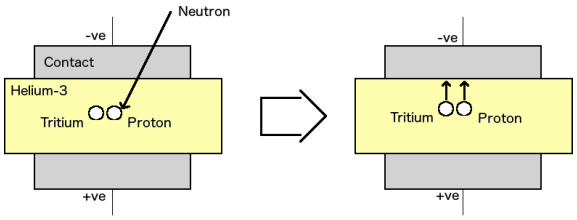

Figure 3.12: Generation of protons due to the (^{3}He, n) interaction and its charge collection process. The positively charged proton is attracted to the negatively biased contact resulting in the collection of one charge per neutron interaction.

yet elegant solution to neutron detection. However in recent years the use of ^{3}He has fallen out of favour for three reasons: one being the limitation in the supply. At the time of writing only one company (U.S. Gas) is legally capable of supplying Britain with ^{3}He in the world (after the self-imposed export ban from Russia) creating a risk factor of supply shortage if that company was either to go into administration or if the US were to impose an export ban. Additionally that said company being of a foreign origin creates some discomfort for military applications. Another reason why ^{3}He is being phased out is due to the sudden inflation in its price. US national reports have suggested that a litre of ^{3}He that was typically traded at around US$100/l in the early 2000s is now being sold at an exorbitant price of US$2000/l and above[166]. One of the reasons behind this sudden increase in price is due to the supply shortage post September 11 2001 terrorist attack on the US where ^{3}He detectors were rapidly deployed within the US to support US national security[167]. The current annual global demand of ^{3}He is 65,000l[167] while its currently available supply is 15,000l per annum[167]. Another reason why helium has fallen out of favour is due to the fast growing development of solid-state detectors. As mentioned earlier in the section, following the development of ^{3}He detectors more convenient non-gaseous, thus robust and stable semiconductor detectors, were developed. It is worth noting that although the interaction material has seen some changes over the years the type of contacts used has very much remained the same. Since its early stages of development it was widely known that lighter metals such as that of titanium and aluminium

is less prone to 'activation'. This is a process where the incoming radiation will interact with metals and displace its atoms from its crystal lattice resulting in the formation of defects[168]. This proved to be particularly important for neutron detectors where J. A. Brinkman has found that neutrons are particularly likely to cause displacement damages[168]. Another aspect of heavy metal activation is radioactivity ruling out the use of gold, a commonly used contact material. This stems from the fact that gold has a large cross-section to neutrons resulting in the absorption of neutrons forming ^{198}Au (as opposed to the stable isotope of gold, ^{197}Au)[169]. This particular isotope is known to have two decay modes: beta (β-ray, 0.97MeV)[170] and isometric transformation (γ-ray, 0.408MeV)[170]. Beta rays being negatively charged could bring rise to a false positive to the charge based neutron count reading. γ-rays could produce an electron-hole pair in diamond that again could cause false readings. Therefore all metals to be used as contacts for this investigation for neutron detection are of light metals such as Cr, Al and Ti.

The most common and established materials used in a neutron detector is silicon and diamond. Although both materials are known to perform very well as neutron detectors neither one of the two are above average in neutron interaction intrinsically. In another words, if one was to detect neutrons, one would need to introduce an additional step to convert the neutrons into an easily detectable form. The process of conversion is typically carried out using a conversion layer, a material with a high neutron cross-section (Table.3.1) that converts neutrons into a charged particle. The most common two are enriched lithium (^{6}Li) and boron (^{10}B) where they produce an α-particle through the following reactions respectively (Eq.3.10)(Eq.3.11):

$$ {}^{1}_{0}n + {}^{6}_{3}Li \rightarrow {}^{3}_{1}H + {}^{4}_{2}\alpha(765keV) \tag{3.10} $$

Neutron, lithium-6 interaction[171].

$$ {}^{1}_{0}n + {}^{10}_{5}B \rightarrow {}^{7}_{3}Li(0.84MeV) + {}^{4}_{2}\alpha(1.47MeV) \tag{3.11} $$

Neutron, boron-10 interaction[171].

Conversion Material	Absorption cross-section to 2200m s^{-1} thermal neutrons (barns)
^{3}He	5333±7
^{6}Li	940±4
^{10}B	3835±9
^{12}C	$3.53\times10^{-3}\pm0.07\times10^{-3}$

Table 3.1: Table of absorption cross-section of various materials common in neutron detection. As seen from the table, ^{3}He has the highest cross-section while ^{12}C has a negligible cross-section to thermal neutrons[172].

However it is worth noting that the figures quoted in Table.3.1 are exclusive to thermal neutrons. For example ^{3}He, ^{6}Li, and ^{10}B may all have high cross-sections to thermal neutrons but a rather diminished cross-section to fast neutrons[169] (Fig.3.13) because the cross-section of ^{12}C to neutrons increases with the energy of neutrons (once it surpasses the 5.8MeV threshold for it to interact with diamond)[149].

Another point to note regarding the conversion layer is the influence of its thickness to device sensitivity. Due to the very nature of the detection mechanism all conversion layers suffer from the dilemma of intractability and signal loss. If one was to have too thin a layer of conversion layer, there will not be a sufficient amount of conversion material for the neutrons to interact with thus one would not be able to produce enough α-particles to be detected. On the other hand if one was to have too thick a layer of conversion material, the generated charge would suffer from scattering within the conversion layer. The α-particles produced will lose momentum and potentially be lost through absorption. Studies by Almaviva *et al.* have shown that the neutron peak develops a greater full width half maximum (FWHM) with increasing conversion layer thickness[150] (Fig.3.14) resulting in poorer detection rates and energy resolutions.

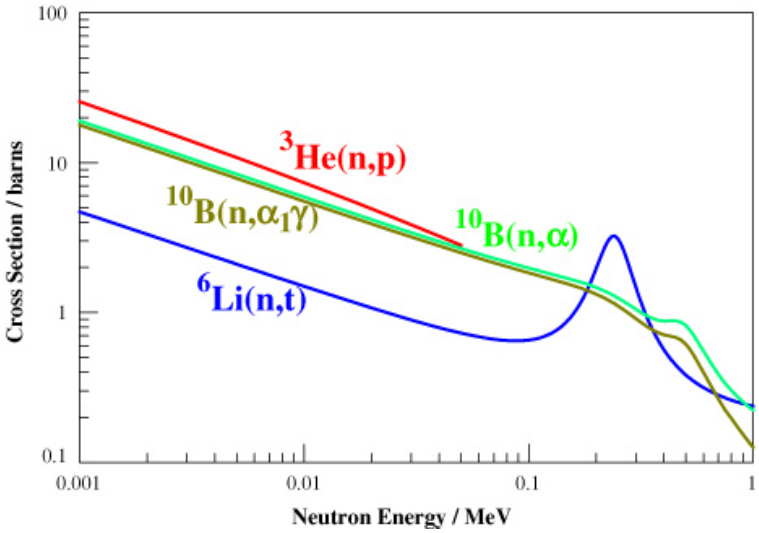

Figure 3.13: The relationship between the cross-section of ^{3}He, ^{6}Li and ^{10}B to neutrons against the relative energies of the neutron to be captured. As one could see the cross-section in general decreases with increasing neutron energies indicating their ability to interact readily with slow, low energy, thermal neutrons but to a lesser degree with their faster variants[169].

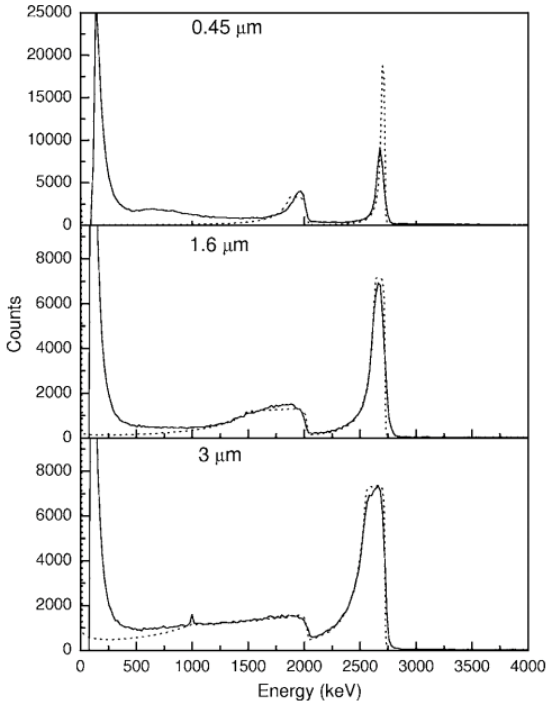

Figure 3.14: Charge counts from detectors with conversion layers of various thickness (^{6}LiF: 0.45μm, 1.6μm and 3μm). The solid lines represent the experimental data and the dotted lines represent simulation. Peaks at 2730keV and 2070keV are that of tritium and α-peaks respectively. As seen from the figure an increase in conversion layer thickness has shown an increase in the full width half maximum of the neutron peaks accordingly[150].

The deciding factor in the thickness of the LiF used was based on its longevity. As mentioned earlier the neutron detectors fabricated in this investigation will be installed aboard a nuclear submarine that has a scheduled lifetime of 25 years, potentially longer. Therefore, this investigation will deposit approx. 3μm of LiF in order to ensure there is enough conversion layer available to facilitate detection during its lifetime while maintaining a respectable FWHM and detection rate[150].

3.1.5 Advantages of Diamond as Neutron Detector Material

Radiation Hardness Recent developments in the field of diamond growth have resulted in a substantial improvement in the crystallinity of diamonds. This has put diamond well above other semiconductors both with regards to its electronic property and to its physical property. Of the many advantages diamond has over other semi-conductor neutron detectors, one property that truly stands out is its radiation hardness. Diamond is known to be able to withstand tremendous amount of radiation in comparison to other semi-conductors making it an ideal candidate for radiation detectors[54][173]. Traditionally, radiation hardness may be achieved in one of two ways: electrically or physically. If one was to take the electrical approach one could use a semi-conductor with a direct band gap such as GaAs that could absorb the energy from the incoming radiation by promoting an electron from the valence band to the conduction band[174][175] (Fig.3.15a). If for instance one was to use a semiconductor with an indirect band gap, such as silicon. One would require a phonon to provide the electron with the correct amount of momentum before promoting it from the valence band into the conduction band [174][175] (Fig.3.15b). If however one was not to have a phonon available at the precise moment when the radiation interacts with the electron, the energy provided by the radiation has nowhere to go other than for it to be converted into heat[175] (Fig.3.15b). The atoms that are heated in this manner typically have enough energy to break out of its crystal lattice, thus displacing the atoms from its original position resulting in defect formation[174]. Defects created in this manner are known as displacement defects and it is one of the major reasons why

silicon detectors becomes redundant after prolonged exposure to radiation[149]. As an example in the world largest magnetic confinement plasma experiment, Joint European Torus (JET)(Oxfordshire, UK) where prospects of nuclear fusion is being researched silicon detectors are required to be replaced annually[149].

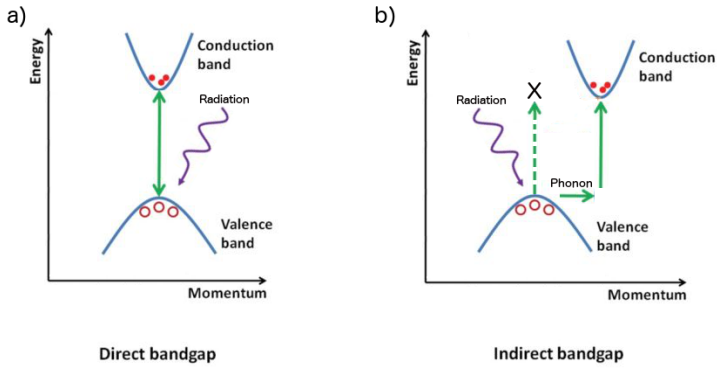

Figure 3.15: a) direct band gap semi-conductor (e.g. GaAs), electrons are able to be promoted from the valence band to the conduction band on demand thus enabling it to respond to radiation absorbing its energy as it comes; b) indirect band gap semi-conductor (e.g. Si), electrons are able to be promoted from the valence band to the conduction band, if and only if there is a phonon of the correct momentum available. If not, the energy of radiation has nowhere to escape with the exception of heat[175].

Diamond on the other hand despite it also being an indirect band gap semi-conductor it is extremely resilient to radiation. This is due to the fact that diamond resists radiation physically through its bond stability of C-C σ–bonds that are able to withstand the heat generated by the radiation[173]. This in conjunction with the fact that diamond has the highest thermal conductivity of all currently known materials allows rapid dissipation of the heat generated limiting thermal damage. Many have tested the limits of diamond radiation harness in the past. Bergonzo *et al.* and Bauer *et al.* showed that the even under the extreme radiation exposure of 5kGy/h for 500h (β and γ-decay, ^{60}Co source, activity of 3.5×10^{14}Bq (9.5×10^{3} Ci), integral dose of 2.5MGy)[173] and exposure to photons (10Mrad)[54], protons (5×10^{13}cm^{-2})[54] and pions (8×10^{13}pions/cm^{2})[54] diamond detectors has shown a negligible drop in its sensitivity.

Diamond is known to have an astonishingly high α and γ ray sensitivity.

Some such as Pomoroski *et al.* has even reported near 100% charge collection efficiency[176] and 100% counting detection efficiency[176] with 0.4%-1.0% energy resolution to α-particles of 5MeV using highly selected single crystalline diamonds[176]. This unusually high radiation sensitivity is attributed to the fact that diamond is the densest material known to man[60]. Findings by Schmidt *et al.*, has shown that diamond has the highest intrinsic efficiency to fission (slow/thermal) neutron detection per unit area and volume due to this density[177]. Ironically the tremendous aptitude of diamond to sense α and γ-ray is also known to cause complications during detection. This is due to the fact that α and γ-ray energies overlaps in some parts of the energy spectrum. Thus if one was to try and measure the number of neutrons through α-particle counts the γ-photons could essentially mimic the α-particles creating a false positive reading. Therefore in general it is desirable for a neutron detector to be γ-ray blind. One approach to achieving this is by using a very thin film of diamond that has a low rate of γ-ray interaction. Jones *et al.* who were working for the De Beers Industrial Diamond division (now Element Six) filed a US patent in 1993[55] outlining this very method where she has used diamond films of thicknesses of less than 50μm, typically between 2 and 30μm[55] to detect α-particles. This claim of α-particle detection from such a thin film has been confirmed by Pomorovski[176] and Schmidt[177]. Most importantly Jones *et al.*'s findings have shown a very low γ-photon detection rate of less than 0.1% and typically 0.03%[55] indicating successful gamma discrimination. An interesting point to note about her approach is the fact that she has integrated ^{10}B, the neutron to α-particle conversion material into the diamond itself[55]. Jones *et al.* has doped the diamond with approximately 1000ppm[55] and 5000ppm[55] of ^{10}B and other isotopes of boron respectively. Boron, as well as being an excellent conversion layer, is also a well-known and established p-type dopant of diamond that naturally has a very high crystal lattice compatibility with diamonds. It was an elegant method of combining the conversion layer and the detection medium together. However this particular approach risks adding complications such as that of scattering from the dopant nuclei, where the charge

produced through neutron to α-particle conversion could be lost also. Although this investigation will not use the embedded boron approach it will use the upper limit of the recommended diamond thickness of 50μm suggested by Jones *et al.*[55] in order to benefit from the γ-ray blindness as well as the robust nature of a thicker diamond film.

Miscellaneous Advantages of Diamonds The charge collector, deposited on either side of the diamond is a well known source of complication for detectors. Leakage currents at the metal-semiconductor interface are known to interfere with measurements. Traditionally this issue has been addressed by creating a p-n junction[149] thus by creating a diode to suspend the charge carrier's flow from the diamond to the metal contacts. Diamond however circumvents the need for a diode entirely by having a wide band gap[60] (5.48 eV) whereby the charge carriers statistically are unlikely to have enough energy to overcome the Schottky barrier. Extensive research by Umezawa *et al.* who tested the leakage resistance of diamond Schottky diode has shown that the diamond-metal interface has a robust resistance to leakage current with a dielectric strengths of 1.2-1.6MV/cm[178], preventing any notable leakage currents[178].

The final point to note regarding the use of diamonds in solid-state neutron detectors are the dark currents. Dark currents are defined as false signals caused by random generations of electron-hole pairs in the depletion zone that is normally excerbated with increasing temperatures. This however unlike other common semiconductors was found to be almost non-existent in diamonds at room temperature[179], negating the need for a cooling device.

3.2 Composites

The definition of composite is extremely simple yet broad, it is defined as: 'a material made up of more than one substance that is used for building things'[180]. Its application varies widely from a highly specialised area of use such as in

aeronautics[181] to something as trivial as cement[5]. The focus of interest for this research however resides in the development of carbon-polymer composites. The field has been heavily developed since the 1970s by Narkis *et al.*[182] and van Beek *et al.*[183]. During this period two schools of carbon composite research has been established. One focuses on its mechanical aspect where the carbon is used as a reinforcement filler to the host polymer causing it to greatly increase its structural strengths[184][185]. The other school that is of particular interest to this research focuses on the change in electrical properties of the composite bought about by the addition of conductive carbon to an insulating polymer host. Development in both camps has been greatly supported by the fact that carbon black (amorphous carbon that consists of random sp^2 and sp^3 carbons) has an extremely high conductivity due to the presence of the free roaming electrons from the π-bonds of the sp^2 structure and with its physical robustness from both the sp^2 and sp^3 structure. Its development however has been greatly limited by the amount of carbon black that is required to achieve conduction or to significantly benefit in hardness[186]. The root of the problem resided in the fact that carbon black is spherical in nature. Structurally speaking it is similar to casting a box full of ball bearings in plastic. Carbon simply has taken too much volume for the plastic to sufficiently bind them together. What one therefore needs is a type of conductive and fibrous carbon with a large aspect ratio that could form a conductive network at low concentrations. Carbon nanotubes discovered by Iijma *et al.* in 1991 have an extraordinarily large aspect ratio[3] and an extremely high conductivity[10] and have therefore proved to be an ideal candidate to replace carbon black[56] (Fig.3.16):

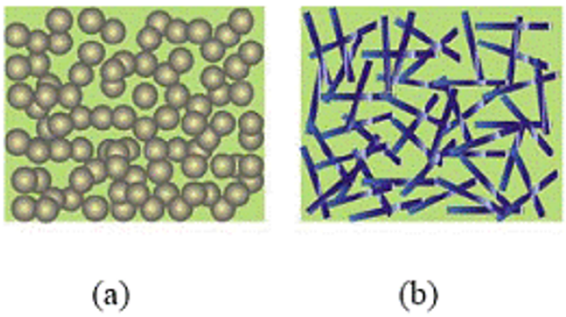

Figure 3.16: a) Carbon black fillers in a polymer host. Its spherical geometry dictates that if one was to achieve conduction one would have to add substantial amounts of filler to the composite. b) Carbon nanotube fillers in a polymer host. Its fibrous nature requires fewer fillers to achieve the same amount of conductivity by forming a conductive network[56].

The fact that carbon nanotubes could create a conductive network as well as exhibit a reinforcement effect on the host polymer (much in the same way a steel I-beam in a concrete building would) using very little amounts of it has been shown through earlier works by Sandler *et al.* who has shown that when comparing the electrical conductivities of carbon nanotubes and carbon black loaded composites it was found that to achieve a respectable conductivity of 10^{-2}Sm^{-1} one would either need 1vol% of carbon black or 0.02vol% of carbon nanotube[186] (Fig.3.17):

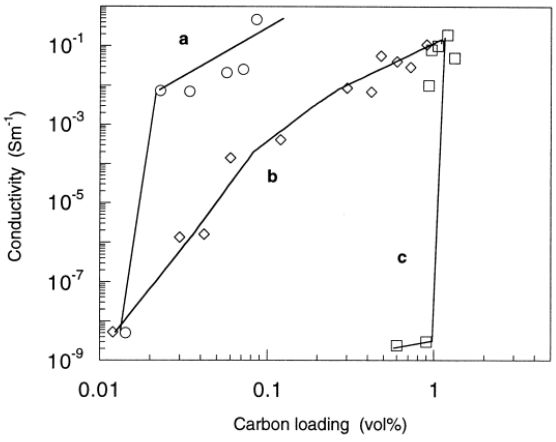

Figure 3.17: c) Carbon black fillers in a polymer host. Its spherical geometry dictates that if one was to achieve conduction one would have to add substantial amounts of filler to the composite. a) Carbon nanotube filler in a polymer host. Its fibrous nature requires fewer fillers to achieve the same amount of conductivity by forming a conductive network[186].

Simple arithmetic suggests that one would effectively need 50 times fewer carbon nanotube to carbon black by volume to achieve the same conductivity with the added benefit of structural reinforcement. This discovery not only has bought dominance of carbon nanotube as composite fillers but it was later found to have a plethora of cost effective and useful applications.

Having identified the ideal composite filler many have then attempted to find its matching ideal polymer host. Although this investigation focuses on two particular types of polymers: epoxy and polydimethylsiloxane (PDMS) many other polymers are known to have shown promising results as well. For this reason it is worth having a read of an excellent review by Bauhofer *et al.*[187] who documented the conductive nature of various different composites. In particular the graph of the polymer host popularity against their respective percolation threshold (transition point between an insulator to a conductor caused by the addition of conductive carbon to an insulating host) is of interest when choosing the polymer host[187] (Fig.3.18).

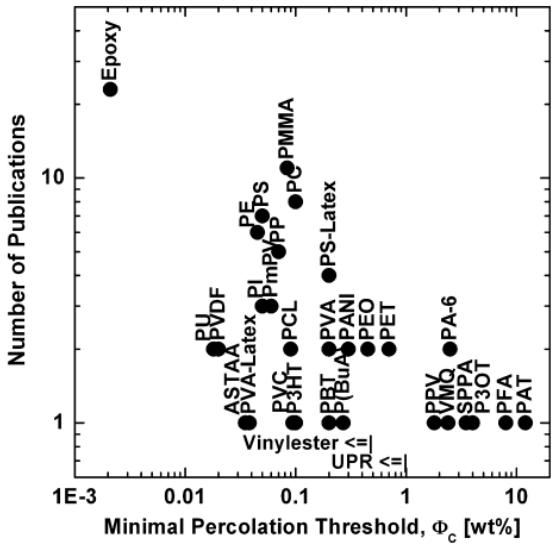

Figure 3.18: The number of publication of a carbon nanotube-polymer composite against its respective minimum percolation threshold under Bauhofer's review[187]

.

Broadly speaking polymer hosts are available in two different types: thermoset

and thermoplastic. The former, thermoset polymer as the name suggests will 'set' upon heating. Thus it will go through a curing process where two chemicals, typically when a monomer (a single unit of the polymer chain) and a hardener (polymerisation agent) are mixed together and heated at a moderate temperature for it to solidify[188]. Polymers such as epoxy and PDMS falls into this category where the curing temperature is typically around 100°C depending on the hardener[188]. However, in general, as long as the temperature does not greatly exceed 100°C the greater the temperature the faster the curing process will be. If one was to substantially exceed the recommended curing temperature, thermal damage to the polymer is to be expected[189]. As a rule of thumb both epoxy and PDMS showed successful curing overnight at 70°C. Notably, thermoset polymers are chemically stable and therefore do not substantially soften upon reheating. Thermoplastic polymers on the other hand are known to soften upon heating to the point that they become re-castable. Many such as Andreas *et al.* and Kharchenko *et al.* have achieved successful results by mixing carbon nanotubes in thermoplastic such as polypropylene (PP)[190][191]. However preliminary investigation with poly-propylene (thermoplastic) has revealed its difficulty in incorporation of carbon nanotubes due to its high viscosity and the narrow mixing temperature window where the plastic could easily face thermal degradation. It is also worth noting that thermoplastics are known to have a non-homogeneous viscosity upon heating due to its poor thermal conductivity where some parts of the polymer in the same container were softer than the other. In order to avoid the said issues thermoset plastics will exclusively be used for this investigation.

3.2.1 Epoxy Resin

As seen from Fig.3.18, epoxy holds a considerable share of the carbon-composite research field. Its popularity is largely attributed to its convenient nature, namely due to its availability, lack of volatile by-products[188], low to negligible toxicity[192], stability at room temperature[188], electrical insulation[188] and its wide range of viscosity[188]. The last two characteristics in particular holds significant im-

portance in Chapter 5: CNT-Epoxy.

As with most chemicals the definition of epoxy is based on its reactive group, epoxide. Epoxy resin is therefore defined as a class of chemicals with two or more epoxide groups in its structure[188]. Its curing agent, also commonly known as its hardener on the other hand has a range of reactive groups such as: amine, alcohol and thiols[193][194], each of which have their own sets of advantages[188] (Fig.3.19):

Type	Advantage	Limitation
Aliphatic amine	Low cost, low viscosity, easy to mix, room temperature-curing, fast reacting	High volatility, toxicity, short pot life, cured network can work up to 80 °C but not above
Cycloalipatic amine	Room temperature-curing, convenient handling, long pot life, better toughness and thermal properties of the resulting network compared with aliphatic amine-cured network	High cost, can work at a service temperature <100 °C poor chemical resistance poor solvent resistance
Aromatic amine	High T_g, better chemical resistance and thermal properties of the resulting network compared with aliphatic- and cycloaliphatic amine-cured network	Mostly solid, difficult to mix, Curing requires elevated temperature
Anhydride	High network T_g compared with amine curing agent, very good chemical and heat resistance of the resulting network	High temperature curing, long post-curing, necessity of accelerator, sensitive to moisture
Dcy	Low volatility, improved adhesion, good flexibility and toughness	Difficult to mix, high temperature curing and long post-curing
Polysulfide	Flexibility of the resulting network, fast curing	Poor ageing and thermal properties, odor
Polyamides	Low volatility, low toxicity, room temperature-curing, good adhesion, long pot life, better flexibility and toughness of the resulting network compared with aliphatic amine-cured networks	Low T_g of the resulting network, high cost and high viscosity

Figure 3.19: Table of different hardener types with its respective advantages[188].

The type of monomer and hardener used is not the only factor that determines the nature of the composite. Its ratio is also known to play a substantial role, particularly in the hardness of the cured polymer. In order for one to accurately determine the optimum mixing ratio one would need to determine the epoxy equivalent weight and the amine equivalent weight for the epoxy resin and hardener respectively. By definition epoxy equivalent weight is the amount of resin that contains one mole of epoxy[188]. The amount of epoxy present in a sample is determined through titration using hydrogen bromide solution in acetic acid[195]. Epoxy and amine equivalent weight therefore is the mass of the said

mole.

The reaction below is a typical reaction between an epoxy and its curing agent[188] (Fig.3.20). During the curing process two (or more) epoxy group reacts with the hydrogen on the amine groups. The polymerisation process occurs in two stages, initially the epoxy group will react with the primary hydrogen on the amine group[188], the process is then followed by a reaction by the secondary hydrogen on the amine with another epoxide group[188]. The hydroxyl group (-OH) produced during this process will then follow a different set of reaction with the epoxy group producing an ether (esterification)[188]. The importance of this esterification process lies with the fact that the polymerised chain could then further react with another unit of monomer creating a even longer chain[188]. What is truly remarkable about this reaction however is the fact that the secondary alcohol produced during the reaction process also acts as a catalyst to the amine-epoxy reaction. This is a process known as auto-catalysis[188] that accelerates the polymerisation process.

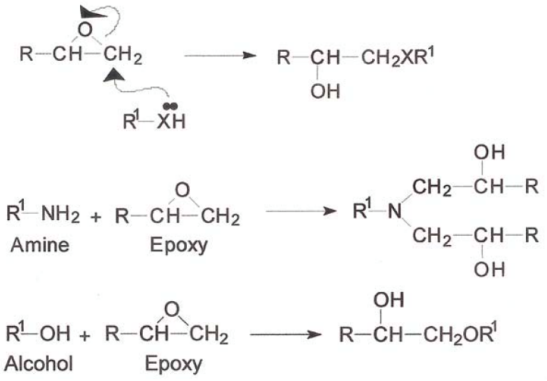

Figure 3.20: The reaction process undergone by an epoxy resin and hardener during polymerisation. (Top): Initial reaction where the hydrogen from the primary amine group reacts with the epoxy ring of the resin. (Middle): Reaction between the amine and epoxy resin creating a polymer chain with an –OH group on either side of the chain. (Bottom): Reaction between the –OH group and epoxy where the alcohol groups on either side of the chain reacts in order for it to grow in lengths enabling further polymerisation[188].

The curing process as seen from Fig.3.19 is highly dependant on the hardener used. Some of which even allows room temperature curing. It is however a prudent

idea to heat the epoxy moderately in order to ensure proper curing. Ratna *et al.* has found that by comparing the differential scanning calorimetry analysis (DSC) of epoxy cured at room temperature for 2 days and the same sample that was cured at 100°C for 2hrs. The sample cured for 2 days at room temperature has shown signs of residual uncured epoxy while the sample cured at 100°C for 2hrs did not[196] (Fig.3.21). For this reason all polymer composite samples used during this investigation were cured at 70°C overnight to ensure complete curing.

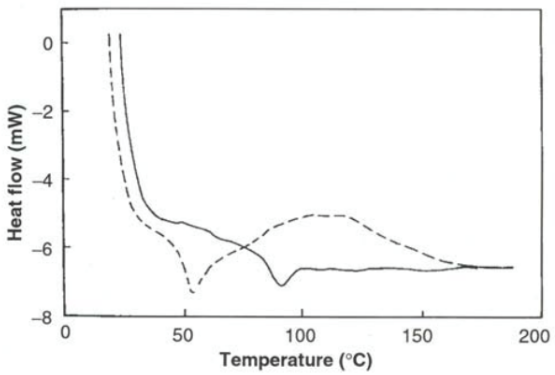

Figure 3.21: Differential scanning calorimetry analysis (DSC) of epoxy cured for 2 days at room temperature (dashed line) and sample cured for 2hrs at 100°C (solid line). The sample cured at room temperature showed signs of incomplete curing whilst the sample cured at 100°C showed no signs of uncured resin or hardeners[196].

It is however of utmost importance that one should not overheat the epoxy samples. Particularly if one was to use a low viscosity curing agent such as aliphatic amine which inherently cannot create a polymer network with a glass transition temperature (softening temperature, Tg) of >120°C[197]. In another words one would not be able to fabricate a heat resistant polymer using aliphatic amine. If on the other hand one was to use aromatic amines which are known to create a more heat resistant polymer one would also need to use higher curing temperature[198][199]. The stability of aromatic amine based epoxy is well entrusted by industry to the extent that it is often used as a host polymer for structural composites[188]. The dependence of carbon-epoxy composite and pure epoxy to heat has been explored as a preliminary part of this investigation. The

results has shown that both the electrical nature of carbon nanotube-epoxy and pure epoxy composite are indeed influenced by temperature and as seen from the Arrhenius plots below (Fig.3.22)(Fig.3.23). The presence of a gradient shows that the conductivity of the sample changes with temperature and more interestingly above certain temperatures the gradient drastically changed indicating a change in activation energy most likely due to a different conduction mechanism. The graphs below represents the Arrhenius plot of the resistance of pure epoxy and CNT-epoxy in air and vacuum (approx. 10^{-2}mBar)(Fig.3.22)(Fig.3.23).

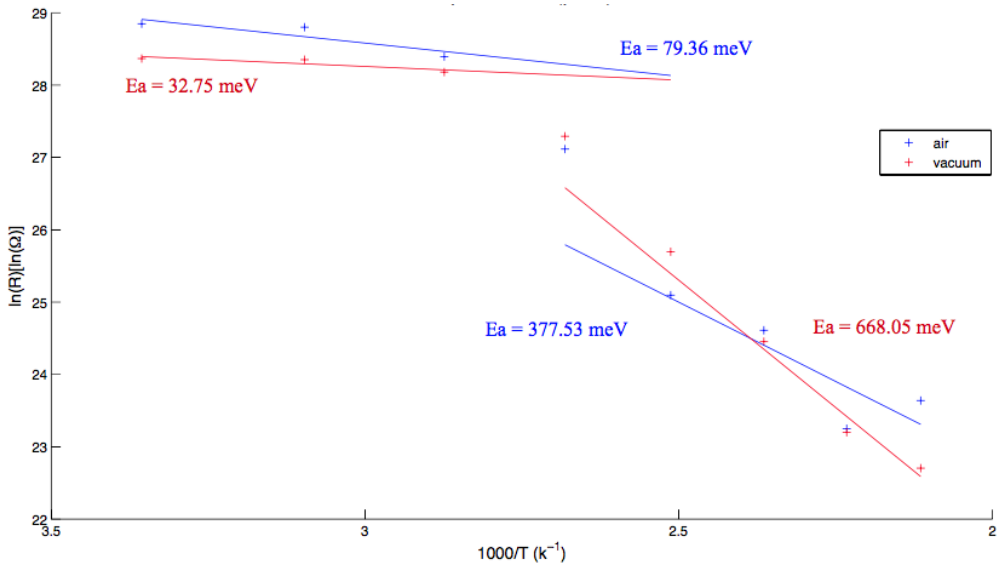

Figure 3.22: Arrhenius plot of electrical resistance of pure epoxy against temperature between 25°C to 200°C both in air and vacuum(approx. 10^{-2}mBar). As seen from the graph the presence of air (and thus atmospheric pressure) did not have a significant impact on the resistance. At greater temperatures it was found that its resistance for both in air and in vacuum drops substantially.

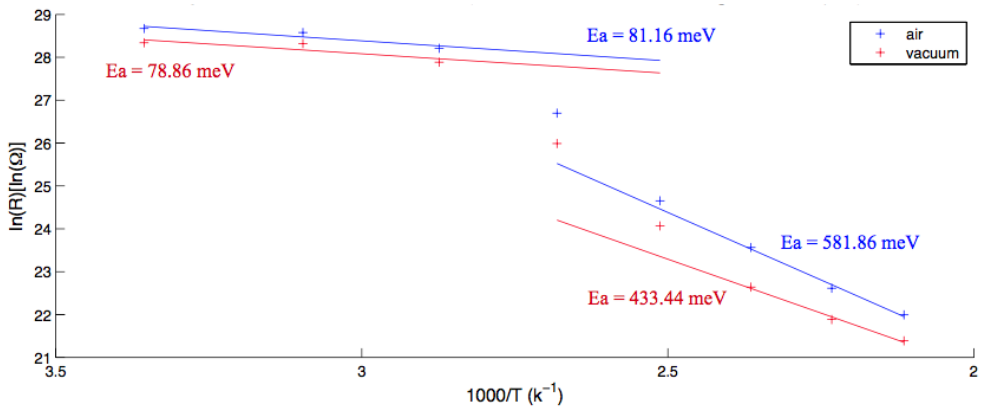

Figure 3.23: Arrhenius plot of electrical resistance of 1wt% CNT-epoxy against temperature between 25°C to 200°C both in air and vacuum(approx. 10^{-2}mBar). The CNTs were: MWCNT diameter: 30-50nm length: 10-20μm.

As mentioned earlier there is a plethora of epoxy resin and hardener that one could choose from. However throughout this investigation a single type of epoxy resin (Epilox T19-36/700, Leuna Harze) and hardener (Epilox H10-31, Leuna Harze) has been used. This resin was specifically chosen for its low viscosity that allows for easier and thorough mixing. A cycloaliphatic amine was chosen as the hardener for its ability to cure at low temperatures, its toughness and its stability (Fig.3.19). The viscosity of the hardener did not present any significant issue due to it being of a lower viscosity than the resin itself(Table.3.2):

	Epilox T 19-36/700		Epilox H 10-31
Viscosity at 25°C (mPa.s)	650-750	Viscosity at 25°C (mPa.s)	400-600
Epoxy equivalent weight (g)	190-210	Amine equivalent weight (g)	112
Density at 20°C	a 1.14	Density at 20°C	1.00± 0.02

Table 3.2: Specification of epoxy resin (Epilox T19-36/700) and its hardener (Epilox H10-31) as published by its manufacturer Leuna Harze[200][201].

3.2.2 Polydimethylsiloxane (PDMS)

Polydimethylsiloxane (PDMS), commonly known as silicone is an organo-silicone that is widely utilised for its biocompatible nature. Most commonly as food additives[202] and breast implants for post surgery reconstruction and augmenta-

tion purposes[203]. Its established track record has been recognised by the World Health Organisation (WHO) and the Food and Drug Administration (FDA, US) both of who have authorised its use. Being a thermoset polymer PDMS consists of two parts: monomers[204] (Fig.3.24.1) and cross-linkers (hardeners)[204] (Fig.3.24.2) that are then polymerised by a platinum based catalyst[204] (Fig.3.24.3):

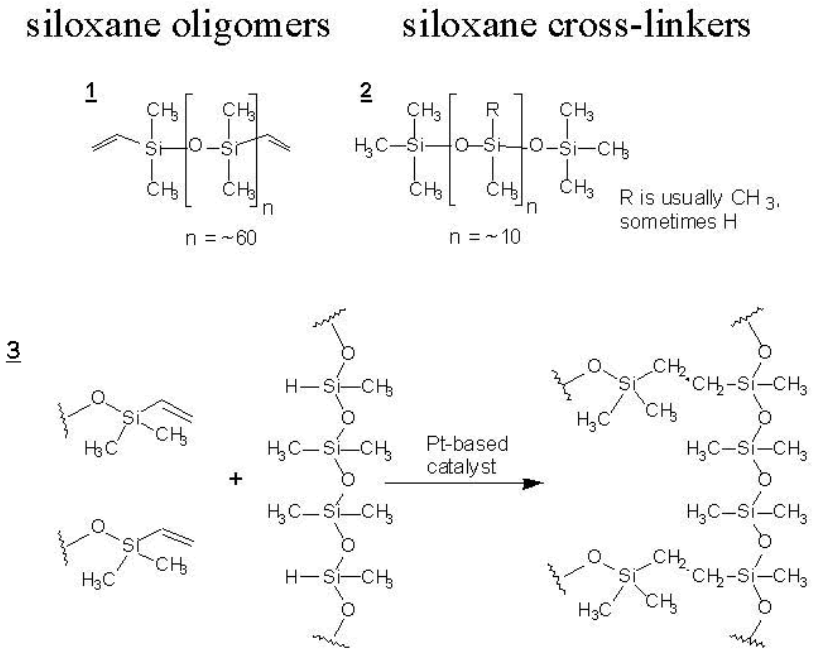

Figure 3.24: 1) PDMS oligomer (few monomer chain), PDMS cross-linker (hardener), 3) polymerisation reaction of PDMS using a platinum based catalyst[204].

A lesser known yet equally important feature however is its flexibility. PDMS is extremely flexible due to its low glass transition temperature[205] of -125°C[206]. This property plays a crucial role in making a composite piezoelectric and this property will hold significance in Chapter 6: CNT-PDMS.

PDMS does have its own set of disadvantages however, its resin (monomer) is rather viscous in comparison to that of epoxy resin (5100mPa s[207] and 650-750mPa s[200] respectively). It is generally accepted that if a polymer is of high viscosity it will be difficult to homogenously distribute the carbon filler due to the lack of turbulence and reduced filler mobility resulting in a poorly distributed conductive network. Naturally, this does imply that polymer hosts of high viscos-

ity require more carbon fillers to be added in order to achieve conduction than its low viscosity counterpart[187].

Throughout this investigation (Chapter 6: CNT-PDMS) the PDMS used were that of Sylgard 184 silicone elastomer, manufactured by Dow Corning mixed at the recommended ratio of 10:1 resin to hardener respectively.

Property	Unit	Result
One or Two Part		Two
Color		Colorless
Viscosity (Base)	cP	5100
	Pa-sec	5.1
Viscosity (Mixed)	cP	3500
	Pa-sec	3.5
Thermal Conductivity	btu/hr ft °F	0.15
	W/m °K	0.27
Specific Gravity (Cured)		1.03
Working Time at 25°C (Pot Life - hours)	hours	1.5
Cure Time at 25°C	hours	48
Heat Cure Time at 100°C	minutes	35
Heat Cure Time at 125°C	minutes	20
Heat Cure Time at 150°C	minutes	10
Durometer Shore		43
Dielectric Strength	volts/mil	500
	kV/mm	19

Property	Unit	Result
Volume Resistivity	ohm*cm	2.9E+14
Dissipation Factor at 100 Hz		0.00257
Dissipation Factor at 100kHz		0.00133
Dielectric Constant at 100 Hz		2.72
Dielectric Constant at 100 kHz		2.68
Linear CTE (by DMA)	ppm/°C	340
Tensile Strength	PSI	980
	MPa	6.7
	Kg/cm^2	69
Refractive Index	@ 589 nm	1.4118
Refractive Index	@ 632.8 nm	1.4225
Refractive Index	@1321 nm	1.4028
Refractive Index	@ 1554 nm	1.3997
UL RTI Rating	°C	150

Figure 3.25: Manufacturer's specification of Sylgard 184 Silicone elastomer[207].

Biocompatibility of PDMS As mentioned earlier PDMS is known for its high biocompatibility. However it is not biocompatible universally under all circumstances, the question one should be asking is where and how is it biocompatible: its where is the blood vessels and its how is its muted reaction to blood and soft tissues. In the interest of this investigation where attempts at the fabrication of an *in vivo* blood pressure sensor was made, one should focus on the hemo-compatibility and inflammatory response of PDMS to blood and soft tissues respectively. Fortunately since much of the human body is comprised of blood, numerous studies has been carried out by Keough *et al.* and McCoy *et al.*, typically through Scan-

ning Electron Microscopy (SEM) to visually identify inflammations and blood coagulations by monitoring the accumulation of platelets, a component of blood that stops bleeding[208]. What truly is interesting is that due to the complexity of the human/swine/canine anatomies of which PDMS was tested on, various studies have slightly different findings in the hemo-compatibility of PDMS[209]. For example Keough *et al.* who tested the platelet accumulation on PDMS under high blood flow rate (200cc/min) has found that PDMS collected moderate amount of platelets (as much as other similarly biocompatible polymers such as low density polyethylene (LDPE))[208], while at low blood flow rates (20cc/min) it was found that PDMS collected more platelets thus implying that PDMS is less hemo-compatible in a low blood flow rate environment[208]. The findings suggests that within acceptable limits PDMS performance improves with higher blood flow. Logically the next question would then be how does this compare to an average rate of blood flow. One benchmark study that the flow rate could be based on is that of Green *et al.* who has examined the blood flow rate of a brachial artery (main artery in a human arm) of six healthy 29±2year old males with systolic and diastolic blood pressures of 125±9mmHg and 83±7mmHg, respectively[210] (a typical healthy male blood pressure of that age group). Green *et al.* found that at rest the brachial blood flow rate is approximately 500cc/min, comfortably surpassing the blood flow rate of 200cc/min where Keough *et al.* found improvement in the hemo-compatibility of PDMS. Other studies such as that of by McCoy *et al.*, has looked into the effect of prolonged exposure of blood to PDMS. Where McCoy *et al.* has found that upon acute exposure (60min), PDMS had a significant amount of platelet accumulation[211]. However after chronic exposure (24hrs) it was found that platelet accumulation decreased over time to the extent that it collected less platelets than other leading biocompatible polymers such as Silastic^{TM}[211]. Suggesting benefits of using PDMS as a long-term installation *in vivo* as a blood pressure sensor. In essence, studies by Keough *et al.* and McCoy *et al.* has both indicated that if one was to make an *in vivo* blood pressure sensor with blood flow rates above 200cc/min and exposure of 24hrs and greater,

which investigation in Chapter 6: CNT-PDMS aims to carry out. It has sufficient grounds to suggest that PDMS will be a suitable candidate for its use as a host polymer.

Another key component of bio-compatibility, inflammation has also been reviewed. Being an *in vivo* device the polymer would naturally have to be accepted by the soft tissues that it is in direct contact with. Studies by Huang *et al.* and Akoum *et al.* who has inserted PDMS into laboratory test rats has found that there were signs of mild inflammatory reaction for the first 2 weeks[212][213] followed by a more discreet inflammation of 6-12 weeks post implantation[212][213]. Some such as Ertel *et al.*, has suggested that the inflammation is a direct response to the physical property of PDMS from having a foreign body in the blood vessel as PDMS has no known toxic components or byproducts[214]. In any case, considering its benign nature to soft tissues PDMS could be considered to be a sound choice as a bio-compatible host polymer.

It is also worth noting that although the choice of animals to be tested on was rats in the studies by Huang *et al.* and Akoum *et al.*, some studies such as that by Goodman *et al.* have shown that swine may be a better candidate for animal testing for this particular application[215].

Mechanical Properties of PDMS As mentioned earlier PDMS is an extremely pliable material with a high flexibility and compressibility[205]. This nature is largely attributed to its very low glass transition (softening) temperature of -125°C[206] that brings rise to a shear modulus (modulus of rigidity) of as little as 100kPa-3MPa[206] depending on the hardener type. Another important physical property is Young's modulus, the measure of elasticity. A study by Armani *et al.* has reported various Young's modulus values for different mixing ratio of PDMS resin and hardener. As mentioned earlier throughout this investigation a mixing ratio of 10:1 for resin and hardener was used. Based on the mixing ratio and the findings by Armani *et al.* the density of PDMS used in this investigation is estimated to be 9.20×10^2kg/m^3[216] with a Young's modulus of

7.50×10^5Pa[216]. However it is important to note that its mixing and curing conditions do play a role in its final properties and the results are not to be taken as a definite value. It does however give a very sound estimate of the PDMS produced using the said ratio. Although the full description will be reserved for Chapter 6: CNT-PDMS the *in vivo* blood pressure sensor fabricated during this investigation relies on its piezoresistive nature which in turn is dependent on the flexibility and compressibility of PDMS. The question is would PDMS meet the flexibility and compressibility requirement at the temperature required, thus at the human core body temperature of 37°C. Studies by van Krevelen *et al.* does seem to suggest that PDMS maintains its physical property from -100°C to +100°C[217] comfortably accommodating body temperature in its operable range, allowing PDMS to maintain its compressibility and flexibility required for its application as a host material for a blood pressure sensor.

3.2.3 Percolation Theory

The principles of percolation theory are key to the understanding of the conductive nature of composites. In essence percolation represents the conductive state of a carbon-polymer composite when it has enough conductive carbon present that it is no longer an insulator but not enough for it to be a conductor. It is therefore a transitional state between insulation and conduction. At low conductive filler concentrations the composite is an insulator as there is no means for the electrons to flow through. At high conductive filler concentrations, conduction could occur through the conductive network formed by the conductive fillers. At its transitional stage however there is a drastic change in conductivity. Typically when the majority of the carbon nanotubes are on the verge of coming fully into contact with each other, at this state its conductive nature is extremely precarious where a small amount of constraint could influence the conductivity into either becoming an insulator or a conductor. Chapter 6:CNT-PDMS exploits this nature by compressing the composite at percolation threshold under blood pressure in order to narrow the gaps between the carbon nanotubes in a composite to increase its

conductivity. The figure below illustrates the state of insulation, percolation and conduction graphically with their respective state of carbon nanotube distribution (Fig.3.26):

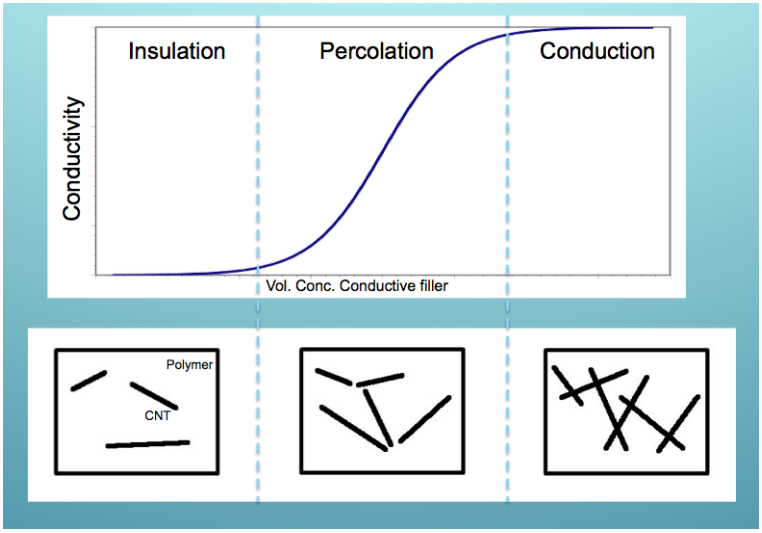

Figure 3.26: The relationship between conductivity of a composite against the concentration of the conductive filler with its graphical representation of the composite. At lower filler concentrations, conductivity is low due to the fact that the carbon nanotubes (CNTs) are spaced too far apart preventing conduction. At higher carbon nanotube concentrations on the other hand the carbon fillers are heavily inter-connected allowing conduction to occur through contact. Percolation on the other hand is a state where some of the carbon nanotubes are in contact with each other but many are on the verge of coming into contact. At this stage conduction could occur through both contact and quantum tunnelling if the carbon nanotubes are close enough.

Heilmann and others algebraically represented the above by defining the states of insulation, percolation and conduction using the filling factor[218]:

$$f = \frac{\frac{m}{v} - \rho_{\text{ins}}}{\rho_{\text{me}} - _{\text{ins}}} \tag{3.12}$$

where:

f is Filling factor

m is Total mass

v is Total volume

$\rho_{\mathbf{ins}}$ is Density of insulating host

$\rho_{\mathbf{me}}$ is Density of conductive filler

The states of insulation, percolation and conduction relative to the percolation threshold (f_c) is defined as[218]:

$f \leq f_{\mathbf{c}}$ insulation

$f \approx f_{\mathbf{c}}$ percolation

$f \geq f_{\mathbf{c}}$ conduction

It is very important to mention that the equation above (Eq.3.12) quickly becomes much more complex once one takes into account the various complications of the composites. Some examples of this are: particle distribution, particle size, particle shape and particle orientation[218] (Fig.3.27):

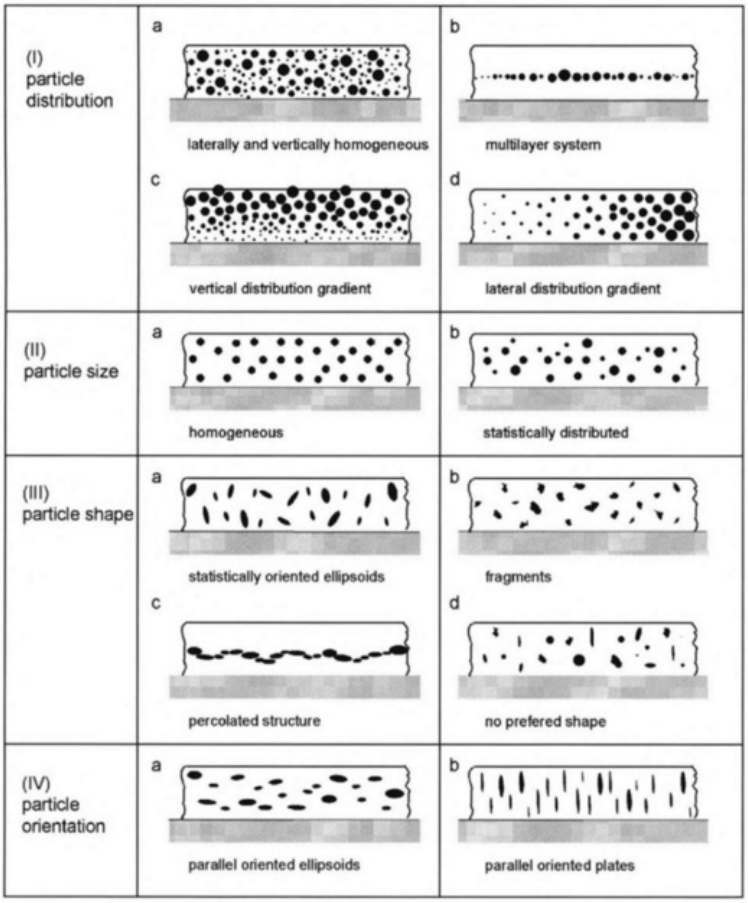

Figure 3.27: Various possible distribution errors in a carbon-polymer composite[218].

Theoretical Approach to Percolation Theory

As with most scientific fields, many have attempted to use simulations to compute the conduction mechanisms in a carbon-polymer composite. A particularly interesting study by Hu *et al.* represented carbon nanotubes as low resistance resistors[219] and the tunnelable inter carbon nanotube gaps as another resistor defined as:

$$R_{\text{tunnel}} = \frac{V}{AJ} = \frac{h^2 d}{Ae^2\sqrt{2m\lambda}} exp(\frac{4\pi d}{h}\sqrt{2m\lambda}) \tag{3.13}$$

where:

V is Electrical potential difference

A is Cross-sectional area of tunneling (cross sectional area of carbon nanotube used as estimate)

J is Tunnelling current density

h is Plank's constant

d is Distance between CNTs

e is Charge of electron

m is Mass of electron

λ is Height of barrier (for epoxy typically 0.5-0.25eV[219])

Although Hu *et al.* has found the theoretical values to have a strong correlation with the experimental data[219], the above simulation has not addressed two important components of tunnelling: temperature and electron scattering/reflection. As mentioned earlier since percolation is a state where the carbon fillers are about to come into contact but not enough to form a full contact conduction[218], if one was to have a sample at percolation naturally many of the carbon nanotubes will have a sliver of polymer separating them introducing scattering and reflection

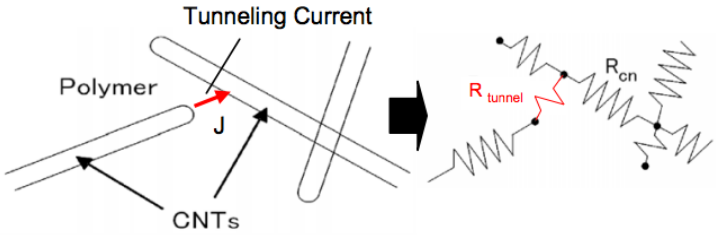

Figure 3.28: Diagram of the equivalent circuit model used by Hu *et al.*, where R_{tunnel} represents the estimated resistance of the tunnelling gap and R_{cn} is the resistance of the carbon nanotube[219].

from the grain boundaries. Temperature on the other hand plays a crucial role in tunnelling, by influencing the probability of successful tunnelling that depen-dends on the electron's energy[220]. Also, higher temperatures will bring rise to a greater number of charge carriers[218] in accordance with the Boltzmann's distribution (Eq.3.14):

$$n = Nexp\frac{-\delta E}{k_{\mathrm{B}}T} \tag{3.14}$$

where:

n is Number of charge carriers

N is Charge carrier density

δE is Activation energy

k_B is Boltzmann's constant

T is Temperature

The number of charge carriers increase with temperature which in turn leads to an increase in the conductivity of the composite[218].

This has indeed been verified earlier in the chapter during the preliminary investigation where the Arrhenius plot of a carbon-epoxy composite has shown signs of having different activation energies at high and low temperatures (Fig.3.22).

An interesting study by the likes of Neugebauer and Webb has modelled the activation energies having the physical parameters (such as radius of filler, spacing between the fillers and dielectric constant of host) as its variables[221].

$$\delta E = \frac{e^2}{4\pi\epsilon_{\text{ins}}}(\frac{1}{R} - \frac{1}{2R+B}) \tag{3.15}$$

where:

δE is Activation energy

e is Charge of electron

ϵ_{ins} is Dielectric constant of host

R is Radius of filler

B is Spacing between two neighbouring fillers

[221]

Fortunately for the purpose of this investigation the influence of temperature is limited as Chapter 5:CNT-Epoxy was carried out at room temperature and Chapter 6:CNT-PDMS was designed to operate at a moderate and most importantly at a constant body temperature of 37°C. In both cases one could expect little fluctuation in the sample's activation energy and in turn its resistance.

3.2.4 Clustering

Throughout this investigation when choosing the polymer resin and hardener its ability to form a homogeneous filler distribution caused by their low viscosity was prioritised above all other benefits such as heat and chemical resistance as well as its curing speed. The low viscosity allows the carbon fillers to be disseminated evenly throughout the composite allowing the maximum spread of the conductive network. The often-overlooked benefit of even distribution is that during the process of achieving it, more often that not it eliminates the issues presented by the

filler particulate sizes and shapes. As seen from Fig.3.27 having an uneven filler size and shape could affect the conductivity of the composite. For instance carbon nanotube naturally prefers to be in a cluster[222] due to the van der Waal's force acting on each other[223]. Therefore unless they are being forced to do otherwise, they would naturally agglomerate into a spherical globule. As discussed earlier in the chapter (Fig.3.17) spherical fillers tends to require more filler present in a composite in order to achieve conduction. Therefore if one was to aim for a low percolation threshold (which in most cases are preferred) it is preferable to separate the carbon nanotubes into individual strands from their parent cluster. Studies by Bauhofer *et al.* have shown that many have tried to achieve this through sonication[224], extrusion[225], ball milling[226], stirring[227] and high shear mixing[228]. Of the many listed however high shear mixing was proven to be the best method of mixing and it was extensively used to fabricate the samples in Chapter 5: CNT-Epoxy. High shear mixing operates by agitating clusters of carbon nanotubes against each other in order to fragment them down into individual carbon nanotubes(Fig.3.29). The process of doing so will also distribute the carbon nanotubes evenly across the composite. A review study by Bauhofer *et al.* however has shown an overwhelming popularity for sonication[187] to both de-agglomerate the clusters and distribute the carbon fillers. However sonication has been reported to break the carbon nanotubes at higher powers[229][230], while high shear mixer is known to preserve the lengths of the carbon nanotubes[231]. The fact that high shear mixing preserves the lengths of carbon nanotubes has allowed the carbon nanotubes to have greater reach to form a conductive network and is believed it holds the current record for the lowest percolation threshold achieved at the time of writing (0.0025wt%)[231]. Therefore considering the extensive benefits bought about by high shear mixing, unless specifically mentioned high shear mixing would be used to fabricate composites in this investigation.

Post separation of carbon nanotubes from its parent cluster was performed in order to maintain its benefits one must aim to preserve its distribution. To do so one must look into the nature of the interaction between the carbon nanotubes

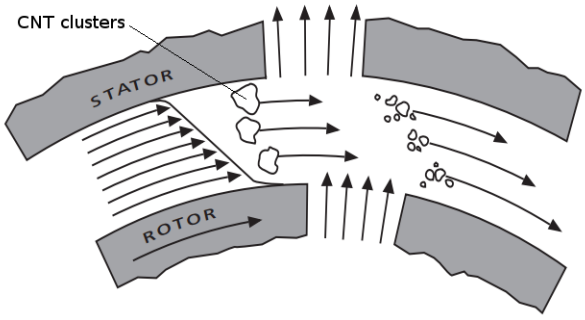

Figure 3.29: Principles of high shear mixing. The CNT clusters are agitated amongs each other within the cavity between the stator and rotor resulting in the break down of clusters into individual CNTs. The clusters are injected from within the rotor exploiting the vacuum created by the high speed rotation of the rotor[232].

and its host polymer. The likes of McCarthy *et al.* has demonstrated that polymer strands typically 'wrap' around carbon nanotubes in a composite[233]. Moreover McCarthy *et al.* has also found dendritic polymer growth nucleating around the defective sites on a carbon nanotube[233], implying not only a single chain but also a whole network of polymer strands form around the proximity of a carbon nanotube. This was later verified by the scanning electron microscopy image taken by Ding *et al.*. They have severed a polymer coated carbon nanotube strand using an atomic force microscope tip[234] (Fig.3.30a). Upon closer inspection they have found clear signs of a thick (10s of nm[234]) layer of polymer sheath encapsulating the carbon nanotube[234] (Fig.3.30b)(Fig.3.30c).

The key principle one should take note here is the effect of polymer wrapping on the mass and volume of the carbon nanotube/polymer bundle. If the carbon nanotubes were to be tethered and ensnared by polymer strands in its proximity, the overall mass and volume of the carbon nanotube-polymer unit will increase. This will in turn give more substance for the high shear mixer (or any other form of carbon nanotube distribution) to mechanically 'grip onto' in the mixing process. The fact that carbon nanotubes are a now a part of a bigger and heavier system deprives carbon nanotubes of their mobility, thus their ability to reintegrate into a cluster, resulting in an improved carbon nanotube distribution.

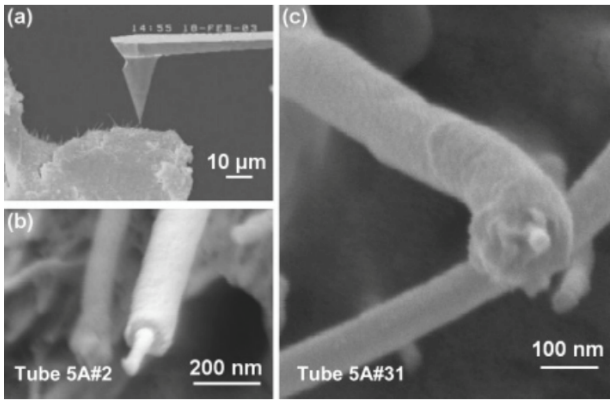

Figure 3.30: a) Atomic force microscope tip severing the polymer coated carbon nanotube in order to expose its cross-section. b), c) Two separate carbon nanotube cross-section with thick layers of polymer sheaths, supporting the theory that polymer chains has a tendency to wrap around carbon nanotubes[234].

3.2.5 Mechanical Properties of Composite

As mentioned earlier the addition of carbon nanotubes have a significant effect on the mechanical strengths of the composite. Although its effect is not of direct concern to this investigation. It does have some relevance to Chapter 6: CNT-PDMS where the composite is mechanically compressed under pressure. Fortunately in terms of actual impact on the investigation it adds very little complication to the experiment as the measurement is taken based on the pressure loaded onto the sample. This holds true regardless of the hardness of the composite. Principally it is important to note that any addition of carbon nanotube will dramatically increase the strengths of the composite. Where Qian *et al.* found that the addition of 1wt% of carbon nanotube into polystyrene has bought about an increase in tensile modulus and break stress by 36-42% and 25% respectively[235]. However this will inevitably lead to the reduction of impact toughness[236][237] thus making it more brittle.

3.2.6 Influence of Functional Groups on Composites

The influence of functional groups on carbon nanotube has long been associated with the mechanical strengths of the composite. For most part this attributes to the fact that with some functionalisations the compatibility between the host poly-

mer and the carbon nanotube could be improved through functionalisation[185] resulting in a greater carbon nanotube distribution, that in turn improves the reinforcement effect. The table below summarises the degree of reinforcement achieved by functionalised and non-functionalised carbon nanotube composite collated by Coleman *et al.*[185] (Fig.3.31):

Nanotube type	Matrix	Y_{Poly} (GPa)	Y_{Max} (GPa)	NT content	dY/dV_f (GPa)
In situ polymerisation					
SWNT	PI	1.0	1.6	1 vol.%	~60
SWNT	PBO	138	167	10 wt.%	~550
Arc-MWNT	PMMA	1.5	2.5	1 wt.%	~150
SWNT	PMMA	0.3	0.38	0.01 wt.%	~960
Functionalisation					
CVD-MWNT/octadecylamine	P(MMA-co-EMA)	1.64	2.62	10 wt.%	~15
CVD-MWNT/Cl-PP	Cl-PP	0.22	0.68	0.6 vol.%	72
SWNT/large organic groups	Epoxy	2.02	3.4	4 wt.%	~95
Arc-MWNT/PMMA	PMMA	2.9	29	20 wt.%	~115
SWNT/PA6	PA6	0.44	1.2	1.5 wt.%	~120
SWNT/OH	PVA	2.4	4.3	0.8 wt.%	305
CVD-MWNT/ferririn protein	PVA	3.4	7.2	1.5 wt.%	~380

Figure 3.31: Table of carbon nanotube (both functionalised and non-functionalised) and polymer composite with its respective Young's modulus for the host polymer (Y_{poly}), the maximum Young's modulus achieved from the composite (Y_{Max}), Nanotube (NT) content and the composite reinforcement factor (dY/dV_f, where V_f stands for the fibre volume fraction of a composite)[185].

What truly is astonishing is the influence of functionalisation of carbon nanotubes to the electrical conductivity of the composite. The findings in Chapter 5: CNT-Epoxy has shown that certain functional groups will significantly improve the conductivity of a composite per percentage loading. It was later concluded that this was due to the improvement in the distribution of carbon nanotubes in the exact same manner as how the improvements in mechanical reinforcement was bought about. The improvement in the distribution that caused structural reinforcement has also resulted in the even distribution of conductive fillers thus an establishment of a wider and better spread conductive network, leading to improvement in the conductivity of the composite.

3.2.7 Toxicity of Carbon Nanotube-Polymer Composite

Ever since the discovery of carbon nanotube in 1991 by Iijima *et al.*[3] its toxicity has been intensely debated. This is due to the fact that carbon nanotube was discovered just after the 'asbestosis shock' where it has become apparent

that asbestos, the thermal insulation used to keep the buildings warm happens to be carcinogenic[238], resulting in the vast majority of buildings with asbestos installed to be a health hazard. The relevance of this historical occurrence lies in the fact that carbon nanotubes are structurally near identical to that of asbestos[239]. Thus it was widely speculated that carbon nanotube may display a similar toxic nature to that of asbestos[240]. Being a carcinogen it has the potential to damage the human genome (DNA) leading to a plethora of symptoms. Li *et al.* and Patlolla *et al.* observed notable damages such as an elongation to mitochondrial DNA[241] and DNA tails[242] respectively. Others such as Shevedova *et al.* claimed to have found a more general damage through an increase in the DNA mutation frequency[243]. A review by S. Toyokuni who collated the toxicological findings of various studies found that 45 of the publications cited reported positive to the carcinogenicity of carbon nanotubes whilst 16 reported back with negative results.

Naturally one may translate this known toxicity of carbon nanotube to the toxicity of the composite itself. To the surprise of many however carbon nanotube composites have been proven to be very biocompatible due to carbon nanotube immobilisation. Studies by Deka *et al.* and Sitharaman *et al.* who used carbon nanotube composites encased in biocompatible hosts: carbon nanotube-polyurethane[244] and carbon nanotube-polypropylene fumerate[245] respectively have found them to exhibit excellent biocompatibility. What is truly notable is that the study by Sitharaman *et al.* has gone even further by claiming that they have observed biocompatibility of carbon nanotube composites in a biodegradable polymer, polypropylene fumerate[245] where carbon nanotubes are expected to be exposed to soft tissues following the decomposition of the host polymer. However, verification study to this claim is yet to be carried out. This may have been caused by one of two reasons: the carbon nanotubes in the composite was few enough for its carcinogenic tissue response to be negligible, or alternatively the polymer chain which as discussed earlier is known to engulf the carbon nanotube has changed the surface interaction chemistry with the tissue, resulting in its muted carcino-

genicity. Although strong caution is advised the evidence suggests the likelihood of biocompatibility from carbon nanotube-polymer composites, such as PDMS.

3.3 Current State of Blood Pressure Sensors

A blood pressure sensor is an umbrella term for any form of pressure sensor in a hemo-active region of a body. There are various different types of blood pressure sensors specialised to measure blood pressure from a specific part of the body. Overall however it is simply a matter of scale, the fundamental principles of measuring the hydraulic pressure of blood remains universal. Of the many measuring systems available the two in particular that are of interest to this investigation are the systems that measure the blood pressure in the brachial and the pulmonary artery. Notably the former has been widely used in identifying the general blood pressure of the body whilst the latter has its use in heart failure detection.

3.3.1 Heart Failure

The definition of heart failure according to the National Health Service (UK) is: a condition caused by the heart failing to pump enough blood around the body at the right pressure[246]. Heart failure is then categorised into three different types: heart failure caused by left ventricular systolic dysfunction (LVSD)[246], where blood has failed to circulate as a result of a weakened left ventricle; heart failure with preserved ejection fraction (HFPEF)[246], typically caused by the stiffening of the left ventricle resulting in a poor filling ratio of the heart chamber; and heart failure caused by diseased or damaged heart valves[246]. In all of the above cases however it has a common symptom that one could exploit to detect heart failure, the change in blood pressure. Pulmonary blood pressure of a heart failure patient is known to decrease (hypotension)[247] as well as increase (hypertension)[248]. Therefore by using an *in vivo* blood pressure sensor to continuously monitor the blood pressure one could directly detect a heart failure immediately.

Heart failure despite its public awareness still remains rife globally and is considered by many leading figures to be a global pandemic[249]. Approximately 26 million adults worldwide lives with heart failure[250], a number comparable to 32 million people living with cancer[251] and 34 million people living with HIV/AIDS[252]. Some studies has shown that up to one in five individuals are expected to develop heart failure at some point in their life even amongst economically developed countries[253]. Alarmingly, despite its global prevalence 17-45% of patients admitted to hospital with heart failure will die within a year of admission and the majority will follow within 5 years of admission[253]. It is however also true that modern advancement in medicine has improved its survival rates[253]. Unfortunately despite the said improvements approximately 2-17% of individuals who has been admitted to hospitals will pass away while being hospitalised[253]. Statistically speaking, studies by Brenner *et al.*, Coleman *et al.* and Siegel *et al.* has shown that the survival rates of heart failure are shockingly poorer than that of bowel[254], breast[255] or prostate[256] cancer. As with many diseases, the general demographic of those who suffer from heart failures are those who are 65 years and older. Supportive studies have shown that in fact very few below 50 years of age suffer from heart failure, whilst more than 80% of heart failures are suffered by those who are 65 years and older[253]. In economically developed countries approximately 1-4% of all hospitals admission are thought to be caused by heart failures[253]. However this figure has to be considered with caution as many cases of heart failures go unnoticed even by specialists[253] particularly if the patient also suffers from other cardiovascular diseases[253]. A large factor that plays a part in the lack of detection comes from the fact that the typical symptoms of heart failure are similar to those of less life threatening conditions such as breathlessness[253], swollen limbs[253] and fatigue[253]. The prevalence of heart failure amounts to a substantial tally of healthcare expenditure through the need of advanced healthcare and repeated hospitalisation of patients that puts formidable pressure onto national healthcare. Typically 1-3% of total healthcare costs in North America[257], Western Europe[258] and Latin America[259] are

believed to be used to treat heart failures. The estimated annual expenditure for hospital, physician, prescription and home healthcare costs associated with heart failure were 20.9 billion US dollars in 2013 with a projected rise to 53.1 billion US dollars by 2030[260]. Much of the cost comes from the readmission to a hospital typically within a month to two-thirds of a year of the heart failure[253]. It is known that a delay in hospital treatment by as little as 4-6 hours after the initial symptom of heart failure will result in a notable increase in the mortality rate[253]. The key is in early, or ideally immediate diagnosis. If one was to devise a method of detecting heart failure as soon as it happens one could in-turn save countless numbers of lives and alleviate the national cost of healthcare. Chapter 6: CNT-PDMS aims to achieve this through fabrication of an *in vivo* blood pressure sensor with wireless feedback mechanism that will allow immediate recognition of heart failure as well as automatic notification designed to muster any nearby medical staff for medical attention in a matter of minutes if not seconds.

One of the main challenges of diagnosing heart failure as mentioned earlier is the fact that its symptoms could often be masked by a more trivial set of symptoms[253], which leads to even trained professionals having difficulty in the diagnosis of heart failure. It is therefore considered ideal to employ a range of techniques to diagnose heart failure if they are at one's disposal. Unfortunately not all hospitals holds the capability of a full diagnostic scan around the world particularly in resource poor settings[261] such as in Africa. In a more fortunate environment, however, various technologies are available. Some of the techniques used for heart failure diagnosis includes: Magnetic Resonance Imagery (MRI)[250], Doppler echocardiograph[262] and cardiac catheterisation[263]. Notably both MRI (based on electro magnetic wave, magnetic field) and Doppler echocardiograph (ultrasound sonogram of heart) are non-invasive diagnostic techniques. As one could imagine much of the current trend is moving towards non-invasive methods for the comfort of the patients. Both methods however suffer from one major shortfall; the monitoring cannot be performed passively. Both methods require at least one operator as well as expensive equipments where con-

stant monitoring of the heart is practically not feasible. Therefore the attention of this investigation was turned to catheterisation. This technique has as extremely unusual origin in that it was invented by an erratic Nobel Prize winning Nazi physician, Werner Forssmann[264] who won the Nobel Prize in medicine for his work in cardiac catheterisation. During his investigation he has inserted a cannula (a tube designed to be inserted into a body) through his own antecubital vein[264] followed by an x-ray imagery to discover his successful catheterisation to his heart. Naturally this method is very invasive, to say the least, considering that it has to physically have a tube passed down a major blood vessel[265] (Fig.3.22):

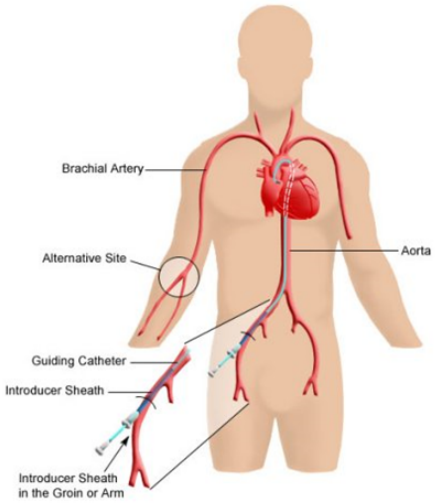

Figure 3.32: A typical cardiac catheterisation for cardiac blood pressure measurement through a major artery in the thigh with an alternative option of insertion through the arm[265].

However recent developments has adapted the technique to measure the pulmonary artery blood pressure which has a sounder ground for safety[266] by avoiding the heart in order to eliminate potential complications. This method has remained to be the gold standard of heart failure detection for many years[263]. Chapter 6: CNT-PDMS aims to improve upon this by adding a greater degree of device sensitivity and wireless technology to reduce invasiveness, namely by using a highly piezo-resistive carbon nanotube-PDMS composite with a simple radio-frequency tag and embedding the device into a pulmonary artery.

In preparation of the device fabrication, the ideal size of the device was inves-

tigated. To benchmark the range of sizes required the maximum and minimum diameter of the pulmonary artery was determined. Investigations carried out by Edwards *et al.* and Weibel *et al.* have shown the main pulmonary artery diameter to be 3.32cm[267] and the mean pulmonary capillary to be 8.3μm[268] respectively. Therefore in order to detect the blood pressure change in the pulmonary artery the diameter of the device should be in between 3.32cm and 8.3μm. These values however should only to be used as a rough guide as this quoted size includes the arterial walls and its shape is not a necessarily a perfect circle, under certain circumstances the cross-section of an artery could be an ellipsoid[269]. There are other factors such as individual variation, gender, age etc. Additionally it is very important to note that there is a trade off in the size of the device. The device fabricated in Chapter 6: CNT-PDMS is designed to be embedded into the artery by physical restriction from the tapering of the blood vessels. Thus the placement of how far down the blood stream the device is embedded in depends entirely on the size of the device. If the device was to be too large, thus be embedded closer to the main artery, this will result in oxygen deprivation to an intolerable number of cells. Thus the device should ideally be as small as possible. However if one was to have a device too small there will be an insufficient amount of composite for the blood to compress in order for the device to register a sufficient amount of resistance change. Therefore the device is required to be sufficiently large enough for it to function. To address the issue one will have to determine the optimum device size. Therefore the minimum threshold of pulmonary embolism, a condition defined by the National Health Service (NHS, UK) as: a blockage in the pulmonary artery[270] was identified. A study by Johnson *et al.* who has investigated the effects of 200μm and 500μm glass beads in a pulmonary artery[271] has shed some light on the matter. Johnson *et al.* have found that with the smaller beads (200μm) the lymph-to-plasma protein concentration ratio (L/P) that was used as a reference to mark the amount of blood depravation caused to be unaltered from an unobstructed blood vessel[271], whilst the 500μm beads L/P has shown a sign of a decrease thus indicating blood depravation[271].

Johnson *et al.* has concluded that this was due to the fact that 200μm the beads that were embedded were sufficiently further down the capillary tree that there were enough parallel pulmonary artery branches that could effectively 'cover' the blood deficiency from another nearby branch[271]. However, the 500μm beads were found to be too large, depriving a whole host of cells of blood resulting in pulmonary embolism. Considering the above results it is clear that 200μm is very close to the maximum size that the device could be made safely. As well as the fact that 200μm falls comfortably in the 3.32cm to 8.3μm size range mentioned earlier. Therefore it was considered prudent to fabricate the heart failure sensor used in Chapter 6:CNT-PDMS at 200μm.

3.3.2 Brachial Blood Pressure

When measuring the systemic arterial pressure, the net output pressure from the heart (cardiac output pressure minus the peripheral vascular resistance)[272], is widely accepted to represent the overall blood pressure of the body. Medical practitioners however most commonly uses the brachial blood pressure as a close indirect substitute[272] due to its significant ease of measurement. Its effectiveness has been proven time and again not only in resource privileged environments but also in poorer settings[273] giving access to the necessary medical care required around the globe. When measuring the brachial blood pressure both the systolic (blood pressure when the heart contracts to expel the blood)[274] and diastolic (blood pressure when the heart relaxes to refill the heart cavity)[275] blood pressure is typically measured. The World Health Organisation has found the mean systolic blood pressure to globally be around 125mmHg[276]. With regard to the dimensions of the brachial artery, ultra-sound scanning has found the diameter of a typical brachial artery to be between 4.73$\pm$0.75mm[277] to 4.46$\pm$0.72mm[277] depending on the physiological stress the subject is under. Whilst the brachial arterial wall thickness was found to typically be between 0.4$\pm$0.05mm[278] to 0.35$\pm$0.06mm[278]. Therefore from the above one could calculate the size of the brachial artery cavity to be:

$$\text{Diameter of brachial artery} - (2 \times \text{Thickness of brachial artery wall}) = \text{Diameter of brachial artery cavity} \quad (3.16)$$

thus: Upper limit (wide artery, thin wall) 4.73mm - (2 × 0.35mm) = 4.03mm
Lower limit (narrow artery, thick wall) 4.46mm - (2 × 0.40mm) = 3.66mm

$$\text{Typical diameter of brachial artery cavity} = 4.03\text{mm} - 3.66\text{mm} \quad (3.17)$$

Therefore from the above one could estimate the typical diameter of the brachial artery to be approximately 4mm. It is important to note however that the refined device post proof of concept in Chapter 6: CNT-PDMS will in fact be much smaller than that of 4mm in order to prevent embolism. Simply put if one was to introduce a device into a major artery the cells further down the arterial tree will suffer from the lack of blood supply. Therefore, as with the pulmonary blood pressure sensor, the brachial blood pressure sensor should also be small enough to prevent oxygen deprivation. However, as discussed earlier in this chapter, it is important to remember that carbon nanotube-polymer composite is expected to require a certain amount of volume for the piezo-resistivity to take place. Thus over-miniaturising the device at such an early stage of the investigation while testing for its viability, is ill advised. This holds particularly true for the 3-dimensional compression where the size of the device is required to be confined from all three dimensions. In contrast, for a 2 dimensional compression one could simply fabricate a film where one could measure the piezo-resistivity across a large area to compensate for the lack of composite to react to pressure. For this reason the device fabricated in Chapter 6: CNT-PDMS will be that of approximately 4mm for experimental purposes pending miniaturisation post proof of concept.

3.3.3 Sphygmomanometer

The most generally accepted form of brachial pressure measurement is perhaps the sphygmomanometer. It is a simple contraption where air pressure is applied through an inflatable cuff over the upper arm in order to measure the blood pressure through its feedback[279] (Fig.3.33):

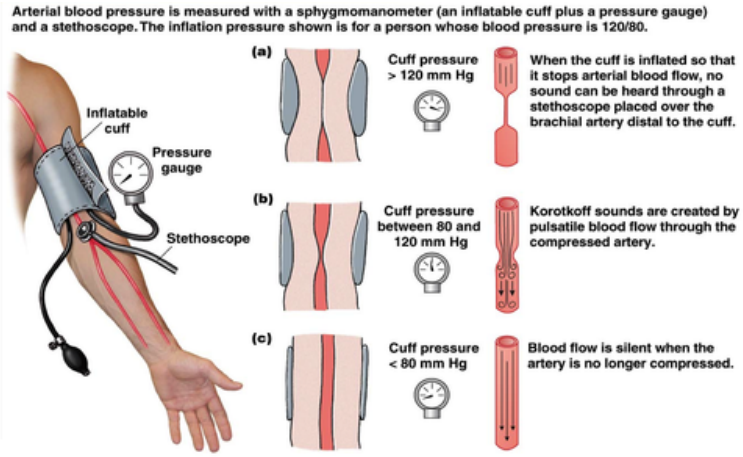

Figure 3.33: Blood pressure measurement using a sphygmomanometer: a) the air pressure from the cuff is applied to the point where the blood circulation is halted, b) the air pressure is relaxed partially restoring blood flow through the artery, c) the blood flow is fully restored returning to its normal operating pressure[279].

Its invention is accredited to Samuel von Basch in 1881[280] where the design was refined by the likes of Scipione Riva-Rocci[280] and Harvey Cushing[280] in 1896 and 1901 respectively. The design was quickly adopted by the medical industry internationally and remains at the forefront of medical care to this day. Naturally, if one was to develop a brachial blood pressure measurement device it is only logical to design a device similar to that of a sphygmomanometer so that it is backwards compatible to the blood pressure data collected over the last century. The main issue presented by the use of a sphygmomanometer is its intrusiveness. Having an inflatable cuff around one's arm is convenient during an occasional visit to the general practitioner but not necessarily so to those who are hospitalised for a prolonged period of time. Chapter 6: CNT-PDMS aims to develop a brachial blood pressure sensor where one could have the device embedded within a blood vessel with the capability of wireless data extraction designed to allow physicians

to monitor a patient's blood pressure over an extended period of time using a non-invasive monitoring system as simple as a bedside scanner.

3.3.4 Human Flesh Analogue

For many years throughout history, swine flesh has been used as a human analogue, particularly for ballistic and forensics testing purposes[281]. However for some applications it is preferable to have a chemically synthesised analogue to achieve a closer mimicry of the human flesh. For the application in Chapter 6: CNT-PDMS it is preferable that one could physically see the composite and wirings to examine for short circuits and broken connections, as well as forming a tight seal around the composite in order to achieve a better transfer of pressure from the analogue to the composite. Therefore for Chapter 6: CNT-PDMS a castable analogue known as ballistic gelatine, a solidified solution of water and gelatine was used. This substance is known to accurately simulate the human flesh by having near identical mechanical properties[282] with a proven track record of its use by forensics specialists and biomedics[282]. Its density (1060kg/m^3[283]) is near identical to that of human muscle tissues(1040kg/m^3[284]). There are two standard recipes for the mixture: the Fackler gelatine and the NATO gelatine. The Fackler gelatine requires 10% gelatine and 90% water solidified at 4^{o}C[285] whilst the NATO gelatine requires 20% gelatine and 80% water solidified at 10^{o}C[285]. Of the two recipes the Fackler gelatine is by far the most common for financial reasons since Fackler gelatine requires only half of the gelatine that the NATO recipe requires. Therefore throughout this investigation the ballistic gelatine used in Chapter 6: CNT-PDMS will be that of Fackler gelatine to save experimental costs.

Chapter 4

Experimental Methods

4.1 Raman Spectroscopy

Raman spectroscopy is a radiation scattering effect where the scattered radiation has a different wavelength to the incident radiation[286]. It was first discovered in 1928 by C.V. Raman and K.S. Krishnan[287] and it later proved to be particularly useful in identifying chemical species and their electronic states. This is due to the fact that the incident radiation could lose its energy to physical matter through inelastic scattering[287]. The the amount of energy lost is dependant on the vibrational, rotational and various other low energy states of the chemical bonds[286]. Since chemical bonds are formed by electrons that has quantised energy levels, the energy lost by the incident radiation will also be quantised[288] (Fig.4.1). The energy levels are unique to individual chemical species and their electronic states, which in turn allows identification of the species in question. The amount of energy lost is often represented as the shift in wavelength based on the photon energy equation: $E = \frac{hc}{\lambda}$. A histogram of this shift is known as the Raman spectrum[289] where the peak positions indicate the chemical species and their respective electronic states while the height represents amongst other things their abundance. Naturally, since the measurement relies on wavelength shift the incident radiation is preferable for it to be monochromatic[286] to avoid confusion and for the ease of filtering during data processing.

In the interest of this investigation Raman spectroscopy will be used to identify the purity of the diamond(sp^3), which is known to have a signature peak position of 1333.33cm^{-1}[290] and its main contaminant graphitic carbon(sp^2) at 1575cm^{-1}[291]. The full width half maximum(FWHM) of the peak is used as a yardstick to determine its crystallinity[290]. The breadth of the FWHM originates in the additional virtual states caused by the grain boundaries[292]. Therefore the finer the grain is (and in turn the greater the number of grain boundaries) the greater the FWHM of the sp^3 peak will be[293][294][295].

Although Raman spectroscopy has a plethora of operational classes[286], where an excellent review by Ulness, Kirkwood and Albrecht can be found in the Encyclopedia of Chemical Physics and Physical Chemistry[286], the basic premise of the process remains the same.

Radiation scattering comes in three different types: Rayleigh, Stokes and Anti-Stokes[286][288] (Fig.4.1).

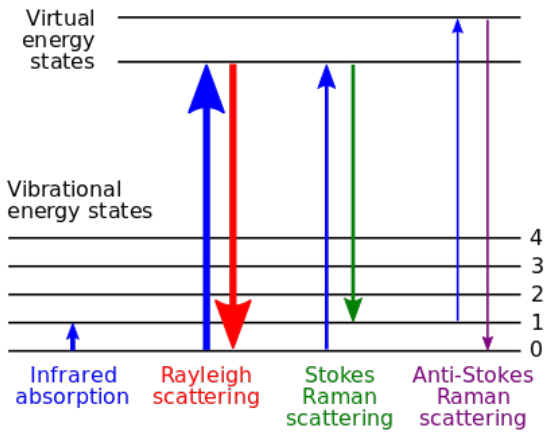

Figure 4.1: Three types of radiation scattering undergone during Raman measurements[288].

Rayleigh scattering is purely elastic, thus the resulting scattered radiation has the exact same energy as the incoming photon[286]. Naturally due to the lack of measurable change in energy this type of scattering will not yield any information and will be filtered out. It is however worth noting that the process of filtering has been a challenge in the past due to the abundance of the Rayleigh scattering in

comparison to the information bearing Stokes and anti-Stokes scattering. At room temperature the majority of the information obtained is from Stokes scattering where most of the scattering occurs from the energetically low ground state.

All information deduced from the Raman scattering therefore comes from the inelastic Stokes and anti-Stokes scattering that falls into a different energy state from its original. This means the photon before and after scattering has a different energy[286] and therefore wavelength. Thus by measuring the wavelength shift from the Stokes and anti-Stokes scattering one can determine the energy level profiles to identify the species and their electronic states.

4.2 X-Ray Photo-Electron Spectroscopy (XPS)

The core principle of XPS exploits the photo-electric effect generated by X-rays to determine the outer-most species and their respective abundance on a sample surface[286]. This is carried out by measuring the number of and the kinetic energy of the released photo-electrons. The energies of the photo-electrons are:

$$E_k = h\nu - E_b - \phi \tag{4.1}$$

where:

E_k is Kinetic energy of the photo-electron

h is Plank's constant

ν is Frequency of the exciting radiation

E_b is Binding energy of the photo-electron with respect to the Fermi level of the sample

ϕ is Work function of the surface under test

Since the kinetic energy of the released electron is dependant on the binding energy which is unique to the chemical elements one can use it as a means for

spectroscopy. Therefore by identifying the binding energy of a species and their abundance one could deduce the identity of the outer most element and their percentage coverage[286]. As with Raman spectroscopy, the peak position is used to identify the species. However caution is recommended as it is known that peak binding energy could shift depending on its underlying species. This is due to the energy change brought about by the chemical bonds between the outermost species and its underlying element. Since the energy levels of the core electrons are dependant on the bond state of the atom[286] any chemical bonds to the outermost element is known to cause a binding energy shift typically in the order of 0-3eV[286]. In general, the binding energies increase with increasing oxidation state[286]. This shift has in fact been observed in Chapter 8: SEE where LiO termination peak was found to be slightly out of place from its expected position.

It is important to note at this point that the XPS inherently is a surface measurement[286], limited by the mean free path of the excited electrons[286] where approximately 50% of the electrons are known to originate from the outermost layer[286]. As a general rule it is safe to assume that XPS measurements examine for the top 0 to 10nm of the sample.

It is worth noting that XPS does have its limitation in light element detection. Although XPS is known for its ability to detect almost every chemical element in the periodic table it finds it incredibly difficult to measure lighter elements(such as H and He)[286]. This proves to be rather problematic when attempting to measure the H-termination on a diamond surface.

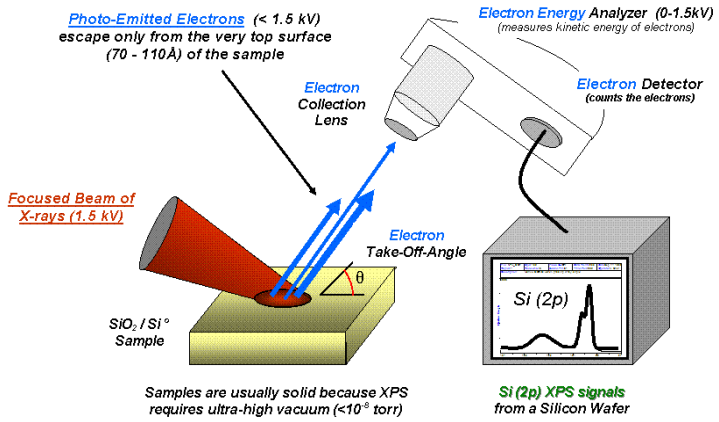

Figure 4.2: XPS system[296].

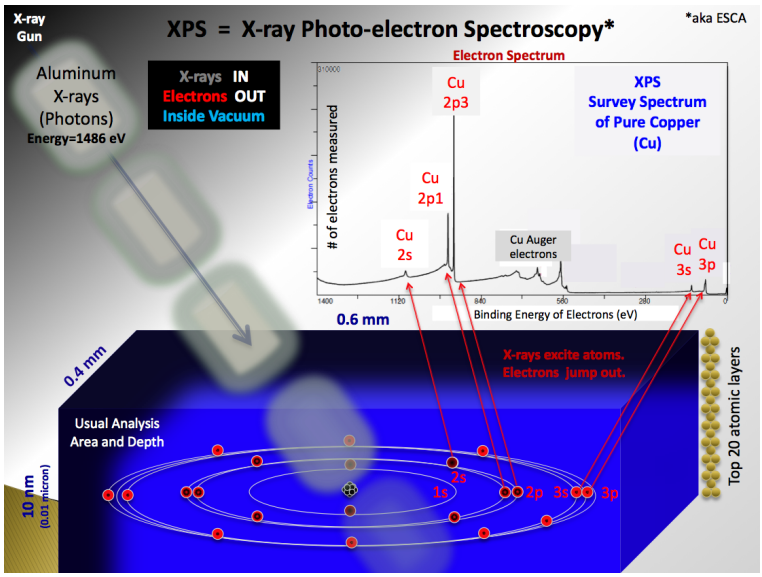

Figure 4.3: Photo-electric effect from copper under XPS[296].

4.3 Impedance Spectroscopy

Impedance spectroscopy was first developed as a means to measure the double layer capacitance of electro-chemical devices[**?**][297]. Although it was originally reserved for specialised applications its popularity has grown substantially since the invention of the super capacitors[298]. Studies has shown that the hybrid nature of the device has both the energy density of a battery[299] and a discharge speed of a capacitor[299] to excel in a plethora of modern technologies such as in

electrical cars and mobile phones. In regards to this investigation however its true value is in its ability to identify grain boundaries[300], composite filler dispersion and measure resistances.

Impedance is a measure of obstruction to the flow of current typically caused by the resistance of a material and the resistance to change in the direction of the current. Naturally for direct current (DC) the impedance will be equal to that of the resistance of the material as there is no change in the current's polarity. Therefore for DC:

$$E = IR \tag{4.2}$$

where:

E is Applied potential

I is Resulting current

R is Resistance

For alternating current(AC):

$$E = IZ \tag{4.3}$$

where:

Z is Impedance

The key concept here is the dependence of impedance on frequency[301]. If one was to imagine a steadily flowing electron and it was suddenly brought to a halt and change direction, the electrons will have a certain response time to the change. The difficulty for an electron to respond to the change in direction increases with frequency. Therefore the latency in electron response i.e. the delay in change of current direction after change in applied voltage direction could be described as a phase difference between the two[302]. If one was to mathematically represent this it is prudent to use a function that is sinusoidal in nature. Thus:

$$E_t = E_0 \sin(\omega t) \tag{4.4}$$

$$I_t = I_0 \sin(\omega t + \phi) \tag{4.5}$$

where:

ω is $2\pi f$ (ω in rad/s and f in Hz)

E_0, I_0 is Max. amplitude of applied voltage and current respectively

ϕ is Phase shift in radians

By applying this to Eq.4.3:

$$Z_t = \frac{E_t}{I_t} = \frac{E_0 \sin(\omega t)}{I_0 \sin(\omega t + \phi)} = Z_0 \frac{\sin(\omega t)}{\sin}(\omega t + \phi) \tag{4.6}$$

Thus the impedance could be expressed in terms of the magnitude of the impedance (Z_0) and phase shift (ϕ). By applying Eq.4.6 to the Euler's formula:

$$e^{j\phi} = \cos\phi + j\sin\phi \tag{4.7}$$

The impedance could be represented by its real and imaginary components:

$$Z(\omega) = \frac{E}{I} = Z_0 e^{j\phi} = Z_0(\cos\phi + j\sin\phi) = Z_0\cos\phi + jZ_0\sin\phi \tag{4.8}$$

$$Z(\omega) = \mathrm{Re}(Z) + \mathrm{Im}(Z) \tag{4.9}$$

$$\phi = \tan^{-1}\left(\frac{\mathrm{Im}(Z)}{\mathrm{Re}(Z)}\right) \tag{4.10}$$

Eq.4.9 is often represented by an $\mathrm{Im}(Z)$ vs $\mathrm{Re}(Z)$ graph known as a Cole-Cole (or Niquist) plot (Fig.4.4) with its iconic semi-circle. Alternatively one could plot a Bode plot ($\mathrm{Re}(Z)$ vs frequency)(Fig.4.5). Most importantly both plots reveals

various aspects of the sample, typically its: resistance, capacitance, presence of grain boundaries and sample behaviour at high and low frequencies. In order to explain this, one needs to understand the Randles equivalent circuit(Fig.4.6).

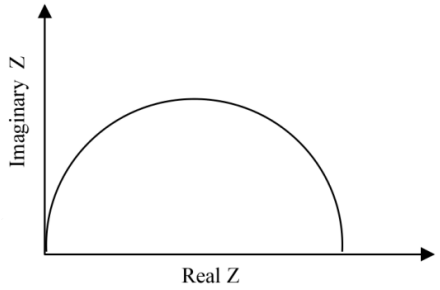

Figure 4.4: Cole-Cole(Niquist) plot[303].

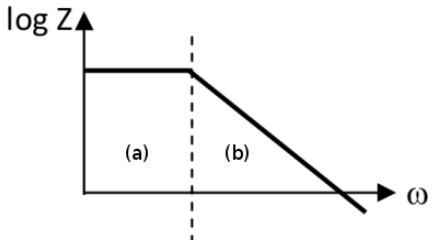

Figure 4.5: Bode plot, a) steady real impedance (Z) values indicated a resistive nature of the sample, b) the steady decrease in Z indicates the capacitive nature of the sample[303].

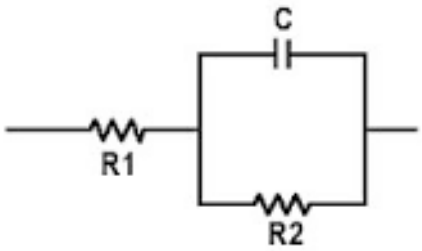

Figure 4.6: Randles eqivalent circuit[304].

By applying Eq.4.8 to the Randles equivalent circuit:

$$Z(\omega) = \frac{E}{I} = R_1 + \frac{1}{(\frac{1}{R_2} + jC\omega)} = R_1 + \frac{R_2}{(1+\omega^2C^2R_2^2)} - \frac{j\omega C^2R_2^2}{1+\omega^2C^2R_2^2} \quad (4.11)$$

Note: The **red** part of the equation is **real** and the **blue** part is **imaginary**.

where:

E is Applied voltage

I is Current

R_1, R_2 is Resistances

C is Capacitance

In Eq.4.11 if ω was to tend to zero, $Z(\omega)$ will equal to (R_1+ R_2) and as ω approaches infinity, $Z(\omega)$ equals R_1. Meaning at infinite (or sufficiently high) frequencies the current will conduct through the C branch of the Randles equivalent circuit making R_1 the sole source of impedance. While at zero frequency the current will go through the R_2 branch making the impedance (R_1+R_2). It is very important to understand that both R_1 and (R_1+R_2) are **real**. If the frequency was moderate (thus neither zero or infinite) the imaginary component will have value meaning it has an imaginary component. This is precisely the reason why Cole-Cole plots are semi-circular in nature. At 0Hz and at very large frequencies the imaginary component is non-existent while at frequencies in between, the imaginary component gradually increases then eventually decrease as it tends to large frequencies. Pure resistance values could therefore be found at zero and at infinite frequency, since the current going through the C branch is at its greatest under maximum imaginary impedance. The capacitance could be determined from the peak of the semi-circle. Where:

$$\omega_{max} R_2 C = 1 \tag{4.12}$$

$$C = \frac{1}{2\pi f_{max} R_2} \tag{4.13}$$

Thus one could deduce the resistive and capacitive components of impedance from the equations above. Another use of a Cole-Cole plot is in the identification of grain boundaries from the presence of smaller semi-circles strcture[300]. Thus

revealing its non-crystalline nature. A Bode plot on the other hand has its value in two areas: the determination of resistance from highly conductive samples and sample behaviour at certain frequencies. At times when measuring a highly conductive and/or non-homogeneous sample, such as highly conductive carbon composites, the Cole-Cole plot may be extremely erratic making it nearly impossible for one to fit the semi-circle with the Randles equivalent circuit model. This is caused by the unstable and precarious conduction network of carbon composites with constantly changing conduction path which, depending on the capability of the apparatus,, is unable to cope with the minuscule phase change between the applied voltage and the current. A Bode plot at 0Hz on the other hand is equal to (R_1+R_2) as discussed earlier giving the overall resistance of the sample that stands immune to the phase change. This is because at 0Hz one is effectively passing a DC current through the sample that follows Ohm's law (Eq.4.2) allowing one to deduce its pure resistance. One could also determine if the device is more capacitive or resistive at certain frequencies based on the fact that Bode plots have a steady decline when capacitive (Fig.4.5) and a steady real impedance when resistive (Fig.4.5).

4.4 Scanning Electron Microscope (SEM) and Tunnelling Electron Microscope (TEM)

SEM and TEM are both methods of imaging a sample using electrons as a means of image capture[286]. The narrow wavelength of the electron beam is known to surpass the resolution of conventional light microscopes by several order of magnitudes[286]. The crucial difference between the two however is in its mode of imaging. SEM is a surface imaging method, thus it focuses the electron beam on the smallest possible spot size and scan across the area of interest[286] (Fig.4.7). TEM is a transmission imaging method, thus it relies on the scattering of the electron caused by sample features while filtering through the sample[286] (Fig.4.7). Naturally, to avoid electron beam absorption the sample is required to be thin,

preferably no more than 200nm[286]. Sample preparation therefore has proven to be rather challenging in the past. One effective method of slicing the sample to the required thickness is to cryogenically freeze the sample before sectioning that allows for a cleaner cut aided by the increased rigidity of the sample[286]. Crucially however unlike the SEM, TEM uses the 'flood beam illumination' method that illuminates a large area of the sample[286] (Fig.4.7). The significance of this is in the spacial resolution of the image. For a scanned beam all effects are local and confined to the spot size. Thus spacial resolution is identical to the achievable spot size[286]. Therefore in general SEM that uses a focused beam has a higher resolution than a TEM[286].

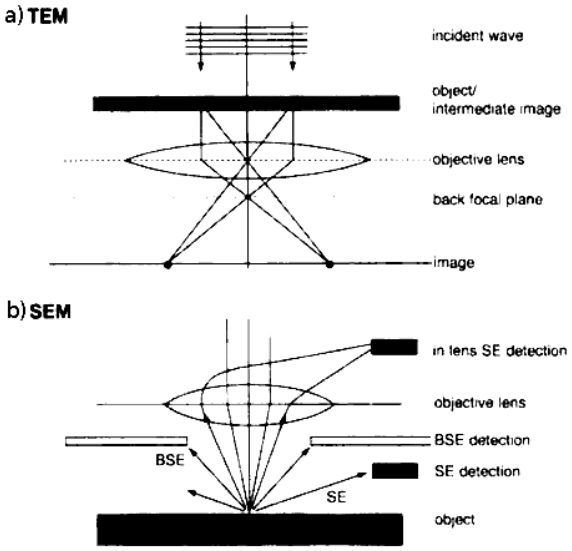

Figure 4.7: Typical electron beam path of: a) TEM and b) SEM. The TEM beam spot size is substantially bigger than that of SEM which has been focused by a lens[286].

In the interest of this investigation samples imaged under the TEM in Chapter 5: CNT-Epoxy was prepared through cryo-sectioning. The transmissive nature of the TEM has allowed for the sub-surface CNTs in the CNT-Epoxy composite to be imaged. This results in a successful determination of its dispersion pattern within the composite.

Additional information can be found in a review by Schroder and Muller who

extensively collated the different image processing and sample preparation methods including biological samples which are notoriously difficult due to its aqueous nature[286].

4.5 Atomic Force Microscope (AFM) and Surface Profiler

AFM AFM was first invented to address the shortcomings of the Scanning Tunnelling Microscope(STM), namely its inability to image a non-conductive sample[286]. The most interesting feature of the AFM is in its imaging method. AFM unlike the SEM and TEM is a non-radiative microscopy where imaging is carried out by an incredibly fine tip that physically 'feels' the surface where the deflection caused by the surface structure that forces the tip to deflect is registered by the change in the laser angle[305] (Fig.4.8). By scanning the tracks for surface undulation and collating the data collected AFM could then generate a topographical image.

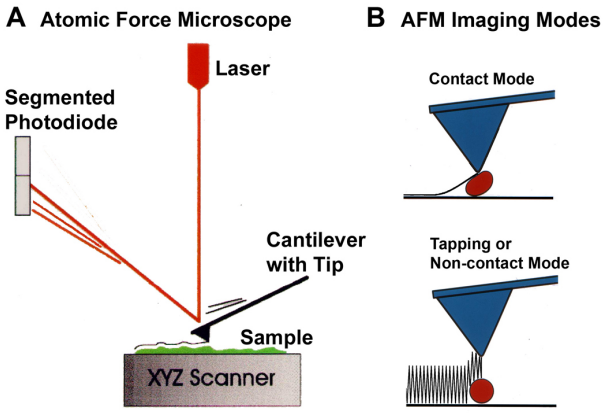

Figure 4.8: A) a typical AFM system and B) the three modes of AFM measurements.

A point to note is the overall resolution difference between an AFM and a STM. The resolution of AFM is dependant on the finess of the tip[286]. Although very fine AFM tips such as those made of carbon nanotube are in existence, STM that relies on an atomically fine tip and electron tunnelling to determine the

position of each atom has been proven to show greater resolution[286].

AFM has three main modes of imaging: contact, non-contact and tapping. Contact as the name suggest is a mode where the AFM tip is physically in contact with the sample surface. It measures the topography by dragging the tip across the surface[286]. Naturally both damages to the tip and the sample is to be expected. However many have exploited this destructive nature by using it as a means to manipulate atomic scale materials[286]. Non-contact mode on the other hand allows the AFM tip to hover over the sample surface at its resonant frequency where the surface topography is measured through the change in tip to surface attraction caused by the change in van der Waal's force[286]. This method has astonishingly allowed for true atomic resolution imaging[286]. However it was proved to have its own set of issues. Non-contact mode relies on having one full interaction with the surface per oscillation. Therefore if a change in van der Waal's interaction were to occur over multiple oscillations it could potentially face resolution issues[286]. Tapping mode is in essence a mode that benefits from both the contact and non-contact mode. This mode is designed to 'tap' the surface once per oscillation [286] thus circumvents the resolution loss faced by the non-contact mode while the contact force and duration is notably smaller (typically at a force of <5nN)[286] thus with limited tip and sample damage. All AFM images taken during this investigation will be taken in tapping mode.

For further information please refer to the review by Spencer and Jarvis[286].

Surface Profiler Surface profiler is a surface imaging system that operated analogously to an AFM where a stylus is traced over the sample surface to measure the surface undulation. Initially it was developed as a means to determine the roughness of a sample. However recent development has allowed for a more accurate determination of the surface features that proved to be particularly useful in measuring the height of sample features. It is worth noting that the main difference between a surface profiler and an AFM is in its dimensions. An AFM will return a 2 dimensional image of the sample while a surface profiler will return

a 1 dimensional height change in its track. Although both methods return sample height data, it is much easier to determine the height of the sample feature from a surface profile without the need to extract the data from an AFM image. As with AFM, the tip radius dictates the data resolution. Typically a surface profiler tip ranges from 20nm to 50μm. The surface profiler will be used extensively in Chapter 7: BAE Neutron Detectors to identify the thickness of the diamond film and metal contacts as well as surface defects.

4.6 Metallisation (Evaporation and Sputtering)

Evaporation Of the many available metallisation methods evaporation is perhaps the most common. This is due to the fact that the procedure is extremely simple and versatile allowing a quick and easy metallisation as well as having a plethora of deposition materials that it could deposit.

This particular method relies on melting the deposition material using a heating element and slowly bringing it to evaporation. The evaporated metal is then able to attach itself or to the substrate. Naturally this method will require a large mean free path of the deposited material. This is achieved by carrying out the process in a vacuum, typically in the range of 10^{-6} to 10^{-7}mBar. The heating of the deposited material is carried out through Joule heating thus by passing a current through a crucible that contains the deposited material. The resistance of the crucible generates heat that in turn melts and evaporates the material it contains. This method particularly excels in metallising large areas and it will be used to coat the surface of neutron detectors with LiF conversion layers.

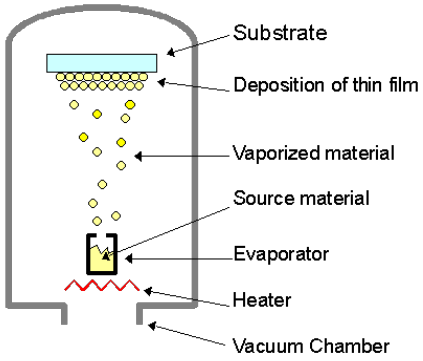

Figure 4.9: Evaporation metallisation system. The evaporator and heater used in this investigation (denoted separately in this diagram) is a single unit of graphite crucible[306].

Sputtering Sputtering is a rather unconventional form of metallisation that relies on ionic bombardment instead of heat (evaporation) to coat the surface of a sample[307].The main advantage of using sputtering over evaporation is in the wider range of deposition material, since sputtering relies on ionic bombardment to remove the atoms from the metal source it is able to deposit metals of higher melting and boiling points. In the interest of this investigation sputtering was specifically used to allow Ti to be deposited onto the surface of diamonds. The added momentum of the deposition metal has allowed the formation of the chemically and physically stable TiC bond. The origin of the added momentum is in the sputtering plasma (typically with energies in the 10 to a few 100keV range[307]). An inert gas plasma such as Ar is used to bombard the surface of the metal target that transfers momentum upon collision. The momentum will cascade down over several generations[307] until the target atom is energetically released from the surface followed by its deposition on the substrate[308] (Fig.4.10).

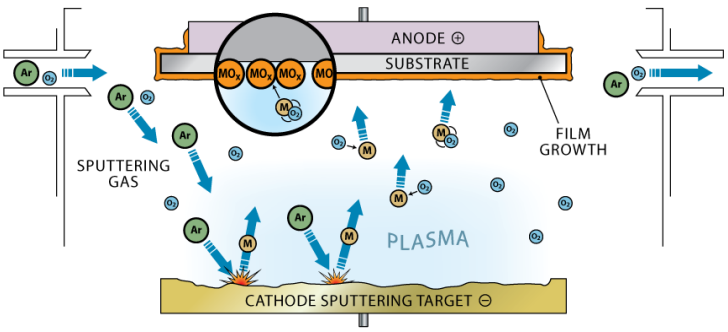

Figure 4.10: Sputtering system with Ar plasma[308].

Chapter 5

CNT-Epoxy

5.1 Introduction

Carbon Nanotubes (CNTs) are renowned for their high electrical conductivity[7] and tensile strength[8], and as such CNTs are seen as a promising material to be used as additives to polymers so that one could utilise them to enhance their electrical conductivity. By having conductive CNT fillers encased within an insulating host (the polymer) a network of conduction paths can form that alters the overall conductivity of the composite, where the degree of change in conductivity is relative to the concentration of the CNTs added[309]. Since the cost of CNTs are relativly high compared to the host polymer[40], there is considerable interest in identifying the lowest concentration required to acheive electrical conduction. In particular the transitional stage between insulation and conduction, percolation is of particular interest as in this state the CNTs are near enough from each other to the degree that conduction could occur through quantum tunneling[310]. The significance of this lies in the fact that the conductivity of the composite in percolation will be extremely sensitive to a wide variety of external constraints, such as pressure due to its very nature of it being at the 'tipping point' from an insulator to a conductor[311][312]. This precarious conductive nature makes this particular state extremely interesting in the field of sensor engineering, with the conductive network formation being the key to its conductivity. Naturally, the as-

pect ratio of the CNTs used, and the extent to which they might be aligned within the composite will strongly influence the concentration required for the onset of percolation. In this investigation the conductivity of multi-wall CNT-polymer composites produced using CNTs of various widths, lengths and surface functionalisation (–OH and –COOH) will be investigated. Epoxy was chosen as the host polymer based on its monomer's extremely low viscosity[313] allowing the polymer and CNTs to be mixed efficiently and effectively through high shear mixing, a process that is known for its excellent capability of mixing CNTs homogenously within the composite[226]. In addition, epoxy is known to be extremely stable physically in its cured state such that it is capable of immobilising the CNTs that have been distributed within the composite, limiting post-cure CNT migration. The said dispersive states of CNTs were later examined under transmission electron microscopy (TEM) to identify the origin of the difference in resistivity observed from composites encasing various different types of CNTs.

5.2 Experimental Methods

CNTs were mixed into an epoxy using a high-shear mixer (IKA Ultra-Turrax T18 basic), where the epoxy mixing ratio was based on the manufacturer recommendation and the mixing speed and duration was based on the preliminary studies by the collaborators Tagliaferro *et al.*. The CNTs were pre-functionalised by their respective manufacturers. Epoxy monomers (Epilox T19-36/700), CNTs (Table.5.1) and epoxy hardeners (Epilox H10-31) were added together and mixed simultaneously with a monomer to hardener ratio of 5:3 respectively. The uncured composite was mixed at 11,000 RPM for 30seconds, followed by further mixing at 20,000RPM for 90 seconds. The composite was then added to a polystyrene rectangular mould (117mm×91mm×3mm), degassed in a rough vacuum (approx. 10^{-1}mbar) for 30min to remove the entrapped air bubbles formed during the high shear mixing and cured at 70°C for 4h in an oven at atmospheric pressure. Once cured, the sample was diced into a 5mm^2×3mm piece and two spots of silver paste

were applied and left to dry overnight to form contacts. Once the silver contacts have dried the impedance of the samples was measured by applying a frequency sweep between 0.1Hz-10^7Hz through a two-point probe impedance system (Solatron SI1260A) using a bias voltage of 0.1V and 1V. The impedance data was then fitted using the Randles equivalent circuit model on its Cole-Cole plot to determine the sample resistance. TEM (JEOL 2100F FEG) was used to determine the distribution of CNTs within the composite at a beam voltage of 200kV over a scan area of 200μm^2 with 20μm^2 survey grids. This gives a sample set of 100 where 200μm is expected to show a general representation of the composite given the filler dimensions being in the nm range.

Sample	CNT Conc.(wt%)	Diameter(nm)	Length(nm)	Functionalisation	Source
MW01	1	30-50	0.5-2.0	no func	Cheaptubes
MW03	3	30-50	0.5-2.0	no func	Cheaptubes
MW11	1	30-50	10-20	no func	Cheaptubes
MW13	3	30-50	10-20	no func	Cheaptubes
MWF01	1	30-50	10-20	COOH	Cheaptubes
MWF03	3	30-50	10-20	COOH	Cheaptubes
MWF021	1	30-50	10-20	OH	Cheaptubes
MWF023	3	30-50	10-20	OH	Cheaptubes
MW71	1	25-45	>10	no func	Nanothinx NTX-3
MW81	1	6-10	>10	no func	Nanothinx NTX-4
MW91	1	110-170	5-9	no func	Sigma Aldridge

Table 5.1: Dimensions and functionalisations of CNTs fillers added to CNT-Epoxy composites.

Figure 5.1: Image of the CNT-epoxy sample under impedance spectroscopy.

5.3 Results

As one could see from Fig.5.2, -COOH and -OH functionalised CNT composites had substantially lower resistances than that of its non-functionalised variant. A resistance difference of $10^{12}\Omega$ (non-functionalised CNT) and $10^{7}\Omega$ (-COOH, -OH functionalised CNT) have been observed. Upon increase in CNT content from 1wt% to 3wt%: non-functionalised, -COOH and -OH functionalised CNT composites all showed decrease in resistance ranging from $10^{8}\Omega$ to $10^{6}\Omega$. Notably the -COOH terminated samples showed a slightly greater degree of decrease in resistance in comparison to that of the -OH functionalised sample (Fig.5.2).

The 1wt% non-functionalised CNT sample (Fig.5.3a) had sizeably larger CNT clusters: average length: 4.08±3.72μm, average width: 2.39±2.08μm and greater number of clusters than the other 1wt% samples (3 clusters). The 1wt% -COOH functionalised CNT sample (Fig.5.3b) had no clusters and the –OH functionalised CNT sample (Fig.5.3c) had 1 small cluster of size: length, 1.85μm; width, 1.14μm.

3wt% CNT samples showed similar results to that of 1wt% with greater number of CNT clusters and larger cluster sizes. For example the 3wt% non-functionalised CNT sample (Fig.5.4a) had 6 clusters (as opposed to 3 from the 1wt% sample) with an average size of: length, 4.89±2.89μm; width, 3.05±1.79μm,

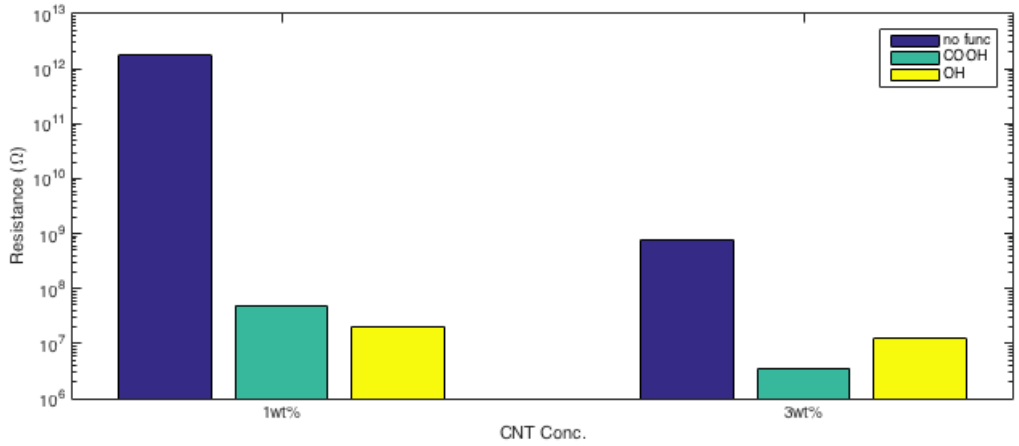

Figure 5.2: Impedance measurement results of resistance of CNT-epoxy composite with its filler concentration of non-functionalised, -OH and –COOH termination.

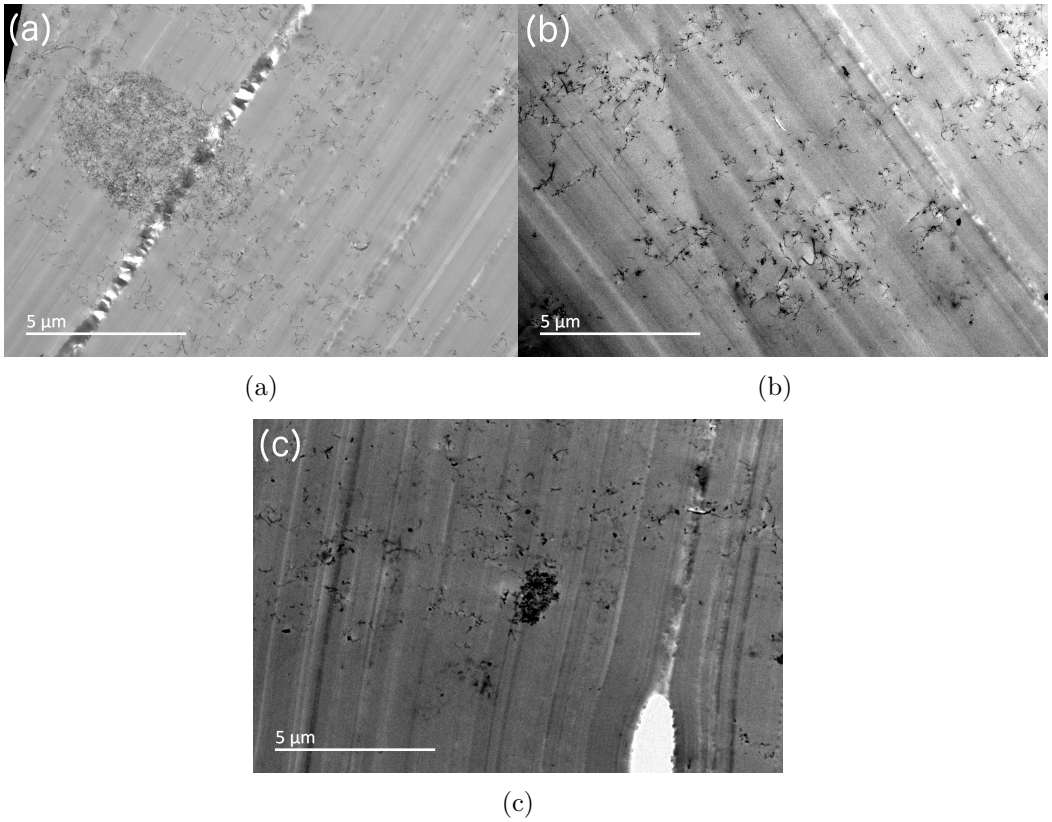

(a) (b)

(c)

Figure 5.3: (a) TEM images of non-functionalised 1wt% concentration CNT-Epoxy (b) TEM of –COOH functionalised 1wt% concentration CNT-Epoxy (c) TEM of –OH functionalised 1wt% concentration CNT-Epoxy. All images were taken over a scan area of 200μm.

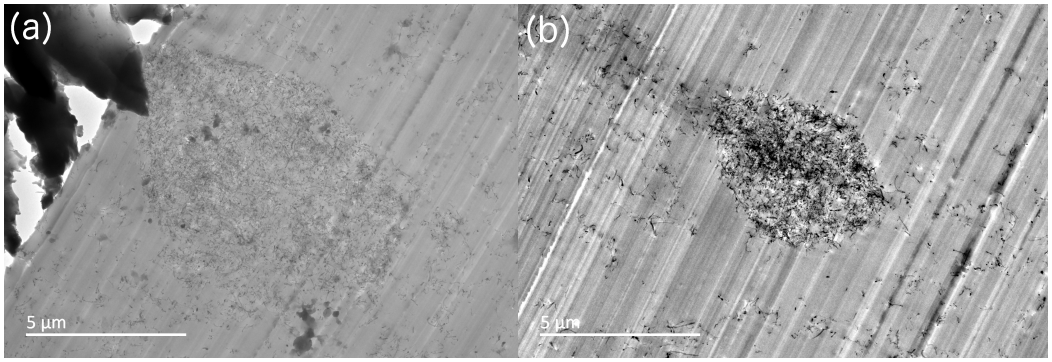

(a) (b)

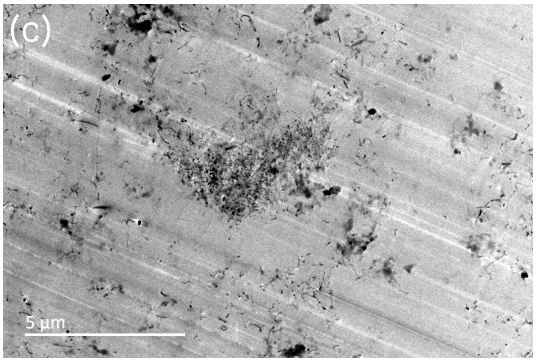

(c)

Figure 5.4: (a) TEM images of non-functionalised 3wt% concentration CNT-Epoxy (b) TEM of -COOH functionalised 3wt% concentration CNT-Epoxy (c) TEM of -OH functionalised 3wt% concentration CNT-Epoxy. All images were taken over a scan area of 200μm.

a notably larger size than that of its 1wt% variant. –OH functionalised sample experienced a similar increase in the number of clusters (from 1 cluster for 1wt% to 5 for 3wt%) as well as an increase in their cluster sizes with an average size of: length, 2.91$\pm$1.62μm; width, 1.68$\pm$0.698μm (Fig.5.4c). Interestingly clusters were observed from the 3wt% -COOH sample (5 clusters with an average size of: length, 3.69$\pm$2.18μm; width, 2.05$\pm$1.36μm) (Fig.5.4c) when not one cluster was present in its 1wt% varient. The cluster found was slightly larger in size than its -OH varient, although overall it remains to be on par in scale.

CNT Conc. (wt%)	Functionalisation	Number of clusters	Average lengths (μm)	Average width (μm)
1	non-functionalised	3	4.08	2.39
1	COOH	none	N/A	N/A
1	OH	1	2.87	1.64
3	non-functionalised	6	6.25	4.13
3	COOH	5	3.69	2.05
3	OH	5	2.91	1.68

Table 5.2: The number and size of CNT clusters in a 200μm scan area of different functionalisation and concentration observed under TEM.

CNT length (μm)	Resistance (No func, Ω)
0.5-2.0	5.28×10^{12}
10-20	1.8×10^{12}

Table 5.3: Resistance of composite against length of CNTs.

CNT diameter (nm)	Resistance (No func, Ω)
6-10	4.59×10^{12}
25-45	3.34×10^{12}
110-170	3.78×10^{12}

Table 5.4: Resistance of composite against the diameter of CNTs.

5.4 Discussion

Previous research by Gojny *et al.*[314] (amination of CNTs) and Chen *et al.*[315] (amination of acrylicnitrile modified CNTs) has shown that functionalisation of CNTs affects the conductivity of the polymer-nanoparticle composite. In particular they have found amine groups to enhance conduction when incorporated into polymers due to the improved integration of CNTs into polymer chains through covalent bonding[315]. In contrast, So *et al.* found –COOH groups to decrease composite conductivity[316]. This investigation has found contradicting evidence where -COOH group was found to substantially increase conductivity (Fig.5.2). As seen from Fig.5.2 the resistance of –COOH and –OH functionalised CNT composites were found to be 5 and 2 order of magnitude lower than that of its non-functionalised counterpart for 1wt% and 3wt% respectively. One explanation of the origin of this sudden drop in resistance is the chemical bonds that were formed between the functional groups and the epoxy chain. Nakazawa *et al.* (based on observation by Glazer[317]) found that –OH functional groups are capable of forming a hydrogen bond between the main body of the epoxy chain and metal nano-particles[318]. Although strictly speaking CNTs are not metal nano-particles, the premise of the –OH functional group on the CNT to exhibiting similar bond nature with the epoxy chains is likely to be feasible. The CNTs are effectively being 'tethered' to the heavier polymer chain increasing its overall mass. Since polymer chains have the tendency to 'wrap' around the CNT dendrically[319]. It is likely that the CNTs are not being bound to the epoxy chain via single hydrogen bond leading to multiple epoxy chains being attached to the CNTs further increasing the mass of the CNT-polymer matrix. The overall mass of the matrix is of particular interest since CNTs in general are very fine in size and shape they entropically tend to form clusters[320][321]. Therefore by having a larger mass to act upon, it will enable the mixing process to separate the individual CNTs easier from their parent cluster thus allowing the CNTs to be distributed more evenly in the composite. A better dispersion of CNTs

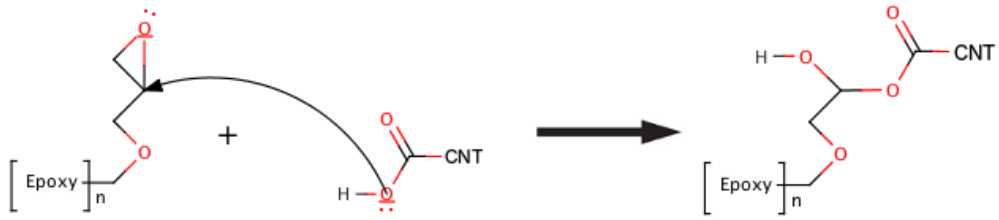

Figure 5.5: Expected chemical reaction between epoxy and –COOH functionalised CNT forming an esterbond between the two reactants.

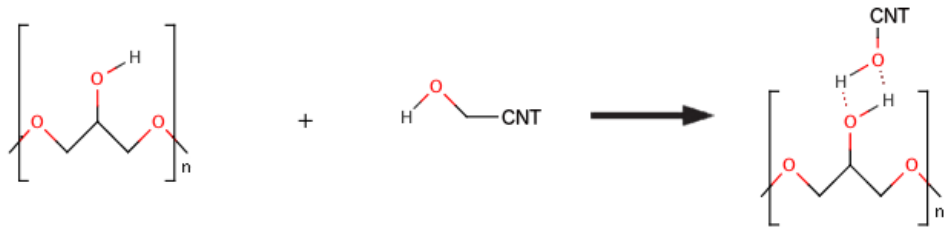

Figure 5.6: Expected chemical reaction between epoxy and –OH functionalised CNT forming two hydrogen bonds between the two reactants.

will in turn create a greater number of conduction paths and therefore reduces the composite resistance. This results in the reduction of -COOH and -OH functionalised CNT-epoxy composite resistance. The –OH and –COOH functionalised CNTs however are expected to bond to epoxy chains through two different type of chemical bonds. –COOH functionalised CNT is likely to undergo an esterification process that will attach the CNT to the polymer via a hydroxyl group reaction to the amine group creating a stable ester bond[322] (Fig.5.5). The influence of a water molecule produced during the esterification was considered unlikely to affect the measurement considering that 97wt% to 99wt% of the composite is epoxy and the majority of the remaining 1wt% to 3wt% is CNT where the functional group is only present on the surface as well as the fact that functionalisation of CNTs are known to cover approximately 10% or less of the CNT surface due to its requirement of breaking σ-bonds. Therefore the role of water produced by esterification was considered to be negligiable. The -OH functional group on the other hand would most likely attach itself to the aforementioned hydroxyl group on the epoxy via hydrogen bond (Fig.5.6)[316].

However findings by So *et al.* have suggested that hydrogen bonds may also be present in the –COOH functionalised CNTs as well[316]. It is therefore likely that the –COOH functional groups that did not undergo esterification was attached to the epoxy chain via a relatively weak hydrogen bond[316].

A potential explanation to the conflicting results presented by So *et al.* where they have found the resistance to increase as a result of –COOH functionalisation[316] could be explained by the difference in the degree of dispersion of CNTs. This investigation employed high shear mixing as its distribution method that is designed to break down the CNT clusters into individual CNTs allowing CNTs to be well dispersed, that in turn allows the CNTs to have a greater chance of being individually attached to a polymer chain. So *et al.* used stirring as a dispersion procedure[316], a process known to exhibit poor CNT dispersion[187]. If the declustering of the CNTs are not sufficient CNT bundles are formed and most CNTs are then likely to be forced to remain within the clusters where the surrounding polymer strands could then form interlocking chains to 'lock-in' the CNTs. This most likely will lead to a poorly spread CNT distribution that reduces the number of conduction paths directly resulting in the increase in composite resistance.

One method of verifying the above prediction of the difference in dispersion of CNTs by its functional groups is by taking the TEM images and inspecting the CNTs' distribution pattern visually[323]. TEM images of the midsection of the epoxy composite samples were taken at 200kV beam voltage with an inspection grid area of $20\mu m^2$ over a 200μm2 total inspection area. The number of CNT clusters within the area were counted and their size measured (Fig.5.3)(Fig.5.4). The middle portion of the sample was chosen in order to have an accurate representation of the whole composite as it is believed to be independent of surface entropic effects. The 1wt% CNT TEM images have shown that the non-functionalised sample has the largest CNT clusters (average length: 4.08μm, average width: 2.39μm) (Fig.5.3a) and also the greatest number of clusters (3 clusters), while the 1wt% –COOH composite had none in the same scan area (Fig.5.3b). This agrees with the above prediction that the –COOH functionalisation leads to a

strong ester bonding between the CNT and the polymer chain forcing the CNT to be separated from its cluster. The resistance of 1wt% -COOH functionalised CNT composite was much smaller ($4.98\times10^{7}\Omega$) than the 1wt% non-functionalised composite ($1.80\times10^{12}\Omega$) supports this finding since the greater the dispersion of CNTs are the greater the number of conduction path will be which will lead to a reduction in composite resistance. –OH on the other hand did have some clusters. However they were very small in size (length, 1.64μm; width, 2.87μm) and less numerous (1 cluster per 20μm^2) compared to its non-functionalised variant (Fig.5.3c). One possible explanation for the presence of clusters in the 1wt% –OH functionalised composite when its -COOH varient was completely free of them is its bonding strength. As mentioned above it is expected that the –COOH functional group attaches itself to the polymer chain via ester bond and hydrogen bond while –OH groups rely solely on hydrogen bonds. It is known than the bonding strength of ester bond is substantially stronger than the combined strength of two hydrogen bonds (424.3±6.3kJ mol^{-1} and 2×6±2kJ mol^{-1} respectively)[129][324]. In another words if the bonds are stronger they have less of a chance for the CNT and polymer to be separated during high shear mixing, maintaining the mass of the CNT-epoxy matrix required for a good dispersion. Thus when the CNTs were being mixed one could assume that the weaker hydrogen bonds were more likely to be broken resulting in the now stray CNTs to recluster but to a lesser degree than that of a non-functionalised CNT composite where neither ester nor hydrogen bonds were present. The similarity in the composite resistance of the -COOH and -OH functionalised samples most likely originated from the fact that both -COOH and -OH samples were already at percolation where the CNT dispersion was near optimum[325] and also by the fact that both the ester and hydrogen bonds have shown to have sufficient bond strengths between the epoxy chain to benefit from the improved dispersion. Provided that there are enough bond strengths to withstand the high shear process, the CNTs will still be connected to the epoxy chain. Thus after a certain bond strength the CNT-epoxy matrix will be immune to the CNT-epoxy separation. In essence, the CNTs were

sufficiently bound to both the -OH and -COOH functionalised samples such that they were able to benefit from the increased mass that led to the improved spread of conduction paths. Therefore only a small degree of difference in conductivity was observed between the -COOH and -OH samples due to the similarity in the spread of the conductive network.

The 3wt% CNT concentration samples has shown the same trend as to that of 1wt%, where –COOH and –OH functionalised CNT loaded samples had lower resistances ($3.57\times10^{6}\Omega$ and $1.24\times10^{7}\Omega$ respectively) than that of their non-functionalised sample ($7.52\times10^{8}\Omega$) variants. However, judging from the increase in the size and number of clusters observed from the 3wt% samples. It is likely that much of the additional CNTs could be said to have contributed to the formation of clusters rather than the formation of conduction paths resulting in a much more moderate decrease in resistivity. Most notably the TEM images revealed the presence of previously unseen clusters in the 3wt% –COOH sample that were not observed from its 1wt% variant. One can speculate that at 3wt% CNT loading there are significant numbers of CNT near to each other such that they mutually attract to create a 'seeding site' where the CNTs could bundle to form a cluster. One observation to support this theory is the fact that -COOH sample that contained no clusters at 1wt% was found to have 5 clusters at 3wt%, while those samples where CNT clusters pre-existed in its 1wt% sample were also found to contain clusters in their 3wt% variants. However a substantial increase in their number have been observed. The non-functionalised sample that originally contained 3 clusters at 1wt% was found to have 6 clusters at 3wt%, whilst -OH functionalised samples that contained 1 clusters at 1wt% had 5 at 3wt%. In terms of size an increase in length and width of 4.08μm to 6.25μm and 2.39μm to 4.13μm respectively for non-functionalised samples was found (Fig.5.4a)(Fig.5.4c). Interestingly -OH seemed to have maintained its cluster size (length: 2.87μm to 2.91μm and width: 1.64 to 1.68μm respectively). Considering the results found from non-functionalised and -COOH samples however it is logically sound to suggest that the general trend for the size and number of cluster is to increase with increasing CNT concentra-

tion regardless of the functionalisation. TEM results have shown that there has not been much increase in the number of CNTs in the area between the clusters suggesting that after a certain concentration the CNTs are being added to the clusters rather than to its more sparsely filled areas. One could speculate that this is due to the CNT clusters acting as a CNT sink much in the same way as a needle to a pin-cushion, where the excess CNTs are being embedded in the CNT clusters.

In addition to the above experiments the influence of the length and width of the CNTs were also investigated. As seen from Table.5.3 and Table.5.4 one could see that the greater the length of the CNTs are, the lower the resistance of the composites were. This stems from the fact that the longer the CNTs are the greater its 'reach' to form a conductive network will be, while their diameters showed very little resistance variation. This is most likely due to the limited change in the reach achieved in comparison to the change in length.

5.5 Conclusion

In conclusion this investigation has successfully shown that composites formed with –OH and –COOH functionalised CNTs has a reduced composite resistance due to the formation of a heavier, easily separable CNT-polymer chain complex. Composite resistance difference between the non-functionalised and the -OH, -COOH functionalised samples were $10^{12}\Omega$ to $10^{7}\Omega$ respectively. The bondings responsible for the said resistance difference seen from the –COOH group is expected to be caused by a combination of ester bond and hydrogen bond and while –OH relied solely on hydrogen bonds. TEM images of the composite has verified the distribution pattern that lies in agreement with the said resistance change whilst –OH bond showed a lesser degree of homogeneous distribution due to its weaker bonding strength. Further addition of CNTs from 1wt% to 3wt% have shown to force clusters to be formed and reduces composite resistance. The influence of the functionalisation was found to be the same as those observed from

that of 1wt%. However it was found that after a certain CNT concentration any addition of CNTs seems to show a reduced benefit to composite resistance due to the fact that added CNTs are being absorbed into the CNT clusters. The length of the CNT was also found to influence the resistance where the longer the CNTs are the lower the composite resistance will be. The diameter proved to have little influence on the composite resistance.

Chapter 6

PDMS-CNT Blood Pressure Sensor

6.1 Introduction

One approach to achieve a cost-effective, non-invasive and staff-free monitor is to fabricate a wireless piezo-resistive blood pressure sensor (Fig.6.1). The particular design used in this investigation is designed to embed itself into a pulmonary artery, passively monitoring the change in resistance caused by the blood pressure change while wirelessly sending the resistance reading out of the body using a radio frequency (RF) tag. As discussed earlier the signature symptom of heart failure is either the decrease or increase in blood pressure, with the pulmonary artery being the currently preferred monitoring location[266]. Therefore if one was to place a piezo-resistive material in the pulmonary capillary, one could both measure the change in blood pressure quantitatively and detect heart failure through the change in its resistance. The resistance reading will be measured through an output signal generated by the RF tag that harvests both the energy required for resistance measurement and output signal from the input RF signal. In principle, this device will be able to monitor heart failure constantly and non-intrusively by utilising a RF scanner located in a discreet location such as attached to the patient's bed, as well as having a potential device lifetime of 8 to 10 years based on

the implant replacement recommendation of PDMS (of which the piezo-resistive composite is made of) by both plastic surgeons[326] and the FDA[327]. The benefit of this particular design is in the fact that it is applicable to any type of hydraulic pressure change whether it is in the pulmonary artery for heart failure detection or in the brachial artery to measure the systemic arterial (general body) blood pressure[272]. Although further optimisation is required the device could also be beneficial to the measurement of other physiological pressure change such as eye pressure for glaucoma[328].

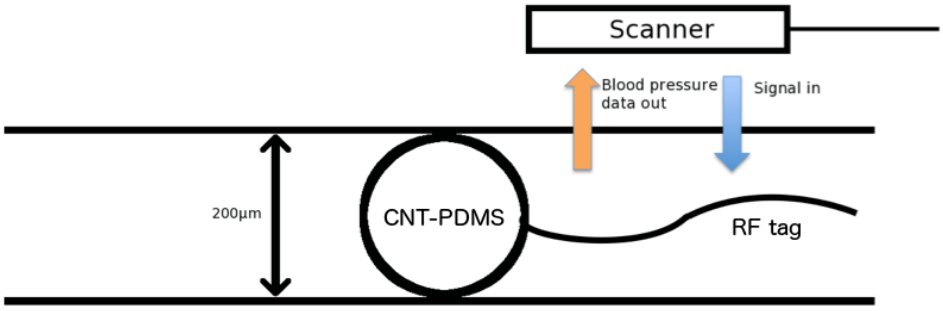

Figure 6.1: The proposed design for the CNT-PDMS composite piezo-resistive blood pressure sensor. The device is designed to be injected into a pulmonary or brachial artery where the blood pressure change will be registered as a resistance change. A wireless scanner will induce a current in the RF tag for it to measure the resistance of the composite and return the resistance reading to the scanner.

This investigation will focus on the development of the piezo-resistive composite that will be used to register the blood pressure change as a change in its resistance. The composite will consist of two components: polydimethyl-siloxane (PDMS) and carbon nanotubes (CNTs). The former has long been established in the medical industry as implants particularly for reconstructive surgery for breast cancer[203]. PDMS has four desirable properties: electrical insulation (resistivity of $2.9\times10^{14}\Omega$ cm[207]), hemo-compatibility[208][211], muted inflammatory response[212][213][214] and its flexibility due to its extremely low glass transitioning temperature[205], while CNTs are known for their extremely high electrical conductivity[7], tensile strength[8] and aspect ratio. Most importantly the conductive CNTs are known to be able to form a conductive network within

an insulating polymer host[186][218]. The conductivity of the CNT-polymer composite is dependant on the concentration of the infused CNTs[186]. In essence if the CNT concentration is low the insulating nature of the polymer host (such as PDMS) will dominate causing the CNT-PDMS composite to be an insulator. On the other hand if the concentration of the CNT is substantial the composite will be conductive due to the formation of the conductive CNT network. At its transitional state, percolation however much of the CNTs in the PDMS are close enough to each other for conduction to occur through quantum tunnelling[310]. This particular state is known for its precarious nature where the composite could drastically change its resistance, for this reason at percolation the conductivity of the composite is extremely sensitive to external constraints such as pressure[311]. If a small amount of pressure was applied to the composite the conductive CNTs will come closer together causing the conductivity of the composite to increase dramatically. One could therefore exploit this acute dependence of conductivity to pressure to fabricate a highly sensitive blood pressure sensor.

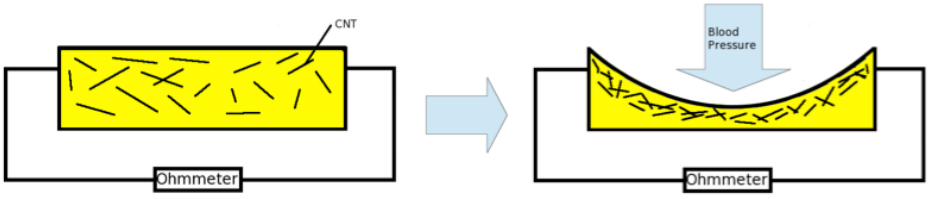

Figure 6.2: The piezo-resistivity mechanism of the CNT-PDMS composite. The composite in percolation would be compressed under the blood pressure. CNTs during the compression will be brought closer together allowing conduction from CNT to CNT to occur either through contact or by increasing the probability of quantum tunnelling of electrons.

This investigation will be carried out in three stages: firstly, the fabrication of CNT-PDMS composite of different CNT concentrations in order to identify whether the composite is in fact capable of achieving percolation by measuring their resistance through impedance measurements. If they are capable of doing so, the ideal (thus percolation) concentration where the composite will be most

sensitive to pressure will be identified. Secondly CNT-PDMS composite films of various concentrations with thickness equivalent to a pulmonary artery cavity diameter (200μm)[271] will be placed under a range of 2-dimensional (2D) mechanical pressures (0-150.01mmHg) that is equivalent to the possible pulmonary blood pressure[276][329][330] in order to demonstrate the proof of concept of its piezo-resistivity at the required pressure regime from the required dimension. Lastly the pressure sensitivity of a composite will be tested under 3-dimensional (3D) compression by mimicking a human arm and blood pressure using a sphygmomanometer and ballistic gelatine, a human body analogue commonly used in forensic analysis to simulate human muscle tissues[282]. The primary objective is to investigate the feasibility of fabricating a systemic arterial blood pressure sensor for a brachial artery that could also be utilised as a heart failure detection system.

6.2 Experimental Methods

Sample preparation - Necessary amount of CNTs (diameter: 110-170nm, length: 5-9μm, multi-walled, Sigma-Aldrich), PDMS-monomer (Sylgard 184 silicone elastomer, monomer, Dow Corning) and PDMS-hardener (Sylgard 184 silicone elastomer, hardener, Dow Corning) for the desired CNT concentration has been weighed out where the ratio of monomer to hardener used was 10:1 respectively. PDMS-monomer was added to the CNT and hand mixed for 10 min until the consistency of the mixture was thoroughly homogenous. PDMS-hardener was then added and further mixed for 5min. The CNT-PDMS mixture was degassed in a vacuum chamber at 10^{-3}mBar for 30min. The mixture was poured into a mould and cured overnight at 70°C.

Stirring was specifically selected as the preferred mixing method over other processes that are traditionally considered to produce better CNT dispersion in the composite, such as high shear mixing and sonication[187]. This decision was based on the results from the preliminary study that compared the resistance of

the hand mixed composite and high shear composite before and after 2D compression. The study has shown that between the two mixing methods there is a sizeable difference in resistance from the same CNT concentration before and after compression. The said resistance differences found were $5.62\times10^{8}\Omega$ to $6.31\times10^{5}\Omega$ (a difference of 3 order of magnitude) and $1.00\times10^{10}\Omega$ to $5.01\times10^{7}\Omega$ (a difference of 2.30 order of magnitude) for stirring and high shear mixing respectively. Naturally, a greater difference in resistance before and after the compression was preferred as it translates to a greater degree of sensitivity due to the greater change in resistance per pressure. A possible explanation to this surprising finding is the viscosity of the uncured PDMS (5100mPa s)[207]. High shear mixing relies heavily on the vacuum created by the turbulence to feed its contents to the shearing mechanism[331]. Therefore if the contents were to be viscous, high shear mixing will show a decrease in effectiveness, while stirring stands relatively immune to this effect. A study by Bauhofer *et al.* has shown that the importance of mixing speed (RPM) diminishes with CNT concentration where beyond 0.1wt% the resistance of the composite mixed with lower RPMs (50 RPM) are identical to those which are mixed at higher RPMs (2000 RPM)[187]. Therefore considering that CNT concentrations used in this investigation ranged from 2-20wt%, hand mixing at low RPM was considered to be equally as effective as high RPM and sufficient for this investigation.

Impedance - Throughout this investigation impedance measurements were carried out under: 2-point measurement, 0.1Hz to 1GHz frequency sweep and 0.01V to 1V bias. The resistance of the sample was determined through the Cole-Cole plot fit where a three element equivalent circuit (Randles equivalent circuit) consisting of one real resistor, one imaginary resistor and one imaginary capacitor where the real and imaginary components are in series and the two imaginary components are in parallel was used.

Impedance of CNT-PDMS of various CNT concentrations - CNT-PDMS pellets of 1cm in diameter, 5mm in depth and CNT concentrations of 2-20wt% in 2wt% intervals have been prepared. Impedance measurements were

taken for each and their respective resistances calculated. The results were then used to identify the CNT concentration at which percolation could be observed.

Impedance of CNT-PDMS under 2D pressure - CNT-PDMS samples of CNT concentration 2-16wt% in 2wt% intervals, 200μm in thickness, 1.5cm in length and 1cm in width have been prepared. The sample has been attached to a contact plate with 1cm separation designed to measure the impedance across the sample (Fig.6.3). The sample was placed under a load of 0N to 2N in 0.2N intervals from a pressure bolt of 1cm^2 in area, amounting to an equivalent of 0-150.01mmHg in pressure. At each interval its resistance was determined through impedance measurements.

200μm was chosen as the sample thickness to simulate the pulmonary artery cavity of an adult male which is known to vary from 3.32cm[267] to 8.3μm[268].

A force of 0-2N exerted from a 1cm^2 area was chosen as it translates to an equivalent pressure of 0-150.01mmHg, which comfortably covers the optimal systolic arterial pressure of 125mmHg[276] that is often used as a benchmark to diagnose hypotension (<90mmHg)[329] and hypertension (140-159mmHg and above)[330].

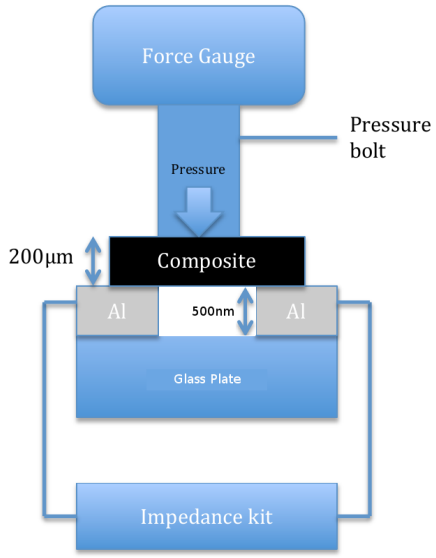

Figure 6.3: 2D-compression kit. The design allows the force gauge to apply pressure to the CNT-PDMS composite while the impedance kit takes measurements across the sample through the 500nm thick aluminium contacts.

Impedance of CNT-PDMS under 3D compression - A $4mm^3$ CNT-PDMS sample of 10% CNT concentration with 0.1mm copper filament contacts that was insulated using a thin polyethylene film (an insulating barrier thin enough to avoid structural reinforcement but thick enough to achieve electric insulation) and insulation tape was prepared. Ballistic gelatine was made using 10% gelatine (Fluke Analytical) and 90% water. Gelatine was gradually added to warm water at 40°C whilst stirring and stored at 5°C for 2h after mixing to hydrate the gelatine. The mixture was then reheated to 40°C and poured into a cylindrical mould of 10cm in diameter with the CNT-PDMS samples in its core with both ends of the wire exposed and attached to the impedance kit. Impedance measurements were then taken between 20-180mmHg at 10mmHg intervals. The pressure was applied through the sphygmomanometer surrounding the ballistic gelatine. Once 180mmHg was reached the pressure was lowered in 10mmHg intervals from 180mmHg to 20mmHg, measuring the sample's impedance values at each interval. This was carried out to investigate whether the pressure has any permanent effect on the resistance values.

Ballistic gelatine was used to simulate a human arm based on its sound, track record for its use as a human body analogue in the field of bio-medical engineering[282] with a similar density to muscle tissues (1040kg/m^3[284] and 1060kg/m^3[283] for muscle tissue and ballistic gelatine respectively). Thus is able to transfer pressure to the sample embedded within the gel in a similar manner to how a patient's arm would. A cylindrical mould of 10cm in diameter was chosen based on the average upper arm circumference for individuals over 20 year olds across all ethnicities and genders[332]. The size of the CNT-PDMS sample was chosen based on the average brachial artery cavity diameter derived from the average brachial artery cross-sectional diameter (4.73±0.75mm to 4.46±0.72mm)[277] and wall thickness (0.4±0.05mm to 0.35±0.06mm)[278] respectively. In practice it is unrealistic to use a sample as large as 4mm^3 in a patient's body due to concerns of causing embolism. However for the purpose of the proof of concept a more workable scale was used prior to its miniaturisation.

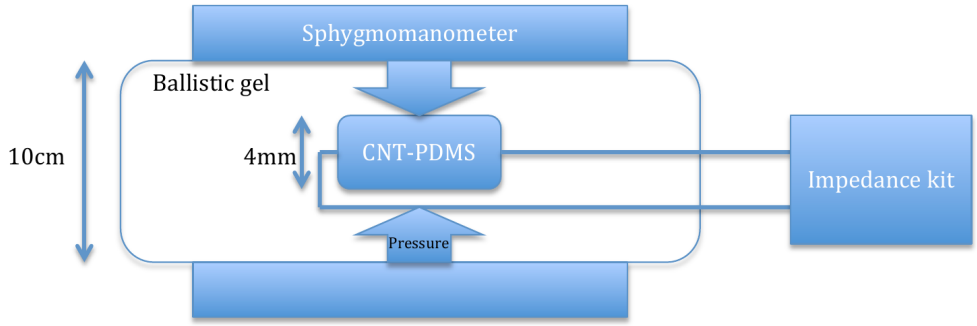

Figure 6.4: 3D compression kit. The CNT-PDMS sample was encased in a ballistic gelatine cylinder simulating a human arm. The sphygmomanometer applies pressure through the ballistic gelatine to the sample where the impedance kit was used to take measurements through the copper filament attached to the composite.

6.3 Results

The relationship between the resistance and CNT concentration of CNT-PDMS composites without applied pressure is shown in Fig.6.5. As seen from the figure

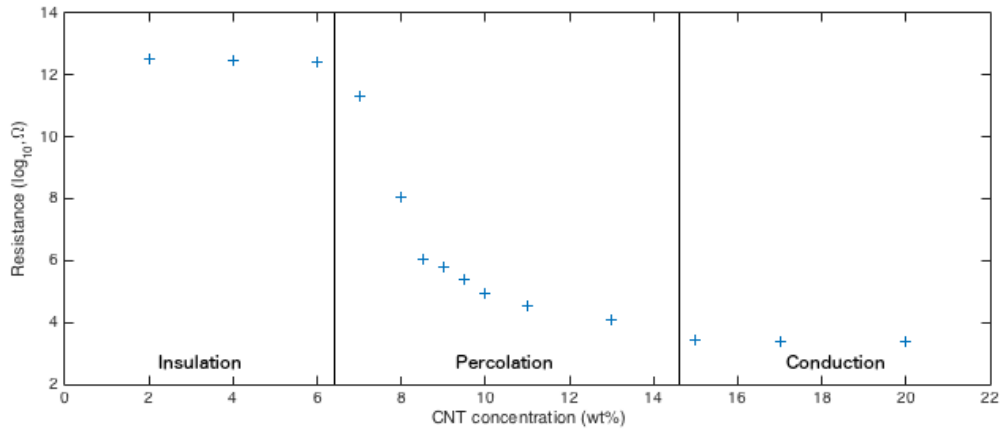

Figure 6.5: The relationship between the CNT-PDMS composite resistances and their respective CNT concentrations. The percolation threshold was found to be at 8wt% and the state of percolation was defined to be to and from the first point of deviation from the plateau.

the curve illustrates a signature sigmoidal curve that you will see from a percolation capable composite. The insulating portion at the lower end of the CNT concentration (2-6wt%) has a resistance of $10^{12}\Omega$ while the conductive portion of the curve (14-20wt%) has a resistance of $10^{3}\Omega$. The percolation threshold (the greatest point of resistance change per CNT concentration) is at 8wt% with a 9 orders of magnitude resistance difference from the state of insulation to the state of conduction ($10^{12}\Omega$ to $10^{3}\Omega$). Additionally, saturation in conductivity at 15wt% was observed indicating that the conductive CNT network has been fully established to the extent where any addition of CNTs will no longer benefit its conductivity.

Fig.6.6 represents the relationship between the resistance of the CNT-PDMS composite against its respective applied force in 2D. As one could see at lower concentrations (2-8wt%) the samples were insulating with no signs of percolation. However one should note that an overall decrease in resistances from $10^{11}\Omega$ to $10^{9}\Omega$ have been observed with increasing CNT-concentrations, indicating a general decrease in resistance caused by an increase in the number of conduction path. Surprisingly 8wt%, the CNT concentration that was most likely to show percolation under load based on the results from Fig.6.5 did not. Instead a clear

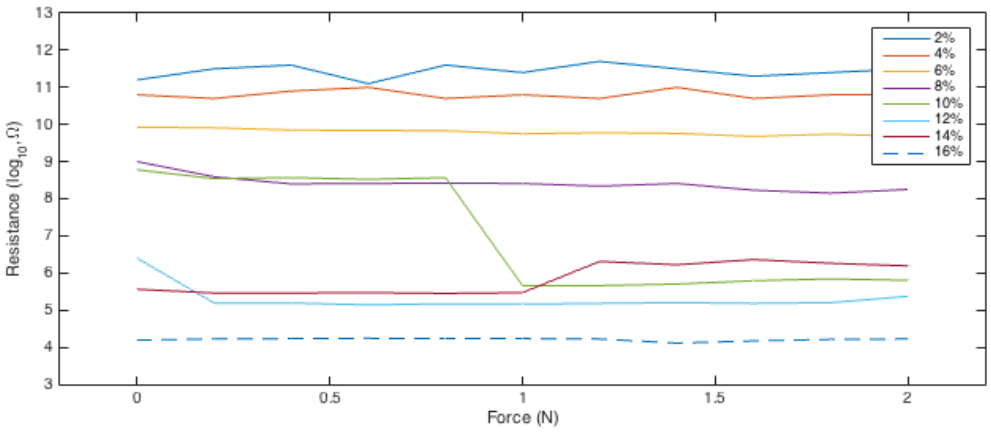

Figure 6.6: The relationship between the composite resistance and the force applied to the CNT-PDMS composite in 2D from samples of CNT concentration 2wt% to 16wt%. Notably the graph has shown 10wt% to be the CNT concentration where pressure sensitivity could be observed from. Conductivity of other concentrations were stable due to the dominance of the conductive CNTs or the insulating PDMS.

sign of percolation has been seen from the 10wt% sample between the forces of 0.8-1.0N, where the resistance before and after the percolation was $10^9\Omega$ and $10^5\Omega$ respectively. Samples of greater CNT concentrations (12-16wt%) like those of concentrations lower than 10wt% did not show percolation. However like the 2-8wt% samples they have shown stable conductivities where the resistance of the sample ranged from $10^6\Omega$ to $10^4\Omega$ respective to increasing CNT concentrations. Notably, the composite resistance of the non-conductive samples (2-8wt%) and conductive samples (12-16wt%) were confined to either side of the percolation threshold of 10wt%. This further reinforces the notion of the 10wt% sample being at percolation as by definition a small addition of conductive fillers will drastically increase the composite conductivity once the state of percolation is reached.

Based on the evidence from Fig.6.6 that has shown 10% CNT-PDMS to be the concentration where piezo-resistivity could be observed. 3D compression test was carried out on a $4mm^3$ 10% CNT-PDMS sample. Fig.6.7 represents the relationship between the real and imaginary components of the sample's impedance (Cole-Cole plot). Interestingly all measurements taken have shown signs of having two semi-circles. Implying the existence of two separate conduction mechanisms.

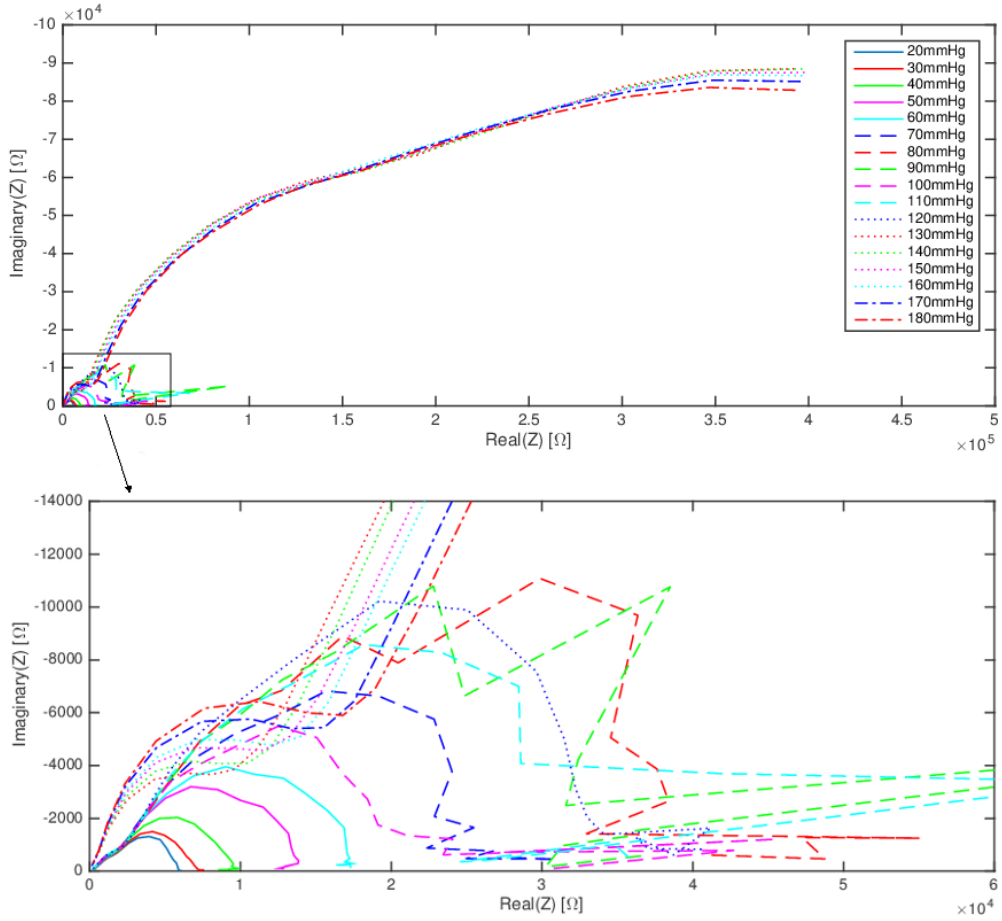

Figure 6.7: The Cole-Cole plots of the 10wt% CNT-PDMS sample under 3D pressure load of 20-180mmHg in 10mmHg intervals. Two semi-circles were observed, indicating the presence of two types of conduction mechanisms.

The first semi-circles were found to be substantially smaller than the second. Although not as pronounced or frequent, 2D results on occasion did show two semi-circles. One possible origin of these semi-circles may be the presence of clusters. CNTs being a fibrous nano-particle is known to form clusters in the composite[320][321]. Therefore there may be a mechanism that is dictated by cluster to cluster conduction and another that of by CNT to CNT conduction. Since clusters are globular and CNTs are fibrous, CNTs require less fillers to form percolation[186]. This combined with the fact that clusters tend to be less numerous than CNTs indicate that of the two fillers: CNTs and their clusters. CNTs will most likely form percolation first before clusters. Therefore of the two semi-circles the one that has a greater piezo-resistive response most likely is

caused by the CNTs. Thus given a certain CNT concentration, if one system has a substantially more pronounced piezo-resistivity than the other. The more muted response such as the one seen in Fig.6.9 is likely to originate from globular clusters whilst the most pronounced response such as those seen from Fig.6.10 originates from the fibrous CNTs. This also agrees with why both the 1st and 2nd semi-circles showed signs of piezo-resistivity. This most likely did not present itself as an issue for the 2D compression as CNTs are dimensionally comparable (diameter: 110-170nm, length: 5-9μm) to the thickness of the sample (200μm) and therefore it is likely that there were not many clusters overlapping in the direction of compression to cause piezo-resistivity (Fig.6.8).

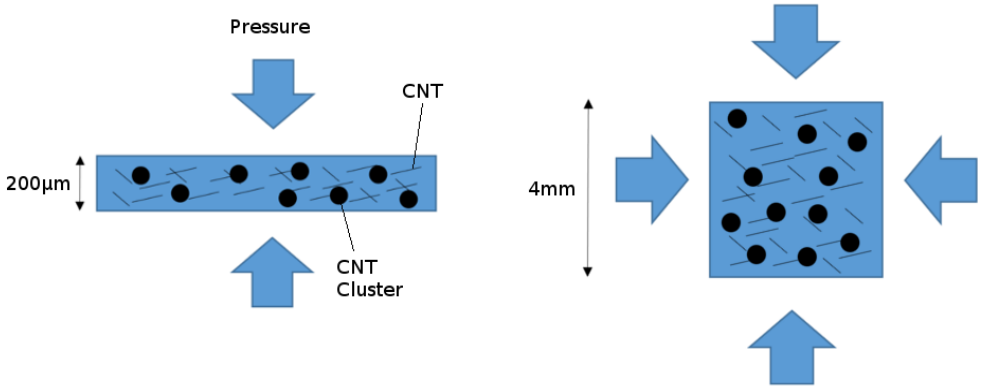

Figure 6.8: (left) 2D compression sample where due to the limited number of overlapping clusters, limited amount of cluster piezo-resistivity was observed. (right) 3D sample where sample dimensions allow for a noticeable amount of cluster piezo-resistivity.

Fig.6.9 represents the resistance of the composite deduced by fitting the Randles equivalent circuit to the 1st semi-circle from the Cole-Cole plot above (Fig.6.7) against pressure. As one could see the sample has shown a very limited piezo-resistive response with the exception of a mild increase in resistance between 120mmHg to 180mmHg where the resistance has increased from 5kΩ to 20kΩ for the 1st compression. The 2nd compression on the other hand has shown signs of hysteresis where a gradual decrease in resistance from 20kΩ to 8kΩ has been observed between the pressure of 180mmHg to 40mmHg.

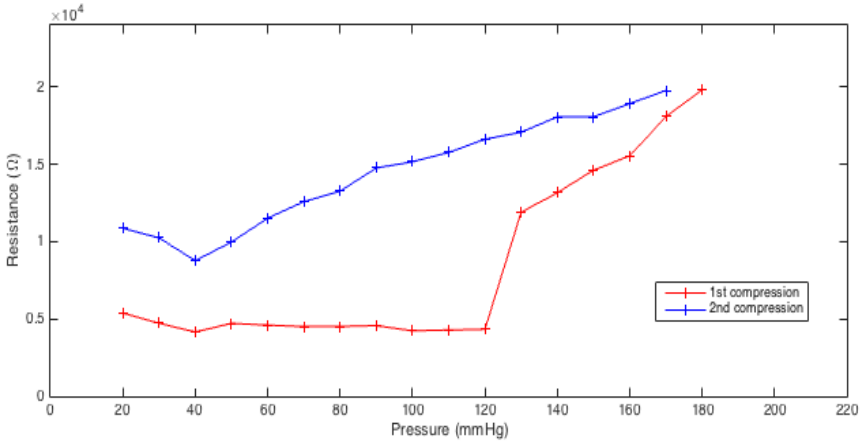

Figure 6.9: Resistance values deduced from the 1st semi-circle of the Cole-Cole plots against their respective pressures. A minor degree of piezo-resistivity (5kΩ to 20kΩ) with hysteresis has been observed. This most likely is caused by the cluster to cluster conduction mechanism.

In contrast to the 1st semi-circle (Fig.6.9) the resistances deduced from the 2nd semi-circle was found to have a strong dependence on pressure. In the interest of this investigation where one aims to develop a blood pressure sensor, Fig.6.10 was separated into three sections: hypotension(<90mmHg), normal(90-160mmHg) and hypertension(>160mmHg) to highlight the pressure ranges of interest. At lower pressures (20-70mmHg) a marginal increase in resistance from 4kΩ to 24kΩ has been observed (Fig.6.10a). This was then followed by a slightly greater degree of increase (24kΩ to 140kΩ) between the pressure of 70-120mmHg (Fig.6.10b). Most importantly the segment of the graph that followed has shown a sudden and substantial increase in resistance of 140kΩ to 750kΩ over the narrow pressure range of 120-130mmHg (Fig.6.10c). This was then followed by saturation where beyond the pressure of 130mmHg a stable resistance between 750-780kΩ has been observed (Fig.6.10d). It is important to note at this point that the overall shape of the graph is sigmoidal much akin to the results found from the 2D compression test demonstrating the strong dependence of the composite resistance to pressure. Rather fortunately, the position of the percolation was in the middle of the normal blood pressure range, a pressure range of medical interest. Interestingly the direction of the sigmoidal nature is in reverse to that of which

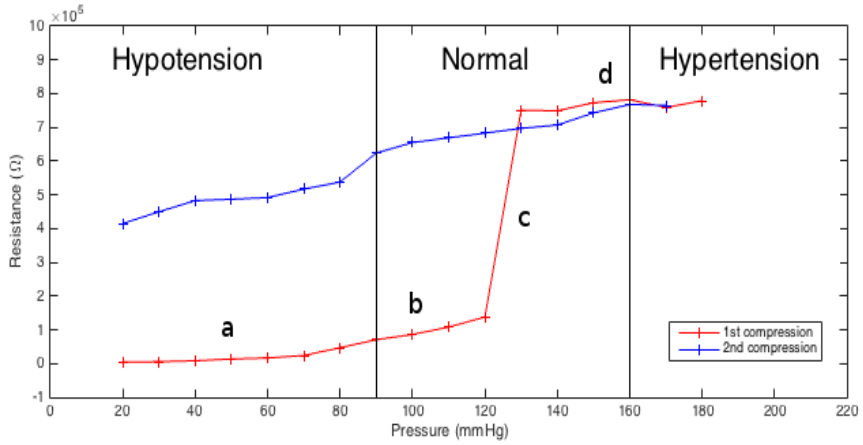

Figure 6.10: Resistance values deduced from the 2nd semi-circle of the Cole-Cole plots against their respective pressures. A sizeable increase in resistance of $1\times10^5\Omega$ to $8\times10^5\Omega$ occurs between 120mmHg and 130mmHg for the 1st compression. Signs of hysteresis has been observed on the 2nd compression, where the resistance gradually decreases to 98.96% resistance recovery over time. This particular part of the composite impedance is understood to be caused by CNT to CNT conduction mechanism.

was observed from 2D compression. Thus the greater the pressure the greater the resistance became. As with the likes of the 1st semi-circle, 2nd semi-circle also experienced hysteresis where a steady decrease in resistance from 765kΩ to 415kΩ has been observed over the pressure range of 180-20mmHg.

It has become apparent from Fig.6.9 and Fig.6.10 that there are two piezo-resistive systems in play. Having two piezo-resistive system could be of issue if the degree of piezo-resistivity is similar since the overall resistance of the composite could prove difficult to predict (i.e. does not strictly follow the sigmoidal curve). It is therefore important to identify the degree of interference the two systems have over each other. Fig.6.11 illustrates the impedance values of the 1st and 2nd semi-circles from the first compression. As one can see, the resistance change undergone by the 1st semi-circle is dwarfed by the 2nd. It is therefore possible to consider the piezo-resistive effect of the 1st semi-circle to have a negligible influence on the overall resistance of the sample, where the entirety of the composite resistance could be said to be from the 2nd semi-circle.

Following the rather unexpected findings from the 3D compression test, a non

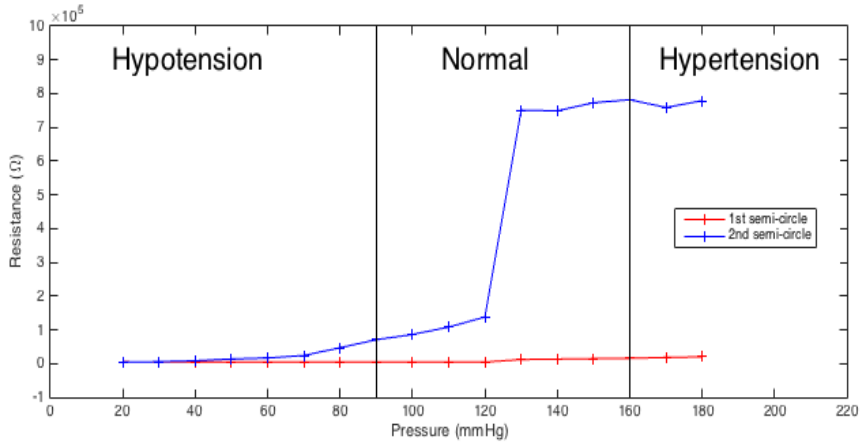

Figure 6.11: Resistance values deduced from the 1st and 2nd semi-circles of the Cole-Cole plot against pressure from the 1st compression demonstrating the difference between the piezo-resistivity of the cluster to cluster mechanism (1st semi-circle) and CNT to CNT conduction mechanism (2nd semi-circle). One can see the piezo-resistivity of the cluster to cluster mechanism being negligibly smaller than the CNT to CNT mechanism.

quantitative 2D compressive verification test has been carried out. The sample was removed from the ballistic gelatine cladding, rinsed in water and remeasured a few days after the initial measurement under no applied pressure and remeasured again under 2D pressure exerted from the pressure bolt used for the 2D measurement. It was found that when under no pressure the composite resistance has fallen to 12kΩ a resistance equivalent to that of which was found between 40-50mmHg in the initial run (Fig.6.10). This pressure notably is comfortably outside of the normal blood pressure range (80-160mmHg) and before percolation indicating the composite's ability to return true to its near original state (98.96% resistance recovery). This suggests its ability to be able to cycle back and forth in response to pressure, given enough recovery time. Upon compression however the resistance increased to 185kΩ, a value substantially smaller than that of from the 3D compression (750kΩ), although the said resistance is in the same order of magnitude as that of from the 3D compression. This suggests that the composite is still capable of exhibiting piezo-resistivity. The likely cause of the lack of resistance change is due to the surface area of which the pressure was applied to the sample. From the 2D compression, pressure could only be applied from two sides

whilst 3D compression exerts pressure from nearly all sides.

6.4 Discussion

The ability of a composite to be able to exhibit percolation is usually judged based on the presence of the signiture sigmoidal curve[309] of which Fig.6.5 has clearly shown to have. However, more importantly so the resistance difference before and after the percolation was found to be rather large with a difference of 9 orders of magnitude. This significant difference in resistance is promising in that it demonstrates that the composite is in fact capable of hosting a large resistance change that usually translates to a large change in resistance per pressure. Another matter of interest is the percolation threshold of 8wt%. Reports by Bauhofer *et al.* who compiled the minimum percolation threshold of various CNT-polymer hosts has found the percolation threshold to range from as low as 0.002wt%[333] to as large as 10wt%[334]. Therefore the percolation threshold of 8wt% is relatively high in comparison to other CNT-polymer composites. This was most likely caused by the high viscosity of the uncured PDMS[207], where Socher *et al.* has shown that the viscosity of the host polymer contributes to the increase in percolation threshold[335] citing its increased difficulty in mixing. This however is not too great a concern considering that the primary objective of the investigation is to fabricate a CNT-PDMS composite that is capable of piezo-resistivity. It is indeed food for thought for future research considering the financial merit of using less CNTs. However for this particular application the percolation threshold of 8wt% will suffice.

As seen from Fig.6.6 CNT-PDMS composites of lower CNT concentrations (2-8wt%) were unable to neither establish a conductive network nor were the CNTs close enough for the pressure to bring the CNTs close enough for the resistance to change. However CNT concentrations did have an effect on the overall resistance where their resistance has decreased according to the amount of CNTs it contained. This occurred as a result of some CNTs being able to form conduction

paths but not numerous enough to create a state of percolation. Another observation from Fig.6.6 is the unexpected finding of the percolation being at 10wt% as opposed to the expected 8wt%. One possible explanation to this rather surprising result is the non-linear relationship between the piezo-resistive stress and applied stress of the composite. Investigations by Wang *et al.* have found that when examining sp^2 carbon (graphite flakes of 10μm in diameter and 0.1μm in thickness) infused epoxy and polyurethane under light and heavy stress, the piezo-resistivity coefficient of the composite decreased non-linearly (more negatively) and exponentially negative for light and heavy stress respectively[336]. In another words the more compressed a sample was the less piezo-resistive it became. Therefore to compensate for the lack of piezo-resistive response from the sample the composite may have required additional CNTs. Although the authors did not state the origin of this phenomenon, one likely explanation is the non-linear elastic response of the host polymer to stress[337]. The more the polymer is being compressed the less elastic it became as it approached the elastic limit, thus the less piezo-resistive the composite became. This explains the piezo-resistive response from the 10wt% sample and not the expected 8wt%. Most importantly however Fig.6.6 has shown a resistance difference of 4 orders of magnitude before and after percolation ($10^9\Omega$ to $10^5\Omega$) from the said 10wt% sample that is likely to be significant enough for one to measure the blood pressure change from. This in turn, has shown 200μm to have enough CNT matrix housed within it to show piezo-resistivity. The resistance of the samples with high CNT-concentrations (12-16wt%) were low due to its abundant availability of the conduction paths. However one should note that the resistance of both insulating and conducting samples were confined to either side of the percolation seen from the 10wt% sample, illustrating the transition between the state of conductivity and insulation.

The 3D compression results were unexpected in many ways. Most apparent of all is the presence of two semi-circles in the Cole-Cole plot that indicates the presence of two separate conduction mechanisms[301]. One explanation to this finding is that this may have been caused by the composite's tendency to host

both CNT clusters and individual CNT strands. As suggested earlier it is likely that the more piezo-resistive 2nd semi-circle was caused by the CNT strands and the 1st semi-circle by the clusters. It is somewhat fortunate that the results from Fig.6.11 has shown that the degree of interference by the CNT clusters are negligiably small. Having discussed the above it is therefore of utmost importance that the results seen in Fig.6.10 (second semi-circle, composite impedance) that contains information regarding the piezo-resistivity of the composite is discussed. Four key findings could be deduced from the graph: piezo-resistivity, position of percolation, hysteresis and the direction of the piezo-resistivity. First of all Fig.6.10 has shown that it is in fact possible to achieve piezo-resistivity from a CNT-PDMS composite with a respectable difference in resistance of 4kΩ to 750kΩ (2 orders of magnitude). Secondly, the percolation threshold where the greatest rate of change in resistance per pressure could be found is in the middle of the normal blood pressure range (80-160mmmHg). This alone is somewhat useful, ideally however one would like this change to be spread across the whole range of interest thus have a wider gradient so one could quantitatively measure the blood pressure. There are several potential methods of achieving this. However, the easiest of all perhaps is to increase the stiffness of the host polymer by increasing the ratio of hardener so that the effect of pressure is moderated and to slightly increase the CNT concentration so the percolation could be achieved at a slightly lower pressure. However CNTs are known for their reinforcement effect when infused into a polymer host[338]. Therefore the addition of extra CNTs alone may suffice. In either case, considering that the percolation threshold is clearly in the middle of the range of interest it is simply a matter of optimisation. A topic of greater interest is hysteresis, as one could see from the impedance of the 2nd compression the composite clearly has a rather long recovery time. This was rather surprising considering PDMS's renowned elasticity[205][206], however one possible explanation to this is the nano-scopic relationship between the CNT and the PDMS. CNTs are known to be substantially stiffer than PDMS[8][207] and when curing PDMS (or any other polymer chains) is known to 'wrap' around

the CNT dendrically[234] caused by the CNTs acting as a seeding site. This in combination with the fact that CNTs have a known reinforcement effect[338] creates a polymer 'pill' with a CNT core[234]. It is therefore possible that even though the bulk of the PDMS has sprung true to its original shape immediately, locally the CNT reinforced PDMS may be recovering at a slower pace caused by the slow untangling of the dendritic polymer strands around the CNTs. However the verification study where the sample that has been left untouched for several days before re-measurement has shown that the sample does eventually revert to its original resistance (98.96% recovery). Permanent damage however has been observed where the new resting resistance post compression was found to be 12kΩ as opposed to 4kΩ of the non-compressed sample. This could be explained by the state of CNTs post-compression. Although CNTs are known for their extraordinary strengths[8], fundamentally they are a nano-scopic particle that consists of a small number of atoms that could break under moderate force[339]. The most typical failure mechanism undergone by a multi-walled CNT such as the one used in this investigation is what is colloquially known as a 'sword-in-sheath' failure where the outer shell of the CNT is compromised first with the inner layer that has remained intact sliding out[339] although simple fractures are also to be expected under the same conditions[340]. Wagner *et al.* for example found soft polymers hosts such as polyurethane to be able to fragment the stiff CNTs[340] suggesting the possibility of PDMS doing the same. Since CNT based percolation relies on the large aspect ratio of the CNTs the very situation where CNTs are being fragmented most likely will lead to some degree of permanent increase in composite resistance due to the filler's shorter profile[341]. This may however be of little issue in practice due to homeostasis, as blood pressure has a tendency to remain the same and does not generally swing from one extreme to another, thus under normal operating conditions, hysteresis is not likely to present too much of an issue due to its limited need for recovery. After all, the main purpose of the device is to measure the blood pressure quantitatively under normal blood pressure and automatically alert medical staff when the blood pressure exceed critical

point (heart failure). Beyond this, such as when the patient is in the Intensive Care Unit (ICU), other invasive, staffed methods, such as Invasive Arterial Blood Pressure (IAP) measurements[342] and oscillometry[342] is preferred. Lastly and perhaps most interestingly the direction of percolation has reversed. Previously with the likes of 2D compression the resistance decreased upon increase in pressure where the resistance most likely decreased as a result of the conductive CNTs coming closer together increasing the probability of forming a greater number of conduction paths. For the 3D compression however the resistance increase was observed upon increase in pressure. Verification test has also allowed one to rule out the possibility of CNTs breaking under the stress causing their aspect ratio to decrease which in turn increase the resistance as the composite has made a 98.86% recovery. This implies that no significant permanent damage (such as the shortening of the CNTs) has taken place. One explanation to this unexpected increase in resistance with pressure is the dimension of the samples in comparison to the CNTs (diameter: 110-170nm, length: 5-9μm). Unlike 2D compression samples where the sample was confined a thickness of 200μm, 3D compression samples had 4mm. A thickness difference of 3 order of magnitude. This most likely has resulted in the composite being able to 'stretch' when the pressure was applied causing the CNTs to separate (Fig.6.12a) increasing the composite resistance, whereas for a 2D compression sample, due to the 200μm thickness being similar to that of the CNTs' dimensions resulting in them coming closer together (Fig.6.12b). One explanation to this unexpected finding of increasing resistance with pressure is the direction of the pressure applied. Although it is not as directional as the 2D pressure bolt, the sphygmomanometer is ultimately a tube applying pressure to the sample cylindrically, applying pressure from the x and y direction. Due to the presence of the ballistic gelatine and the wide pressure cuff of the sphygmomanometer it is expected that at least some of the pressure is exerted in the z direction. In comparison to the x and y direction, z direction will always experience less pressure, leading to pressure escaping in the z direction causing the sample to expand, increasing the distance in between the CNT fillers.

The distance increase caused in this manner may be nominal but considering that at percolation much of the conduction is dependant on quantum tunnelling[219] that has an exponential relationship with resistance[219]. A resistance change of 4kΩ to 750k is quite possible if not likely.

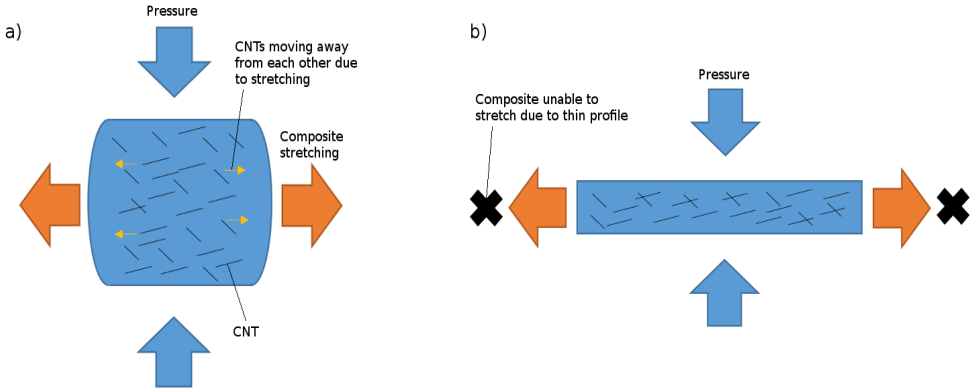

Figure 6.12: a)(left) 3D compression of CNT-PDMS sample. Although the sphygmomanometer set up is designed to cover as much compression angle as possible. Due to the openings at both ends, pressure on the sample could experience less pressure than the other areas, resulting in the stretching of the sample, causing CNTs to separate reducing composite resistance. b)(right) 2D compression of CNT-PDMS where the thin sample profile (200μm) comparable to the filler diameter inhibits the influence of stretching, limiting the CNT separation and in turn limit the increase in composite resistance.

For future works it is therefore worth investigating the pressure response in a true 3D pressure setting. Preferably in an *in vivo* setting as one of the most apparent limitation of this study was the lack of a close enough flesh analogue. Although ballistic gelatine is an established alternative, it lacks the muscle fibres and bone structures that are likely to have some influence on the pressure applied. Moreover it lacks the true 3D pressure exerted from the blood. Having established grounds that 200μm CNT-PDMS composite hosts enough CNTs to exhibit piezoresistivity, it is perhaps best to fabricate a 200μm diameter CNT-PDMS microsphere adapting the drop-precipitation method used by Chai *et al.*[343] and carry out a true 3D compression test using a pressure chamber followed by animal testing.

6.5 Conclusion

In conclusion this investigation has successfully demonstrated the piezo-resistive nature of CNT-PDMS within the normal blood pressure range of an average adult human. From a 10wt% CNT-PDMS sample one was able to obtain a resistance difference of $10^9\Omega$ to $10^5\Omega$ before and after compression respectively for 2D and 4kΩ to 750kΩ before and after compression respectively for 3D. The resistance difference is likely to be able to achieve quantitative blood pressure measurement. Although both 2D and 3D compressions showed signs of piezo-resistivity the composite resistance decreased upon 2D compression, most likely due to the increased proximity of the conductive CNT fillers. In contrast, composite resistance increased upon 3D compression due to the increased separation of the CNTs caused by the sample stretching. Suggestions for future works includes the development of $200\mu m^3$ samples where one could investigate the piezo-resistivity from a device that is of a closer dimension to the final product in a pressure chamber or *in vivo*, as well as minor adjustments including the increased CNT content and hardener ratio.

Chapter 7

BAE Neutron Detectors

7.1 Introduction

Current generation neutron detectors used in nuclear reactors are heavily reliant on the exorbitantly expensive helium-3[344][167]. Post 9/11 attack on the US, price of helium-3 has seen substantial inflation for national security purposes leaving a severe disparity in supply and demand[344][167]. The preferred alternative silicon is however prone to radiation damage with a limited lifespan[345]. This leaves no alternative to the expensive helium-3 and radiation vulnerable silicon suitable for neutron detection in a nuclear submarine, where the detector is expected to be operational for 25+ years. Here we show a working: radiation hard, affordable and γ-ray transparent diamond neutron detector used on board a nuclear submarine, HMS Artful. A submarine currently in service with the Royal Navy (UK). The findings have shown that diamond films of previously unavailable surface area (7.2mm^2), low profile (50μm) and purity was able to successfully demonstrate neutron detection, sizeably exceeding conventional dimensions by 134%[147] and quality allowing greater neutron capture surface area enhancing neutron counts whilst maintaining γ-ray transparency and long charge carrier mean free path for efficient signal collection. This research has demonstrated the potential of a large surface diamond neutron sensor that rivals that of other substantially less radiation hard solid-state neutron detectors such as

silicon. The device has a plethora of applications in military, civil and medical environments where neutron detection is required. Some examples include: condensed matter neutron scattering[346], neutron microscopy; neutron/gamma ray tomography[347], Prompt Gamma Neutron Activation Analysis (PGNAA) on subterranean rock analysis[348], Neutron Activation Analysis (NAA) on nuclear reactor samples[349], light nuclei detection (neutron probe) for soil water content analysis[350], cancer treatment (boron capture)[351], counter terrorism[167] and post nuclear disaster relief such as Chernobyl and Fukushima.

7.2 Procedure, Results and Discussion

Current generation neutron detectors consists of three components: the conversion layer that converts the neutrons into a more easily detectable form of radiation; α-particle, the detection medium (diamond) that allows the said α-particle to deposits its energy to form charge bearing electron-hole pairs and the charge collector (contacts) that detects the charge from the said electron-hole pairs. For this investigation LiF, a material with a high neutron cross section[169] that is known to convert neutrons into α-particles has been used as the conversion layer[352]. The contacts used comprised of 25nm titanium, 50nm chromium and 500nm aluminium from the diamond surface respectively. Lighter metals were specifically chose over other common contact metals such as gold in order to avoid the radioactivation issue associated with heavier metals[169][168]. Titanium in particular was chosen as the immediate interface metal due to its ability to form a robust TiC bond with the diamond surface, while chromium was chosen as an adhesive layer to bind the aluminium bulk that constitutes the majority of the contact and titanium together. The detection layer, diamond of 7.2mm$\times$7.2mm$\times$50μm has been used, an area 134% larger than the currently used as standard for neutron detectors of 4.7mm$\times$4.7mm$\times$0.5mm[147]. Traditionally most diamond films of this size has been reserved for the multifaceted polycrystalline diamond (PCD) due to its technical challenges in the large area growth process. However recent

development in growth technology has enabled the use of a large area single crystalline diamond (SCD). Since PCD suffers from a low charge carrier mean free path due to the presence of grain boundaries[84][85] that often results in poor signal detection efficiency[173], the use of SCD of its purest grade (known as IIa) was considered to be imperative. In addition a diamond film as thin as 50μm has been used in this investigation in order to achieve γ-ray transparency[55]. This will prevent false positive counts generated by the γ-rays that are often mistaken for neutron counts. Naturally, to ensure the diamond film is in fact capable of γ-discrimination its thickness as well as its crystallinity, absence of surface contaminants and defects have been examined.

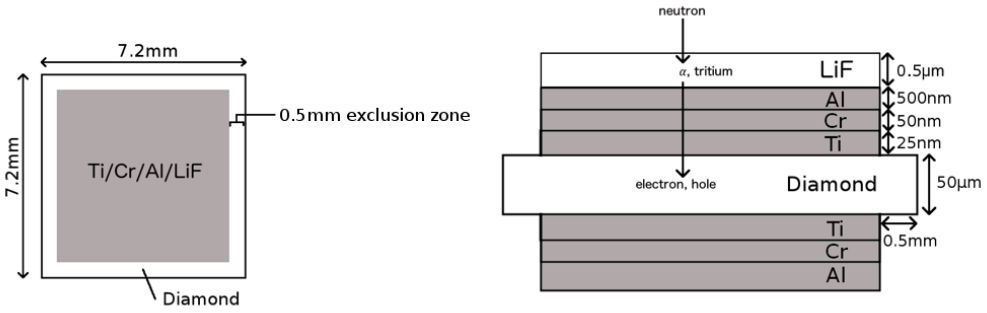

Figure 7.1: Diamond neutron detector post inspection, metallisation and LiF deposition.

A bulk diamond sample was first laser sliced and polished into six 50μm films (outsourced to DDK Inc., US). The films were then solvent rinsed in isopropanol and acetone respectively to remove contaminants such as grease and dust. The samples were then deep cleaned through strong oxidation in hot, saturated and concentrated sulphuric acid (acid bath). This process is designed to remove any graphitic carbon (sp^2) contamination formed during the laser slicing process as well as remove any residual contaminants that were unable to be removed by the solvent rinse.

The cleaned samples were then examined for surface defects. The film surfaces were inspected under optical microscopy ($\times$5, $\times$10, $\times$20 and $\times$50). Any visible surface defects found such as pits and hairline fractures were inspected under a

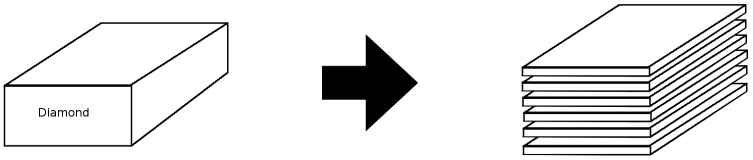

Figure 7.2: Thinning of a single SCD diamond into six 50μm thick diamond films.

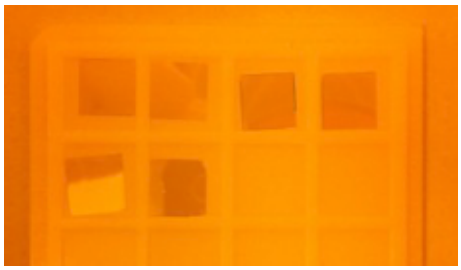

Figure 7.3: Six single crystalline diamond film samples.

surface profiler to identify whether they could cause cross surface short-circuiting that will annul the signal detection. Results have shown that even the deepest of pits found were <7% of the total thickness implying the likely absence of short-circuiting. The bowing (difference in height from the peak of the sample to the edge) has also been measured in order to ensure that the films have not been excessively polished, to the extent that quantum tunneling could occur through the thinned edges. Surface profiling results have shown that the bowing was limited to <10% of the total height per side ruling out the possibility of cross surface short-circuiting. Short circuiting has also been examined electrically across the top and bottom contacts through the diamond film using a 2 point IV measurement system where no signs of short circuiting were found. The average thickness of the films were determined to be 49.25μm by measuring across 4 times in the x-direction and 4 times in the y-direction per sample, a thickness generally accepted to be γ-ray transparent[55].

Figure 7.4: Surface defect (pit) under optical microscopy.

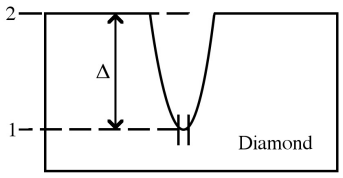

Figure 7.5: The measurement of the most noticeable crevasse (the largest of its kind under an optical microscope). 2=3.500μm, 1=0.029μm and Δ=3.471μm, 7% of the total thickness of the sample.

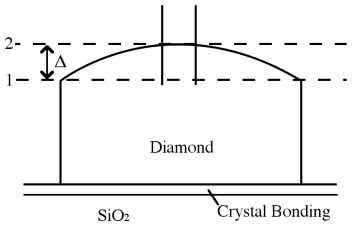

Figure 7.6: The bowing of the diamond film and the calculation of its height. 2=55.2μm, 1=49.5μm and Δ=5.7μm.

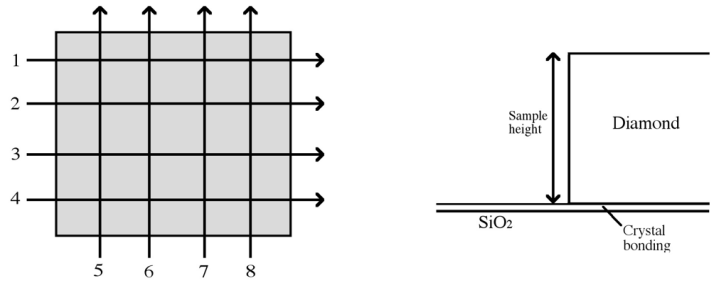

Figure 7.7: (Left), Surface profiler track number over the diamond sample (bird's eye view); (Right), Sample height measurement process (landscape view).

The scans have shown that the samples have a tendency to bow in the middle as illustrated by Table.7.1.

Track No.	1	2	3	4	5	6	7	8
Average sample height	46μm	50μm	51μm	51μm	50μm	50μm	49μm	47μm

Table 7.1: The variation in the average height of the sample with its respective track number.

Once the results have shown the film to be free of cross-surface conduction the purity of the samples were examined through Raman spectroscopy. By carrying out Raman spectroscopy on the diamond film one could identify the presence of any foreign elements and non sp^3 (diamond) carbon bonds. As one could see from Fig.7.8 the two prominent peaks present were that of 520.11cm^{-1} from the silicon support substrate[353] and 1333.33cm^{-1} from the diamond[290]. Control scan has revealed that smaller peaks flanking the 1333.33cm^{-1} peaks are that of the water soluble temporary adhesive used to bind the silicon substrate and the diamond film (Fig.7.9).

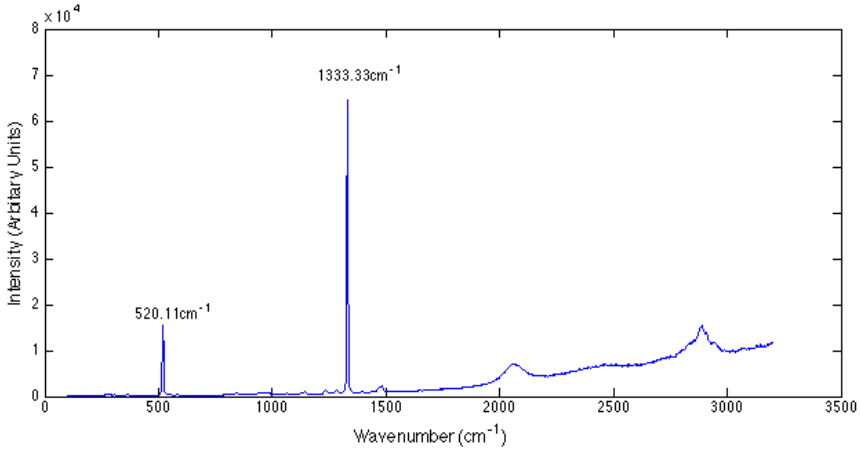

Figure 7.8: Raman spectrum of the diamond film mounted on silicon substrate with crystal bonding showing two prominent peaks at 520.11cm^{-1} and 1333.33cm^{-1} corresponding to the silicon substrate and the diamond sample respectively.

From the absence of the graphite peak at 1575cm^{-1}[291] and any other notable peaks one could confirm that the diamond film consisted solely of pure diamond. The peaks at 2100cm^{-1} and 2900cm^{-1} corresponds to carbyn[354] and C-H bonds[355] respectively that originates from the surface that is unlikely to influence the characteristic of the bulk. Another feature that one could deduce from

the Raman scan is its cystallinity. It is known that the full width half maximum (FWHM) of the diamond peak of a SCD is 2-4cm^{-1}[293][294] whilst PCD such as micro and nano-crystalline diamond has a FWHM of 8cm^{-1}[295] and 24cm^{-1}[295] respectively. The FWHM of the diamond film used in this investigation was 6.514cm^{-1} falling slightly on the larger side of the SCD. However this may be due to the surface roughness of the film that is known to introduce multiple surface states that results in the broadening of the Raman peak implying the possibility of the bulk of the diamond being highly crystalline. For confirmation an atomic force microscopy (AFM) scan has been carried out to measure the surface roughness. As one could see from Fig.7.10a the surface of the diamond film was extremely rough in comparison to the pristine bulk diamond sample (Fig.7.10b). Calculation of the root mean square roughness value has shown that the roughness of the diamond sample surfaces (calculated using Eq.7.1) ranged from 0.60-10.4nm with an average of 4.91±3.02nm.

$$\text{Root mean square roughness} = \sqrt{\frac{\Sigma Z_i^2}{N}} \tag{7.1}$$

Z is the height of a point on an AFM image and N the number of points taken.

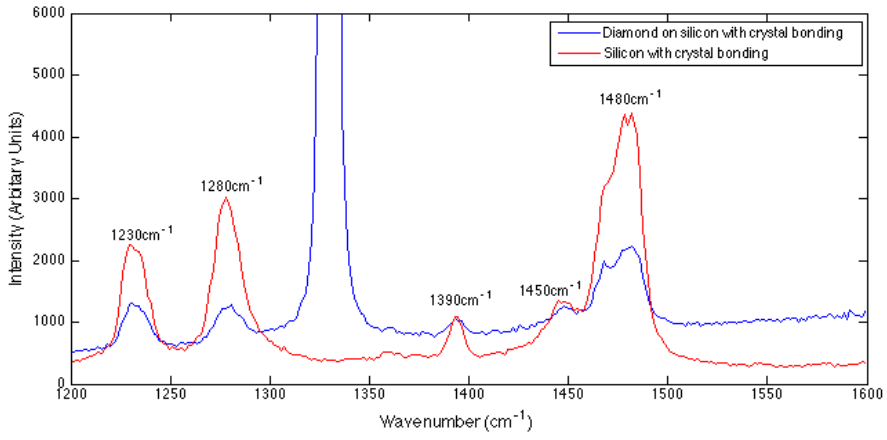

Figure 7.9: Raman spectrum of the diamond film on silicon and silicon with crystal bonding. The minor peaks position align with that of the crystal bonding indicating that the peaks do not originate from the diamond itself.

FWHM	Author	Sample type	Grain size
6.5140cm^{-1}	BAE	SCD	N/A
2cm^{-1}	Muchnikov *et al.*	Homoepitaxial Single Crystalline Diamond (SCD)	N/A
4cm^{-1}	Dong *et al.*	Homoepitaxial Single Crystalline Diamond (SCD)	N/A
8cm^{-1}	Luong *et al.*	Micro crystalline diamond (MCD)	1600nm
24cm^{-1}	Luong *et al.*	Nano crystalline diamond (NCD)	40nm

Table 7.2: The FWHM value of the 1333.33cm^{-1} diamond peaks from this study and diamond samples of similar research and different crystallinity[293][294][295].

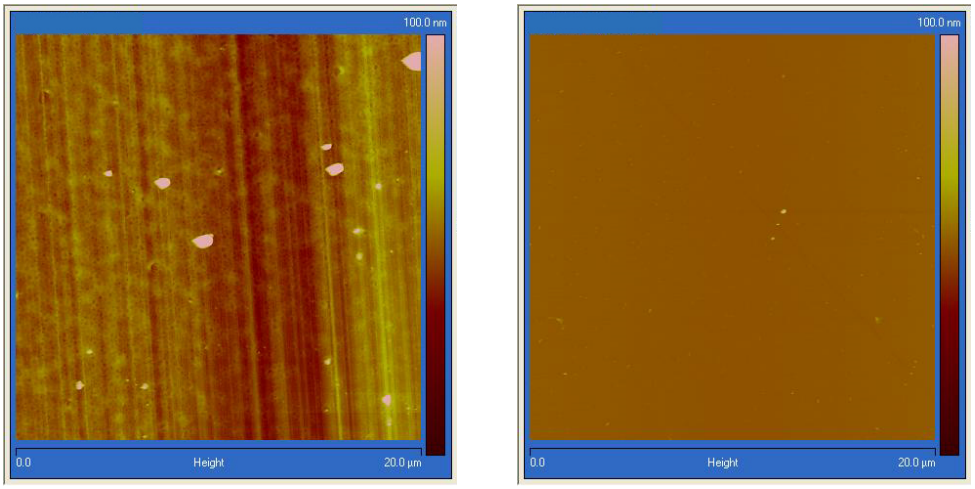

(a) (b)

Figure 7.10: AFM image of: (a) the roughest diamond sample (roughness: 10.4nm) and (b) the smoothest diamond sample (roughness: 0.60nm).

Following the inconclusive analysis into crystallinity. Further investigation has been carried out through impedance spectroscopy. It is known that grain boundaries seen in PCD manifests as small semi-circles in the Cole-Cole plot[300]. One can see from Fig.7.11 only a single semi-circle was observed indicating the single crystalline nature of the diamond film. Having two agreeing cross examination results one could safely assume that the diamond film is in fact a SCD that is free of any charge carrier scattering facets.

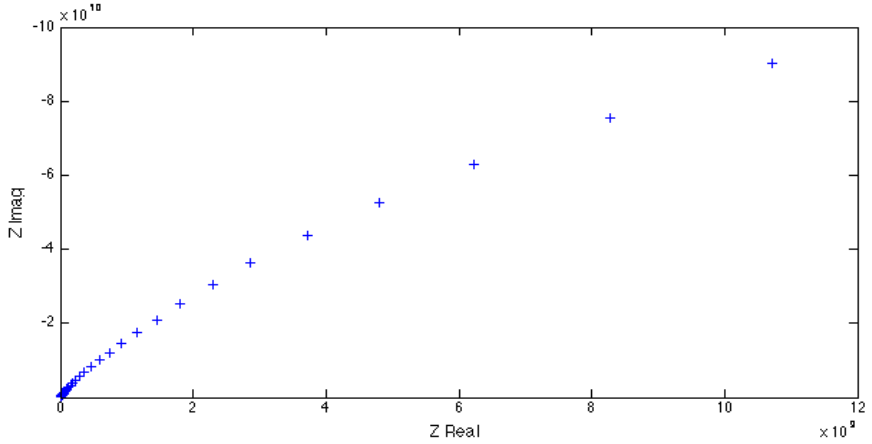

Figure 7.11: Cole-Cole plot of the diamond sample.

Once the quality of the diamond has been deemed satisfactory, metallisation (sputtering) of the contacts has been carried out. A 0.5mm exclusion zone has been masked off to prevent short-circuiting across the edges of the sample, where 25nm of titanium, 50nm of chromium and 500nm of aluminium has been sequentially sputtered. Following mask removal and annealing in hydrogen to improve contact adhesion the thickness of the contacts were examined, the logic being if excessive amount of contacts were to be deposited it risks metal to α-particle interaction reducing the detection counts. Surface profiling has shown that the average thickness of the contacts were 570.28±16.47nm, ±5% of the expected 575nm (Table.7.3). The contacts were then further examined by a 4-point probe for its electrical resistivity and sheet resistance which were determined to be $(91.33\pm0.18)\times10^{-6}\Omega$cm and 0.125±0.0155Ω/SQ respectively. These were found to be in line with values found by Panta *et al.* (electric resistivity: $31\sim69\times10^{-6}\Omega$cm, sheet resistance: 1.39∼5.62Ω/SQ)[356] who measured a pristine sheet of defect free aluminium. Therefore from this, one could conclude that the contacts were in fact pure and largely defect free, thus deemed suitable for obtaining reliable radiation detection data.

The radiation detection test itself has been carried out in two stages: firstly through α-particles/γ-ray detection test to identify the capabilities of the device to capture and detect the α-particles as well as discriminate γ-rays that could be

	Thickness (nm)	Electrical resistivity (Ωcm)	Sheet resistance (Ω/SQ)
Sample 1	588.3, 586.5	91.6×10^{-6}, 91.2×10^{-6}	0.1251, 0.1250
Sample 2	546.3, 564.9	91.2×10^{-6}, 91.6×10^{-6}	0.1250, 0.1254
Sample 3	559.1, 576.6	91.5×10^{-6}, 91.3×10^{-6}	0.1251, 0.1250
Average	570.28±16.47	$91.33\pm0.175\times10^{-6}$	0.1251±0.0155

Table 7.3: Thickness, electrical resistivity and sheet resistance of the contacts (side a and side b respectively).

erroneously counted as an alpha count. This test will allow for the verification of whether the device is in fact capable of detecting the α-particles that is produced by the neutron to α conversion process of the LiF conversion layer. This test is then followed by the LiF deposition process to prepare the device for neutron capture. Once complete, the detectors were exposed to neutrons to identify its capabilities of detecting the α-particles produced by the LiF layer.

As seen from the graphs below the α-tests has shown that all three of the detectors were in fact capable of detecting α-particles. Most notably each detectors had a large enough Q-factor (conventionally defined as the energy of radioactive decay products in nuclear physics) where in this case its importance lies with the separation between the signal peak that resides between 0-40 channels and the α-peak allowing clear determination of the number of incoming α-particles. It is also worth noting that there were no signs of γ-rays as seen from the absence of its detection peak (Fig.7.12) suggesting successful γ discrimination. As a general trend, of the 50V, 150V and 200V bias applied, the 200V detection had the tendency to have the greatest peak channel number thus indicating that the electron/hole pair collected were more numerous suggesting its greater collection efficiency. This most likely was due to the fact that with greater bias comes greater probability of charge carriers to be able to tunnel through defects in a diamond layer resulting in a successful count. Overall by comparing the three devices at 200V(Fig.7.12) one could see that detector 1 had the greatest collection efficiency, most probably due to the fact that one of its sides were the highly-polished surface that was not laser cut resulting in a reduced number of

charge scattering surface states. For future works to improve on the collection efficiency it may be a sensible option to flatten the surface by using methods such as Reactive Ion Etching (RIE) or mild CVD growth in order to reduce the said number of surface states. Of the three devices fabricated the best performing detector (detector 1) was used for neutron detection testing. Once the α-particle detection has been successfully carried out it is common practice to convert them into charge collection efficiencies and radiation energies by carrying out a calibration test using a near perfect detector. Although for national security reasons the exact energies and thus in turn its collection efficiencies from the nuclear submarine cannot be presented (as one could use the collection efficiency to calculate the exact energy spectrum of the source) in addition to the fact that the 'on-land' calibration data was not collected in order to meet the submarine's launch date. It is however within agreed boundaries to compare the obtained data to similar research. In fact the samples used by Bergonzo *et al.* is a near exact replica both in quality and dimension (single crystalline CVD diamond of 25μm). This could evidently be seen through the similarities in the signal profiles (Fig.7.16, CVD(CEA)(25μm))[173][357], where they have calculated the collection efficiency to range between 20%-80% with its peak at 40%[173][357]. From this one could calculate their spectrum to range between 1.1MeV-4.4MeV with 2.2MeV as its peak[173][357]. Naturally, considering its near identical fabrication process and sample dimension, it is likely that the energy range and charge collection efficiency will be in a similar ballpark. A particularly interesting comparison one could invite is with the commercially available type IIa diamond and commercial detector grade CVD diamond (Fig.7.16). In comparison to the signals obtained from the above two, the results seen from CVD(CEA) Fig.7.16 (and by association results from this investigation, Fig.7.12) clearly has a significantly greater collection efficiency, suggesting reliable α-detection properties.

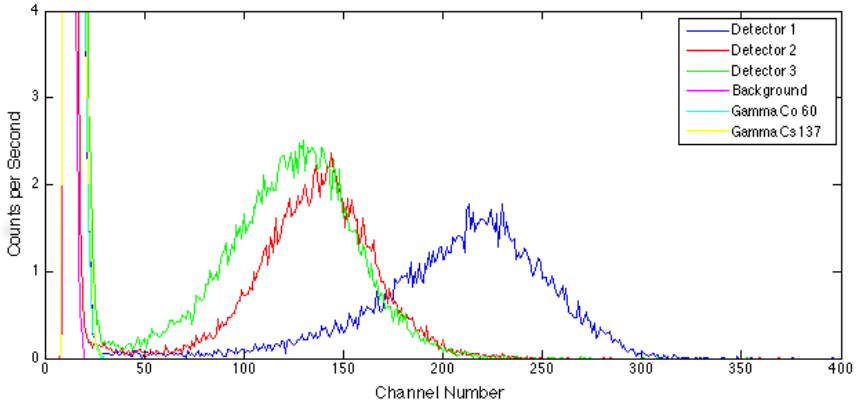

Figure 7.12: α-particle and γ-ray detection by detectors 1,2 and 3 under 200V bias.

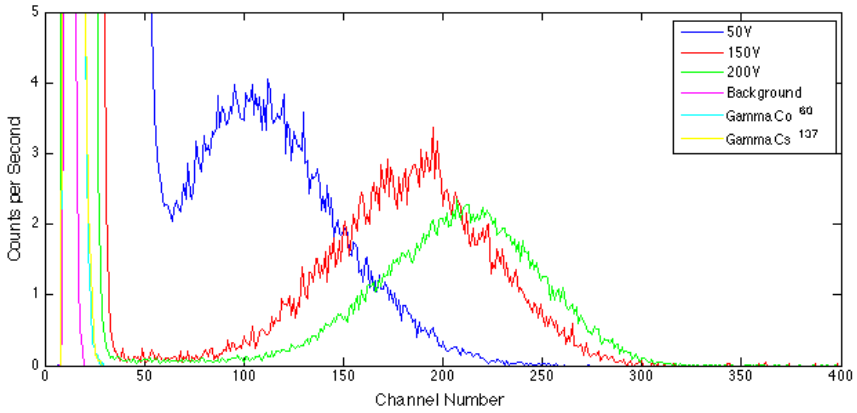

Figure 7.13: α-particle and γ-ray detection by detector 1 under 50V, 150V and 200V bias.

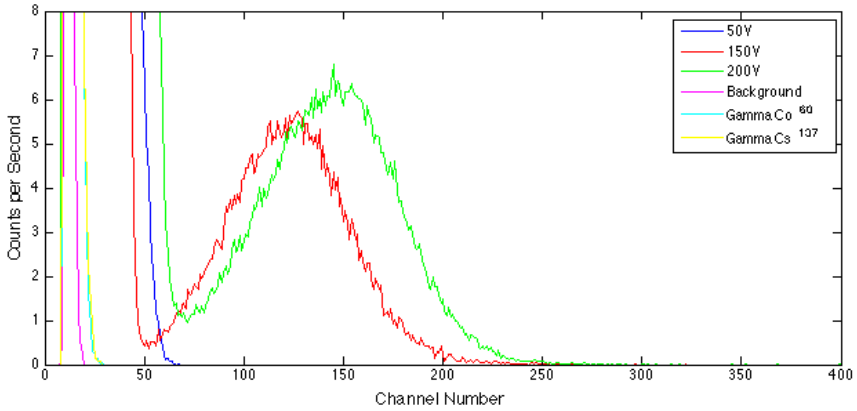

Figure 7.14: α-particle and γ-ray detection by detector 2 under 50V, 150V and 200V bias.

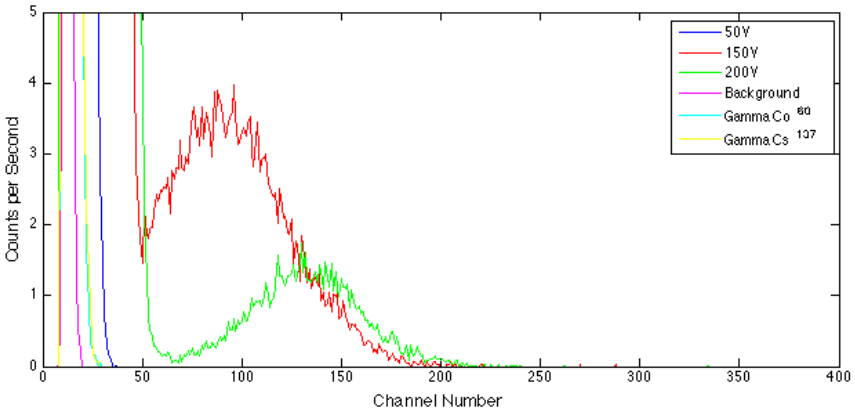

Figure 7.15: α-particle and γ-ray detection by detector 3 under 50V, 150V and 200V bias.

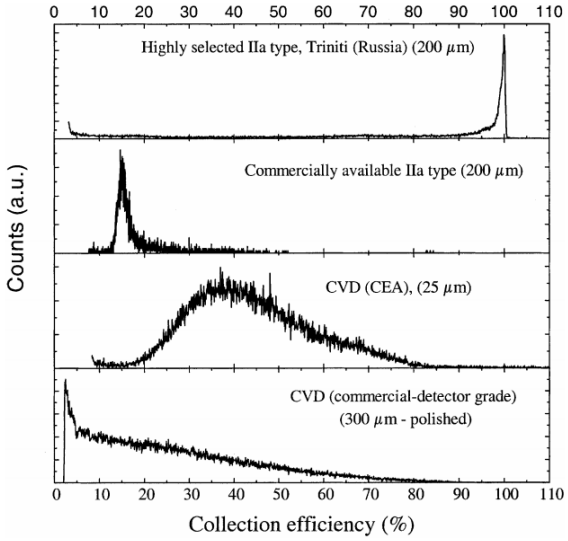

Figure 7.16: Am-241 alpha detection spectrum: (from top to bottom) a near perfect highly selected IIa diamond, commercially available natural IIa diamond, CVD diamond by CEA (the closest equivalent to this investigation) and a commercially available CVD diamond.

Although one is unable to present the charge collection efficiency, from the number of counts detected one could determine the device efficiency. This could be determined by calculating the radiative α-particle loss and the absorption by the medium it travels in and comparing the number of counts detected against the number of incident α-particles. The former determines the actual number of α-particle that reached the detector by accounting for the radiative loss and

the latter determines the number of α-particle lost to absorption. The former could be calculated through geometric calculations following the inverse square law and the solid angle the detector occupies using Eq.3.4 and Eq.3.6. The issue of absorption could be assumed to be negligible due to α-particle's ability to maintain its intensity with distance until its terminal range[161]. α-particles of 5.3MeV are known to travel 38.4mm [162] a distance that comfortably covers the 6.5mm source to detector separation used in this investigation. Based on the calculations outlined above the device efficiency for α-particles was determined to be 32.2%.

Once the alpha detection capabilities have been confirmed all three detectors were coated with a LiF conversion layer. Out of these, the best performing detector (detector 1) was tested for its neutron detection capabilities, leaving the other two as spares. The detector was mounted on a modified α-particle testing kit where the detector was placed away from the source in a neutron moderating Bonner sphere. This equipment will allow for the scattering of neutrons towards the detector it houses to increase the area of neutron detection. The neutron source used was a Am/Be-241 source with peak energies of 3.5MeV and 5.0MeV where the Bonner sphere of 8inch in diameter was used to allow for optimal neutron detection with a detection rate of 80%[161]. As seen from Fig.7.17 the detector has successfully detected the incoming neutrons both with and without the Bonner sphere, where the data taken without the Bonner sphere clearly show the 3.5MeV and 5.0MeV peaks. The data taken with the Bonner sphere on the other hand show a clear single detection peak of the moderated neutrons suggesting its successful moderation process. As well as having sufficient clearance from the signal peak allowing an accurate count of the incoming neutrons. However it is important to remember that the said single peak constitutes of 2 overlapping peaks (α peaks at 2.07MeV and tritium peaks at 2.73MeV[150][61]). Studies by Almaviva *et al.* and Sussmann *et al.* have found that the detection spectrum of neutrons contains both α peaks and tritium peaks. However, they have also found that with increasing thickness of the LiF conversion layer the two peaks becomes

merged due to peak broadening caused by the energy of the decay product being absorbed by the LiF layer[150][61] which α is known to be particularly prone to[150][61] (although the neutron to α/tritium count ratio remain to be 1:1 as the α and tritium separates orthogonally after interaction). Since the objective of this investigation is to fabricate a neutron detector for a nuclear submarine that is planned to be operational for 25+ years the thickness of LiF and hence the longevity of the conversion layer was prioritised over peak resolution resulting in the merging of the peaks. Given time was not a factor the experiment could be run for longer to allow for the two peaks to emerge. However for this particular investigation the determination of which decay product was being detected is not of any interest as one is interested in the dosage and thus the number of incoming neutrons.

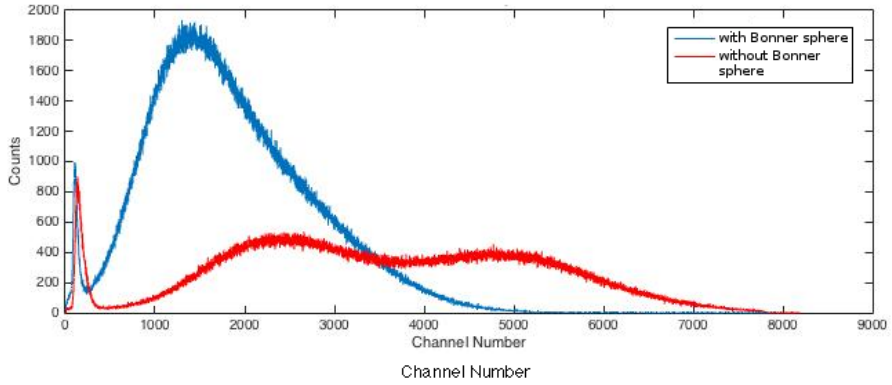

Figure 7.17: Neutron detection by detector 1 of Am/Be-241 source of peak energy 3.5MeV and 5.0MeV with and without Bonner sphere.

The calibration of channel numbers to charge collection efficiency and energy were not permitted for security and launch schedule reasons. However it is within acceptable boundaries for one to calculate the device efficiency which could be calculated using Eq.3.4 and Eq.3.5. It is worth noting that the area of projection (which in the previous calculation for α-particles was the size of the detector) is now the size of the Bonner sphere as the device allows the scattering of neutrons towards the detector that increases the number of neutrons that the detector interacts with (although one must account for the 20% loss to stray scattering). It

is also worth considering that unlike α-particles, neutron intensities are known to decrease exponentially with absorber depth[161]. However the limited cross-section of neutrons to air (9.8×10^{-24}cm[163]) means that the mean free path of neutrons in air is as long as 18970mm[163][161]. Therefore, over the source to detector distance of 457mm the neutron absorption was considered to be negligible. Taking into account the points mentioned above the device efficiency to neutrons was found to be 48.3%. The likely cause of improvement from the 32.2% seen from α-particle efficiency is believed to be from the fact that the Bonner sphere has a pan-directional scattering[161] that allows for detection not only from the front surface but also from the back of the detector increasing the capture surface.

7.3 Experimental Methods

Acid Bath - Diamond sample surfaces were cleaned of surface contaminants through oxidation by using 30ml conc. sulphuric acid (H_2SO_4, >95% pure) saturated with 10g ammonium persulphate ($[NH_4]_2S_2O_8$, 99.2% assay) to increase its oxidation capability. The acid mixture was heated to 200°C on a hotplate and the diamond sample was added. The diamond sample was then heated for 30min and washed in a neutralisation solution mixture of 10ml hydrogen peroxide (H_2O_2, 50wt%) and 10ml ammonium hydroxide (NH_4OH, 50% v/v) for 10min. The sample was then further rinsed in de-ionised water followed by blow-drying using a nitrogen gun and annealed at 200°C for 30min to dehydrate the sample.

Raman spectroscopy - Acid cleaned diamond sample was mounted on a silicon wafer using a water-soluble crystal bond before undergoing the scan. The silicon substrate was placed on a heater at 70°C, the crystal bond was applied and the diamond sample was placed on top of it. The bonded sample was cooled in air before being loaded into the measurement chamber. The scan was carried out over 100-3200cm^{-1} with: 1% laser power, 514nm laser, 1800line/mm grating, 50s^{-1} exposure time, 3 accumulation and with cosmic ray removal. The above range is designed to cover the expected silicon, sp^3 carbon (diamond) and sp^2 carbon

(graphite) peaks at 520.11cm^{-1}, 1330-1360cm^{-1} and 1550-1580cm^{-1} respectively.

Impedance spectroscopy - Impedance measurements were performed using a two-point probe system where the impedance of the diamond sample both across the top and bottom surfaces were measured. A frequency scan was carried out between 0.1Hz and 1GHz at a sampling voltage of 0.1V. The Randles equivalent circuit (one real resistor, one imaginary resistor and one imaginary capacitor) Cole-Cole plot fitting model was used to determine the presence of grain boundaries.

Sputtering contact metallisation - 0.5mm perimeter exclusion zone of the diamond sample was masked off using cleanroom tapes (Fig.7.18).

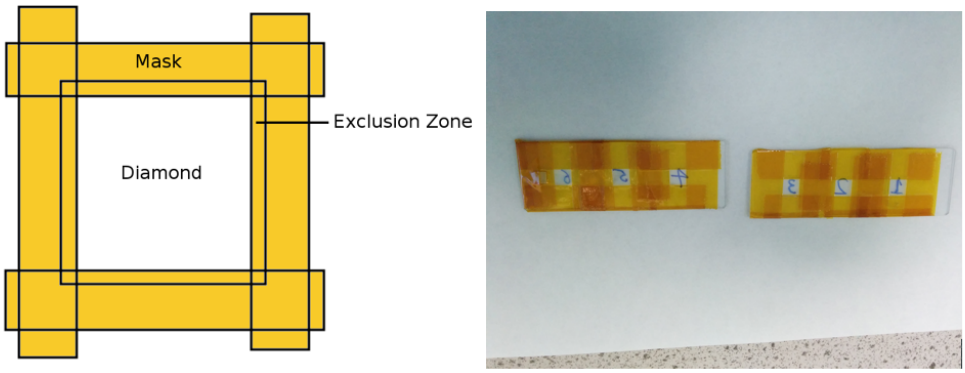

Figure 7.18: Masking process of the diamond sample using clean room tapes. (Left): Illustration of the masked diamond sample. (Right): Masked diamond samples pre-metallisation.

Pre-deposition sputtering system chamber pressure was set to $<1.6\times10^{-6}$mBar. Ti, Cr and Al metallisation targets were sequentially exposed to argon plasma maintained by: the flow rate of 10SCCM; power, 150W; current, 0.40A; voltage, 372V in the net chamber pressure with argon of 3.0×10^{-3}mBar. 25nm of Ti, 50nm of Cr and 500nm of Al was deposited at the rate of 3.19nm/min, 9.57nm/min and 12.60nm/min respectively. Transitions between metallisation targets were given a 5min buffer to remove the surface layer of the source metal targets to avoid contamination. Upon completion the mask was removed by acetone rinsing.

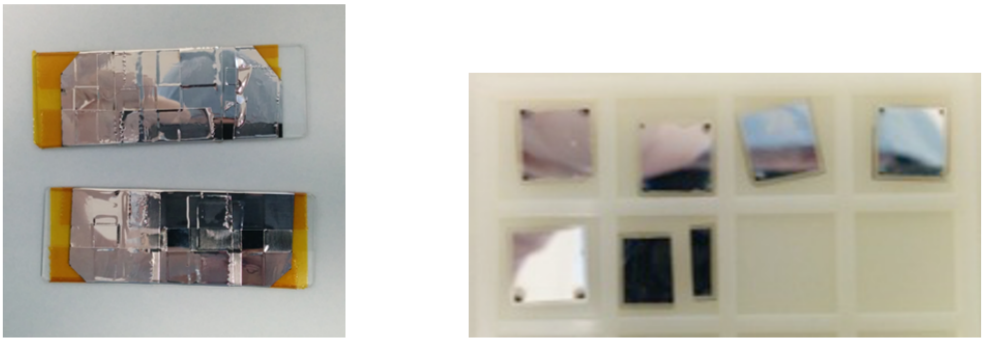

Figure 7.19: (Left): Diamond sample post-contact metallisation, (Right): Diamond samples post-mask removal.

Annealing - Post-metallisation annealing was carried out in order to improve amalgamation between the contact layers and to encourage the diamond surface to form a robust TiC bond. The samples were placed on a hotplate in a vacuum chamber of pressure 2×10^{-3}mBar in the presence of hydrogen gas at 155SCCM (net pressure with hydrogen, 20Torr) and heated to 400°C for 3hrs.

Alpha/Gamma-testing - The metallised diamond was connected to a pre-amplifier where a bias of 50V, 150V and 200V was applied across the diamond, where 200V was the maximum available voltage of the instrument. Upon exposure to an α-source (americium-241, activity: 392kBq, decay peak energy: 5.486MeV, source size: 1mm diameter sphere) a signal was generated by the diamond-alpha particle interaction that generates multiple electron-hole pairs. The signal was then amplified and logged by the spectroscopy amplifier and the multi channel analyser with a channel bin of 0-400. The α-radiation source was placed 6.5mm away from the diamond detector in air. Along with the α-radiation, background radiation and γ-radiation from two sources (Co^{60}, activity: 381kBq and Cs^{137}, activity: 422kBq) were examined as control to determine the background count and gamma transparency.

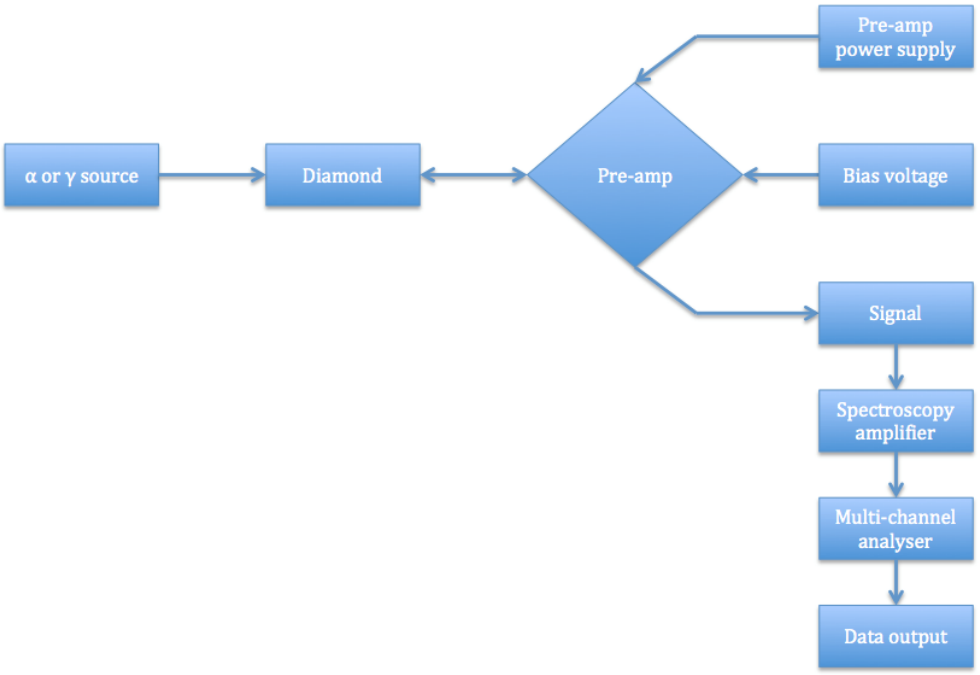

Figure 7.20: α-ray testing setup.

LiF-deposition - 2.8±0.42μm of LiF conversion layer has been deposited on the surface of the diamond sample over the contacts through evaporation. The LiF pellets were first placed in a graphite crucible and melted at 3A joule heating before being deposited at 10A under 10^{-6}Torr base pressure and a crucible to sample distance of approx. 250mm.

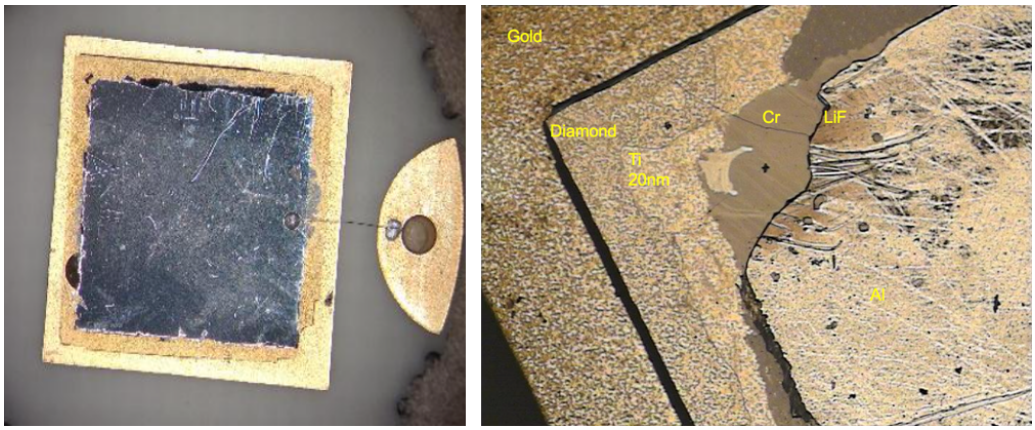

Figure 7.21: (Left) Plan view of the LiF-coated neutron detectors. (Right) angled view of the detector layers.

Neutron testing - In order to test the detector's neutron capabilities the experimental settings of α-testing described above has been modified. The LiF coated diamond detector was placed 457mm away from the Am/Be-241 neutron source (activity: 1.019×10^7neutrons/s, decay peak energy: 3.5MeV and 5.0MeV, source size: 30mm diameter; length: 60mm cylinder, dosage of 646.6μSv/h). This was housed inside an 8inch polyethylene moderation sphere (Bonner sphere) that allows for up to 80% detection of the scattered neutrons from the greater interaction silhouette of the Bonner sphere. The detector was exposed for 23seconds and measured over 0-8200 channels. Measurements were taken with both with and without the Bonner sphere to allow for the identification of the two neutron decay peaks, as well as take the moderated neutron measurements.

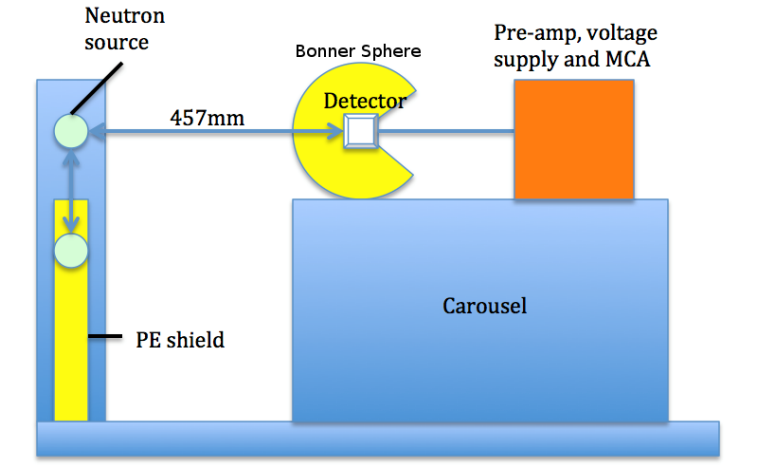

Figure 7.22: Adapted neutron set up. The detector was shielded in a polyethylene (Bonner) sphere that moderates the neutrons. The neutron source was shielded in the polyethylene containment column until measurement. The carousel ushered the detector to 457mm from the source. Neutron counts were measured by the pre-amp, voltage supply and multichannel analyser (MCA) system.

7.4 Conclusion

In conclusion this investigation has successfully fabricated a large area, high purity CVD diamond neutron detectors for a nuclear submarine, that has successfully measured both α-particles and neutrons whilst being γ-ray discriminant allowing

the prevention of false positive neutron counts. As well as calculating its device efficiency (32.3% for α and 48.3% for neutrons) which by knowing the device count and its efficiency together one could determine the number of neutron exposure accurately. Despite its purity, the diamond layer itself did find room for improvements, namely regarding the number of surface states that are most likely caused by the surface roughness. This has resulted in the loss of charge collection efficiencies that also has lead to the broadening of the detection peaks and low Q-factors. For future works therefore either a mild regenerative growth or a light plasma etch process to smooth out the surface is recommended.

Chapter 8

Secondary Electron Emission from Diamonds

8.1 Introduction

The primary objective of this investigation is to further develop the capabilities of a low signal amplifier, namely for photo multipliers in night vision goggles. In night vision goggles, the limited number of photons available are converted into electrons by a scintillator where the converted electrons alone are too weak a signal to be measured. By developing a diamond amplifier with a high gain one could develop night vision goggles with greater signal amplification and in turn greater sensitivity. Benefits to both military and civil applications are to be expected particularly for night time military operations and CCTV cameras. One of the key requirements during the development of the said device is the presence of a strong gain from nano-diamonds (NDs). Most modern night vision amplifiers consists of tightly clustered glass tubes secured in a plate commonly known as a multi-channel plate (MCP). This particular design allows the electrons to bounce within the inner surface of the tube where amplification by the factor of the gain could occur at each cascading generation (refer to Chapter 2, Fig.2.48).

By design the inner surface of the MCP tubes are required to be coated in diamond. The most common practice to achieve this is by seeding the inner

surface of the tube with NDs that has the mobility to access the narrow tubes and for the NDs to then be grown into a film using chemical vapour deposition (CVD). The surface of the ND film will then be terminated with LiO to achieve SEE and in turn signal amplification.

In order to achieve the above, this investigation will be carried out in 5 stages: firstly, the potential of the aforementioned LiO termination will be explored by examining the maximum achievable gain from a H terminated and LiO terminated poly-crystalline diamond(PCD) film on conductive silicon where its large crystal grains allows for greater gains, providing an ideal test-bed to benchmark the achievable performance of the terminations. Secondly, the H and LiO terminated ND films will be examined for SEE to identify the possible gains one could expect when applied to an MCP. Thirdly, in order to determine the origin of any differences in PCD and ND gains, the crystallinity of the films will be examined under a scanning electron microscope (SEM). Fourthly, further testing into heat/electron-bombardment resistance of LiO and H termination will be carried out by examining the gain decay upon electron beam exposure and annealing. Lastly, the effectiveness of the LiO deposition method used during the investigation will be evaluated through X-ray photo-electro spectroscopy (XPS).

8.2 Experimental Methods

Degreasing – Sample rinsing was carried out using a sequential rinse in acetone, isopropanol (IPA) and de-ionised (DI) water respectively to remove surface contaminants. The sample was then dried using a nitrogen blow-gun.

Hydrogen termination/ND growth – Following the sample loading into a vacuum chamber its chamber pressure was decreased to $<10^{-6}$mBar. Hydrogen gas was slowly added until a chamber pressure of 3torr was achieved followed by its microwave plasma ignition. The chamber pressure was then further increased to 40torr through hydrogen flow increase. The sample was exposed to hydrogen plasma for 5min at 700°C. Once the exposure was complete the sample was left to

cool to room temperature in hydrogen. Alternatively by adding methane to the hydrogen gas in a 1:100 mixing ratio respectively after the sample temperature has reached 700°C the same process could also be used to grow the NDs into a film through CVD. At the end of the growth run, a 5min hydrogen plasma exposure was carried out to terminate the surface with hydrogen. This process has the added benefit of removing any sp^2 carbon (graphite) contaminants that forms during growth.

Oxygen termination – A hydrogen terminated sample was loaded into a vacuum chamber and its pressure was pumped down to approximately 10^{-2}mBar. The chamber was then flushed with oxygen 7 times after being filled to 100mBar in order to remove any residual non-oxygen gas. The sample was then annealed at 200°C for 1h to dehydrate the sample surface. This was followed by an ozone (O_3) exposure at 200°C for 30min. Once the exposure is complete the sample was cooled in ozone to room temperature. This process will replace the hydrogen termination on the sample surface with a more energetically stable oxygen termination[129].

Lithium termination – Once the oxygen terminated sample has been loaded into the vacuum chamber the pressure was decreased to $<10^{-7}$mBar. The sample was then annealed at 200°C for 1hr to dehydrate the surface. The sample was then heated to 450°C and exposed to lithium by passing a current through the lithium source (Li getter, SAES), where a total of 1.1mg of lithium was exposed to the sample at a distance of approximately 5cm from the source to the sample. Upon exhaustion of the lithium source the sample was cooled in vacuum to room temperature. Once the sample has reached room temperature the sample was rinsed and left in water for 1hr to react away the excess lithium so that a monolayer of LiO would be left on the surface. Following the rinse, the sample was gently blow-dried using a nitrogen blow-gun. During the preliminary stages of the investigation the effectiveness of rinsing as a lithium removal method was tested by comparing the gain values of a rinsed sample and a sample sonicated in water for 1hr. The results has shown that there is almost no difference to the final

gain values and thus this investigation has employed a less resource consuming rinsing as its excess lithium removal method.

ND seeding – A degreased conductive silicon sample (n-type arsenic doped, Resistivity: 0.001-0.005Ωcm) was added to 0.05g/l ND solution (particulate size: 4.7±0.5nm, NanoCarbon Research Institute Ltd.) and sonicated for 10min. Following the sonication the sample was gently dried using a nitrogen blow-gun.

SEE measurement – A sample was loaded into the vacuum chamber and its chamber pressure was decreased to $<10^{-7}$mBar. Once the desired pressure was reached the sample was annealed at 190°C for 1hr to dehydrate the sample. The electron gun was then set at a beam current of approximately 1.15μA and a beam energy of 700eV. Using the Faraday cup (Fig.8.1) (a device designed to capture the entire electron output from the electron gun) the total beam current, I_B was measured. Once the beam current has been established a bias of -500V has been applied to the sample. Its coulombic repulsion was used to slow down the primary electrons to fine-tune the net beam energy (Fig.8.1)(Eq.8.1). This is defined as:

$$\text{Net beam energy} = \text{Primary electron beam energy} + \text{Sample bias} \tag{8.1}$$

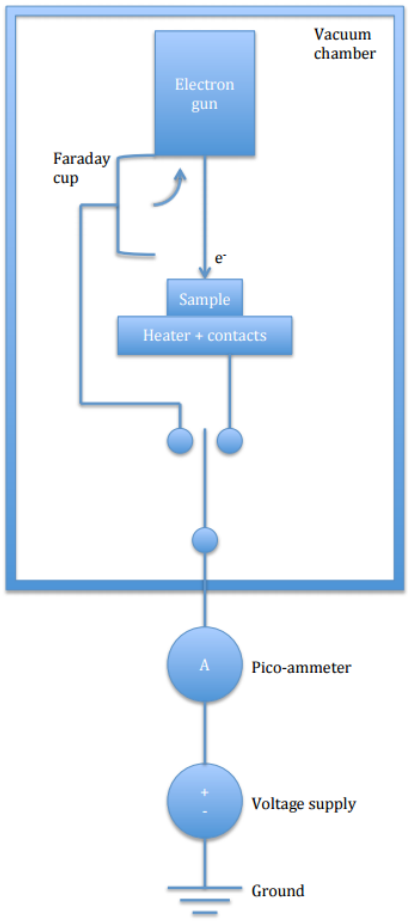

Figure 8.1: Diagram of the SEE measurement set up. The electrons bombarded at the sample from the electron gun was slowed down by the bias applied to the sample by the voltage supply. Primary electrons with the net energy will then impact the sample generating secondary electrons. The sample current (the total measured current after loss of electrons through SEE) will be measured by the pico-ammeter. When measuring the beam current the Faraday cup will cover the ejection port of the electron gun collecting the entirety of the emitted primary electrons.

PCD – Two PCD on conductive silicon samples (courtesy of Oliver Williams, Cardiff University, which was grown at 870°C under 0.55% $CH_4/(H_2+CH_4)$ plasma for 315min under 40Torr chamber pressure with 850°C 5% $CH_4/(H_2+CH_4)$plasma incubation) was degreased then H and LiO terminated individually. The samples were then tested for SEE and its gain values were calculated. An XPS measurement (pass energy 200eV, energy step 1.000eV, total acquisition time 4min 32sec) was taken from the LiO sample to examine the extent of LiO coverage. The thick-

ness and grain size of the diamond film was determined by taking SEM images of the cleaved cross-section and surface of the sample.

ND film grown on silicon – A conductive silicon sample was degreased and ND seeded. It was grown for 1hr and terminated with H. SEE measurements were taken and the sample was then cleaved to expose its cross-section. Both the cross-section and surface of the NDs were imaged using a SEM to determine its film thickness and grain size. Following its SEM a 2hr grown H-ND sample was prepared and its film thickness and grain size was determined again through SEM followed by their SEE measurements. Through this it was established that the 1hr growth period provided the optimum growth period with the ideal thickness that produced the best gain. Following this a LiO terminated sample with 1h ND growth was prepared. Its SEE measurements were taken and its gains were calculated. A control sample of a H-terminated non-seeded sample was also evaluated. The hydrogen and LiO-terminated samples were then tested for their electron bombardment resistance by measuring their gain decay over a period of 1hr under the exposure of a 700eV electron beam. The LiO sample was then further tested for its thermal resistance by annealing the sample at 800°C and comparing its gain before and after the anneal.

8.3 Results and Discussion

The benchmark test on the PCD, testing the capabilities of H and LiO terminations has proved to be rather promising. The H-PCD sample achieved a respectably high peak gain of 21.75 whilst the LiO-PCD sample has produced a moderate gain of 9.50. As mentioned earlier electron multiplication occurs over several generations in a MCP(Fig.**??**)[358]. Therefore a single electron could effectively generate a significant number of electrons from a LiO-PCD surface culminating to a viable amount of signal.

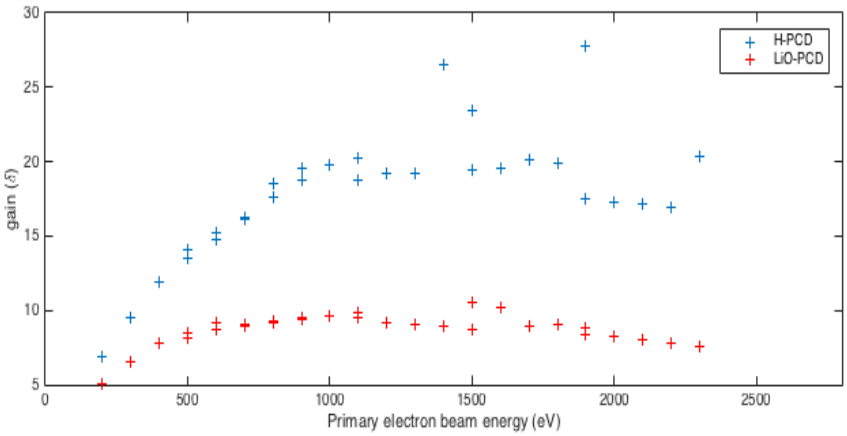

Figure 8.2: Graph of gain against the primary electron beam energy from H-PCD and LiO-PCD samples. The peak gains determined through the fit were 21.75 and 9.50 for the H-PCD and LiO-PCD samples respectively.

The unusually high hydrogen gain most likely originated from a combination of the diamond film having the right thickness and grain size. The diamond film was sufficiently thick enough for the primary electron to interact fully losing most of its momentum to secondary electron generation through inelastic scattering[359] before it reached the underlining silicon substrate, as well as having a coarse enough grain size that will allow for a greater mean free path without experiencing interruptions from the grain boundaries[83]. Additionally PCD will most likely have a neatly packed crystal grain structure that will have a relatively small number of defects such as traps and voids where the secondary electrons could be lost to[359]. The key principle here is crystallinity, through examination of the SEM images of the cross-section and the surface of the PCD film (Fig.8.3a)(Fig.8.3b) its thickness and average grain size was determined to be 337.9nm and 271$\pm$73.88nm respectively. These values will later be used to estimate the ideal film thickness and grain size of the diamond film.

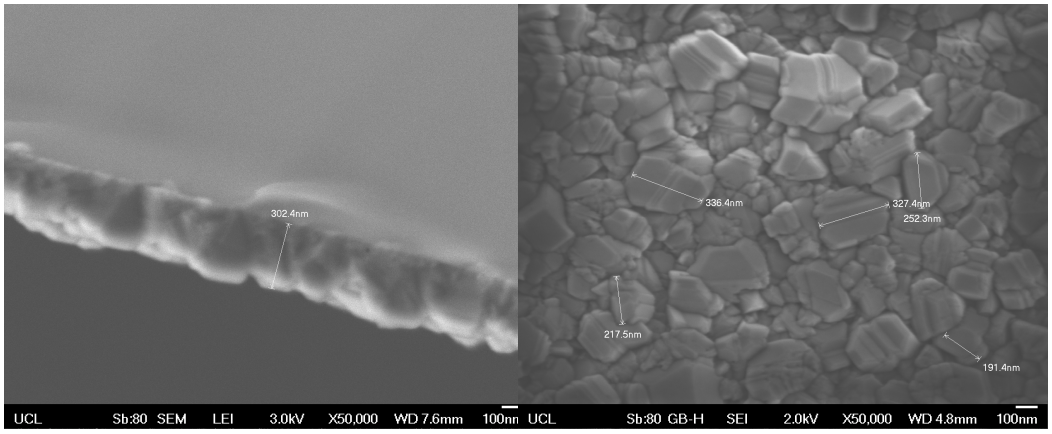

(a) (b)

Figure 8.3: SEM images of: (a) PCD film cross-section (thickness: 337.9nm), (b) PCD film surface (grain size: 271±74nm).

Following the successful gain acquisition from the H-PCD and LiO-PCD. Gain measurements were repeated on H-ND and LiO-ND samples. As seen from Fig.8.4 the benefits brought about by the H and LiO termination observed from the PCD samples have also been seen from the ND samples. The peak gains of the H-ND, LiO-ND and H terminated silicon (control, no NDs) were determined to be 11.02, 6.77 and approx. 2 respectively. As with PCD, hydrogen has shown to generate the greater gain of the two terminations. However while the decrease in gain from H-PCD to LiO-PCD was 56% the decrease in gain from H-ND to LiO-ND was limited to 39%. In another words ND when being converted to LiO termination from H were able to maintain more gain than PCD that has suffered a greater loss of gain from the same conversion. This may have been caused by the fact that the surface of the ND film is rougher due to its finer grain size than those found on the PCD surface (Fig.8.3)(Fig.8.5), providing a greater surface area for the ozone to react with, that in turn could replace the H with O. This will ultimately result in a greater O-termination coverage for the Li to react with to form the SEE generating LiO termination, which then has also allowed the NDs to maintain a higher than expected gain when being converted from H to LiO termination. Most importantly the results have shown that NDs despite its expected prevalence of defects and thus its expected reduction in gain were able

to maintain a surprisingly sizeable portion of the gain which has been seen from the PCD samples.

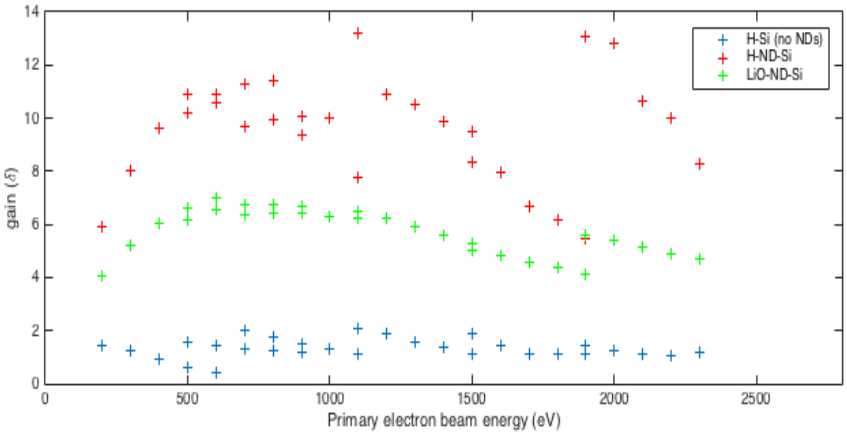

Figure 8.4: The graph of gain against the primary electron beam energy from H-ND, LiO-ND and the control sample with no ND seeding. The peak gains determined through the fit were 11.02, 6.77 and 2 for the H-ND, LiO-ND and the control sample, respectively.

As with PCD, ND film samples were examined under SEM to determine its thickness and grain size (Fig.8.5a)(Fig.8.5b). Both factors are known to have a significant impact on the gain values. However these values alone may not necessarily be a good measure of identifying the ideal crystal structure of the diamond film. For example if a sample was to have a respectable grain size but a very large thickness the gain will be low due to the distance and grain boundaries the secondary electrons are required to travel through. A large grain size is known to support large electron drift distance[83], while a large thickness will deliver the greatest gain if it is both sufficiently thick enough for the primary electrons to generate secondary electrons through inelastic collision whilst being thin enough so that the secondary electron generated will not be lost to the diamond bulk before emission.

Table.8.1 shows the gain, film thickness, grain size and thickness to grain size ratio of PCD, ND (1hr growth), ND (2hr growth) and two other cases of similar research carried out by Ascarelli *et al.*[359] and Trucchi *et al.*[360] followed by a table of their respective growth conditions [359][360] (Table.8.2).

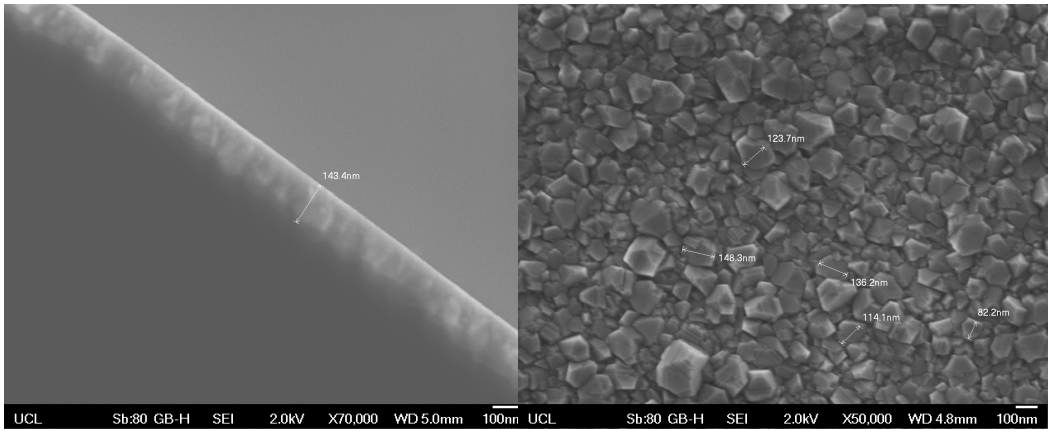

(a) (b)

Figure 8.5: SEM images of: (a) 1hr grown ND film cross-section (thickness: 143.4nm), (b) 1hr grown ND film surface (grain size: 121±25nm).

	Gain	Thickness	Grain size	Thickness to grain size ratio
H-ND (1hr growth)	11.02	143.4nm	120.9±25.2nm	1.186
H-ND (2hr growth)	N/A	337.5nm	309±79.89nm	1.091
H-PCD	21.75	337.9nm	271±73.88nm	1.247
Ascarelli *et al.*	10	2-5μm	1-2μm	approx. 2
Trucchi *et al.*	9	15.6μm	5-7μm	approx. 3

Table 8.1: The gain, thickness, grain size and thickness to grain size ratio of the ND and PCD samples with data from similar research[359][360].

	Film type	Temp (°C)	Methane/Hydrogen ratio	Chamber pressure
H-ND (1hr growth)	ND	700	1%	1.186
H-PCD	PCD	870	0.55%	40
Ascarelli *et al.*	ND	650	0.5-1.6%	10
Trucchi *et al.*	ND	770	0.5%	12

Table 8.2: The growth conditions of the ND and PCD samples with data from similar researches[359][360].

As expected the ratio between the thickness and grain size of the H-PCD that produced a large gain of 21.75 had a very low value of 1.247, implying that the secondary electrons generated travelled through a locally near single crystalline piece of diamond. Gains reported by Ascarelli *et al.* and Trucchi *et al.* of 10[359] and 9[360] had a ratio of 2[359] and 3[360] respectively. This is in line with the prediction that a high thickness to grain size ratio will result in poor gain due to the increased number of grain boundaries. Surprisingly however the ratio of the 1hr grown H-ND film that delivered a moderate gain of 11.02 was very low at 1.186 a value better than the H-PCD sample that had a gain of 21.75. This most likely was caused by the fact that the overall thickness of the film was insufficiently thin (143.4nm, almost half of the PCD sample) depriving the primary electrons of the chance to interact with the diamond. Therefore in order to achieve a greater gain the growth period of the H-ND sample was increased to 2hrs in order to increase the film thickness. Post growth, the thickness and the thickness to grain size ratio of the ND film was near identical to that of PCD (337.5nm and 337.9nm in thickness for ND and PCD respectively) (Fig.8.6a)(Table.8.1). Surprisingly however its gain value as seen from Fig.8.7 and Table.8.1 was much lower than expected (approx. 12) and erratic.

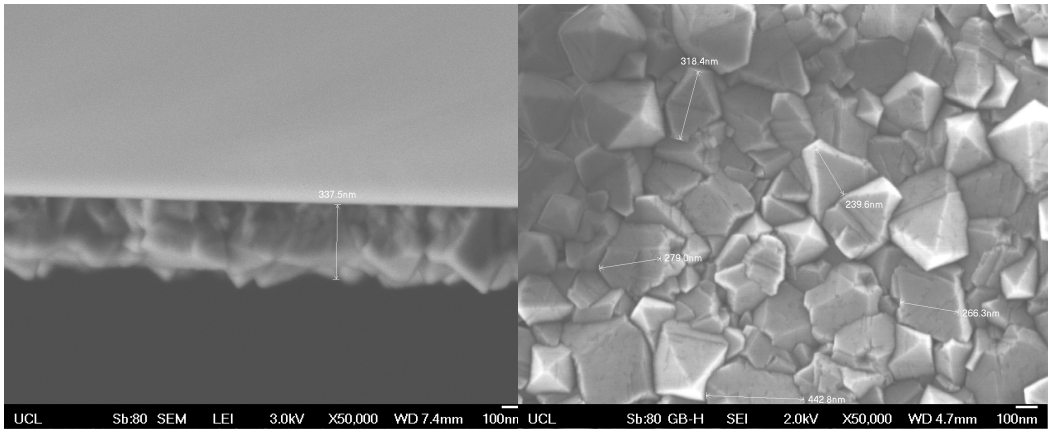

(a) (b)

Figure 8.6: SEM images of: (a) 2hr grown ND film cross-section (thickness: 337.5nm), (b) 2hr grown ND film surface (grain size: 309±80nm).

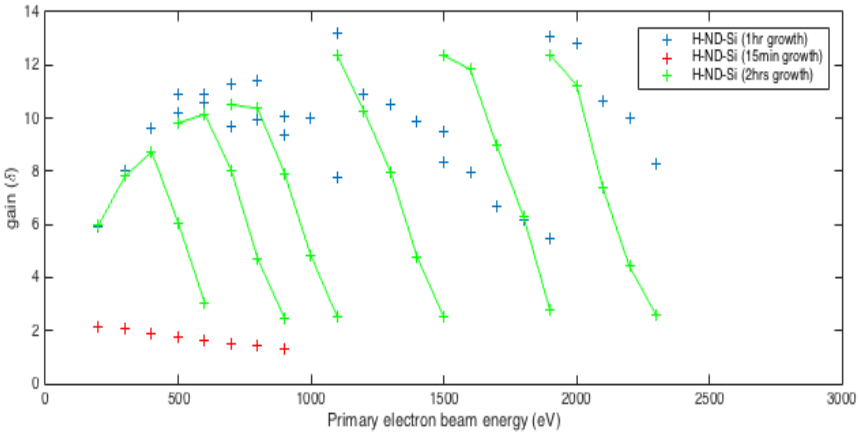

Figure 8.7: The graph of gain against the primary electron beam energy from H terminated ND sample of different growth rate (15min, 1h and 2h). The peak gains determined through the fit were 11.02 for the 1h and approx. 2 for the 15min grown sample. The 2h grown sample was far too unstable to establish a fit to determine an accurate gain. However the gain value determined from the lower energy and high bias measurements suggest a likely gain of approx. 12.

One possible explanation to this rather strange finding is the grain structure of the 2h grown ND film. It is highly probable that under the growth conditions used the grains may have maintained the grain size found from the 1hr growth, while deceivingly on the sample surface the grains may have fused together into a cluster that appeared as though it is a large single grain on the surface concealing the grain boundaries. There are two evidences to support this theory: one being

the partially fused ND clusters that were observed from the SEM images and the other being the abrupt decrease in gain seen in Fig.8.7. While taking the SEM images of the 2h-grown sample it has become apparent that many of the grains on the surface were in fact partially fused clusters of smaller grains, suggesting the presence of hidden facets in the bulk of the film. Analytically speaking however this only confirms the fusion of the grains at the surface and not in the deeper layer of the bulk. Evidence to support the clustering in the bulk could be seen from Fig.8.7. The gains determined from the weaker beam energies under strong bias (700eV beam energy under 500V-300V biases for example) were able to return plausible gains, while at higher beam energies and weak bias this tendency seems to diminish. This could be explained by the penetration depth of the primary electrons with low energies. If the electrons were to have low energies it will in turn have a shallow penetration depth, these electrons will encounter less grain boundaries across its penetration track. Naturally, the secondary electrons generated by the low energy primary electrons are required to travel across the same small number of grain boundaries resulting in greater SEE at shallow penetration depth. Under strong bias the secondary electrons are provided with enough potential to tunnel through defects and the grain boundaries allowing SEE. Deeper penetration and weak bias on the other hand will lead to the generation of secondary electrons deep in the bulk with greater numbers of grain boundaries to cross with little support from the bias and thus will result in a diminished gain. This suggests the dense presence of grain boundaries in the bulk of the 2hr grown ND film. The above finding is key to the improvement of this investigation as the PCD samples that showed superior gain most likely were able to avoid this issue by having a high temperature growth condition as high temperature growth is known to have a low tolerance towards stray non-bonded carbon that does not follow the crystal structure of the grain that acts as a nucleation site for a new grain to form, improving crystallinity[361]. High temperature growth also has an advantage in its accelerated growth rate due to the increase in reaction rate[362]. Interestingly, this investigation has found evidence to the contrary where the PCD

sample (grown at 870°C) and the 2hr grown ND sample (grown at 700°C) that were both found to be of the same thickness (approx. 337nm) required 315min and 120min to grow respectively implying lower temperature growth rate was faster. This odd finding may be a direct consequence of the plasma ratio. Williams *et al.* who has grown the PCD have used approximately 5% methane to 95% hydrogen plasma[361] while this investigation has used 1% methane to 99% hydrogen. It is therefore likely that the diamond growth rate has been slower due to the abundance of methane that deposits unstable non-bonded carbon and the presence of high temperature carbon etching hydrogen plasma that removes the said carbon resulting in slower net growth rate. As well as the higher temperature hydrogen plasma being more aggressive on the grown diamond layer. Therefore the above results have shown that in order to achieve improved gain one will not only need to investigate the termination of the diamond film but the structure of the film itself by altering its growth conditions. In doing so a higher temperature of 870°C and greater methane content of 5% is recommended where the optimum growth period that yields maximum SEE gain should be determined empirically using a combination of SEM and SEE measurements using the electron gun.

The results found in this investigation seems to fall in agreement with similar research that was carried out by, Harniman *et al.*, Shih *et al.* and Malta *et al.*, where they have found H-termination to increase the SEE gain[363][133][364]. Although their gain values are not entirely comparable to the values obtained from this investigation due to the differences in sample nature and measurement method. Namely the use of IIb natural diamond by Malta *et al.* who has achieved a gain of 30[364], where its high gain was most likely caused by the greater crystallinity of IIb diamonds than the PCD used in this investigation (and thus has a greater carrier mean free path) and the use of field emission[363] by Harniman *et al.*. Shih *et al.* however has carried out a very similar investigation to the one outlined in this chapter, with the exception of the use of a boron doped plasma grown diamond on silicon[133]. Their maximum gain was 11.3±0.4 from an H-terminated boron doped diamond film of 100μm to 200μm in thickness[133], a thickness com-

parable to this research. Two possible reasons as to why the H-terminated PCD used in this investigation has shown a much greater gain of 27 may be due to the inclusion of boron in the diamond bulk and the grain size. Shih *et al.* have found that with moderate to low boron doping the gain values increased, however with high boron content the gain value decreased[133]. Therefore it is possible that the samples examined by Shih *et al.* have been doped greater than its optimal amount. It is also worth considering the influence of grain size. Although there was no exact mention of the grain size of the diamond film used by Shih *et al.* considering that the PCD samples used in this investigation had a near single grain diamond film. The large mean free path brought about by the large grain size may have played a role in it performing better than the sample by Shih *et al.* who had a similar film thickness for their samples. As a general observation, the results seen from the PCD and ND measurements are very similar in profile to those found from Shih *et al.*, where at lower energies the gain was low followed by an increase in gain at the mid-energy range followed by a reduction in gain towards the higher energies[133]. Interestingly the energy range that peak gain was observed by Shih *et al.* was similar to this research at 800eV to 900eV[133]. Most likely caused by having a comparable sample thickness resulting in a similar optimal penetration depth.

As discussed earlier one of the main benefits of using LiO over H is for its superior binding energy, resulting in their stability to electron bombardment and temperature. In order to investigate this both H-ND and LiO-ND samples were tested for their resistance by exposing the sample to 700eV electron beam over a period of 1h as well as their gain values before and after annealing were compared. As one could see from Fig.8.8 both the H-ND and LiO-ND samples did experience gain decay over the period of 1h. However whilst the H-ND sample had a steady decrease, LiO experienced a rapid decrease in the first minute followed by a steady decrease. One of the possible explanations to this sudden initial decrease in gain is the residual excess lithium atoms that were unable to be removed in the DI water rinse. Lithium being a positive ion likely has been coulombically attracted

to the underlying negative oxygen without the formation of a chemical bond. Naturally, coulombic attraction being inherently weaker than ionic bonds due to the greater nuclei separation they may have been removed by the initial exposure to the electron beam. As a result the overall decrease in gain over the period of 1h for LiO has been 72% of which 8.5% of the decrease occurred within the first minute, while the decay in gain from a H-PCD sample was 83%. Therefore LiO has proven itself to be slightly more resistant to electron bombardment than hydrogen. It is also worth noting that there has been a 64% decrease in gain for LiO-ND over the period of the last 59min. During the period of 1h the samples were exposed to 1.15μA of electron beam current, resulting in an exposure to 2.584×10^{16} electrons. For a device that is designed to amplify a signal that starts as a single electron, this resistance is expected to suffice for its application.

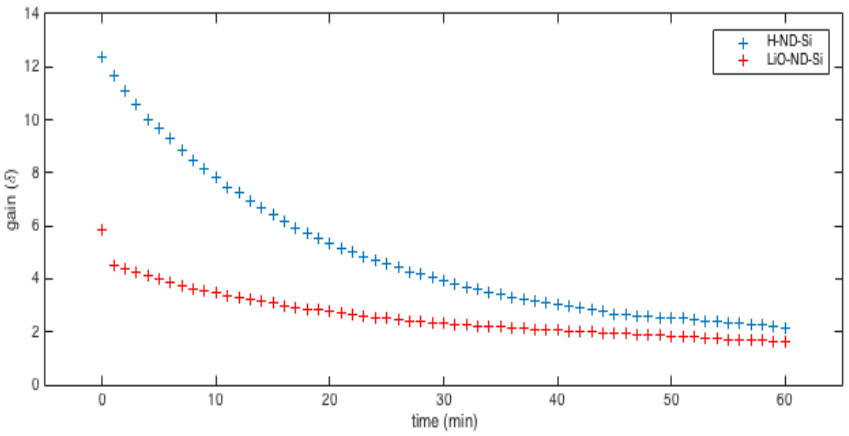

Figure 8.8: Gain decay of H-ND and LiO-ND samples from a 700eV beam energy electron beam over a period of 1h. Gain decrease of 83% and 72% has been observed for H and LiO termination respectively where for the LiO a much slower decrease of 64% has been observed after the first minute.

In order to investigate the thermal resistance of the LiO termination a ND sample was annealed at 800°C and its gain values before and after annealing was compared. Naturally due to the fact that the sample was annealed to 450°C during lithium deposition to encourage LiO formation this process will prove the thermal resistance of LiO termination between 450°C and 800°C. As seen from Fig.8.9 annealing has had a substantial influence on the gain where the

pre-annealing gain of 9.50 has been reduced to the post-annealing gain of 5.79. Interestingly findings by those who have carried out similar research such as that of by O'Donnell *et al.* have made claims to the opposite where 800°C anneal has said to have enhance the gain[118], citing the formation of LiO bonds that encouraged the transition from a PEA to NEA as its reason[118]. There are two possible explanations to the difference in findings: one being their method of oxygen termination, where O'Donnell *et al.* have used oxygen plasma and acid wash[118] while this investigation used ozone. It is known that acid has a tendency to add carboxylic groups (-COOH) and hydroxyl (-OH) groups as its terminal groups as well as oxygen[80]. Therefore it is possible that their sample required a high temperature anneal to remove the hydrogen from the pre-existing –OH and –COOH group in order for the Li to bond to the underlying oxygen before observing notable SEE. Energetically speaking C-O bonds are known to have a substantially stronger bond than O-H with their respective dissociation energies being 1076.5kJ mol^{-1}[129] and 428kJ mol^{-1}[129]. Thus C-O bonds are likely to be capable of surviving the annealing temperature far beyond the tolerance of O-H bonds. Once the annealing has been completed the Li and H present will compete over the newly vacant O. Statistically the Li deposited on the surface, which is far more abundant in comparison to the H due to bulk deposition will most likely take the lion's share of the available bonding sites thus explaining the increase in gain found by O'Donnell *et al.*. The other possible explanation is the miniscule amount of contamination. O'Donnell *et al.* has carried out their annealing in an ultra high vacuum (UHV, 10^{-10}mBar)[118] while this investigation was carried out under high vacuum (HV, 10^{-7}mBar). Although the number of contaminants were heavily limited under HV, it is entirely possible that the surface of the sample may have had contaminants present that may have impeded SEE. Considering both accounts it is perhaps best for future works to be carried out in UHV and continue to use ozone, an oxygen exclusive termination method. It is worth noting at this point that the presence of gain after 800°C anneal suggests that one of the primary objectives of finding a more thermally resistant alternative to CsO (that

is known to dissociate at 500°C[127]) has been successfully achieved.

The increase in gain upon heating was also seen by Shih *et al.*[133], where Shih *et al.* has found the gain to be as large as 44 when heated to 900°C for 5 min[133]. Citing the desorption of hydrocarbons on the air-exposed diamond as its reason based on observations by Thoms *et al.*[365]. What is particularly interesting however is that unlike O'Donnell *et al.*'s observation, the gain increase with temperature did eventually come to an end when the sample was heated to 1000°C for 15 min[133] citing hydrogen desorption as its reason[366]. Suggesting the presence of a thermal 'sweet-spot' for SEE yield where up to a certain temperature the gain will benefit from annealing, while after a certain temperature it will rapidly lose its gain once the thermal agitation overcomes the bond between the diamond and the terminal species. For hydrogen, this is between 800°C and 1000°C, where the results from this investigation above suggest that LiO has a lower optimal annealing temperature than hydrogen. For future work, therefore, it may be advisable to incrementally heat the sample in order to find the optimal temperature to achieve a higher gain.

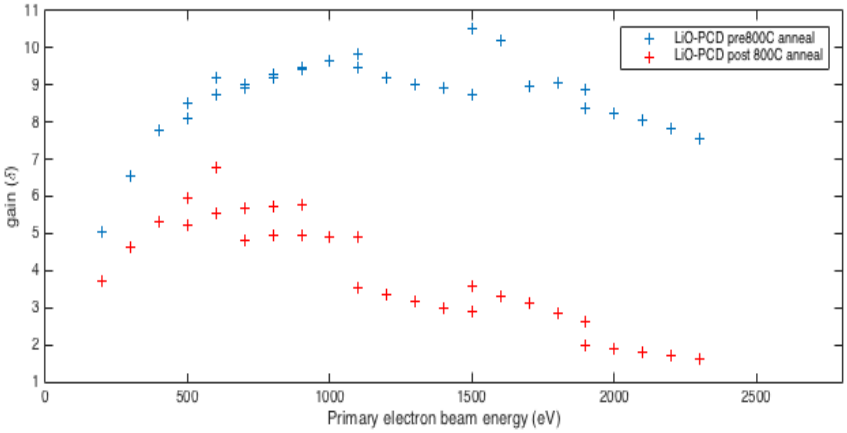

Figure 8.9: The graph of gain against the primary electron beam energy of LiO terminated PCD sample before and after the 800°C anneal. The peak gain of the sample before and after the anneal was 9.50 and 5.79 respectively, a decrease in gain by 39%.

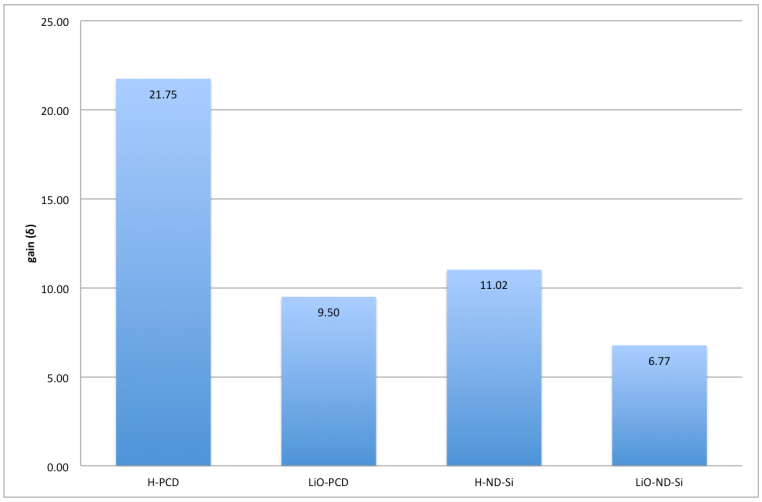

Figure 8.10: A bar chart of the peak gain of the H and LiO terminated PCD and ND samples. A decrease of 56% and 39% has been observed between the H and LiO terminated PCD and ND respectively, whilst a difference of 49% and 29% has been observed between H-PCD to H-ND and LiO-PCD to LiO-ND respectively.

Fig.8.10 summarises the gain values obtained from H and LiO terminated PCD and ND samples. It has become apparent through the findings in particular from the difference in gain decrease between H to LiO seen from PCD and ND that there is a sound probability that the sample may not have had a perfect coverage of H and LiO terminations. In order to address this concern a XPS of the LiO-PCD sample has been taken. Results have shown the surface coverage of Li to be 15.36% while oxygen was 11.41% (Fig.8.11). This indicates the unexploited potential area of the diamond sample surface. It is worth noting at this point that improper incorporation of Li will not only produce poorer gain through the lack of SEE but it also hamper the gain by exposing the SEE inhibiting O termination. Additionally XPS has also shown evidence of bare diamond patches where the surface is believed to neither be covered by O nor Li, indicating the need for improvement in both the oxygenation and the lithiation process. However the actual percentage of elements detected through XPS is best taken as approximate as only 50% of the XPS signal is said to come from the outer most element, since XPS generally has a penetration depth of 10nm of which only approx. 0.1nm is LiO[118]. Therefore it is possible that the underlying diamond (carbon) has

somewhat distorted the outcome. Regardless the Li coverage of 15% is far from ideal and one could safely assume the need for improvement in Li coverage.

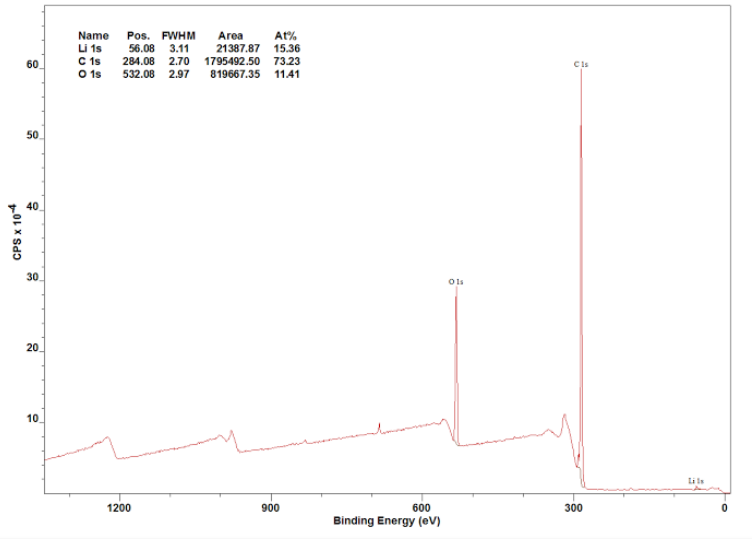

Figure 8.11: XPS scan of the LiO terminated PCD sample.

There are two possible reasons behind the poor Li coverage: one being the lack of oxygen coverage pre-Li deposition depriving Li of bonding sites. Therefore by improving the oxygen termination process (such as by longer exposure to ozone at higher temperatures) one could improve LiO coverage. The other cause for poor Li coverage is the lack of Li exposure. Since the Li released from the source (getter) is radiative in nature it will follow the inverse square law. Therefore it is entirely possible that the separation of 5cm even under HV conditions may have drastically reduced the actual amount of Li exposed to the sample. To circumvent this issue it is perhaps best to reduce the sample-to-source separation to 1cm or less.

8.4 Conclusion

In conclusion this investigation has identified LiO-termination as a viable alternative source of amplification to CsO and H through the process of SEE with sound potential for its use in night vision goggles. High resistance to electron bombardment and temperature beyond the normal operational range of the device was

found. Future works and improvements includes the amendment of growth conditions of the NDs to 870°C and 5% methane plasma where it was found to grow films of a more suitable grain size relative to its thickness. An improved oxygenation process is also advised to increase the O-termination coverage namely by increasing the exposure time and temperature of the sample to ozone, based on the understanding that the C-O bonds are able to withstand higher annealing temperature due to its large dissociation energy. Similarly it is also prudent to improve the lithiation process by carrying out the deposition in a UHV environment at under higher temperatures with a smaller sample-to-Li source separation to reduce the possibility of contamination and to improve the LiO coverage.

Chapter 9

Conclusion

In this investigation four separate aspects of sp^2 and sp^3 carbons have been discussed. Two of which were based on exploiting the conductive nature of sp^2 carbon hosted in an insulating polymer to form a composite and two of which that exploited the novel properties of sp^3 carbon, namely its radiation hardness/detection and its electron multiplication.

In chapter 5, where the influence of functionalisations on the conductivity of the CNT-epoxy composite has been examined. It has been found that both -OH and -COOH functionalisation of the multi-walled CNTs causes a large decrease ($10^{12}\Omega$ to $10^{7}\Omega$) in composite resistance. This was later attributed to the improved integration between the CNTs and the epoxy due to the formation of ester bonds and hydrogen bonds between the -COOH and -OH functionalised CNT and the epoxy chains respectively. The greater mass of the CNT-epoxy chain matrix formed in this manner has allowed for a greater CNT distribution, directly resulting in the greater spread of the conductive CNT network improving conductivity. Increase in the concentration of the CNTs has resulted in saturation of CNTs where the excess CNTs have started to form CNT clusters. The influence of the diameter and lengths of CNTs has also been investigated. Results has shown an improved composite conductivity with increased CNT length while the diameter had very little influence to the conductivity. This is likely due to the limited improvement in the 'reach' of the conductive CNT in comparison to the length of

the CNTs.

Chapter 6 discussed the viability of using CNT-PDMS as a form of blood pressure/heart failure sensor exploiting the piezo-resistivity of the CNT-polymer composite. Results has shown that the composite exhibits a large change in resistance with increased CNT load where a difference of $10^{12}\Omega$ to $10^{3}\Omega$ has been observed from the state of insulation to conduction respectively with its percolation threshold at 8wt%. Unexpectedly, when transferring this finding to the 2D compressive piezo-resistivity test it has been found that the CNT concentration that displayed piezo-resistivity was 10wt%. This most likely was due to the host polymer 'fighting back' against the compressive force making it difficult for the compressive force to bring the CNTs closer together to alter its resistance. Therefore, it was concluded that this has caused the lack of increase in composite conductivity. At 10wt% it has been found that the resistance has dropped from $10^{9}\Omega$ to $10^{6}\Omega$ before and after percolation respectively which in the interest of this investigation of developing an electrical sensor was deemed sufficient. When carrying out the 3D compressions it was found that the resistance of the composite did indeed respond to 3D pressure giving a positive outlook to the realisation of the device. A resistance increase of $4k\Omega$ to $750k\Omega$ has been observed. A point to note here is the direction of change in resistance. From the 2D compression test it was found that the resistance decreased with pressure due to the conductive CNT fillers coming closer together increasing the conductivity. However unlike the 2D compression where the CNTs were confined to its local area, 3D compression on the other hand is believed to have a greater degree of freedom where the CNTs could move to any direction with least pressure resulting in a greater CNT to CNT distance increasing the composite resistance, regardless considering the sufficient amount of resistance change before and after percolation. This investigation has successfully shown the viability of CNT-PDMS composite as a blood pressure/heart failure sensor.

In Chapter 7, a neutron sensor has been developed for the Trident nuclear submarine, HMS Artful using a large area, high purity IIa CVD diamond. Results

from the α-particle/γ-ray detection test have shown that with 200V bias that was applied across the diamond detector one could successfully detect α-particles with a large Q-factor allowing an accurate determination of the number of α counts, as well as achieving γ-discrimination to prevent false positive counts. Upon application of the LiF neutron to α conversion layer, it was found that the neutrons were successfully detected with a sufficient Q-factor to determine the number of detected neutrons. Through geometric calculations the efficiency of the device was calculated, where the detector was found to have an efficiency of 32.3% for α and 48.3% for neutrons. The improved efficiency for neutron is believed to originate from the increased detection surface brought about by the presence of a Bonner sphere. Through the preliminary experiments carried out to inspect the quality of the diamond layer, it was found that the quality of the diamond was high both in purity and crystallinity. However AFM images of the diamond have revealed its surface roughness of the laser-cut and polished surface to be as high as 10.4nm. This most likely has allowed for the formation of surface states that most likely has reduced the charge collection efficiency that has ultimately led to reduced α and neutron detection rates. Regardless by knowing both the device count of neutrons and the device efficiency one could determine the number of incoming neutrons. Thus this investigation has successfully fabricated a working neutron detector that is capable of accurately determining the number of neutrons emitted by the nuclear reactor in a nuclear submarine.

The final experimental chapter, Chapter 8 investigates the secondary electron emission (SEE) effect where its electron multiplication effect has been exploited to achieve signal amplification. It has been found that a large gain of 21.75 could be achieved from a H-terminated poly-crystalline diamond (PCD) that traditionally has been seen to be a difficult material to achieve SEE due to its grain boundaries. The high gain is most likely a product of its large crystal grain grown under high temperature (870^{o}C) and high methane concentration (5%) plasma. Although notably smaller, a respectable gain of 9.5 has also been obtained from a LiO terminated PCD; a termination that is predicted to have a greater ther-

mal/electron bombardment resistance. The findings of this research has shown that LiO is in fact more resistant to electron bombardment than H where signs of thermal damage to LiO was only observed at temperatures as high as 800°C. When attempting to recreate the above using NDs where its mobility is key to the production of a signal amplifier it was found that the overall gain has decreased (11.02 to 6.72 for H and LiO terminated NDs respectively). Given that one uses the improved growth conditions (870°C and 5% methane plasma) the values are expected to be closer to those found from PCDs. In terms of the growth period it has been found that the optimum growth period was 1hr based on the SEM images and the SEE test. However, it is advisable to re-evaluate this and tailor it according to the revised growth conditions for future research. Lastly when evaluating the effectiveness of the Li deposition through XPS it has been found that only 15% of the surface is covered by Li. It is therefore apparent that the diamond surface could benefit from an improved Li and O coverage. Improved O termination through longer and higher temperature ozone exposure and closer source to sample distance Li exposure in a lower pressure (UHV) vacuum is recommended.

Chapter 10

Future Works

Although the investigation was carried out to the best it could within its time constraint, there is always room for improvement. CNT-Epoxy for example despite its relatively sound logic falls short in statistical backing. Ideally, if the conclusion was drawn based on a larger sample size it would have had a greater weight as evidence. Unfortunately, due to the limitation in time for the TEM this was not possible. Therefore given more time the CNT-Epoxy chapter will most likely benefit from a greater sampling of the composite under a TEM. CNT-PDMS on the other hand was more to do with the design of the investigation. The use of sphygmomanometer has resulted in an unexpected error of the pressure being applied to the 3D sample in 2D despite it being encased in ballistic gelatine. To rectify this problem, it is perhaps best to test the device in a pressure chamber where the pressure could be applied in all directions uniformly. Following this, miniaturisation of the device, perhaps by creating a micro-scale $200\mu m^3$ mould using lithography and metallisation will be logical. The device could then be tested *in vivo* as per the initial design. In contrast, area of improvements to be made for BAE neutron detectors are not in design but performance. From the detection peaks, it has become apparent that the device with the least surface defects, i.e. the smoothest device had the greatest charge collection efficiency. Therefore, if surface roughness correction could be carried out it is likely that the performance of the detectors could be improved. As suggested earlier this probably will best

be achieved by either etching the surface using plasma or by growing a thin film of diamond using methane and hydrogen plasma. Out of the four investigations however SEE perhaps has the greatest room for improvement. Firstly, the ND film crystal structure could be improved where a greater grain size and thinner film depth (i.e. reduced number of grain boundaries) is expected to increase gain. The most apparent way of achieving this is by increasing the methane content of the growth plasma to 5% and at a higher growth temperature of 870°C. The second improvement is somewhat related to the first. One of the reasons why this investigation required a rather thick film is due to the model of the electron gun that was available. The particular model in discussion is designed to release electrons in the range of MeV and thus this investigation used the lowest possible settings available. Ideally however, a thinner film and lower energy electrons are preferred. This is mainly to reduce the cost of production of ND loaded multi-channel plates which is implemented as amplifiers for night vision goggles, as well as to increase the SEE yield by reducing the penetration depth of the primary electrons. The last area of improvement perhaps is the easiest to achieve as it is a simple matter of improving the coverage of SEE inducing surface terminations. From the XPS results one could see that both O and Li termination coverage is less than ideal (11.41% and 15.36% respectively). Therefore, by improving the O termination, namely by increasing the sample temperature during O termination to >200°C (thus increasing the overall number of O that is bonded to the diamond surface) it most likely will allow a greater number of Li to be bonded to the surface *via* O. The coverage of Li itself could also be improved by having a smaller source to sample distance (<1cm) in ultra-high vacuum (10^{-10}mBar) to increase exposure and to avoid contamination.

Chapter 11

References

[1] V. Danilenko, "On the history of the discovery of nanodiamond synthesis," *Physics of the Solid State*, vol. 46, no. 4, pp. 595–599, 2004.

[2] J. C. Angus, A. Argoitia, R. Gat, Z. Li, M. Sunkara, L. Wang, and Y. Wang, "Chemical vapour deposition of diamond," *Philosophical Transactions of the Royal Society of London A: Mathematical, Physical and Engineering Sciences*, vol. 342, no. 1664, pp. 195–208, 1993.

[3] S. Iijima *et al.*, "Helical microtubules of graphitic carbon," *nature*, vol. 354, no. 6348, pp. 56–58, 1991.

[4] M. Reibold, P. Paufler, A. Levin, W. Kochmann, N. Pätzke, and D. Meyer, "Materials: Carbon nanotubes in an ancient damascus sabre," *Nature*, vol. 444, no. 7117, pp. 286–286, 2006.

[5] P. Bartos, *Nanotechnology in construction*, vol. 292. Royal Society of Chemistry, 2004.

[6] R. Martel, T. Schmidt, H. Shea, T. Hertel, and P. Avouris, "Single-and multi-wall carbon nanotube field-effect transistors," *Applied Physics Letters*, vol. 73, no. 17, pp. 2447–2449, 1998.

[7] M. Miao, "Electrical conductivity of pure carbon nanotube yarns," *Carbon*, vol. 49, no. 12, pp. 3755–3761, 2011.

[8] B. Demczyk, Y. Wang, J. Cumings, M. Hetman, W. Han, A. Zettl, and R. Ritchie, "Direct mechanical measurement of the tensile strength and elastic modulus of multiwalled carbon nanotubes," *Materials Science and Engineering: A*, vol. 334, no. 1, pp. 173–178, 2002.

[9] "The nobel prize in physics 2010." `http://www.nobelprize.org/nobel_prizes/physics/laureates/2010/`. Accessed: 12-06-2016.

[10] K. Balasubramanian and M. Burghard, "Chemically functionalized carbon nanotubes," *Small*, vol. 1, no. 2, pp. 180–192, 2005.

[11] M. Smith, *March's Advanced Organic Chemistry: Reactions, Mechanisms, and Structure*. March's Advanced Organic Chemistry, Wiley, 2013.

[12] H. Godwin, "Half-life of radiocarbon," *Nature*, vol. 195, 1962.

[13] "Carbon allotropes." `http://en.wikipedia.org/wiki/File:Eight_Allotropes_of_Carbon.png`. Accessed: 08-02-2016.

[14] R. Madan, *Organic Chemistry*. Tata McGraw-Hill, 2013.

[15] V. Thakur and M. Thakur, *Chemical Functionalization of Carbon Nanomaterials: Chemistry and Applications*. CRC Press, 2015.

[16] "Orbital hybridisation sp2 1." `http://chemwiki.ucdavis.edu/Organic_Chemistry/Organic_Chemistry_With_a_Biological_Emphasis/Chapter__1%3A_Chapter_1%3A_Introduction_to_organic_structure_and_bonding_I/Section_1.5%3A_Valence_bond_theory%3A_sp,_sp2,_and_sp3_hybrid_orbitals`. Accessed: 08-02-2016.

[17] "Orbital hybridisation sp2 2." `https://jahschem.wikispaces.com`. Accessed: 08-02-2016.

[18] D. R. Cooper, B. D'Anjou, N. Ghattamaneni, B. Harack, M. Hilke, A. Horth, N. Majlis, M. Massicotte, L. Vandsburger, E. Whiteway, *et al.*, "Experimental review of graphene," *ISRN Condensed Matter Physics*, vol. 2012, 2012.

[19] K. I. Bolotin, K. Sikes, Z. Jiang, M. Klima, G. Fudenberg, J. Hone, P. Kim, and H. Stormer, "Ultrahigh electron mobility in suspended graphene," *Solid State Communications*, vol. 146, no. 9, pp. 351–355, 2008.

[20] M. Prince, "Drift mobilities in semiconductors. ii. silicon," *Physical Review*, vol. 93, no. 6, p. 1204, 1954.

[21] C. Lee, X. Wei, J. W. Kysar, and J. Hone, "Measurement of the elastic properties and intrinsic strength of monolayer graphene," *science*, vol. 321, no. 5887, pp. 385–388, 2008.

[22] P. Avouris, "Molecular electronics with carbon nanotubes," *Accounts of chemical research*, vol. 35, no. 12, pp. 1026–1034, 2002.

[23] "Formation of sp2 allotropes." `http://www.enago.com/blog/graphene-thin-is-in-physics-nobel-prize-2010/`. Accessed: 08-02-2016.

[24] "Graphene layer." `http://glossary.periodni.com/glossary.php?en=graphite`. Accessed: 08-02-2016.

[25] "Graphene top." `http://www.nano-enhanced-wholesale-technologies.com/images/structure-graphene.gif`. Accessed: 08-02-2016.

[26] A. Hirsch, "The era of carbon allotropes," *Nature materials*, vol. 9, no. 11, pp. 868–871, 2010.

[27] "Fullerene top." `http://www.3dchem.com/molecules.asp?ID=218`. Accessed: 08-02-2016.

[28] "Fullerene layer." http://www.carbonallotropes.com/13-carbon-onions-50-54-layers-100mg. Accessed: 08-02-2016.

[29] Y. Gao, Y. S. Zhou, M. Qian, X. N. He, J. Redepenning, P. Goodman, H. M. Li, L. Jiang, and Y. F. Lu, "Chemical activation of carbon nano-onions for high-rate supercapacitor electrodes," *Carbon*, vol. 51, pp. 52–58, 2013.

[30] Z. Chen, W. Thiel, and A. Hirsch, "Reactivity of the convex and concave surfaces of single-walled carbon nanotubes (swcnts) towards addition reactions: Dependence on the carbon-atom pyramidalization," *ChemPhysChem*, vol. 4, no. 1, pp. 93–97, 2003.

[31] K. Holczer, O. Klein, S. Huang, R. B. Kaner, K.-j. Fu, R. L. Whetten, and F. Diederich, "Alkali-fulleride superconductors- synthesis, composition, and diamagnetic shielding," *Science*, vol. 252, no. 5009, pp. 1154–1157, 1991.

[32] S. Campidelli, T. Brandmüller, A. Hirsch, I. M. Saez, J. W. Goodby, and R. Deschenaux, "An optically-active liquid-crystalline hexa-adduct of [60] fullerene which displays supramolecular helical organization," *Chemical communications*, no. 41, pp. 4282–4284, 2006.

[33] K. Komatsu, M. Murata, and Y. Murata, "Encapsulation of molecular hydrogen in fullerene c60 by organic synthesis," *Science*, vol. 307, no. 5707, pp. 238–240, 2005.

[34] G. Dennler, M. C. Scharber, and C. J. Brabec, "Polymer-fullerene bulk-heterojunction solar cells," *Advanced Materials*, vol. 21, no. 13, pp. 1323–1338, 2009.

[35] X. Lu and Z. Chen, "Curved pi-conjugation, aromaticity, and the related chemistry of small fullerenes," *Chemical Reviews*, vol. 105, no. 10, pp. 3643–3696, 2005.

[36] "Cnt chirality." http://sustainable-nano.com/2014/03/04/

turning-plastic-bags-into-carbon-nanotubes/. Accessed: 08-02-2016.

[37] "Cnt chirality 2." http://phycomp.technion.ac.il/~talimu/structure.html. Accessed: 08-02-2016.

[38] "Cnt chirality 3." http://teachers.yale.edu/curriculum/viewer/initiative_10.05.02_u. Accessed: 08-02-2016.

[39] M. Pacurari, V. Castranova, and V. Vallyathan, "Single-and multi-wall carbon nanotubes versus asbestos: are the carbon nanotubes a new health risk to humans?," *Journal of Toxicology and Environmental Health, Part A*, vol. 73, no. 5-6, pp. 378–395, 2010.

[40] "Cnt prices 2016." http://www.sigmaaldrich.com/catalog/product/ritann/659258?lang=en&region=. Accessed: 08-02-2016.

[41] B. Zheng, C. Lu, G. Gu, A. Makarovski, G. Finkelstein, and J. Liu, "Efficient cvd growth of single-walled carbon nanotubes on surfaces using carbon monoxide precursor," *Nano Letters*, vol. 2, no. 8, pp. 895–898, 2002.

[42] M. Kumar and Y. Ando, *Carbon nanotube synthesis and growth mechanism*. INTECH Open Access Publisher, 2011.

[43] J. Kong, A. M. Cassell, and H. Dai, "Chemical vapor deposition of methane for single-walled carbon nanotubes," *Chemical Physics Letters*, vol. 292, no. 4, pp. 567–574, 1998.

[44] Y. Murakami, Y. Miyauchi, S. Chiashi, and S. Maruyama, "Characterization of single-walled carbon nanotubes catalytically synthesized from alcohol," *Chemical Physics Letters*, vol. 374, no. 1, pp. 53–58, 2003.

[45] Y. Li, W. Kim, Y. Zhang, M. Rolandi, D. Wang, and H. Dai, "Growth of single-walled carbon nanotubes from discrete catalytic nanoparticles of various sizes," *The Journal of Physical Chemistry B*, vol. 105, no. 46, pp. 11424–11431, 2001.

[46] A. Hirsch, "Functionalization of single-walled carbon nanotubes," *Angewandte Chemie International Edition*, vol. 41, no. 11, pp. 1853–1859, 2002.

[47] E. V. Basiuk, M. Monroy-Peláez, I. Puente-Lee, and V. A. Basiuk, "Direct solvent-free amination of closed-cap carbon nanotubes: a link to fullerene chemistry," *Nano Letters*, vol. 4, no. 5, pp. 863–866, 2004.

[48] H. Hu, P. Bhowmik, B. Zhao, M. Hamon, M. Itkis, and R. Haddon, "Determination of the acidic sites of purified single-walled carbon nanotubes by acid–base titration," *Chemical Physics Letters*, vol. 345, no. 1, pp. 25–28, 2001.

[49] J. Zhao, H. Park, J. Han, and J. P. Lu, "Electronic properties of carbon nanotubes with covalent sidewall functionalization," *The Journal of Physical Chemistry B*, vol. 108, no. 14, pp. 4227–4230, 2004.

[50] J. Chen, M. A. Hamon, H. Hu, Y. Chen, A. M. Rao, P. C. Eklund, and R. C. Haddon, "Solution properties of single-walled carbon nanotubes," *Science*, vol. 282, no. 5386, pp. 95–98, 1998.

[51] J. Zhang, H. Zou, Q. Qing, Y. Yang, Q. Li, Z. Liu, X. Guo, and Z. Du, "Effect of chemical oxidation on the structure of single-walled carbon nanotubes," *The Journal of Physical Chemistry B*, vol. 107, no. 16, pp. 3712–3718, 2003.

[52] K. Shiral Fernando, Y. Lin, and Y.-P. Sun, "High aqueous solubility of functionalized single-walled carbon nanotubes," *Langmuir*, vol. 20, no. 11, pp. 4777–4778, 2004.

[53] J. L. Bahr and J. M. Tour, "Covalent chemistry of single-wall carbon nanotubes," *Journal of Materials Chemistry*, vol. 12, no. 7, pp. 1952–1958, 2002.

[54] C. Bauer, I. Baumann, C. Colledani, J. Conway, P. Delpierre, F. Djama, W. Dulinski, A. Fallou, K. Gan, R. Gilmore, *et al.*, "Radiation hardness

studies of cvd diamond detectors," *Nuclear Instruments and Methods in Physics Research Section A: Accelerators, Spectrometers, Detectors and Associated Equipment*, vol. 367, no. 1, pp. 207–211, 1995.

[55] B. L. Jones, T. L. Nam, and R. J. Keddy, "Diamond neutron detector," June 1 1993. US Patent 5,216,249.

[56] "Carbon filler shape difference diagram." `https://cfpub.epa.gov/ncer_abstracts/images/fckimages/index.cfm?imgid=812`. Accessed: 02-04-16.

[57] M. Dresselhaus, G. Dresselhaus, P. Eklund, and A. Rao, "Carbon nanotubes," in *The Physics of Fullerene-Based and Fullerene-Related Materials*, pp. 331–379, Springer, 2000.

[58] S. Heinze, J. Tersoff, and P. Avouris, "Electrostatic engineering of nanotube transistors for improved performance," *Applied Physics Letters*, vol. 83, no. 24, pp. 5038–5040, 2003.

[59] M. Bockrath, W. Liang, D. Bozovic, J. H. Hafner, C. M. Lieber, M. Tinkham, and H. Park, "Resonant electron scattering by defects in single-walled carbon nanotubes," *Science*, vol. 291, no. 5502, pp. 283–285, 2001.

[60] R. Ahmed, *Diamond Nanostructure Devices for Chemical Sensing Application*. UCL, 2010.

[61] R. Sussmann, *CVD Diamond for Electronic Devices and Sensors*. Wiley Series in Materials for Electronic & Optoelectronic Applications, Wiley, 2009.

[62] R. Davis, *Diamond Films and Coatings: Development, Properties, and Applications*. Hébert, Alexandre-Martin-Stanislas, Noyes Pub., 1993.

[63] M. Wolfer, J. Biener, B. S. El-Dasher, M. M. Biener, A. V. Hamza, A. Kriele, and C. Wild, "Crystallographic anisotropy of growth and etch rates of cvd

diamond," *Diamond and Related Materials*, vol. 18, no. 5, pp. 713–717, 2009.

[64] "Diamond phase diagram." `http://lbruno.home.cern.ch/lbruno/documents/Bibliography/LHC_Note_78.pdf`. Accessed: 08-02-2016.

[65] H. Pierson, *Handbook of Carbon, Graphite, Diamond, and Fullerenes: Properties, Processing, and Applications*. Materials science and process technology series, Noyes Publications, 1993.

[66] A. Krueger, "The structure and reactivity of nanoscale diamond," *Journal of Materials Chemistry*, vol. 18, no. 13, pp. 1485–1492, 2008.

[67] P. A. Thrower, *Chemistry & Physics of Carbon*, vol. 25. CRC Press, 1996.

[68] Y. Orlov, *The Mineralogy of the Diamond: Orig. Tit.: Minearlogiia Almaza*. John Wiley, 1977.

[69] J. C. Angus, H. A. Will, and W. S. Stanko, "Growth of diamond seed crystals by vapor deposition," *Journal of Applied Physics*, vol. 39, no. 6, pp. 2915–2922, 1968.

[70] P. W. May, "Diamond thin films: a 21st-century material," *Philosophical Transactions of the Royal Society of London A: Mathematical, Physical and Engineering Sciences*, vol. 358, no. 1766, pp. 473–495, 2000.

[71] J. C. Angus, Y. Wang, and M. Sunkara, "Metastable growth of diamond and diamond-like phases," *Annual Review of Materials Science*, vol. 21, no. 1, pp. 221–248, 1991.

[72] J. Gracio, Q. Fan, and J. Madaleno, "Diamond growth by chemical vapour deposition," *Journal of Physics D: Applied Physics*, vol. 43, no. 37, p. 374017, 2010.

[73] S. Matsumoto, Y. Sato, M. Tsutsumi, and N. Setaka, "Growth of diamond

particles from methane-hydrogen gas," *Journal of Materials Science*, vol. 17, no. 11, pp. 3106–3112, 1982.

[74] M. Kamo, Y. Sato, S. Matsumoto, and N. Setaka, "Diamond synthesis from gas phase in microwave plasma," *Journal of Crystal Growth*, vol. 62, no. 3, pp. 642–644, 1983.

[75] K. Volkov, V. Danilenko, and V. Elin, "Synthesis of diamond from the carbon in the detonation products of explosives," *Combustion, Explosion, and Shock Waves*, vol. 26, no. 3, pp. 366–368, 1990.

[76] O. Shenderova, V. Zhirnov, and D. Brenner, "Carbon nanostructures," *Critical Reviews in Solid State and Material Sciences*, vol. 27, no. 3-4, pp. 227–356, 2002.

[77] Z. Pan, H. Sun, Y. Zhang, and C. Chen, "Harder than diamond: superior indentation strength of wurtzite bn and lonsdaleite," *Physical review letters*, vol. 102, no. 5, p. 055503, 2009.

[78] A. Vul' and O. Shenderova, *Detonation Nanodiamonds: Science and Applications*. Pan Stanford, 2014.

[79] F. H. Ree, N. W. Winter, J. N. Glosli, and J. A. Viecelli, "Kinetics and thermodynamic behavior of carbon clusters under high pressure and high temperature," *Physica B: Condensed Matter*, vol. 265, no. 1, pp. 223–229, 1999.

[80] V. N. Mochalin, O. Shenderova, D. Ho, and Y. Gogotsi, "The properties and applications of nanodiamonds," *Nature nanotechnology*, vol. 7, no. 1, pp. 11–23, 2012.

[81] E. Ōsawa, "Monodisperse single nanodiamond particulates," *Pure and Applied Chemistry*, vol. 80, no. 7, pp. 1365–1379, 2008.

[82] "Crystallinity of diamond." `http://www.jhaj.net/jasjeet/tcad/Learn1/l1a_files/image001.gif`. Accessed: 12-02-2016.

[83] C. Nebel, "Electronic properties of cvd diamond," *Semiconductor Science and Technology*, vol. 18, no. 3, p. S1, 2003.

[84] J. E. Butler and A. V. Sumant, "The cvd of nanodiamond materials," *Chemical Vapor Deposition*, vol. 14, no. 7-8, pp. 145–160, 2008.

[85] W. Gajewski, P. Achatz, O. A. Williams, K. Haenen, E. Bustarret, M. Stutzmann, and J. A. Garrido, "Electronic and optical properties of boron-doped nanocrystalline diamond films," *Physical Review B*, vol. 79, no. 4, p. 045206, 2009.

[86] O. A. Williams, M. Nesladek, M. Daenen, S. Michaelson, A. Hoffman, E. Osawa, K. Haenen, and R. Jackman, "Growth, electronic properties and applications of nanodiamond," *Diamond and Related Materials*, vol. 17, no. 7, pp. 1080–1088, 2008.

[87] O. A. Williams, "Nanocrystalline diamond," *Diamond and Related Materials*, vol. 20, no. 5, pp. 621–640, 2011.

[88] J. E. Butler and I. Oleynik, "A mechanism for crystal twinning in the growth of diamond by chemical vapour deposition," *Philosophical Transactions of the Royal Society of London A: Mathematical, Physical and Engineering Sciences*, vol. 366, no. 1863, pp. 295–311, 2008.

[89] H. Eyring, *Physical Chemistry: An Advanced Treatise*. No. v. 5 in Physical Chemistry: An Advanced Treatise, Academic Press, 1970.

[90] F. Maier, M. Riedel, B. Mantel, J. Ristein, and L. Ley, "Origin of surface conductivity in diamond," *Physical review letters*, vol. 85, no. 16, p. 3472, 2000.

[91] "Diamond termination." `https://www.tus.ac.jp/tlo/ritann/expert/image/takeshi_kondo_2.jpg`. Accessed: 13-02-2016.

[92] O. A. Williams, J. Hees, C. Dieker, W. Jager, L. Kirste, and C. E. Nebel,

"Size-dependent reactivity of diamond nanoparticles," *ACS nano*, vol. 4, no. 8, pp. 4824–4830, 2010.

[93] K. Buschow, *Encyclopedia of materials : science and technology. 11. Indexes*. No. v. 11, Elsevier, 2001.

[94] R. Wentorf Jr and H. P. Bovenkerk, "Preparation of semiconducting diamonds," *The Journal of Chemical Physics*, vol. 36, no. 8, pp. 1987–1990, 1962.

[95] T. Borst and O. Weis, "Boron-doped homoepitaxial diamond layers: Fabrication, characterization, and electronic applications," *physica status solidi (a)*, vol. 154, no. 1, pp. 423–444, 1996.

[96] K. Ushizawa, K. Watanabe, T. Ando, I. Sakaguchi, M. Nishitani-Gamo, Y. Sato, and H. Kanda, "Boron concentration dependence of raman spectra on {100} and {111} facets of b-doped cvd diamond," *Diamond and Related Materials*, vol. 7, no. 11, pp. 1719–1722, 1998.

[97] S. Yamanaka, H. Watanabe, S. Masai, D. Takeuchi, H. Okushi, and K. Kajimura, "High-quality b-doped homoepitaxial diamond films using trimethylboron," *Japanese journal of applied physics*, vol. 37, no. 10A, p. L1129, 1998.

[98] F. Jia, Y. Bai, F. Qu, J. Zhao, C. Zhuang, and X. Jiang, "Effect of b/c ratio on the physical properties of highly boron-doped diamond films," *Vacuum*, vol. 84, no. 7, pp. 930–934, 2010.

[99] X. Zhang, J. Guo, Y. Yao, R. Wang, G. Chen, W. Zhou, and S. Yu, "p-type doping of diamond films with a novel organoboron source," *Applied Physics A*, vol. 56, no. 5, pp. 425–428, 1993.

[100] P.-N. Volpe, J. Pernot, P. Muret, and F. Omnès, "High hole mobility in boron doped diamond for power device applications," *Applied Physics Letters*, vol. 94, no. 9, p. 2102, 2009.

[101] T. Teraji, H. Wada, M. Yamamoto, K. Arima, and T. Ito, "Highly efficient doping of boron into high-quality homoepitaxial diamond films," *Diamond and related materials*, vol. 15, no. 4, pp. 602–606, 2006.

[102] V. Mortet, M. Daenen, T. Teraji, A. Lazea, V. Vorlicek, J. D'Haen, K. Haenen, and M. D'Olieslaeger, "Characterization of boron doped diamond epilayers grown in a nirim type reactor," *Diamond and Related Materials*, vol. 17, no. 7, pp. 1330–1334, 2008.

[103] R. Edgington, *Diamond at the Brain-Machine Interface*. UCL, 2012.

[104] J.-P. Lagrange, A. Deneuville, and E. Gheeraert, "Activation energy in low compensated homoepitaxial boron-doped diamond films," *Diamond and Related Materials*, vol. 7, no. 9, pp. 1390–1393, 1998.

[105] E. Bustarret, P. Achatz, B. Sacépé, C. Chapelier, C. Marcenat, L. Ortega, and T. Klein, "Metal-to-insulator transition and superconductivity in boron-doped diamond," *Philosophical Transactions of the Royal Society of London A: Mathematical, Physical and Engineering Sciences*, vol. 366, no. 1863, pp. 267–279, 2008.

[106] "Band diagram boron." `http://www.webexhibits.org/causesofcolor/images/content/5z.jpg`. Accessed: 13-02-2016.

[107] R. Farrer, "On the substitutional nitrogen donor in diamond," *Solid State Communications*, vol. 7, no. 9, pp. 685–688, 1969.

[108] M. Nesladek, "Conventional n-type doping in diamond: state of the art and recent progress," *Semiconductor Science and Technology*, vol. 20, no. 2, p. R19, 2005.

[109] S. Koizumi, M. Kamo, Y. Sato, S. Mita, A. Sawabe, A. Reznik, C. Uzan-Saguy, and R. Kalish, "Growth and characterization of phosphorus doped n-type diamond thin films," *Diamond and Related Materials*, vol. 7, no. 2, pp. 540–544, 1998.

[110] S. Kajihara, A. Antonelli, J. Bernholc, and R. Car, "Nitrogen and potential n-type dopants in diamond," *Physical review letters*, vol. 66, no. 15, p. 2010, 1991.

[111] E. Gheeraert, S. Koizumi, T. Teraji, and H. Kanda, "Electronic transitions of electrons bound to phosphorus donors in diamond," *Solid state communications*, vol. 113, no. 10, pp. 577–580, 2000.

[112] D. Saada, J. Adler, and R. Kalish, "Sulfur: A potential donor in diamond," *Applied Physics Letters*, vol. 77, no. 6, p. 878, 2000.

[113] L. Wang and A. Zunger, "Phosphorus and sulphur doping of diamond," *Physical Review B*, vol. 66, no. 16, p. 161202, 2002.

[114] A. Chaudary, *Electronic properties and applications of nanodiamond*. UCL, 2012.

[115] R. U. Martinelli, "Infrared photoemission from silicon," *Applied Physics Letters*, vol. 16, no. 7, pp. 261–262, 1970.

[116] J. Scheer and J. Van Laar, "Gaas-cs: A new type of photoemitter," *Solid State Communications*, vol. 3, no. 8, pp. 189–193, 1965.

[117] R. Nemanich, P. Baumann, and J. Weide, "Diamond negative electron affinity surfaces, structures and devices," tech. rep., Government Printing Office, Washington, DC (United States), 1995.

[118] K. M. O'Donnell, T. L. Martin, M. T. Edmonds, A. Tadich, L. Thomsen, J. Ristein, C. I. Pakes, N. A. Fox, and L. Ley, "Photoelectron emission from lithiated diamond," *physica status solidi (a)*, vol. 211, no. 10, pp. 2209–2222, 2014.

[119] J. Yater and A. Shih, "Interpretation of low-energy feature in energy spectra measured from surfaces with low or negative electron affinity," *Applied surface science*, vol. 143, no. 1, pp. 219–222, 1999.

[120] P. Baumann and R. Nemanich, "Surface cleaning, electronic states and electron affinity of diamond (100),(111) and (110) surfaces," *Surface science*, vol. 409, no. 2, pp. 320–335, 1998.

[121] C. H. Goeting, F. Marken, A. Gutiérrez-Sosa, R. G. Compton, and J. S. Foord, "Electrochemically induced surface modifications of boron-doped diamond electrodes: an x-ray photoelectron spectroscopy study," *Diamond and Related Materials*, vol. 9, no. 3, pp. 390–396, 2000.

[122] K. O'Donnell, T. Martin, N. Fox, and D. Cherns, "Ab initio investigation of lithium on the diamond c (100) surface," *Physical Review B*, vol. 82, no. 11, p. 115303, 2010.

[123] W. E. Pickett, "Negative electron affinity and low work function surface: cesium on oxygenated diamond (100)," *Physical review letters*, vol. 73, no. 12, p. 1664, 1994.

[124] L. Pauling, *The Nature of the Chemical Bond and the Structure of Molecules and Crystals: An Introduction to Modern Structural Chemistry*. George Fisher Baker Non-Resident Lecture Series, Cornell University Press, 1960.

[125] L. C. Allen, "Electronegativity is the average one-electron energy of the valence-shell electrons in ground-state free atoms," *Journal of the American Chemical Society*, vol. 111, no. 25, pp. 9003–9014, 1989.

[126] A. Allred, "Electronegativity values from thermochemical data," *Journal of inorganic and nuclear chemistry*, vol. 17, no. 3, pp. 215–221, 1961.

[127] K. P. Loh, X. Xie, S. Yang, J. Pan, and P. Wu, "A spectroscopic study of the negative electron affinity of cesium oxide-coated diamond (111) and theoretical calculation of the surface density-of-states on oxygenated diamond (111)," *Diamond and related materials*, vol. 11, no. 7, pp. 1379–1384, 2002.

[128] M. Kataoka, C. Zhu, F. A. Koeck, and R. J. Nemanich, "Thermionic elec-

tron emission from nitrogen-doped homoepitaxial diamond," *Diamond and Related Materials*, vol. 19, no. 2, pp. 110–113, 2010.

[129] Y.-R. Luo, *Comprehensive handbook of chemical bond energies*. CRC press, 2007.

[130] "Bond dissociation energy." `B.Rusic,http://atct.anl.gov/index.html`. Accessed: 16-12-2010.

[131] Z. Zhang and J. T. Yates Jr, "Band bending in semiconductors: chemical and physical consequences at surfaces and interfaces," *Chemical reviews*, vol. 112, no. 10, pp. 5520–5551, 2012.

[132] J. B. Miller and G. R. Brandes, "Effects of dopant concentration, crystallographic orientation, and crystal morphology on secondary electron emission from diamond," *Journal of applied physics*, vol. 82, no. 9, pp. 4538–4545, 1997.

[133] A. Shih, J. Yater, P. Pehrsson, J. Butler, C. Hor, and R. Abrams, "Secondary electron emission from diamond surfaces," *Journal of applied physics*, vol. 82, no. 4, pp. 1860–1867, 1997.

[134] "Electron volt definition." `http://www.britannica.com/science/electron-volt`. Accessed: 17-05-2016.

[135] D. Takeuchi, M. Riedel, J. Ristein, and L. Ley, "Surface band bending and surface conductivity of hydrogenated diamond," *Physical Review B*, vol. 68, no. 4, p. 041304, 2003.

[136] J. Yater, J. Shaw, B. Pate, and T. Feygelson, "Sub-band gap photo-enhanced secondary electron emission from high-purity single-crystal chemical-vapor-deposited diamond," *Journal of Applied Physics*, vol. 119, no. 5, p. 055703, 2016.

[137] "Modes of see." `http://www.chm.bris.ac.uk/pt/diamond/image/electron-multiplication.gif`. Accessed: 18-05-2016.

[138] "Structure of mcp 1." http://www.made-in-china.com/showroom/product-images/China-Microchannel-Plate-HrheWdodHlkb3Ue-IohxFzjTMCVZ.html. Accessed: 18-05-2016.

[139] "Structure of mcp 2." http://pe1hmm.nl/xx1080/Introduction%20to%20Image%20Intensifier%20Tubes_files/mcp.gif. Accessed: 18-05-2016.

[140] H. Webster, "Possible existence of a neutron," *Nature*, vol. 129, pp. 402–402, 1932.

[141] O. Hahn and F. Straßmann, "Über den nachweis und das verhalten der bei der bestrahlung des urans mittels neutronen entstehenden erdalkalimetalle," *Naturwissenschaften*, vol. 27, no. 1, pp. 11–15, 1939.

[142] "Nuclear fission reaction." http://pe1hmm.nl/xx1080/Introduction%20to%20Image%20Intensifier%20Tubes_files/mcp.gif. Accessed: 27-02-16.

[143] E. Lewis, *Fundamentals of Nuclear Reactor Physics*. Elsevier/Academic Press, 2008.

[144] A. Einstein, "Does the inertia of a body depend upon its energy-content," *Annalen der Physik*, vol. 18, no. 13, pp. 639–641, 1905.

[145] B. Watt, "Energy spectrum of neutrons from thermal fission of u 235," *Physical Review*, vol. 87, no. 6, p. 1037, 1952.

[146] J. Frenje, C. Li, F. Seguin, D. Casey, R. Petrasso, D. McNabb, P. Navratil, S. Quaglioni, T. Sangster, V. Y. Glebov, *et al.*, "Measurements of the differential cross sections for the elastic n- h 3 and n- h 2 scattering at 14.1 mev by using an inertial confinement fusion facility," *Physical review letters*, vol. 107, no. 12, p. 122502, 2011.

[147] "Diamond detectors limited public relations report." http://www.npl.co.uk/upload/pdf/091104_nuc_galbiati.pdf. Accessed: 27-02-16.

[148] R. Scott, J. Pauwels, R. Eykens, J. Byrne, P. Dawber, and D. Gilliam, "The characterisation of 10b and 6lif reference deposits by the measurement of neutron induced charged particle reactions," *Nuclear Instruments and Methods in Physics Research Section A: Accelerators, Spectrometers, Detectors and Associated Equipment*, vol. 314, no. 1, pp. 163–170, 1992.

[149] "Universita di roma diamond report." `http://www-norhdia.gsi.de/talks/4th/G_Verona-Rinati.pdf`. Accessed: 27-02-16.

[150] S. Almaviva, M. Marinelli, E. Milani, G. Prestopino, A. Tucciarone, C. Verona, G. Verona-Rinati, M. Angelone, D. Lattanzi, M. Pillon, *et al.*, "Thermal and fast neutron detection in chemical vapor deposition single-crystal diamond detectors," *Journal of applied physics*, vol. 103, no. 5, p. 054501, 2008.

[151] D. Meier, W. Adam, C. Bauer, E. Berdermann, P. Bergonzo, F. Bogani, E. Borchi, M. Bruzzi, C. Colledani, J. Conway, *et al.*, "Proton irradiation of cvd diamond detectors for high-luminosity experiments at the lhc," *Nuclear Instruments and Methods in Physics Research Section A: Accelerators, Spectrometers, Detectors and Associated Equipment*, vol. 426, no. 1, pp. 173–180, 1999.

[152] S. Field, "Early and late normal tissue damage after fast neutrons," *International Journal of Radiation Oncology* Biology* Physics*, vol. 3, pp. 203–210, 1977.

[153] R. F. Barth, A. H. Soloway, R. G. Fairchild, and R. M. Brugger, "Boron neutron capture therapy for cancer. realities and prospects.," *Cancer*, vol. 70, no. 12, pp. 2995–3007, 1992.

[154] J. Chadwick, "Bakerian lecture. the neutron," *Proceedings of the Royal Society of London. Series A, Containing Papers of a Mathematical and Physical Character*, vol. 142, no. 846, pp. 1–25, 1933.

[155] J. Marion and J. Fowler, *C. H. Johnson, page 247, Fast Neutron Physics.* No. pt. 1, 1960.

[156] J. Marion and J. Fowler, *Calvert et al., page 123, Fast Neutron Physics.* No. pt. 1, 1960.

[157] J. Marion and J. Fowler, *R. S. White, page 297, Fast Neutron Physics.* No. pt. 1, 1960.

[158] J. Marion and J. Fowler, *Swartz et al., page 211, Fast Neutron Physics.* No. pt. 1, 1960.

[159] J. Marion and J. Fowler, *Batchelor et al., page 413, Fast Neutron Physics.* No. pt. 1, 1960.

[160] D. Delacroix, J. Guerre, P. Leblanc, and C. Hickman, "Radionuclide and radiation protection data handbook 2002," *Radiation Protection Dosimetry*, vol. 98, no. 1, pp. 1–168, 2002.

[161] G. F. Knoll, *Radiation detection and measurement.* John Wiley & Sons, 2010.

[162] W. P. Jesse and J. Sadauskis, "The range-energy curves for alpha-particles and protons," *Physical review*, vol. 78, no. 1, p. 1, 1950.

[163] A. Teitsma, "Air scattering of neutrons," *Nuclear Instruments and Methods*, vol. 174, no. 1-2, pp. 325–326, 1980.

[164] F. Brooks and H. Klein, "Neutron spectrometry—historical review and present status," *Nuclear Instruments and Methods in Physics Research Section A: Accelerators, Spectrometers, Detectors and Associated Equipment*, vol. 476, no. 1, pp. 1–11, 2002.

[165] T. Crane and M. Baker, "Neutron detectors," *Passive Nondestructive Assay of Nuclear Materials*, pp. 379–406, 1991.

[166] T. Feder, "Us government agencies work to minimize damage due to helium-3 shortfall," *Physics today*, vol. 62, no. 10, p. 21, 2009.

[167] R. T. Kouzes, J. H. Ely, L. E. Erikson, W. J. Kernan, A. T. Lintereur, E. R. Siciliano, D. L. Stephens, D. C. Stromswold, R. M. Van Ginhoven, and M. L. Woodring, "Neutron detection alternatives to 3 he for national security applications," *Nuclear Instruments and Methods in Physics Research Section A: Accelerators, Spectrometers, Detectors and Associated Equipment*, vol. 623, no. 3, pp. 1035–1045, 2010.

[168] J. A. Brinkman, "On the nature of radiation damage in metals," *Journal of Applied Physics*, vol. 25, no. 8, pp. 961–970, 1954.

[169] A. Carlson, "The neutron cross section standards, evaluations and applications," *Metrologia*, vol. 48, no. 6, p. S328, 2011.

[170] C. L. Peacock and R. G. Wilkinson, "The disintegration of scandium 46, gold 198, and tungsten 1 8 5, 1 8 7," *Physical Review*, vol. 74, no. 3, p. 297, 1948.

[171] E. Zschech, G. Auerswald, E. Klinkenberg, and B. Novgorodov, "Nuclear instrument and methods in physics research," *A*, vol. 308, p. 255, 1991.

[172] V. F. Sears, "Neutron scattering lengths and cross sections," *Neutron news*, vol. 3, no. 3, pp. 26–37, 1992.

[173] P. Bergonzo, A. Brambilla, D. Tromson, C. Mer, B. Guizard, F. Foulon, and V. Amosov, "Cvd diamond for radiation detection devices," *Diamond and related materials*, vol. 10, no. 3, pp. 631–638, 2001.

[174] H. Spieler, "Introduction to radiation-resistant semiconductor devices and circuits," in *AIP Conference Proceedings*, pp. 23–49, IOP Institute of Physics Publishing LTD, 1997.

[175] "Universita di roma diamond report." `http://www.intechopen.com/source/html/9889/media/image1.jpg`. Accessed: 14-03-16.

[176] M. Pomorski, E. Berdermann, M. Ciobanu, A. Martemyianov, P. Moritz, M. Rebisz, and B. Marczewska, "Characterisation of single crystal cvd diamond particle detectors for hadron physics experiments," *physica status solidi (a)*, vol. 202, no. 11, pp. 2199–2205, 2005.

[177] G. Schmid, J. Koch, R. Lerche, and M. Moran, "A neutron sensor based on single crystal cvd diamond," *Nuclear Instruments and Methods in Physics Research Section A: Accelerators, Spectrometers, Detectors and Associated Equipment*, vol. 527, no. 3, pp. 554–561, 2004.

[178] H. Umezawa, T. Saito, N. Tokuda, M. Ogura, S.-G. Ri, H. Yoshikawa, and S.-i. Shikata, "Leakage current analysis of diamond schottky barrier diode," *Applied physics letters*, vol. 90, no. 7, p. 073506, 2007.

[179] H. Pernegger, S. Roe, P. Weilhammer, V. Eremin, H. Frais-Kölbl, E. Griesmayer, H. Kagan, S. Schnetzer, R. Stone, W. Trischuk, *et al.*, "Charge-carrier properties in synthetic single-crystal diamond measured with the transient-current technique," *Journal of Applied Physics*, vol. 97, no. 7, p. 073704, 2005.

[180] "Definition of composite." `http://dictionary.cambridge.org/dictionary/english/composite`. Accessed: 24-03-16.

[181] A. Paipetis and V. Kostopoulos, *Carbon Nanotube Enhanced Aerospace Composite Materials: A New Generation of Multifunctional Hybrid Structural Composites*. Solid Mechanics and Its Applications, Springer Netherlands, 2012.

[182] M. Narkis, "Crazing in glassy polymers: Studies on polymer-glass bead composites," *Polymer Engineering & Science*, vol. 15, no. 4, pp. 316–320, 1975.

[183] L. Van Beek and B. Van Pul, "Non-ohmic behavior of carbon black-loaded rubbers," *Carbon*, vol. 2, no. 2, pp. 121–126, 1964.

[184] X.-L. Xie, Y.-W. Mai, and X.-P. Zhou, "Dispersion and alignment of carbon nanotubes in polymer matrix: a review," *Materials Science and Engineering: R: Reports*, vol. 49, no. 4, pp. 89–112, 2005.

[185] J. N. Coleman, U. Khan, W. J. Blau, and Y. K. Gun'ko, "Small but strong: a review of the mechanical properties of carbon nanotube–polymer composites," *Carbon*, vol. 44, no. 9, pp. 1624–1652, 2006.

[186] J. Sandler, M. Shaffer, T. Prasse, W. Bauhofer, K. Schulte, and A. Windle, "Development of a dispersion process for carbon nanotubes in an epoxy matrix and the resulting electrical properties," *Polymer*, vol. 40, no. 21, pp. 5967–5971, 1999.

[187] W. Bauhofer and J. Z. Kovacs, "A review and analysis of electrical percolation in carbon nanotube polymer composites," *Composites Science and Technology*, vol. 69, no. 10, pp. 1486–1498, 2009.

[188] D. Ratna, *Handbook of Thermoset Resins*. Handbook Series, iSmithers, 2009.

[189] K. Street, A. Russell, and F. Bonsang, "Thermal damage effects on delamination toughness of a graphite/epoxy composite," *Composites science and technology*, vol. 32, no. 1, pp. 1–14, 1988.

[190] R. Andrews, D. Jacques, M. Minot, and T. Rantell, "Fabrication of carbon multiwall nanotube/polymer composites by shear mixing," *Macromolecular Materials and Engineering*, vol. 287, no. 6, pp. 395–403, 2002.

[191] S. B. Kharchenko, J. F. Douglas, J. Obrzut, E. A. Grulke, and K. B. Migler, "Flow-induced properties of nanotube-filled polymer materials," *Nature materials*, vol. 3, no. 8, pp. 564–568, 2004.

[192] C. HlNE, J. Kodama, H. Anderson, D. Simonson, J. Wellington, *et al.*, "The toxicology of epoxy resins.," *Arch. Indust. Health*, vol. 17, no. 2, pp. 129–44, 1958.

[193] C. May, *Epoxy Resins: Chemistry and Technology, Second Edition,*. Taylor & Francis, 1987.

[194] R. Bauer, A. C. S. D. of Organic Coatings, and P. Chemistry, *Epoxy resin chemistry II: based on a symposium sponsored by the ACS Division of Organic Coatings and Plastics Chemistry at the 183rd meeting of the American Chemical Society, Las Vegas, Nevada, March 28-April 2, 1982*. ACS symposium series, American Chemical Society, 1983.

[195] A. Durbetaki, "Direct titration of oxirane oxygen with hydrogen bromide in acetic acid," *Analytical Chemistry*, vol. 28, no. 12, pp. 2000–2001, 1956.

[196] D. Ratna, M. Patri, B. Chakraborty, and P. Deb, "Amine-terminated polysulfone as modifier for epoxy resin," *Journal of applied polymer science*, vol. 65, no. 5, pp. 901–907, 1997.

[197] D. Ratna and A. K. Banthia, "Toughened epoxy adhesive modified with acrylate based liquid rubber," *Polymer International*, vol. 49, no. 3, pp. 281–287, 2000.

[198] D. Ratna and G. Simon, "Thermal and mechanical properties of a hydroxyl-functional dendritic hyperbranched polymer and trifunctional epoxy resin blends," *Polymer Engineering & Science*, vol. 41, no. 10, pp. 1815–1822, 2001.

[199] D. Ratna, R. Varley, and G. Simon, "Toughening of trifunctional epoxy using an epoxy-functionalized hyperbranched polymer," *Journal of Applied Polymer Science*, vol. 89, no. 9, pp. 2339–2345, 2003.

[200] "Epoxy resin data." `http://www.leuna-harze.de/fileadmin/user_upload/Datenblaetter/englisch/Resins/T19-36-7e.pdf`. Accessed: 08-04-16.

[201] "Epoxy resin data." `http://www.leuna-harze.de/fileadmin/user_`

upload/Datenblaetter/englisch/Hardeners/H10-31e.pdf. Accessed: 08-04-16.

[202] "Pdms as food additives." http://apps.who.int/food-additives-contaminants-jecfa-database/chemical.aspx?chemID=2755. Accessed: 08-04-16.

[203] "Fda summary of safety and effectiveness, pma p990074." http://www.accessdata.fda.gov/cdrh_docs/pdf/p990074b.pdf. Accessed: 08-04-16.

[204] "Pdms polymerisation reaction." http://education.mrsec.wisc.edu/background/PDMS/images/pdmsrx.gif. Accessed: 08-04-16.

[205] J. Lötters, W. Olthuis, P. Veltink, and P. Bergveld, "The mechanical properties of the rubber elastic polymer polydimethylsiloxane for sensor applications," *Journal of Micromechanics and Microengineering*, vol. 7, no. 3, p. 145, 1997.

[206] S. Clarson and J. Semlyen, *Siloxane Polymers*. Polymer science and technology series, Prentice Hall, 1993.

[207] "Sylgard 184 silicone elastomer, form no., 11-3184b-01, 2014." http://www.dowcorning.com/DataFiles/090276fe80190b08.pdf. Accessed: 08-04-16.

[208] E. Keough, W. Mackey, R. Connolly, T. Foxall, K. Ramberg-Laskaris, J. McCullough, T. O'Donnell, and A. Callow, "The interaction of blood components with pdms (polydimethylsiloxane) and ldpe (low-density polyethylene) in a baboon ex vivo arteriovenous shunt model," *Journal of biomedical materials research*, vol. 19, no. 5, pp. 577–587, 1985.

[209] M.-C. Bélanger and Y. Marois, "Hemocompatibility, biocompatibility, inflammatory and in vivo studies of primary reference materials low-density polyethylene and polydimethylsiloxane: A review," *Journal of biomedical materials research*, vol. 58, no. 5, pp. 467–477, 2001.

[210] D. Green, C. Cheetham, C. Reed, L. Dembo, and G. O'Driscoll, "Assessment of brachial artery blood flow across the cardiac cycle: retrograde flows during cycle ergometry," *Journal of Applied Physiology*, vol. 93, no. 1, pp. 361–368, 2002.

[211] T. J. McCoy, T. G. Grasel, A. Z. Okkema, and S. L. Cooper, "Acute and chronic canine ex vivo blood interactions with nhlbi-dtb primary reference materials," *Biomaterials*, vol. 10, no. 4, pp. 243–250, 1989.

[212] B. Huang, Y. Marois, R. Roy, M. Julien, and R. Guidoin, "Cellular reaction to the vascugraft® polyesterurethane vascular prosthesis: in vivo studies in rats," *Biomaterials*, vol. 13, no. 4, pp. 209–216, 1992.

[213] A. Akoum, Y. Marois, R. Roy, M. King, R. Guidoin, M. Sigot, and M.-F. S. Luizard, "Use of myxalin for improving vascular graft healing: evaluation of biocompatibility in rats," *Journal of Investigative Surgery*, vol. 5, no. 2, pp. 129–141, 1992.

[214] S. I. Ertel, B. D. Ratner, A. Kaul, M. B. Schway, and T. A. Horbett, "In vitro study of the intrinsic toxicity of synthetic surfaces to cells," *Journal of biomedical materials research*, vol. 28, no. 6, pp. 667–675, 1994.

[215] S. L. Goodman, "Sheep, pig, and human platelet-material interactions with model cardiovascular biomaterials," *Journal of biomedical materials research*, vol. 45, no. 3, pp. 240–250, 1999.

[216] D. Armani, C. Liu, and N. Aluru, "Re-configurable fluid circuits by pdms elastomer micromachining," in *Micro Electro Mechanical Systems, 1999. MEMS'99. Twelfth IEEE International Conference on*, pp. 222–227, Ieee, 1999.

[217] D. van Krevelen, *Properties of Polymers*. Elsevier Science, 2012.

[218] A. Heilmann, *Polymer Films with Embedded Metal Nanoparticles*. Physics and Astronomy Online Library, Springer, 2003.

[219] N. Hu, Y. Karube, C. Yan, Z. Masuda, and H. Fukunaga, "Tunneling effect in a polymer/carbon nanotube nanocomposite strain sensor," *Acta Materialia*, vol. 56, no. 13, pp. 2929–2936, 2008.

[220] Y. Ando and T. Itoh, "Calculation of transmission tunneling current across arbitrary potential barriers," *Journal of applied physics*, vol. 61, no. 4, pp. 1497–1502, 1987.

[221] C. Neugebauer and M. Webb, "Electrical conduction mechanism in ultrathin, evaporated metal films," *Journal of Applied Physics*, vol. 33, no. 1, pp. 74–82, 1962.

[222] B. P. Grady, "The use of solution viscosity to characterize single-walled carbon nanotube dispersions," *Macromolecular Chemistry and Physics*, vol. 207, no. 23, pp. 2167–2169, 2006.

[223] A. Thess, R. Lee, P. Nikolaev, and H. Dai, "Crystalline ropes of metallic carbon nanotubes," *Science*, vol. 273, no. 5274, p. 483, 1996.

[224] J. M. Brown, D. P. Anderson, R. S. Justice, K. Lafdi, M. Belfor, K. L. Strong, and D. W. Schaefer, "Hierarchical morphology of carbon single-walled nanotubes during sonication in an aliphatic diamine," *Polymer*, vol. 46, no. 24, pp. 10854–10865, 2005.

[225] B. Hornbostel, P. Pötschke, J. Kotz, and S. Roth, "Single-walled carbon nanotubes/polycarbonate composites: basic electrical and mechanical properties," *physica status solidi (b)*, vol. 243, no. 13, pp. 3445–3451, 2006.

[226] A. Moisala, Q. Li, I. Kinloch, and A. Windle, "Thermal and electrical conductivity of single-and multi-walled carbon nanotube-epoxy composites," *Composites science and technology*, vol. 66, no. 10, pp. 1285–1288, 2006.

[227] M. Park, H. Kim, J. P. Youngblood, S. W. Han, E. Verplogen, and A. J. Hart, "Excellent dispersion of mwcnts in peo polymer achieved through a

simple and potentially cost-effective evaporation casting," *Nanotechnology*, vol. 22, no. 41, p. 415703, 2011.

[228] Y. Li and H. Shimizu, "Toward a stretchable, elastic, and electrically conductive nanocomposite: morphology and properties of poly [styrene-b-(ethylene-co-butylene)-b-styrene]/multiwalled carbon nanotube composites fabricated by high-shear processing," *Macromolecules*, vol. 42, no. 7, pp. 2587–2593, 2009.

[229] I. Cotiuga, F. Picchioni, U. S. Agarwal, D. Wouters, J. Loos, and P. J. Lemstra, "Block-copolymer-assisted solubilization of carbon nanotubes and exfoliation monitoring through viscosity," *Macromolecular rapid communications*, vol. 27, no. 13, pp. 1073–1078, 2006.

[230] K. Lu, R. Lago, Y. Chen, M. Green, P. Harris, and S. Tsang, "Mechanical damage of carbon nanotubes by ultrasound," *Carbon*, vol. 34, no. 6, pp. 814–816, 1996.

[231] J. Sandler, J. Kirk, I. Kinloch, M. Shaffer, and A. Windle, "Ultra-low electrical percolation threshold in carbon-nanotube-epoxy composites," *Polymer*, vol. 44, no. 19, pp. 5893–5899, 2003.

[232] "High shear mixing theory." `https://www.ika.com/media/pdf/6b/6a/a1/ika_ut_18_b.pdf`. pg. 16, Accessed: 24-10-2016.

[233] B. McCarthy, J. Coleman, R. Czerw, A. Dalton, M. In Het Panhuis, A. Maiti, A. Drury, P. Bernier, J. Nagy, B. Lahr, *et al.*, "A microscopic and spectroscopic study of interactions between carbon nanotubes and a conjugated polymer," *The Journal of Physical Chemistry B*, vol. 106, no. 9, pp. 2210–2216, 2002.

[234] W. Ding, A. Eitan, F. Fisher, X. Chen, D. Dikin, R. Andrews, L. Brinson, L. Schadler, and R. Ruoff, "Direct observation of polymer sheathing in

carbon nanotube-polycarbonate composites," *Nano letters*, vol. 3, no. 11, pp. 1593–1597, 2003.

[235] D. Qian, E. C. Dickey, R. Andrews, and T. Rantell, "Load transfer and deformation mechanisms in carbon nanotube-polystyrene composites," *Applied physics letters*, vol. 76, no. 20, pp. 2868–2870, 2000.

[236] O. Meincke, D. Kaempfer, H. Weickmann, C. Friedrich, M. Vathauer, and H. Warth, "Mechanical properties and electrical conductivity of carbon-nanotube filled polyamide-6 and its blends with acrylonitrile/butadiene/styrene," *Polymer*, vol. 45, no. 3, pp. 739–748, 2004.

[237] H. Miyagawa and L. T. Drzal, "Thermo-physical and impact properties of epoxy nanocomposites reinforced by single-wall carbon nanotubes," *Polymer*, vol. 45, no. 15, pp. 5163–5170, 2004.

[238] M. Kannerstein and J. Churg, "Pathology of carcinoma of the lung associated with asbestos exposure," *Cancer*, vol. 30, no. 1, pp. 14–21, 1972.

[239] K. Donaldson, R. Aitken, L. Tran, V. Stone, R. Duffin, G. Forrest, and A. Alexander, "Carbon nanotubes: a review of their properties in relation to pulmonary toxicology and workplace safety," *Toxicological Sciences*, vol. 92, no. 1, pp. 5–22, 2006.

[240] S. Toyokuni, "Genotoxicity and carcinogenicity risk of carbon nanotubes," *Advanced drug delivery reviews*, vol. 65, no. 15, pp. 2098–2110, 2013.

[241] Z. Li, T. Hulderman, R. Salmen, R. Chapman, S. S. Leonard, S.-H. Young, A. Shvedova, M. I. Luster, and P. P. Simeonova, "Cardiovascular effects of pulmonary exposure to single-wall carbon nanotubes," *Environmental health perspectives*, pp. 377–382, 2007.

[242] A. K. Patlolla, S. M. Hussain, J. J. Schlager, S. Patlolla, and P. B. Tchounwou, "Comparative study of the clastogenicity of functionalized and non-

functionalized multiwalled carbon nanotubes in bone marrow cells of swiss-webster mice," *Environmental toxicology*, vol. 25, no. 6, pp. 608–621, 2010.

[243] A. Shevedova, E. Kisin, A. Murray, O. Gorelik, S. Arepalli, A. Hubbs, R. Mercer, P. Kohavong, N. Sussman, J. Jin, *et al.*, "Inhalation vs. aspiration of single-walled carbon nanotubes in c57/6 mice: inflammation, fibrosis, oxidative stress, and mutagenesis," *Am. J. Physiol. Lung Cell. Mol. Physiol*, vol. 295, pp. L552–L565, 2008.

[244] H. Deka, N. Karak, R. D. Kalita, and A. K. Buragohain, "Biocompatible hyperbranched polyurethane/multi-walled carbon nanotube composites as shape memory materials," *Carbon*, vol. 48, no. 7, pp. 2013–2022, 2010.

[245] B. Sitharaman, X. Shi, X. F. Walboomers, H. Liao, V. Cuijpers, L. J. Wilson, A. G. Mikos, and J. A. Jansen, "In vivo biocompatibility of ultra-short single-walled carbon nanotube/biodegradable polymer nanocomposites for bone tissue engineering," *Bone*, vol. 43, no. 2, pp. 362–370, 2008.

[246] "Definition of heart failure." `http://www.nhs.uk/conditions/Heart-failure/Pages/Introduction.aspx`. Accessed: 18-04-16.

[247] V. L. Roger, "Epidemiology of heart failure," *Circulation research*, vol. 113, no. 6, pp. 646–659, 2013.

[248] A. Nohria, E. Lewis, and L. W. Stevenson, "Medical management of advanced heart failure," *Jama*, vol. 287, no. 5, pp. 628–640, 2002.

[249] A. P. Ambrosy, G. C. Fonarow, J. Butler, O. Chioncel, S. J. Greene, M. Vaduganathan, S. Nodari, C. S. Lam, N. Sato, A. N. Shah, *et al.*, "The global health and economic burden of hospitalizations for heart failure: lessons learned from hospitalized heart failure registries," *Journal of the American College of Cardiology*, vol. 63, no. 12, pp. 1123–1133, 2014.

[250] A. L. Bui, T. B. Horwich, and G. C. Fonarow, "Epidemiology and risk

profile of heart failure," *Nature Reviews Cardiology*, vol. 8, no. 1, pp. 30–41, 2011.

[251] W. H. Organization *et al.*, "Globocan 2012: Estimated cancer incidence, mortality and prevalence worldwide in 2012," *Lyon, France: International Agency for Research on Cancer.[Links]*, 2014.

[252] "Hiv/aids statistics." `http://apps.who.int/gho/data/node.main.623?lang=en`. Accessed: 18-04-16.

[253] P. Ponikowski, S. D. Anker, K. F. AlHabib, M. R. Cowie, T. L. Force, S. Hu, T. Jaarsma, H. Krum, V. Rastogi, L. E. Rohde, *et al.*, "Heart failure: preventing disease and death worldwide," *ESC Heart Failure*, vol. 1, no. 1, pp. 4–25, 2014.

[254] H. Brenner, A. M. Bouvier, R. Foschi, M. Hackl, I. K. Larsen, V. Lemmens, L. Mangone, and S. Francisci, "Progress in colorectal cancer survival in europe from the late 1980s to the early 21st century: the eurocare study," *International Journal of Cancer*, vol. 131, no. 7, pp. 1649–1658, 2012.

[255] M. Coleman, D. Forman, H. Bryant, J. Butler, B. Rachet, C. Maringe, U. Nur, E. Tracey, M. Coory, J. Hatcher, *et al.*, "Cancer survival in australia, canada, denmark, norway, sweden, and the uk, 1995–2007 (the international cancer benchmarking partnership): an analysis of population-based cancer registry data," *The Lancet*, vol. 377, no. 9760, pp. 127–138, 2011.

[256] A. Jemal, R. Siegel, J. Xu, E. Ward, *et al.*, "Cancer statistics, 2010," *cA Cancer J Clin*, vol. 61, no. 2, pp. 133–134, 2011.

[257] D. Lloyd-Jones, R. J. Adams, T. M. Brown, M. Carnethon, S. Dai, G. De Simone, T. B. Ferguson, E. Ford, K. Furie, C. Gillespie, *et al.*, "Heart disease and stroke statistics—2010 update a report from the american heart association," *Circulation*, vol. 121, no. 7, pp. e46–e215, 2010.

[258] T. Neumann, J. Biermann, A. Neumann, J. Wasem, G. Ertl, R. Dietz, and R. Erbel, "Heart failure: the commonest reason for hospital admission in germany," *Dtsch Arztebl Int*, vol. 106, no. 16, pp. 269–275, 2009.

[259] E. Bocchi, F. Braga, S. Ferreira, L. Rohde, W. d. Oliveira, D. d. Almeida, M. C. Moreira, R. Bestetti, S. Bordignon, C. Azevedo, *et al.*, "Iii brazilian guidelines on chronic heart failure," *Arquivos brasileiros de cardiologia*, vol. 93, no. 1 Suppl 1, p. 3, 2009.

[260] P. A. Heidenreich, N. M. Albert, L. A. Allen, D. A. Bluemke, J. Butler, G. C. Fonarow, J. S. Ikonomidis, O. Khavjou, M. A. Konstam, T. M. Maddox, *et al.*, "Forecasting the impact of heart failure in the united states a policy statement from the american heart association," *Circulation: Heart Failure*, vol. 6, no. 3, pp. 606–619, 2013.

[261] K. Sliwa and B. M. Mayosi, "Recent advances in the epidemiology, pathogenesis and prognosis of acute heart failure and cardiomyopathy in africa," *Heart*, pp. heartjnl–2013, 2013.

[262] T. P. Abraham, V. L. Dimaano, and H.-Y. Liang, "Role of tissue doppler and strain echocardiography in current clinical practice," *Circulation*, vol. 116, no. 22, pp. 2597–2609, 2007.

[263] C. Tschöpe, M. Kašner, D. Westermann, R. Gaub, W. C. Poller, and H.-P. Schultheiss, "The role of nt-probnp in the diagnostics of isolated diastolic dysfunction: correlation with echocardiographic and invasive measurements," *European heart journal*, vol. 26, no. 21, pp. 2277–2284, 2005.

[264] "The nobel prize in medicine 1956." `http://www.nobelprize.org/nobel_prizes/medicine/laureates/1956/forssmann-bio.html`. Accessed: 20-04-2016.

[265] "Diagram of cardiac catheterisation." `http://lh5.ggpht.com/_byy_`

1rr1vTI/S_VOMWp2jiI/AAAAAAAAAh4/7Bq7VH7pPTo/image_thumb.png?imgmax=800. Accessed: 20-04-2016.

[266] C. Binanay, R. Califf, V. Hasselblad, C. O'Connor, M. Shah, G. Sopko, L. Stevenson, G. Francis, C. Leier, and L. Miller, "Evaluation study of congestive heart failure and pulmonary artery catheterization effectiveness: the escape trial.," *Jama*, vol. 294, no. 13, pp. 1625–1633, 2005.

[267] P. Edwards, R. Bull, and R. Coulden, "Ct measurement of main pulmonary artery diameter.," *The British journal of radiology*, vol. 71, no. 850, pp. 1018–1020, 1998.

[268] E. R. Weibel and D. M. Gomez, "Architecture of the human lung," *Science*, vol. 137, no. 3530, pp. 577–585, 1962.

[269] N. G. Pandian, A. Weintraub, A. Kreis, S. Schwartz, M. Konstam, and D. Salem, "Intracardiac, intravascular, two-dimensional, high-frequency ultrasound imaging of pulmonary artery and its branches in humans and animals.," *Circulation*, vol. 81, no. 6, pp. 2007–2012, 1990.

[270] "Definition of embolism." http://www.nhs.uk/conditions/pulmonary-embolism/Pages/Introduction.aspx. Accessed: 21-04-2016.

[271] A. Johnson and A. B. Malik, "Effects of different-size microemboli on lung fluid and protein exchange," *Journal of Applied Physiology*, vol. 51, no. 2, pp. 461–464, 1981.

[272] W. M. Kirkendall, A. C. Burton, F. H. Epstein, and E. D. Freis, "Recommendations for human blood pressure determination by sphygmomanometers," *Circulation*, vol. 36, no. 6, pp. 980–988, 1967.

[273] G. Parati, S. Mendis, D. Abegunde, R. Asmar, S. Mieke, A. Murray, B. Shengelia, G. Steenvoorden, G. Van Montfrans, and E. O'Brien, "Recommendations for blood pressure measuring devices for office/clinic use in

low resource settings," *Blood pressure monitoring*, vol. 10, no. 1, pp. 3–10, 2005.

[274] "Definition of systolic blood pressure." http://medical-dictionary.thefreedictionary.com/Systolic+blood+pressure. Accessed: 27-04-2016.

[275] "Definition of diastolic blood pressure." http://medical-dictionary.thefreedictionary.com/diastolic+blood+pressure. Accessed: 27-04-2016.

[276] "World health organisation, mean systolic blood pressure trends by who regions, 2016." http://apps.who.int/gho/data/view.main.12467REG?lang=en. Accessed: 23-04-2016.

[277] Y. Tomiyama, K. Yoshinaga, S. Fujii, N. Ochi, M. Inoue, M. Nishida, K. Aziki, T. Horie, C. Katoh, and N. Tamaki, "Accurate quantitative measurements of brachial artery cross-sectional vascular area and vascular volume elastic modulus using automated oscillometric measurements: comparison with brachial artery ultrasound," *Hypertension Research*, vol. 38, no. 7, pp. 478–484, 2015.

[278] F. Weidinger, M. Frick, H. F. Alber, H. Ulmer, S. P. Schwarzacher, and O. Pachinger, "Association of wall thickness of the brachial artery measured with high-resolution ultrasound with risk factors and coronary artery disease," *The American journal of cardiology*, vol. 89, no. 9, pp. 1025–1029, 2002.

[279] "Sphygmomanometer." https://qph.is.quoracdn.net/main-qimg-a583a90abd8f71683038d50335b6af52?convert_to_webp=true. Accessed: 27-04-2016.

[280] J. Booth, "A short history of blood pressure measurement.," *Proceedings of the Royal Society of Medicine*, vol. 70, no. 11, p. 793, 1977.

[281] K. G. Schoenly, N. H. Haskell, D. K. Mills, C. Bieme-Ndi, K. Larsen, and Y. Lee, "Recreating death's acre in the school yard: using pig carcasses as model corpses to teach concepts of forensic entomology & ecological succession," *The American Biology Teacher*, vol. 68, no. 7, pp. 402–410, 2006.

[282] J. Kwon and G. Subhash, "Compressive strain rate sensitivity of ballistic gelatin," *Journal of biomechanics*, vol. 43, no. 3, pp. 420–425, 2010.

[283] K. G. Sellier, B. P. Kneubuehl, and L. C. Haag, "Wound ballistics and the scientific background.," *The American Journal of Forensic Medicine and Pathology*, vol. 16, no. 4, p. 355, 1995.

[284] L. Geddes and L. Baker, "The specific resistance of biological material—a compendium of data for the biomedical engineer and physiologist," *Medical and biological engineering*, vol. 5, no. 3, pp. 271–293, 1967.

[285] D. Cronin and C. Falzon, "Characterization of 10% ballistic gelatin to evaluate temperature, aging and strain rate effects," *Experimental mechanics*, vol. 51, no. 7, pp. 1197–1206, 2011.

[286] N. Spencer and J. Moore, *Encyclopedia of Chemical Physics and Physical Chemistry: Fundamentals*. Encyclopedia of Chemical Physics and Physical Chemistry, Institute of Physics Pub., 2001.

[287] C. V. Raman and K. S. Krishnan, "A new type of secondary radiation," *Nature*, vol. 121, pp. 501–502, 1928.

[288] "Raman spectroscopy diagram." `https://en.wikipedia.org/wiki/Raman_spectroscopy`. Accessed: 27-08-2016.

[289] D. Long, "Early history of the raman effect," *International reviews in physical chemistry*, vol. 7, no. 4, pp. 317–349, 1988.

[290] Z. Sun, J. Shi, B. Tay, and S. Lau, "Uv raman characteristics of nanocrystalline diamond films with different grain size," *Diamond and related materials*, vol. 9, no. 12, pp. 1979–1983, 2000.

[291] F. Tuinstra and J. L. Koenig, "Raman spectrum of graphite," *The Journal of Chemical Physics*, vol. 53, no. 3, pp. 1126–1130, 1970.

[292] S. Veprek, F.-A. Sarott, and Z. Iqbal, "Effect of grain boundaries on the raman spectra, optical absorption, and elastic light scattering in nanometer-sized crystalline silicon," *Physical Review B*, vol. 36, no. 6, p. 3344, 1987.

[293] A. Muchnikov, A. Vikharev, A. Gorbachev, D. Radishev, V. Blank, and S. Terentiev, "Homoepitaxial single crystal diamond growth at different gas pressures and mpacvd reactor configurations," *Diamond and Related Materials*, vol. 19, no. 5, pp. 432–436, 2010.

[294] L. Hong-Dong, Z. Guang-Tian, W. Qi-Liang, C. Shao-Heng, L. Bo, L. Jian-Nan, L. Xian-Yi, and J. Zeng-Sun, "High-rate growth and nitrogen distribution in homoepitaxial chemical vapour deposited single-crystal diamond," *Chinese Physics Letters*, vol. 25, no. 5, p. 1803, 2008.

[295] J. H. Luong, K. B. Male, and J. D. Glennon, "Boron-doped diamond electrode: synthesis, characterization, functionalization and analytical applications," *Analyst*, vol. 134, no. 10, pp. 1965–1979, 2009.

[296] "Xps spectroscopy diagram." `https://en.wikipedia.org/wiki/X-ray_photoelectron_spectroscopy`. Accessed: 27-08-2016.

[297] A. J. Bard and I. Rubenstein, *Electroanalytical chemistry: a series of advances*, vol. 19. CRC Press, 1996.

[298] P. Taberna, P. Simon, and J.-F. Fauvarque, "Electrochemical characteristics and impedance spectroscopy studies of carbon-carbon supercapacitors," *Journal of The Electrochemical Society*, vol. 150, no. 3, pp. A292–A300, 2003.

[299] B. Kang and G. Ceder, "Battery materials for ultrafast charging and discharging," *Nature*, vol. 458, no. 7235, pp. 190–193, 2009.

[300] J. Fleig, "The grain boundary impedance of random microstructures: numerical simulations and implications for the analysis of experimental data," *Solid State Ionics*, vol. 150, no. 1, pp. 181–193, 2002.

[301] J. Macdonald and W. Kenan, *Impedance Spectroscopy: Emphasizing Solid Materials and Systems*. Wiley, 1987.

[302] G. Instruments, "Basics of electrochemical impedance spectroscopy," *Gamry Instrument: Warminster, PA, USA*, 2007.

[303] "Impedance diagrams." `http://www.intechopen.com/source/html/46887/media/image3.png`. Accessed: 27-08-2016.

[304] "Randles equivalent circuit." `https://d3i5bpxkxvwmz.cloudfront.net/resized/images/remote/http_s.eeweb.com/members/texas_instruments/blog/2013/04/23/TI-White-Paper-1366755856_222_131.PNG`. Accessed: 27-08-2016.

[305] "Afm spectroscopy diagram." `http://web.physics.ucsb.edu/~hhansma/Image0016-afm.jpg`. Accessed: 27-08-2016.

[306] "Evaporation diagram." `http://web.tuat.ac.jp/~usuilab/English/EVacDepo.gif`. Accessed: 02-09-2016.

[307] R. Behrisch and W. Eckstein, *Sputtering by Particle Bombardment: Experiments and Computer Calculations from Threshold to MeV Energies*. Topics in Applied Physics, Springer Berlin Heidelberg, 2007.

[308] "Sputtering diagram." `http://lnf-wiki.eecs.umich.edu/wiki/images/c/ce/Sputter_Deposition.png`. Accessed: 27-08-2016.

[309] A. Heilmann, *Polymer films with embedded metal nanoparticles*, vol. 52. Springer Science & Business Media, 2013.

[310] C. Gau, C.-Y. Kuo, and H. Ko, "Electron tunneling in carbon nanotube composites," *Nanotechnology*, vol. 20, no. 39, p. 395705, 2009.

[311] T. Chelidze and Y. Gueguen, "Pressure-induced percolation transitions in composites," *Journal of Physics D: Applied Physics*, vol. 31, no. 20, p. 2877, 1998.

[312] W. Li, L. Yu, Y. Zhu, and D. Hua, "External magnetic field induced percolation in polyvinylidene fluoride and nickel composites," *The Journal of Physical Chemistry C*, vol. 114, no. 33, pp. 14004–14007, 2010.

[313] "Epilox t19-36/700." `http://http://www.leuna-harze.de/fileadmin/user_upload/Datenblaetter/englisch/Resins/T19-36-7e.pdf`. Accessed: 28-07-2016.

[314] F. H. Gojny, M. H. Wichmann, B. Fiedler, I. A. Kinloch, W. Bauhofer, A. H. Windle, and K. Schulte, "Evaluation and identification of electrical and thermal conduction mechanisms in carbon nanotube/epoxy composites," *Polymer*, vol. 47, no. 6, pp. 2036–2045, 2006.

[315] I.-H. Chen, C.-C. Wang, and C.-Y. Chen, "Preparation of carbon nanotube (cnt) composites by polymer functionalized cnt under plasma treatment," *Plasma Processes and Polymers*, vol. 7, no. 1, pp. 59–63, 2010.

[316] H. H. So, J. W. Cho, and N. G. Sahoo, "Effect of carbon nanotubes on mechanical and electrical properties of polyimide/carbon nanotubes nanocomposites," *European Polymer Journal*, vol. 43, no. 9, pp. 3750–3756, 2007.

[317] J. Glazer, "Monolayer studies of some ethoxylin resin adhesives and related compounds," *Journal of Polymer Science Part A: Polymer Chemistry*, vol. 13, no. 70, pp. 355–369, 1954.

[318] S. N. S. K. Kaisha, *Nippon Steel Technical Report*. No. nos. 60-63, Nippon Steel Corporation, 1994.

[319] M. Yang, V. Koutsos, and M. Zaiser, "Interactions between polymers and carbon nanotubes: a molecular dynamics study," *The Journal of Physical Chemistry B*, vol. 109, no. 20, pp. 10009–10014, 2005.

[320] B. P. Grady, "Recent developments concerning the dispersion of carbon nanotubes in polymers," *Macromolecular rapid communications*, vol. 31, no. 3, pp. 247–257, 2010.

[321] P.-C. Ma, S.-Y. Mo, B.-Z. Tang, and J.-K. Kim, "Dispersion, interfacial interaction and re-agglomeration of functionalized carbon nanotubes in epoxy composites," *Carbon*, vol. 48, no. 6, pp. 1824–1834, 2010.

[322] J. Zhu, J. Kim, H. Peng, J. L. Margrave, V. N. Khabashesku, and E. V. Barrera, "Improving the dispersion and integration of single-walled carbon nanotubes in epoxy composites through functionalization," *Nano letters*, vol. 3, no. 8, pp. 1107–1113, 2003.

[323] F. H. Gojny, J. Nastalczyk, Z. Roslaniec, and K. Schulte, "Surface modified multi-walled carbon nanotubes in cnt/epoxy-composites," *Chemical physics letters*, vol. 370, no. 5, pp. 820–824, 2003.

[324] W. C. Duer and G. L. Bertrand, "Calorimetric determination of heats of formation of hydrogen bonds," *Journal of the American Chemical Society*, vol. 92, no. 8, pp. 2587–2588, 1970.

[325] M. Castellino, A. Chiolerio, M. I. Shahzad, P. V. Jagdale, and A. Tagliaferro, "Electrical conductivity phenomena in an epoxy resin–carbon-based materials composite," *Composites Part A: Applied Science and Manufacturing*, vol. 61, pp. 108–114, 2014.

[326] S. L. Brown, B. G. Silverman, and W. A. Berg, "Rupture of silicone-gel breast implants: causes, sequelae, and diagnosis," *The Lancet*, vol. 350, no. 9090, pp. 1531–1537, 1997.

[327] "Fda silicon implant removal guidelines." `http://www.fda.gov/MedicalDevices/ProductsandMedicalProcedures/ImplantsandProsthetics/BreastImplants/ucm064106.htm`. Accessed: 24-08-2016.

[328] A. Denniston and P. Murray, *Oxford Handbook of Ophthalmology*. Oxford Medical Handbooks, OUP Oxford, 2009.

[329] S. Myerson, R. Choudhury, and A. Mitchell, *Emergencies in Cardiology*. Ei Series, OUP Oxford, 2009.

[330] D. Katritsis, B. Gersh, P. Camm, and W. Gersh, *Clinical Cardiology: Current Practice Guidelines*. Oxford University Press, USA, 2016.

[331] "Ika ultra-turrax t18 basic." `http://www.ika.com/ika/product_art/manual/ika_ut_18_b.pdf`. Accessed: 25-07-16.

[332] "Us national health statistics report, no.10, pg 25-26, 2008." `http://www.cdc.gov/nchs/data/nhsr/nhsr010.pdf`. Accessed: 24-08-2016.

[333] C. Martin, J. Sandler, M. Shaffer, M.-K. Schwarz, W. Bauhofer, K. Schulte, and A. Windle, "Formation of percolating networks in multi-wall carbon-nanotube–epoxy composites," *Composites Science and Technology*, vol. 64, no. 15, pp. 2309–2316, 2004.

[334] A. Nogales, G. Broza, Z. Roslaniec, K. Schulte, I. Šics, B. S. Hsiao, A. Sanz, M. C. García-Gutiérrez, D. R. Rueda, C. Domingo, *et al.*, "Low percolation threshold in nanocomposites based on oxidized single wall carbon nanotubes and poly (butylene terephthalate)," *Macromolecules*, vol. 37, no. 20, pp. 7669–7672, 2004.

[335] R. Socher, B. Krause, M. T. Müller, R. Boldt, and P. Pötschke, "The influence of matrix viscosity on mwcnt dispersion and electrical properties in different thermoplastic nanocomposites," *Polymer*, vol. 53, no. 2, pp. 495–504, 2012.

[336] Y. Wang, L. Zhang, Y. Fan, D. Jiang, and L. An, "Stress-dependent piezoresistivity of tunneling-percolation systems," *Journal of materials science*, vol. 44, no. 11, pp. 2814–2819, 2009.

[337] T. K. Kim, J. K. Kim, and O. C. Jeong, "Measurement of nonlinear mechanical properties of pdms elastomer," *Microelectronic Engineering*, vol. 88, no. 8, pp. 1982–1985, 2011.

[338] F. Gojny, M. Wichmann, U. Köpke, B. Fiedler, and K. Schulte, "Carbon nanotube-reinforced epoxy-composites: enhanced stiffness and fracture toughness at low nanotube content," *Composites Science and Technology*, vol. 64, no. 15, pp. 2363–2371, 2004.

[339] M.-F. Yu, O. Lourie, M. J. Dyer, K. Moloni, T. F. Kelly, and R. S. Ruoff, "Strength and breaking mechanism of multiwalled carbon nanotubes under tensile load," *Science*, vol. 287, no. 5453, pp. 637–640, 2000.

[340] H. Wagner, O. Lourie, Y. Feldman, and R. Tenne, "Stress-induced fragmentation of multiwall carbon nanotubes in a polymer matrix," *Applied physics letters*, vol. 72, no. 2, pp. 188–190, 1998.

[341] D. Hecht, L. Hu, and G. Gruner, "Conductivity scaling with bundle length and diameter in single walled carbon nanotube networks," *Applied Physics Letters*, vol. 89, no. 13, pp. 133112–133112, 2006.

[342] H. L. Li-wei, M. Saeed, D. Talmor, R. Mark, and A. Malhotra, "Methods of blood pressure measurement in the icu," *Critical care medicine*, vol. 41, no. 1, p. 34, 2013.

[343] Z. Chai, X. Zheng, and X. Sun, "Preparation of polymer microspheres from solutions," *Journal of Polymer Science Part B: Polymer Physics*, vol. 41, no. 2, pp. 159–165, 2003.

[344] D. A. Shea and D. Morgan, "The helium-3 shortage: Supply, demand, and options for congress," Congressional Research Service, Library of Congress, 2010.

[345] G. Lindström, "Radiation damage in silicon detectors," *Nuclear Instruments*

and Methods in Physics Research Section A: Accelerators, Spectrometers, Detectors and Associated Equipment, vol. 512, no. 1, pp. 30–43, 2003.

[346] S. Lovesey, *Theory of Neutron Scattering from Condensed Matter: Nuclear scattering*. International series of monographs on physics, Clarendon Press, 1984.

[347] W. Pfeiffer, G. Schlossbauer, W. Knoll, B. Farago, A. Steyer, and E. Sackmann, "Ultracold neutron scattering study of local lipid mobility in bilayer membranes," *Journal de Physique*, vol. 49, no. 7, pp. 1077–1082, 1988.

[348] D. M. Shaw, "Prompt gamma neutron activation analysis," *Journal of Neutron Research*, vol. 7, no. 3, 4, pp. 181–194, 1999.

[349] *Journal of Radioanalytical Chemistry*. No. v. 68-69, Elsevier Sequoia, 1982.

[350] S. R. Evett, R. C. Schwartz, J. A. Tolk, and T. A. Howell, "Soil profile water content determination: Spatiotemporal variability of electromagnetic and neutron probe sensors in access tubes," *Vadose Zone Journal*, vol. 8, no. 4, pp. 926–941, 2009.

[351] J. A. Coderre and G. M. Morris, "The radiation biology of boron neutron capture therapy," *Radiation research*, vol. 151, no. 1, pp. 1–18, 1999.

[352] B. Fisher, J. Abdurashitov, K. Coakley, V. Gavrin, D. Gilliam, J. Nico, A. Shikhin, A. Thompson, D. Vecchia, and V. Yants, "Fast neutron detection with 6 li-loaded liquid scintillator," *Nuclear Instruments and Methods in Physics Research Section A: Accelerators, Spectrometers, Detectors and Associated Equipment*, vol. 646, no. 1, pp. 126–134, 2011.

[353] J. Parker Jr, D. Feldman, and M. Ashkin, "Raman scattering by silicon and germanium," *Physical Review*, vol. 155, no. 3, p. 712, 1967.

[354] B. Pan, J. Xiao, J. Li, P. Liu, C. Wang, and G. Yang, "Carbyne with finite length: The one-dimensional sp carbon," *Science advances*, vol. 1, no. 9, p. e1500857, 2015.

[355] J. C. Seitz, J. D. Pasteris, and I.-M. Chou, "Raman spectroscopic characterization of gas mixtures; i, quantitative composition and pressure determination of ch 4, n 2 and their mixtures," *American Journal of Science*, vol. 293, no. 4, pp. 297–321, 1993.

[356] G. Panta and D. Subedi, "Electrical characterization of aluminum (al) thin films measured by using four-point probe method," *Kathmandu University journal of science, Engineering and technology*, vol. 8, no. 2, pp. 31–36, 2013.

[357] P. Bergonzo, A. Brambilla, D. Tromson, C. Mer, B. Guizard, R. Marshall, and F. Foulon, "Cvd diamond for nuclear detection applications," *Nuclear Instruments and Methods in Physics Research Section A: Accelerators, Spectrometers, Detectors and Associated Equipment*, vol. 476, no. 3, pp. 694–700, 2002.

[358] "Mcp diagram." `http://pe1hmm.nl/xx1080/Introduction%20to%20Image%20Intensifier%20Tubes_files/mcp.gif`. Accessed: 18-05-2016.

[359] P. Ascarelli, E. Cappelli, F. Pinzari, M. Rossi, S. Salvatori, P. Merli, and A. Migliori, "Secondary electron emission from diamond: Physical modeling and application to scanning electron microscopy," *Journal of Applied Physics*, vol. 89, no. 1, pp. 689–696, 2001.

[360] D. Trucchi, C. Scilletta, E. Cappelli, P. Merli, S. Zoffoli, G. Mattei, and P. Ascarelli, "Optimization of the performance of cvd diamond electron multipliers," *Diamond and related materials*, vol. 15, no. 4, pp. 827–832, 2006.

[361] O. A. Williams, M. Daenen, J. D'Haen, K. Haenen, J. Maes, V. Moshchalkov, M. Nesládek, and D. Gruen, "Comparison of the growth and properties of ultrananocrystalline diamond and nanocrystalline diamond," *Diamond and related materials*, vol. 15, no. 4, pp. 654–658, 2006.

[362] Y. Hayashi, W. Drawl, and R. Messier, "Temperature dependence of nucleation density of chemical vapor deposition diamond," *Japanese journal of applied physics*, vol. 31, no. 2B, p. L193, 1992.

[363] R. L. Harniman, O. J. Fox, W. Janssen, S. Drijkoningen, K. Haenen, and P. W. May, "Direct observation of electron emission from grain boundaries in cvd diamond by peakforce-controlled tunnelling atomic force microscopy," *Carbon*, vol. 94, pp. 386–395, 2015.

[364] D. Malta, J. Posthill, T. Humphreys, R. Thomas, G. Fountain, R. Rudder, G. Hudson, M. Mantini, and R. Markunas, "Exposure of diamond to atomic hydrogen: secondary electron emission and conductivity effects," *MRS Online Proceedings Library Archive*, vol. 339, 1994.

[365] B. D. Thoms, P. E. Pehrsson, and J. E. Butler, "A vibrational study of the adsorption and desorption of hydrogen on polycrystalline diamond," *Journal of applied physics*, vol. 75, no. 3, pp. 1804–1810, 1994.

[366] A. Shih and C. Hor, "Secondary emission properties as a function of the electron incidence angle," *IEEE Transactions on Electron Devices*, vol. 40, no. 4, pp. 824–829, 1993.